



HAL
open science

**Excitation and fragmentation of C_nN^+ ($n=1-3$)
molecules in collisions with He atoms at intermediate
velocity; fundamental aspects and application to
astrochemistry**

Thejus Mahajan

► **To cite this version:**

Thejus Mahajan. Excitation and fragmentation of C_nN^+ ($n=1-3$) molecules in collisions with He atoms at intermediate velocity; fundamental aspects and application to astrochemistry. Atomic and Molecular Clusters [physics.atm-clus]. Université Paris Saclay (COMUE), 2018. English. NNT : 2018SACLS311 . tel-02301992

HAL Id: tel-02301992

<https://theses.hal.science/tel-02301992>

Submitted on 1 Oct 2019

HAL is a multi-disciplinary open access archive for the deposit and dissemination of scientific research documents, whether they are published or not. The documents may come from teaching and research institutions in France or abroad, or from public or private research centers.

L'archive ouverte pluridisciplinaire **HAL**, est destinée au dépôt et à la diffusion de documents scientifiques de niveau recherche, publiés ou non, émanant des établissements d'enseignement et de recherche français ou étrangers, des laboratoires publics ou privés.

Excitation and fragmentation of C_nN^+ ($n=1-3$) molecules in collisions with He atoms at intermediate velocity; fundamental aspects and application to astrochemistry

Thèse de doctorat de l'Université Paris-Saclay
préparée à l'Université Paris-Sud

École doctorale n°572 Ondes et Matière (EDOM),
Spécialité de doctorat: Lasers, molécules, rayonnement
atmosphérique

Thèse présentée et soutenue à Orsay, le 28 septembre 2018, par

Thejus Mahajan

Composition du jury:

Alain Dubois Professeur, Université Pierre-et-Marie-Curie	Président
Jean-Christophe Loison Directeur de recherche, ISM Bordeaux	Rapporteur
Patrick Rousseau Maître de conférences, Université de Caen Normandie	Rapporteur
Séverine Boyé-Péronne Professeure, Université Paris-Sud	Examinatrice
Karine Béroff Directrice de recherche, ISMO Orsay	Directrice de thèse
Bernard Pons Professeur, Université de Bordeaux	Invité

Synthèse

Dans cette thèse nous avons étudié des collisions entre des projectiles C_nN^+ ($n=1-3$) et des atomes d'Hélium à vitesse intermédiaire (2.25 u.a). A cette vitesse, proche de la vitesse des électrons sur les couches de valence externes des atomes et molécules, de nombreux processus électroniques prennent place avec une forte probabilité: ionisation (simple et multiple), excitation électronique, capture d'électron (simple et double). Nous avons mesuré les sections efficaces absolues de tous ces processus.

Un autre aspect intéressant de la collision concerne la fragmentation des molécules excitées, que nous avons également mesurée précisément grâce au dispositif dédié AGAT. L'utilisation de la cinématique inverse (l'objet d'étude étant l'objet accéléré) permet de récolter tous les fragments (cations, anions et neutres) dans un cône angulaire restreint et de les identifier et détecter avec 100% d'efficacité. Les expériences ont été effectuées auprès de l'accélérateur Tandem d'Orsay avec des faisceaux moléculaires C_nN^+ de quelques MeV d'énergie cinétique. Le dispositif AGAT a permis de réaliser les collisions (en condition de collision unique) et de mesurer tout à la fois les sections efficaces des processus et la fragmentation associée.

Parallèlement nous avons simulé ces collisions d'un point de vue théorique en utilisant le modèle à Atomes et Electrons Indépendants (IAE) couplé à des calculs CTMC (Classical Trajectory Monte Carlo). Dans ce modèle la molécule est supposée composée d'atomes (ions) indépendants, placés à la géométrie d'équilibre de la molécule qui est gelée pendant la collision rapide (10^{-16} s). Les probabilités des processus d'excitation électronique, ionisation et capture électronique dans les collisions entre les constituants atomiques et l'Hélium, fonctions du paramètre d'impact de collision, ont été calculées par la méthode CTMC.

Sur cette base, nous avons prédit les sections efficaces des différents processus électroniques qui se sont trouvées être en bon accord avec les mesures, à l'exception de la double capture d'électrons.

Avec le même modèle IAE/CTMC nous avons calculé le dépôt d'énergie dans les molécules associé au processus d'excitation électronique. Pour faire ce calcul nous avons utilisé les probabilités d'excitation électronique dans différents niveaux d'excitation calculées par la méthode CTMC et l'énergie associée à ces niveaux d'excitation atomique extraite des tables NIST. Un bon accord a été obtenu lors de la comparaison avec la distribution d'énergie obtenue en utilisant les rapports de branchement de dissociation mesurés.

Ces expériences nous ont permis de construire des «Breakdown Curves»(BDC), véritables cartes d'identité des molécules qui permettent de prévoir, dans le cadre d'une fragmentation statistique, comment va fragmenter un système dont on connaît l'énergie interne. Avec ces BDC nous avons pu prédire et recommander des rapports de branchement pour les voies de sortie de différents processus physiques et chimiques d'intérêt astrochimique impliquant la formation de complexes moléculaires C_nN ($n=2-3$) et C_nN^+ ($n=2-3$). Les réactions considérées sont : les réactions ion-molécule, les réactions neutre-neutre, la recombinaison dissociative avec des électrons et le processus d'échange de charge en collision avec He^+ . Les prédictions de notre modèle seront insérées dans la base internationale d'astrochimie «Kinetic Data Base for Astrochemistry»KIDA <http://kida.obs.u-bordeaux1.fr>.

Cette thèse a été réalisée dans le cadre de l'Ecole Doctorale Ondes et Matière (EDOM) à l'Institut des Sciences Moléculaires d'Orsay (ISMO), à l'Université Paris-Sud Paris Saclay.

Acknowledgements

This section for acknowledgement section begins and ends with the director of my thesis Dr. Karine Béroff. From the process of my application of Ph.D to the deposit of this thesis to the library of Université Paris-Sud, Karine along with her meticulous nature is of great help. I thank Dr. Béroff for guiding me and helping me in properly installing, in finishing administration and in introducing me to other prominent researchers in the area.

I wish to extend my thanks along with my supervisor to Dr. Marin Chabot and his doctoral student Tijani IdBarkach for the smooth and uninterrupted conduct of experiments at the Tandem accelerator at Orsay. The author wish to acknowledge Dr. Arnaud Le Padellec, Dr. Thibaut Launoy, Dr. Maëlle Bonnin and all the others who helped in conducting the collision experiments at the Tandem accelerator. I thank Dr. Aurélie Jallat for helping me with the data analysis code during the initial phase of my PhD.

I thank Dr. Laurent Tassan-Got for introducing me to DP2, the data analysis software used in this work. Dr. Tassan-Got is credited to be a principal author of this software. It filled in me with great joy and respect to discuss with him the various aspects of DP2. The author used several techniques acquired from Dr. Tassan-Got during the course of this work.

I thank my PhD defence jury; Dr. Alain Dubois, Dr. Jean-Christophe Loison, Dr. Patrick Rousseau, Dr. Séverine Boyé-Péronne and Dr. Bernard Pons for going through the thesis carefully, suggesting corrections and recommendations and being present at the defence to evaluate and assess the extend of this work and the presentation. I also thank the jury for their valuable comments on the various techniques

and tools used in this work.

I thank Dr. Sergio Díaz-Tendero and Dr. Nestor Aguirre for calculating the structure of the projectiles used in this thesis.

The author did the Classical Trajectory Monte Carlo (CTMC) (a theoretical model used here) calculations at Madrid and Bordeaux. I thank Universidad Autónoma de Madrid and Centre Lasers Intenses et Applications, Université de Bordeaux for hosting me and providing with a peaceful working environment during the CTMC calculations. The first phase of the CTMC calculations was done at UAM Madrid. I thank Dr. Clara Illescas, UAM Madrid, for introducing me to the exciting world of CTMC. We had several stimulating discussions and the author had the opportunity to study deeply about CTMC under the guidance of Dr. Clara Illescas. I also acknowledge Alba María Jorge Palacios for helping me during the initial phase of CTMC numerical calculations.

The second phase of the CTMC calculations was done at CELIA, Bordeaux. I thank Dr. Bernard Pons for helping me with the calculations. It was Bernard who watered and manured the seeds of CTMC which were sowed at Madrid. The discussions was stimulating and helped me grow my deep appreciation towards this humble classical method in describing the various processes that takes place during the ion-atom collisions at an intermediate velocity.

Shout out to all the Group-C members of Institut des Sciences Moléculaires d'Orsay (ISMO) and all PhD students of ISMO. I thank Dr. Alain Dubois for an exciting course in "Electronic processes in atomic and molécular collisions" organized in the teaching unit "Ultra" fast dynamics of reactive species" (Master of Chemistry, Sorbonne Université). I thank Dr. Bernard Bourguignon, the present director of ISMO for his valuable and suggestions during the course of my Ph.D. I thank the Informatique team of ISMO headed by Mr. Yves Bergougnoux for helping me with the installation and proper maintenance of the work computer. Special mention to the computer team for their immediate responses to any problems that would hinder the smooth flow of the work. I thank the administrative staff of ISMO and Université Paris-Sud who helped me with a smile with all the administrative tasks.

Special mention to Mme. Marie-Claire Paul who would find a solution to any problem related to the administration.

I thank Centre National de la Recherche Scientifique (CNRS), Ecole Doctorale Ondes et Matière (EDOM), Institut des Sciences moléculaires d'Orsay (ISMO), Université Paris-Sud (Université Paris-Saclay) for financing, providing me with an office and ensuring the smooth conduct of research. I thank the government of France and the people of France for welcoming the author to their country, giving me a taste of the celebrated French culture and professionalism. It is the authors' wish to someday give back something substantial to the French society in return. I thank the Government of India, of which the author is a proud citizen, and its Department of Science and Technology (DST) for all the support throughout the years of my scientific development. I acknowledge my friends and family, I love you all. I thank Nimmi Das A (IISC, Bangalore) for her support during the course of this PhD.

Finally, it is with great respect, I acknowledge once again Dr. Karine Béroff. For whatever difficulty or errors that the reader may find in this thesis is solely attributed to the author missing suggestions or recommendations from Dr. Béroff. They instilled in me deep with love and appreciation for the physics of collisions and the "how to's" of accelerator collisions experiments and data analysis. Special mention to their work culture of which the author tried and failed to copy successfully. It was a substantial task and someday the author wish to be as meticulous and detail eyed as Dr. Béroff.

Contents

0.1	Introduction	7
1	Experimental tools	11
1.1	Principle of the experiment	11
1.2	General view of the experiment	13
1.3	The ion source	13
1.4	The Tandem accelerator	17
1.4.1	Description	17
1.4.2	Production of C_nN^+ beams	18
1.5	The AGAT set-up	20
1.5.1	The entrance slits	20
1.5.2	The collision chamber	21
1.5.3	The analysis chamber	24
1.5.4	The detection chamber	26
1.5.4.1	Presentation	26
1.5.4.2	The detectors	27
1.5.4.3	The detector of neutral fragments	31
1.5.4.3.1	The EPI for current shape analysis technique	32
1.5.4.3.2	The CCD camera	33
1.5.4.4	The detector configurations	34
1.6	Electronics and acquisition	35
1.6.1	Electronics	35
1.6.1.1	Electronics for all detectors but CCD camera	35

1.6.1.2	The electronics of CCD camera	38
1.6.2	Acquisition	38
2	Data analysis	43
2.1	Data formatting and data treatment	43
2.2	The DP2 software	46
2.3	Incomplete events	49
2.4	Removing noise by timing selection	53
2.5	The current signal shape analysis	57
2.6	The CCD treatment	61
2.7	Probabilities and dissociation branching ratios	63
2.7.1	The normalisation procedure	63
2.7.2	Background subtraction	64
2.7.3	Dissociation branching ratios (BRs)	64
2.8	Absolute cross sections	65
2.8.1	The single collision condition	65
2.8.2	The special case of anions	67
3	Modelisation of the collision	71
3.1	Molecule-atom collisions : the Independent Atom and Electron (IAE) model	71
3.1.1	Description of the IAE model	72
3.1.2	IAE code: Cross sections calculations and energy deposit cal- culations	76
3.1.2.1	Cross sections	77
3.1.2.2	Energy deposit by electronic excitation	78
3.2	Atom(ion)-atom collisions : Classical Trajectory Monte Carlo (CTMC) calculations	78
3.2.1	The CTMC approach	78
3.2.1.1	Dynamics	79
3.2.1.2	Initial conditions	80

3.2.1.3	One electron calculations	82
3.2.1.4	Two electron calculations	84
3.2.1.5	The model potentials	85
3.2.2	CTMC probabilities results	87
3.2.2.1	Convergence of probabilities with the number of tra- jectories ($2e^-$ calculations)	87
3.2.2.2	Overview of process probabilities ($1e^-$ calculations) .	88
3.2.2.3	Comparison between $1e^-$ and $2e^-$ calculations (target ionization and excitation)	88
3.2.2.4	Comparison between $1e^-$ and $2e^-$ calculations (pro- jectile ionization and excitation)	89
3.2.2.4.1	The electron-He model potential for $1e^-$ cal- culations	90
3.2.2.4.2	Comparison between $1e^-$ and $2e^-$ calculations	91
3.2.2.5	(n, l) classical cross sections	93
3.2.2.5.1	The classical (r, p) to quantum (n, l) corre- spondence	93
3.2.2.5.2	The $2s - 2p$ excitation process; use of quan- tum results	95
3.2.2.5.3	CTMC predictions for (n, l) cross sections .	96
3.2.2.6	Comparison between CTMC and experiment for total cross sections ($C, C^+, N^+ - He$ collisions)	99
4	Results on cross sections	101
4.1	Experimental results on cross sections	101
4.2	Comparison with IAE/CTMC predictions	104
4.2.1	Geometries of $C_n N^+$ molecules	104
4.2.2	The role of the charge position	109
4.2.3	The role of the molecule shape	111
4.2.4	The role of inner shells	111

4.2.5	Comparison between experiment and IAE/CTMC model for projectile ionization	114
4.2.6	Comparison between experiment and IAE/CTMC model for projectile excitation	115
4.2.7	Comparison between experiment and IAE/CTMC model for projectile neutralization	117
4.2.8	Comparison between experiment and IAE/CTMC model for projectile anionic production	117
4.2.9	Conclusions and future	119
5	Dissociation Branching Ratios	121
5.1	Experimental results on dissociation Branching Ratios (BR)	121
5.1.1	Neutral molecules C_nN ($n = 1 - 3$)	121
5.1.2	Singly charged molecules C_nN^+ ($n=1-3$)	123
5.1.3	Doubly charged molecules C_nN^{++} ($n=1-3$)	125
5.1.4	Highly charged molecules C_nN^{q+} ($n=1-3, q>2$)	127
5.1.5	Anionic molecules C_nN^- ($n=1-3$)	128
5.2	Interpretation of dissociation of C_nN^+ molecules using the energy deposit calculation performed within IAE/CTMC model.	134
5.2.1	Correspondence between the final (n,l) state and the energy of the transition	134
5.2.2	Discrete spectra	138
5.2.3	Convolutated spectra	140
5.2.4	Comparison with the internal energy distribution deduced from experimental branching ratios	142
5.3	Ion Pair dissociation	143
5.4	Conclusions and future	145
6	Application to astrochemistry (paper)	147
7	Conclusion	149

A	CTMC probabilities in C, C^+, N, N^+, - He collisions ($v=2.25$ a.u)	153
A.1	$1e^-$ calculation	154
A.1.1	Target ionization	154
A.1.2	Electron capture and attachment.	155
A.1.3	Projectile ionization ($V1, \alpha \neq 0$)	156
A.1.4	Projectile excitation total ($V1, \alpha \neq 0$)	157
A.1.5	Projectile excitation into final (n, l) states $V1, \alpha \neq 0$	158
A.1.5.1	$C2s$ excitation into final n levels, $1e^-$ calculation ($V1, \alpha \neq 0$)	158
A.1.5.2	C^+2s excitation into final n levels, $1e^-$ calculation ($V1, \alpha \neq 0$)	159
A.1.5.3	$N2s$ excitation into final n levels, $1e^-$ calculation ($V1, \alpha \neq 0$)	160
A.1.5.4	$C2p$ excitation into final n levels, $1e^-$ calculation ($V1, \alpha \neq 0$)	161
A.1.5.5	C^+2p excitation into final n levels, $1e^-$ calculation ($V1, \alpha \neq 0$)	162
A.1.5.6	$N2p$ excitation into final n levels, $1e^-$ calculation ($V1, \alpha \neq 0$)	163
A.2	$2e^-$ calculation	164
A.2.1	Target ionization	164
A.2.2	Projectile ionization	165
A.2.3	Projectile excitation total	166
A.2.4	Projectile excitation into final (n, l) states	167
A.2.4.1	$C2s$ excitation into final n levels, $2e^-$ calculation	167
A.2.4.2	C^+2s excitation into final n levels, $2e^-$ calculation	168
A.2.4.3	$N2s$ excitation into final n levels, $2e^-$ calculation	169
A.2.4.4	$C2p$ excitation into final n levels, $2e^-$ calculation	170
A.2.4.5	C^+2p excitation into final n levels, $2e^-$ calculation	171
A.2.4.6	$N2p$ excitation into final n levels, $2e^-$ calculation	172

B Ion pair dissociation (IPD) branching ratios	173
B.1 Relaxation by IPD of $\{CN^{Q+}\}$ species (Q=0,1)	173
B.2 Relaxation by IPD of $\{C_2N^{Q+}\}$ species (Q=0,1,2,3)	174
B.3 Relaxation by IPD of $\{C_3N^{Q+}\}$ species (Q=0,1,2,3)	175
Bibliography	177
List of Figures	184
List of Tables	190

Excitation and fragmentation of C_nN^+ (n=1-3) molecules in collisions with He atoms at intermediate velocity; fundamental aspects and application to astrochemistry

0.1 Introduction

Significant progresses have been made in the past in the understanding of ion-atom collisions (Bransden and McDowell, 1992). It is usual to distinct three velocity regimes, depending on the ratio between the projectile velocity v_p and the velocity of the active electron v_e , from which different theoretical approaches result. The intermediate velocity regime ($v_p \sim v_e$) is considered as the most difficult to apprehend because all basic electronic processes (electron excitation, ionization, electron capture) have the same order of magnitude and multi-electron processes are large.

The same applies to ion-molecule collisions, with some additional difficulty arising from the multi-center nature of the target. Experimentally, pioneering works in the intermediate and high velocity range were performed in the 1990s on small molecules (Watson and Maurer, 1987; Sampoll et al., 1989, 1992). They were pursued in other groups, notably in France, on carbon clusters (Wohrer et al., 1996), diatomics (Adoui et al., 1999) and triatomics (Moretto-Capelle et al., 2000). A large interest was also drawn on collisions with C_{60} (LeBrun et al., 1994; Tsuchida et al., 1998; Reinköster et al., 2001; Bordenave-Montesquieu et al., 2001, ...). Presently the ion-molecule collision studies remain an active area, as observed for instance at ICPEAC (International Conference on Photonic, Electronic and Atomic Collisions) conferences.

From the theoretical side, collision studies involving molecular targets strongly developed in recent years. One of the reason is the radiobiological motivation since understanding the damage to biological tissues requires to know collisional cross sections. In that context, numerous works have been devoted to the H_2O molecule (Lüdde et al., 2009; Illescas et al., 2011; Murakami et al., 2012b,a) and references

therein. In the theoretical treatments, approximations have to be done. In the works of Lüdde et al. (2009) and Murakami et al. (2012b), a quantum-mechanical approach is used but the dynamics of the collision is performed by developing H_2O molecular orbitals (MOs) on a single center basis (oxygen atom). In Illescas et al. (2011), the molecular structure of H_2O is preserved, in the frame of a classical treatment of the collision (Classical Trajectory Monte Carlo or CTMC approach).

Another approach lies in the Independent Atom and Electron (IAE) model (Wohrer and Watson, 1993; Wohrer et al., 1994). In the IAE model, the molecule is supposed to be made of n independent atoms positioned at the equilibrium geometry of the molecule. In that context, the dynamics of the ion-molecule collision is truly reducible to n ion-atom collisions. In an impact parameter formalism and within the independent electron approximation, multi-electron processes may be derived which is a major interest of the method since these are far from being easily “guessable”. We recently tested the IAE model in collision of C_n^+ carbon clusters with He, Ar targets at intermediate velocity using either CTMC or SCAOCC (semiclassical atomic orbital close coupling) calculations for impact parameter probabilities in ion-atom collisions (Labaigt et al., 2015). In this thesis the IAE/CTMC approach will be further tested for the C_nN^+ ($n=1-3$) - He collisions at intermediate velocity ($v=2.25$ a.u.).

Another aspect of ion-molecule collisions resides in the opening of a new relaxation path for excited molecules by fragmentation. A large part of ion-molecule studies refers to the fragmentation analysis that comprises also fundamental and applied aspects. From the fundamental point of view, some questions addressed are: what is the stability of the molecule in regard of its charge and internal energy? How will the molecule dissociate under such specific conditions? How predictable is the result? To answer those questions we used a dedicated setup, able to record the entire fragmentation as will be shown. Although not presented in this thesis but underway, the large set of fragmentation data may be used to test the statistical fragmentation theories such as the Microcanonical Metropolis Monte Carlo method (M3C) recently generalized to polyatomic systems (Aguirre et al., 2017). From a more applied point of view, we may use these fragmentation data in all situations

where statistical fragmentation occurs. This is an approximation that was assumed in predictions of fragmentation branching ratios of molecular species electronically excited in interstellar and planetary atmospheres.

Astrochemistry deals with the study of the content and evolution of the molecular material in astrophysical environments. Modeling of these environments requires the knowledge of a huge amount of data including kinetic data, rate coefficients and also branching ratios for many physical and chemical processes (Wakelam et al., 2012). In Chabot et al. (2013) it was shown how it was possible to predict those branching ratios through a semiempirical method based on the construction of breakdown curves (internal energy dependent branching ratios). The method, initially applied to carbon and hydrocarbon molecules, has been extended to the case of C_nN and C_nN^+ molecular systems studied in this thesis ($n=2-3$).

The plan of the manuscript is the following:

In chapter 1 are presented the experimental tools used in this work: the Tandem accelerator for producing high energy (MeV) molecular species C_nN^+ ; the AGAT setup for recording their excitation and fragmentation following collision with helium atoms, based on the multicoincident detection of all fragments, including the neutral ones. The choice of C_nN^+ molecules was motivated by their presence in interstellar environments (The Astrochymist*, Cologne Database†, 2018) whereas the choice of helium was motivated by the fact that it is a rather simple partner with only two electrons.

In chapter 2 are presented the methods used for data reduction: the DP2 software allowing the visualization and counting of multicoincident events, the methods for determining the number of impinging fragments on the same detector (resolution of a so-called pile-up event), the determination of absolute target density and absolute cross sections.

Chapter 3 is devoted to the theoretical modelisation of the collision. It describes the Independent Atom and Electron (IAE) model that was used to reduce

*<http://www.astrochymist.org/>

†<http://www.astro.uni-koeln.de/cdms>

the molecule-atom collision to several independent ion-atom collisions. Besides we present the results of the Classical Trajectory Monte Carlo (CTMC) method used for calculating impact parameter probabilities of basic electronic processes in those ion-atom collision systems.

Chapter 4 presents the experimental results concerning the cross sections associated to various electronic processes: single and multi-ionisation cross sections of C_nN^+ projectiles, dissociative electronic excitation cross sections, neutralization cross sections (by single electron capture) and anionic production cross sections (by double electron capture). Comparison with predicted cross sections by the IAE/CTMC model is presented and discussed.

In chapter 5 we present fragmentation branching ratios (BR) for the C_nN^{Q+} species with variable charge state ($Q=-1,0,1,2,3$). For cations ($Q=1$) we compare the internal energies deduced from measured BR with calculation within the IAE/CTMC model. Results concerning ion pair dissociation (IPD) BR are also presented.

Chapter 6 is devoted to the application of these experiments to astrochemistry (paper). Semi-empirical breakdown curves of C_2N , C_3N , C_2N^+ and C_3N^+ molecules are presented and used to predict and to recommend products branching ratios of some processes of astrochemical interest to be included in the KIDA[‡] (Kinetic Database for Astrochemistry) database.

Some conclusions and perspectives are given at the end. Two appendices relating to chapter 3 and chapter 5 are joined.

[‡]<http://kida.obs.u-bordeaux1.fr/>

Chapter 1

Experimental tools

1.1 Principle of the experiment

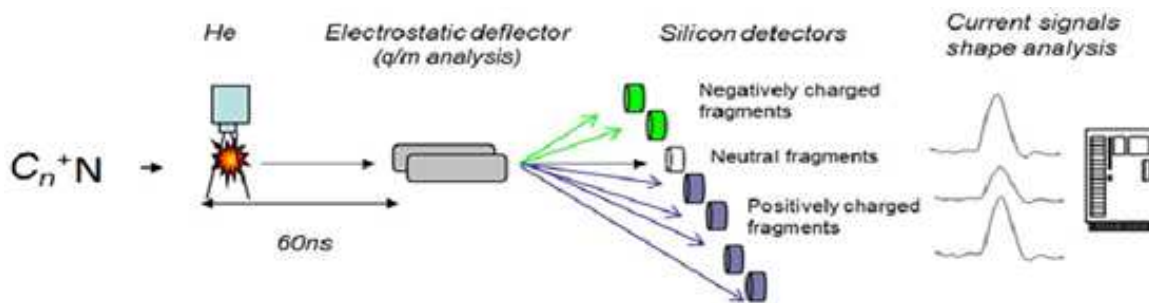


Figure 1-1: Schematic diagram of the AGAT setup

AGAT is the experimental set-up for studying collisions between molecules and atoms in the intermediate velocity regime. The collision is between a molecule accelerated to a velocity of 2.2 au by the accelerator and helium atoms as an effusive jet. The identification and detection of the fragments after collision is realized by using an electrostatic analyser and several detectors placed at suitable positions. The fact to study the projectile instead of the target (inverse kinematics) has several advantages.

The first advantage is that during an inelastic process, the deposited energy is low (a few eV) compared to the energy of the particles (few MeV) and thus the velocity of the center of mass is very little modified. In the laboratory frame, for a fragment

of mass m emitted at 90° from the beam axis with a kinetic energy E_c (eV), the angle of angular opening α is simply written as:

$$\alpha = \tan^{-1}\left(\frac{\sqrt{2E_c/m}}{v_p}\right) \quad (1.1)$$

where v_p is the projectile velocity. Typical value of α is around 1° . It is due to this property that we obtain a solid angle of detection of 4π in the projectile frame with a few (≤ 10) detectors of reasonably small sizes.

In addition to this geometrical aspect, the second advantage of this set-up is the ability to detect all the fragments including the neutral fragments and to identify their mass with silicon detectors. At these velocities, the detectors have an efficiency of 100%. For an incident fragment of mass m and velocity v the detector outputs the kinetic energy. The velocity of the fragments can be considered to be constant before and after fragmentation (a few eV difference compared to few 10^6 eV of incident kinetic energy), then the measured energy is proportional to the mass of the fragment. Each detector intercepts particles of a specific charge to mass (q/m) ratio. Thus we could identify the charge of the impinging fragment by knowing its mass. By doing the same for all the detectors measured in coincidence, we can determine, event by event, the total charge Q of the molecule and thus go back to the process involved in the collision. For example, since the incident projectile is a cation with $Q = 1$, $Q = 0$ after collision corresponds to a single electron capture process, $Q = -1$ to a double electron capture process, $Q = 2$ (resp. 3,4, ...) is due to a single (resp. double, triple, ...) ionization process a.s.o.

We ran 3 experiments with C_nN^+ beams. The first one on March 2015 with CN^+ and C_2N^+ incident beams. The second one in February 2016 with C_3N^+ and C_4N^+ beams and the final one in October 2016 where C_2N^+ and C_3N^+ were done again with a new detector of neutral fragments (CCD camera) in order to totally resolve the fragmentation (see chapter 2). During October 2016 we also worked with an incident N^+ beam of identical velocity ($2.2au$), studied for collision simulation purposes (see chapter 3).

1.2 General view of the experiment

In this chapter, a description of the experimental set-up is given. The experiment comprises of essentially 3 parts (see Figure 1.2):

1. Ion source for the production of C_nN^- ($n \leq 4$) beams.
2. The Tandem accelerator to produce and accelerate the C_nN^+ molecules.
3. AGAT set-up with the associated electronics for collision and data collection.

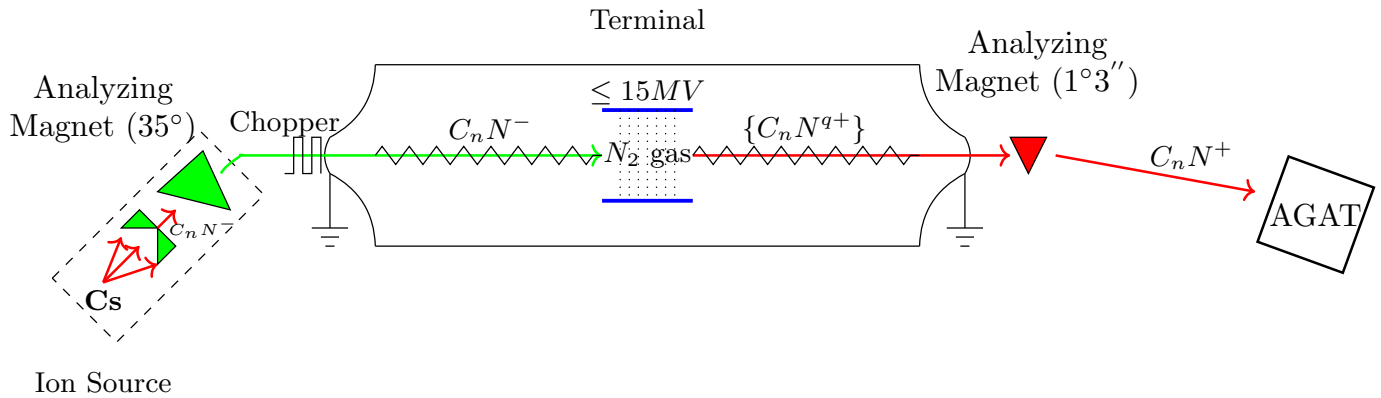


Figure 1-2: A general view of the experimental set-up

1.3 The ion source

A schematic view of the ion source is presented in Figure 1-3. The source HICONEX is one of the sources of ions intended for the production of negative beams at the Tandem d'Orsay. It is mainly dedicated to heavy ions and to atomic ensembles. That's the source we used to get the whole experimental measurements of this thesis. This is a Middletron-type sputtering source. Cesium, heated in a oven at a temperature of the order of 140 °C, will vaporize and then ionize when its passage through a sintered tungsten pellet which is brought to a temperature between 800 °C and 1050 °C. The

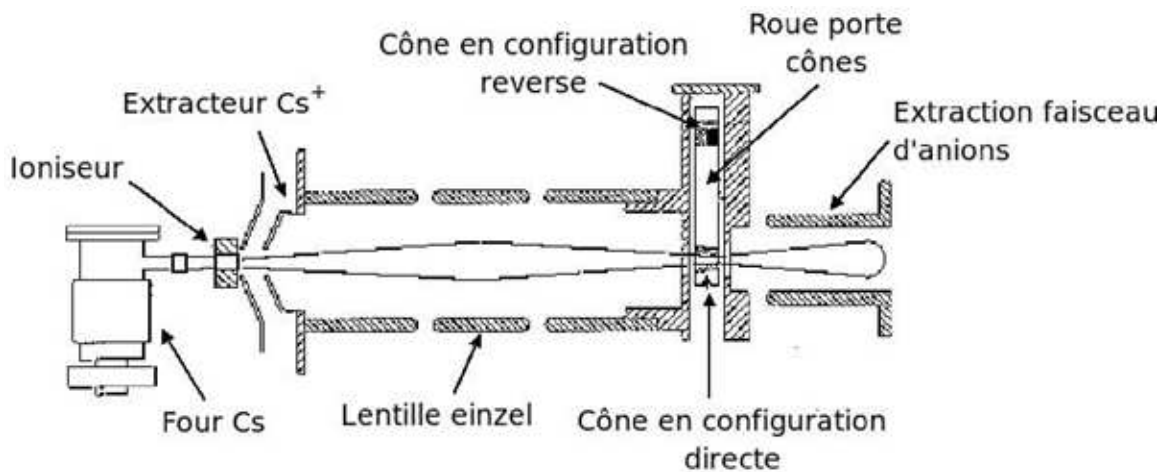


Figure 1-3: View of the HICONEX 384 ion source

beam of Cs^+ then produced is accelerated to a power of the order of 20 keV and will focus with an einzel lens on the material cone. A cone wheel Figure 1-4 allows to choose the type of materials that one wishes to spray. In our experiment, we tested various cones of graphite mixed with TiN and TaN at different concentrations (see below). The vacuum in the source is typically 10^{-7} to 10^{-6} mbar. At the exit of



Figure 1-4: Picture of the wheel cones of the source HICONEX 384

the source at 35° , analyzing magnet allows to analyze the beam of anionic molecules.

The beam is magnetically deflected according to the magnetic rigidity ‘ R ’ defined as

$$R = B\rho = \frac{P}{q} = \frac{mv}{q} = \frac{\sqrt{2E_c m}}{q} \quad (1.2)$$

B = Magnetic field

ρ = Radius of curvature of the species due to this field

P = Momentum

m = Mass

v = Velocity

q = Charge

E_c = Kinetic energy (20 keV due to extraction potential of anions at 20 kV)

On our first run, we used a TiN (Titanium Nitride) and graphite mixture with different concentrations such as 1 : 1, 4 : 1 and 1 : 4. Combination 1 : 1 was chosen as it produced the highest current intensities for the desired beams (see results of 1 : 1 concentration in Table 1.1).

Element (mass in au)	Current (nA)	Magnetic field (G)
CN^- (26)	175	1946
C_2N^- (38)	7	2348
C_3N^- (50)	1.6	2692
C_4N^- (62)	1.5	3000
C_5N^- (74)	1.1	3276

Table 1.1: Beam intensities obtained with a cone made of 50 % of TiN and 50 % of graphite

As Table 1.1 predicts, the magnetic field depends linearly with the square root of mass (see Figure 1-5).

During the second run of February 2016 we realized that C_4N^+ beam was essentially TiN^+ coming from the selection at the source of TiN^- instead of C_4N^- (both having the same mass and TiN^- being much more intense). In October 2016, we tried new cones with TaN (Tantale Nitride) mixed with graphite at various concentrations. Unfortunately the C_nN^- beam intensities with these cones were too small and we had to renounce to a proper C_4N^+ study. As some information is nevertheless

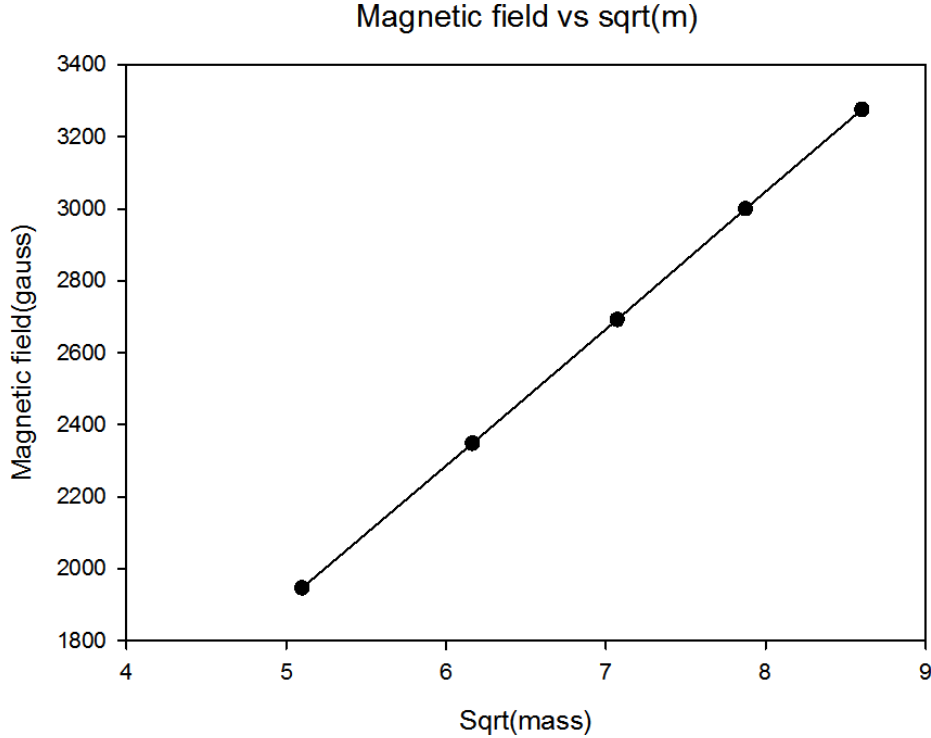


Figure 1-5: Relation between mass and magnetic field for the species of Table 1.1

possibly extractable with this projectile (although not done in this thesis) we will still present in the following some results associated to these species.

As already discussed in previous works on C_n^- clusters (Mezdari, 2005) and $C_nH_m^-$ hydrocarbon molecules (Jallat, 2015) the species produced by sputtering are having some internal energy E^* correlated to the source temperature T_s . From these works T_s can be estimated to be $T_s \sim 3300$ K. The most probable internal energy of a canonical system in thermal equilibrium at a temperature T_s is given by (Andersen et al., 2001):

$$E_p = kT_s(3n - i) \quad (1.3)$$

where T_s is the temperature of the system, n is the number of atoms in the molecule, $i = 5$ (resp. 6) for linear (resp. non-linear) molecules and k is the Boltzmann constant. By knowing the temperature of our source to be ~ 3300 K, we get the most probable internal energy of the molecule (for linear species) reported in Table 1.2. For large molecules, the internal energy distribution is of Gaussian shape with the standard

deviation given by (Andersen et al., 2001):

$$\sigma = kT_s\sqrt{3n - i} \quad (1.4)$$

Values of σ are also given in Table 1.2 for linear species. Finally it is interesting to compare the species' internal energy with its electron affinity EA . Indeed if the internal energy is higher than EA a very small intensity is to be expected. The EA values are given in Table 1.2.

Molecule	Most probable internal energy (eV)	Standard deviation (eV)	C_nN electron affinity (eV)
CN^-	0.28	0.28	3.86 (Bradforth et al., 1993)
C_2N^-	1.14	0.56	2.75 (Garand et al., 2009)
C_3N^-	1.99	0.74	4.31 (Graupner et al., 2006)
C_4N^-	2.84	0.88	3.11 (Garand et al., 2009)

Table 1.2: Species most probable internal energy, standard deviation for the internal energy distribution and C_nN electron affinity.

After selection of the desired C_nN^- species with the 35° magnet, the selected anion is injected in the Tandem accelerator at about 200 keV. Before the Tandem entrance, a chopper allows to pulse the beam (see Figure 1-2). The chopper produces beam pulses of 150 ns large with a frequency of 2.5 MHz or less (f/n). Large n values allow to reduce the beam intensity (we worked with a few thousands of projectile/s or even less when using the CCD camera). With this chopper we also could stop the beam when needed. (see Section 1-6-1-2).

1.4 The Tandem accelerator

1.4.1 Description

The accelerator in the Figure 1-6 is a Van de Graff type electrostatic accelerator. It was commissioned in 1972 by Societe High Voltage Engineering Corporation. The first experiment was conducted on January 1973 (Vergnes, 1977) with atomic ions and in the late 90's with C_{60} clusters.



Figure 1-6: A picture of the Tandem accelerator

The accelerator is comprised of the following parts:

- The accelerator tube, where the particles are transported.
- The voltage terminal and a system to transport charges (Laddertron) in order to increase or decrease the terminal potential. ($V_{max} = 15 \text{ MV}$)
- A gaseous stripper (N_2) placed at the terminal to produce cations from anions by stripping away electrons
- A tank filled with 8 bars of SF_6 gas to isolate the high voltage terminal from surroundings.

1.4.2 Production of $C_n N^+$ beams

The negative ions injected into the accelerator at an energy E_{in} by the injector undergo a first acceleration towards the center of the accelerator by positive high voltage V_t . At the center, the ions are passed through a thin layer of N_2 gas which acts as an electron stripper and render the species positive. They will then be accelerated again

till the end which is grounded.

The final energy of the particles is given by:

$$E = E_{in} + eV_t + neV_t \quad (1.5)$$

Where E_{in} is the energy of anions at the entrance of the accelerator (~ 200 keV), V_t is the potential at the terminal, e is the charge of electron and n is the number of positive charges after stripping ($n = 1$ in our case since C_nN^+ cations are selected).

Numerical application is presented in Table 1.3 using Equation 1.5 for E . Exception arises for N^+ , which cannot be produced from N^- which is highly unstable (ground state self ionizes in 10^{-14} s and some excited levels within ns (Andersen, 2004)). N^+ beam was then produced by fragmentation of CN^+ at the stripper. The energy of N^+ calculates in this case as (velocity is conserved):

$$E = (E_{in} + V_t)\frac{14}{26} + V_t \quad (1.6)$$

Element	Mass (u)	Run	E_{in} (MeV)	V_t (MeV)	E (MV)	E (keV u $^{-1}$)	v (au)
CN^+	26	March 2015	0.20	1.469	3.138	120.7	2.20
C_2N^+	38	March 2015	0.18	2.191	4.562	120.0	2.19
C_2N^+	38	Oct. 2016	0.17	2.186	4.542	119.5	2.19
C_3N^+	50	Feb. 2016	0.18	2.943	6.066	121.3	2.20
C_3N^+	50	Oct. 2016	0.17	2.942	6.054	121.1	2.20
C_4N^+	62	Feb. 2016	0.18	3.673	7.526	121.4	2.20
N^+	14	Oct. 2016	0.18	1.083	1.761	125.8	2.24

Table 1.3: Voltages at the terminal for the production of iso-velocity C_nN^+ species. E is calculated with Equation 1.5, except for N^+ with Equation 1.6 (see text).

It is worth noting that in the stripping process the projectile may gain a little bit of internal energy attributed to the ionization of inner valence shells (Mezdari, 2005). Typical value for the internal energy gained in the stripping process is 1 – 1.5 eV.

At the exit of the Tandem accelerator the beam is reduced using various slits. With the entrance slits of the AGAT set-up, this allows to work with a beam of very small angular divergence (see below). Taking into account the stripping process and

the cuts in the beam size reduce considerably the intensity of cations as compared to anions (roughly 10^3 times smaller).

1.5 The AGAT set-up

The experimental device AGAT (named for AGregat-ATome collision) was schematised in Figure 1-1 and shown on the photo of Figure 1-7.

AGAT is composed of:

- a collision chamber hosting an effusive jet of helium where the collision takes place
- an analysis chamber hosting an electrostatic deflector that deflects the fragments according to their q/m ratio
- a detection chamber where all the detectors are properly positioned in order to detect all the fragments in coincidence

We will describe the successive parts the beam traverses.

1.5.1 The entrance slits

There are two pairs of slits at the entrance of AGAT to reduce the beam size and the beam emittance. We work on a beam size of about 0.1 mm x 0.1 mm and a typical beam angular divergence of less than 0.15 mrad. Before entering the collision chamber, a set of two vertical and horizontal movable slits are used to achieve this. Beam of small dimensions is desirable. Along the vertical axis it allows to cross the jet very near the capillary end where the density is the higher. Along the perpendicular direction the beam dimension should be smaller than the jet size in order to perform a jet profile (see below), necessary for the extraction of absolute cross sections.

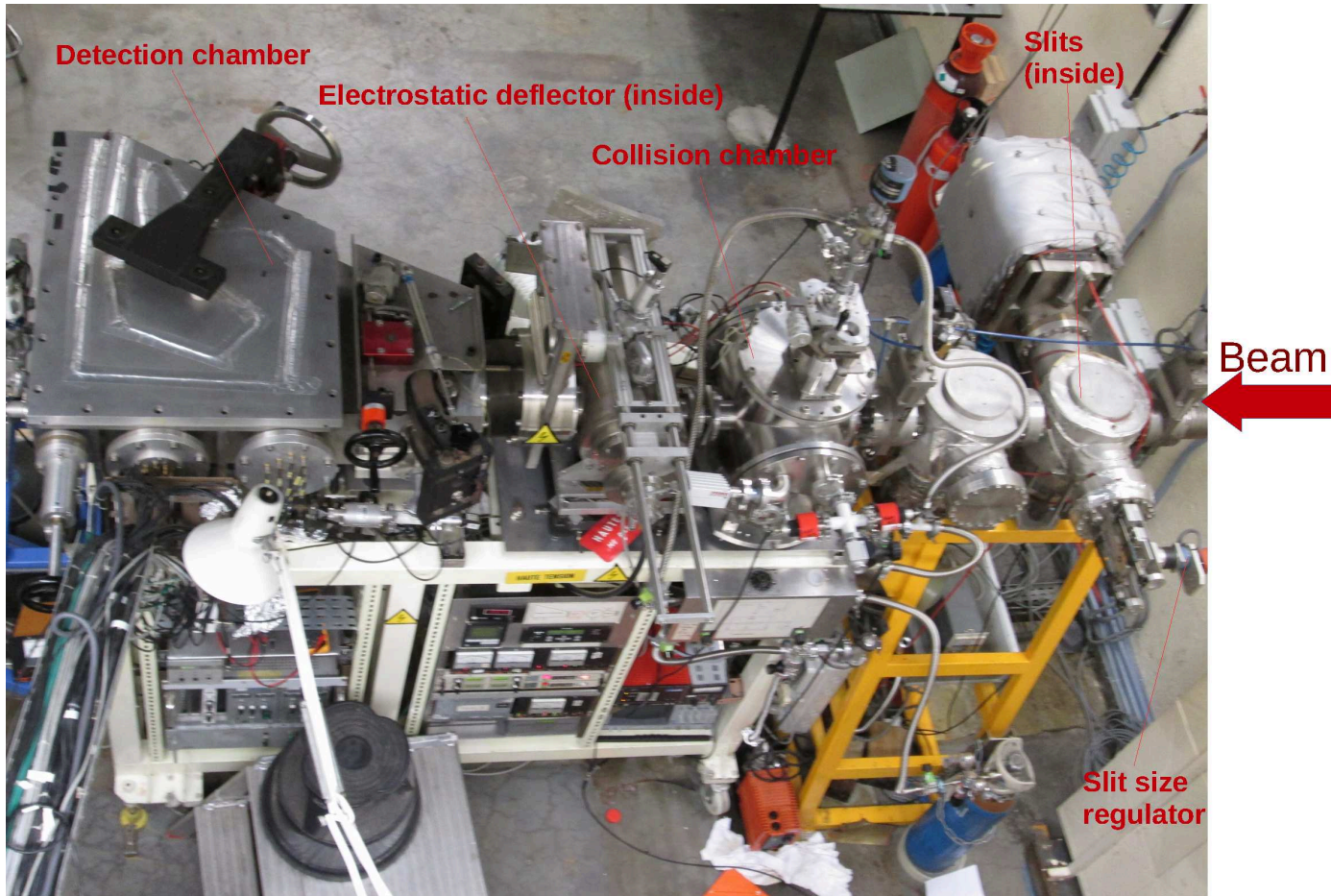


Figure 1-7: Outside view of AGAT set-up

1.5.2 The collision chamber

A view of the interior of the collision chamber is given in Figure 1-8. The gas is injected from the top vertical tube and the incident beam is introduced from the right horizontal tube. The collision happens inside an electrostatic ball which establishes an electrostatic field and that is terminated by a MCP detector. This detector was used only during the run of October 2016 when the detector of neutral fragments was replaced by a CCD camera. Indeed this was imperative to give a start signal or trigger to the CCD camera that would not record the event otherwise. The electric field will accelerate the He^+ ions (few keV) towards the microchannel plates detector which would send a trigger signal to the camera. Basically, microchannel plates or MCP create a cloud of electrons when it is being hit by a particle. Each individual

plate in turn amplifies the charge thus produced and are collected by a terminal. This amplified current signal will act as a trigger to the camera.

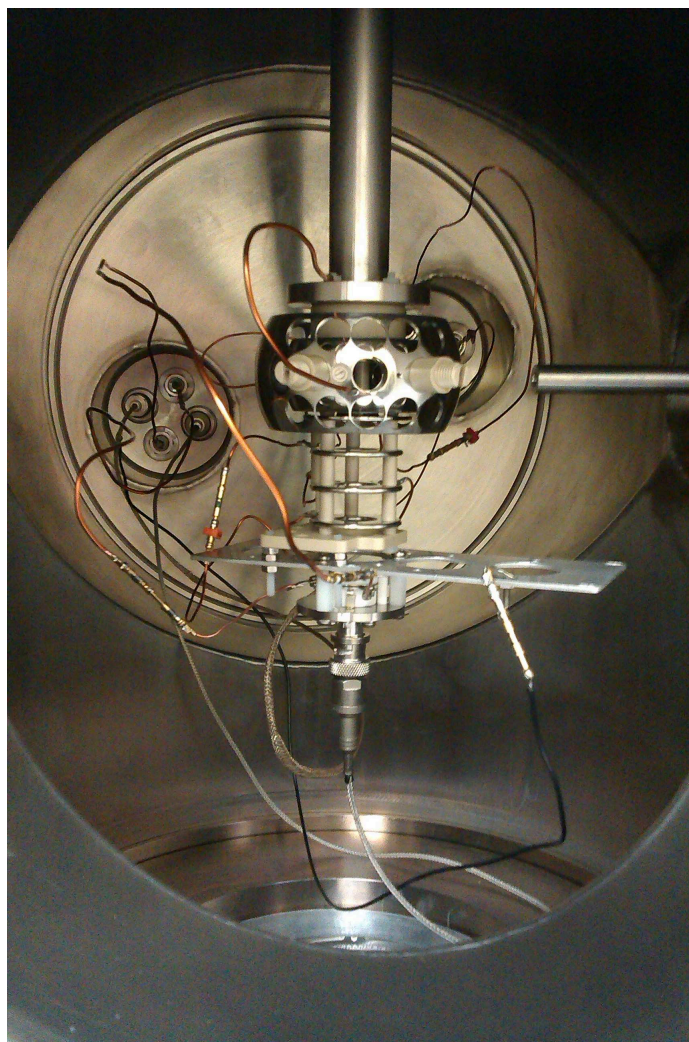


Figure 1-8: Interior of the collision chamber

A capillary tube of 9mm in length and 0.5mm in diameter (not seen on the Figure 1-8 because hidden by the electrostatic ball) is used as a carrier of the effusive He jet. The gas injection system is presented in figure 1.9. The flow rate of the He jet is controlled electronically which operates from 0-2 sccm with a precision of 0.02 sccm. sccm is an acronym for standard cubic centimetre per minute at standard temperature (0°C) and pressure (1atm). In the experiments typical flow rates were between 0.25 *sccm* and 1.1 *sccm* small enough as to ensure (with the exception of anionic production; see Chapter 2) the single collision condition. For each beam three

different flow rates were performed. In order to record event coming only from the jet (and subtract event coming from collision with the residual gas) we used a similar capillary placed on the side of the chamber (see Figure 1.9). The beam will not cross this jet but only the residual pressure induced by the jet in the same conditions as when the beam crosses the vertical jet (same capillary, same flow rate). The procedure to achieve the 'background subtraction' is the following : the experiment is first ran with the vertical jet crossed by the beam by opening $V4$ and closing $V7$ (all other valves open except $V8$ and $V9$ used for pumping), then a second run is performed with $V4$ closed and $V7$ open which will be subtracted from the first one.

In order to extract the absolute target density crossed by the beam necessary to extract absolute cross sections a beam profile is performed. It consists in recording an event probability (for instance electron capture probability) as a function of the lateral position of the jet along y (see Figure 2.19).

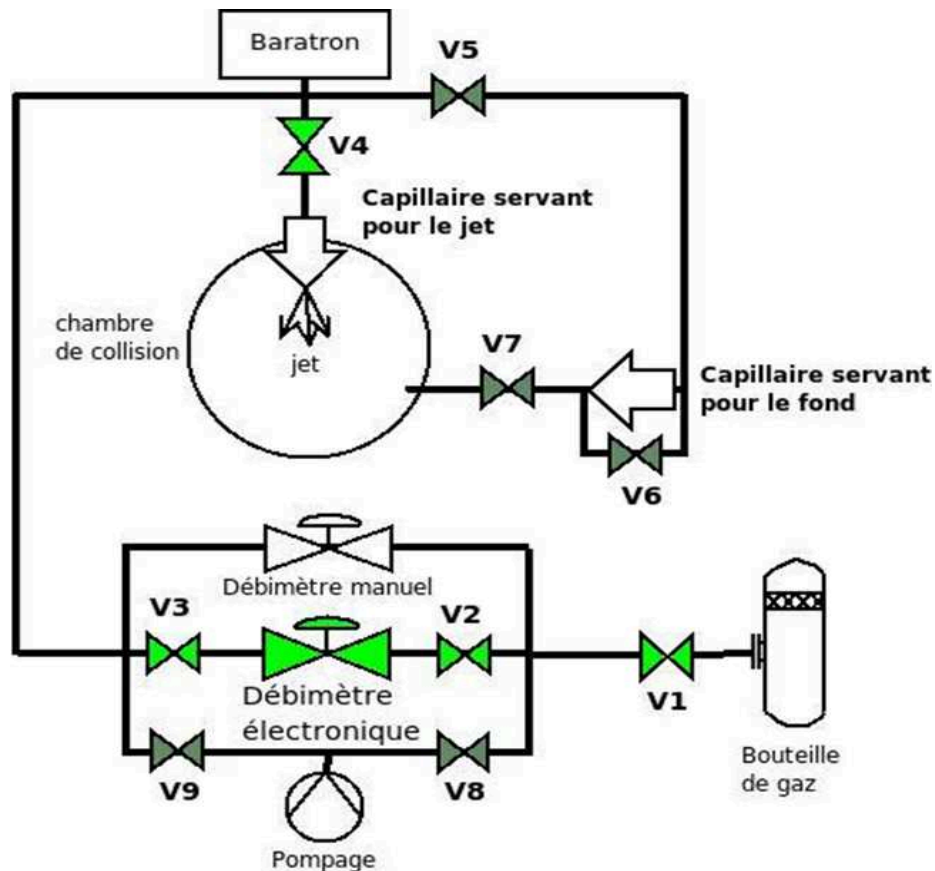


Figure 1-9: Gas injection system

We show in Figure 1-10 a beam profile using probability of single capture of beam C_3N^+ at 1.1 sccm. The precision on the lateral position of the jet is 10μ . The beam-jet overlap is at its maximum for lateral position y around 13.5 mm. At this position the jet over background ratio is around $2.5 \left(\frac{0.014-0.004}{0.004} \right)$. It is limited by the capacity of the turbo-molecular pump which is around 800l s^{-1} . When the jet is in operation, the residual pressure is around 10^{-5} mbar in the collision chamber (and 10^{-6} mbar in the analysis and detection chambers).

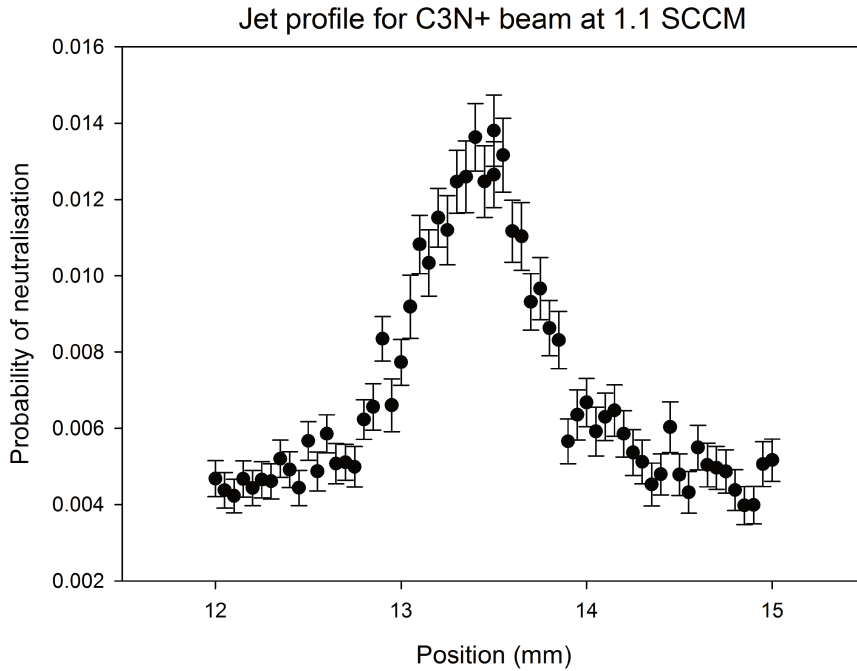


Figure 1-10: Jet profile using probability of single capture of beam C_3N^+ at 1.1 sccm.

1.5.3 The analysis chamber

As mentioned earlier, the fragments are separated according to their charge to the mass ratio (q/m). Basically, the deflector plates are two parallel metal plates having a constant potential difference ΔV between them. The plates used here are 150 mm in length (L) and separated by 45 mm (d , see Figure 1-11 and 1.12). A potential difference $\Delta V \sim 30/40\text{kV}$ was maintained between the two plates.



Figure 1-11: Electrostatic deflector plates; the arrow shows the direction of the beam

The deviation y_{dev} of an ion of charge q , mass m in a constant electric field E perpendicular to the ion velocity v (see Figure 1.12) has the following expression:

$$y_{dev} = \frac{\Delta V}{v^2 d} L \left(\frac{L}{2} + D \right) \frac{q}{m} \quad (1.7)$$

d = Separation between the plates.

D = is the distance from the output of the plates to the detector where the deviation is measured.

$\Delta V = 2V =$ Potential difference.

L = Length of the plates. The deflection angle of the ion α is given by:

$$\alpha = \tan^{-1} \left(\frac{y_{dev}}{D + \frac{L}{2}} \right) \quad (1.8)$$

Except the charge q and mass m , all the other parameters are maintained constant in the experiment. It is thus q/m or "charge to the mass" ratio alone that determines the deflection of the particles. The particles thus deflected (negative will also be deflected by towards the positive plate) will enter into the detection chamber.

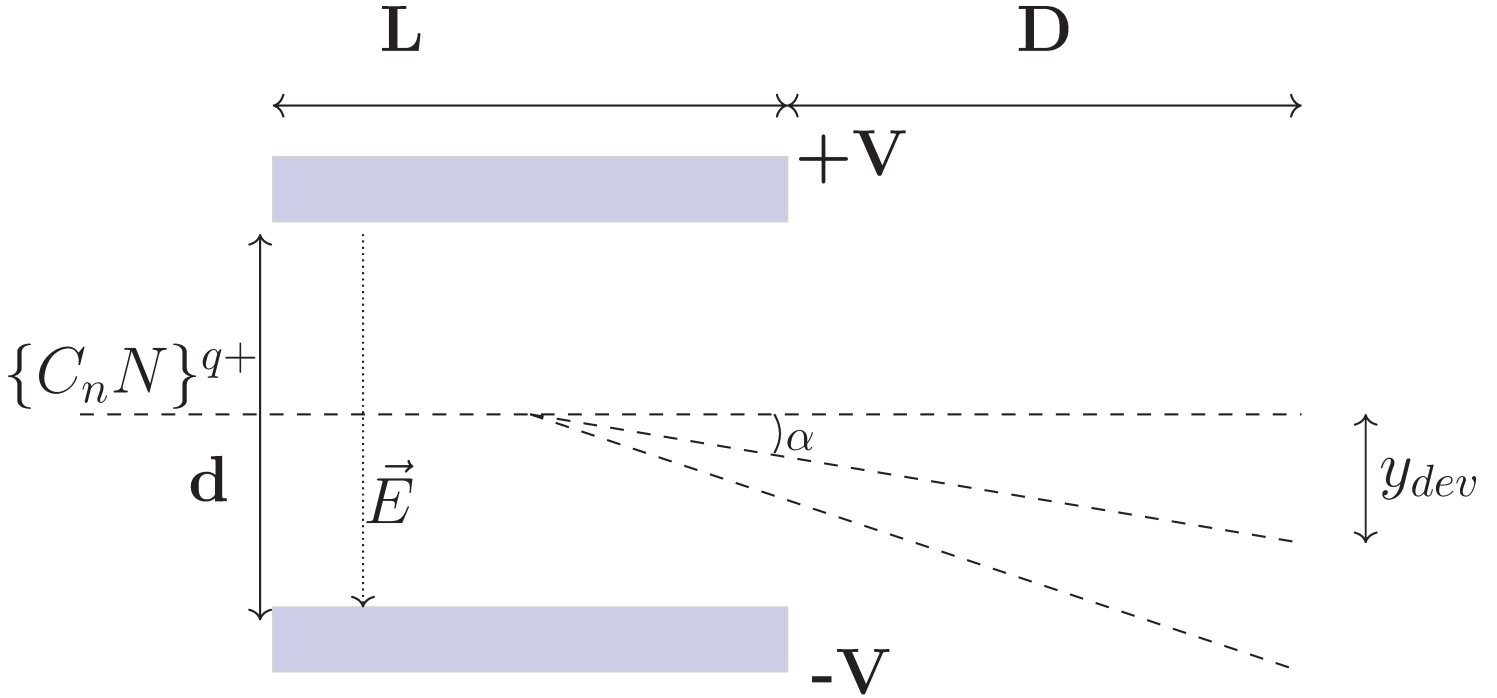


Figure 1-12: Deflector plates under operation

We present the deflection angles α and deviations y_{dev} of the fragments at the detector positions during the run of March 2015 ($\Delta V = 26$ kV, Table 1.4) and February 2016 ($\Delta V = 42$ kV, Table 1.5).

1.5.4 The detection chamber

1.5.4.1 Presentation

A schematic view of the detection chamber is shown in Figure 1-13. There are 5 rails in the detection chamber where to position detectors; 4 were used during the experiments. Rails 3,4 and 5 are situated at the back of the chamber at 1245 mm, 1275 mm and 1290 mm respectively from the center of the plates. These rails are vertically fixed and can be translated along the y axis (axis along which the fragments deflection occurs). Rails 1(PA) and rail 2 (GA) are rotating in the plane of the figure and can move slightly (≤ 10 mm) vertically (out of the plane of the figure). The rotation is centered at the center of the deflector. The rail PA may rotate between -1.5° to 8° with respect to the beam direction whereas the rail GA may rotate between

Fragment	Angle deviation α ($^\circ$)	Position fragment (mm) (at the position detector $D + \frac{L}{2}$ in mm)
C_2N^+	0.665	14.451 (1245)
CN^+	0.972	21.12 (1245)
C_2^+	1.053	22.886 (1245)
C_2N^{++}	1.329	28.909 (1245)
N^+	1.803	40.652 (1290)
CN^{++}	1.944	43.779 (1290)
C^+	2.106	47.427 (1290)
C_2^{++}	2.106	47.427 (1290)
N^{++}	3.606	81.303 (1290)
C^{++}	4.205	94.854 (1290)
N^{+++}	5.401	117.701 (1245)
C^{+++}	6.294	142.280 (1290)
C_2N^-	-0.665	-12.550 (1081)
CN^-	-0.972	-18.340 (1081)
C_2^-	-1.053	-19.870 (1081)
C^-	-2.106	-37.760 (1027)

Table 1.4: Deviations of the fragments at the detector positions during the run of March 2015; $\Delta V = 26kV$

12° and 22° with respect to the beam direction. We placed detector of negative species on rail 1(PA) in March 2015 and February 2016. Those were positioned at closer distances from the deflector centre (see Table 1.4 and Table 1.5). On the rail 2(GA) we put a "finger" which is a steel wire of 60 mm length and 0.5 mm cross section radius (see Figure 1-13). Its main function is to stop the incident beam to keep the detector from damage and also to allow the fragmentation events to be recorded (otherwise the acquisition would be always busy with the incident beam, 100 times more intense than the fragments). This finger is removed during normalisation runs (see chapter 2).

1.5.4.2 The detectors

All the detectors in these experiments are solid-state silicon semiconductor detectors. A semiconductor is defined as that whose electrical conductivity is around mid way between that of the metals (*Cu, Ag ...*) and that of the insulators (wood, rubber). The band theory of solids explains the difference in the electrical conductivity of different

Fragment	Angle deviation α ($^\circ$)	Position fragment (mm) (at the position detector $D + \frac{L}{2}$ in mm)
C_3N^+	0.808	18.200 (1290)
C_2N^+	1.064	23.950 (1290)
C_3^+	1.123	25.280 (1290)
CN^+	1.555	33.790 (1245)
C_3N^{++}	1.616	36.393 (1290)
C_2^+	1.684	36.610 (1245)
C_2N^{++}	2.127	46.240 (1245)
C_3^{++}	2.246	48.820 (1245)
N^+	2.991	65.040 (1245)
CN^{++}	3.220	70.040 (1245)
C^+	3.366	75.880 (1290)
C_2^{++}	3.366	75.880 (1290)
N^{++}	5.758	125.540 (1245)
C^{++}	6.950	151.760 (1245)
N^{+++}	8.601	188.320 (1245)
C^{+++}	10.008	227.640 (1290)
C_3N^-	-0.808	-15.250 (1081)
C_2N^-	-1.063	-20.064 (1081)
C_3^-	-1.123	-21.180 (1081)
CN^-	-1.554	-29.330 (1081)
C_2^-	-1.684	-31.780 (1081)
C^-	-3.366	-51.110 (869)

Table 1.5: Deviations of the fragments at the detector positions during the run of February and October 2016; $\Delta V = 42kV$

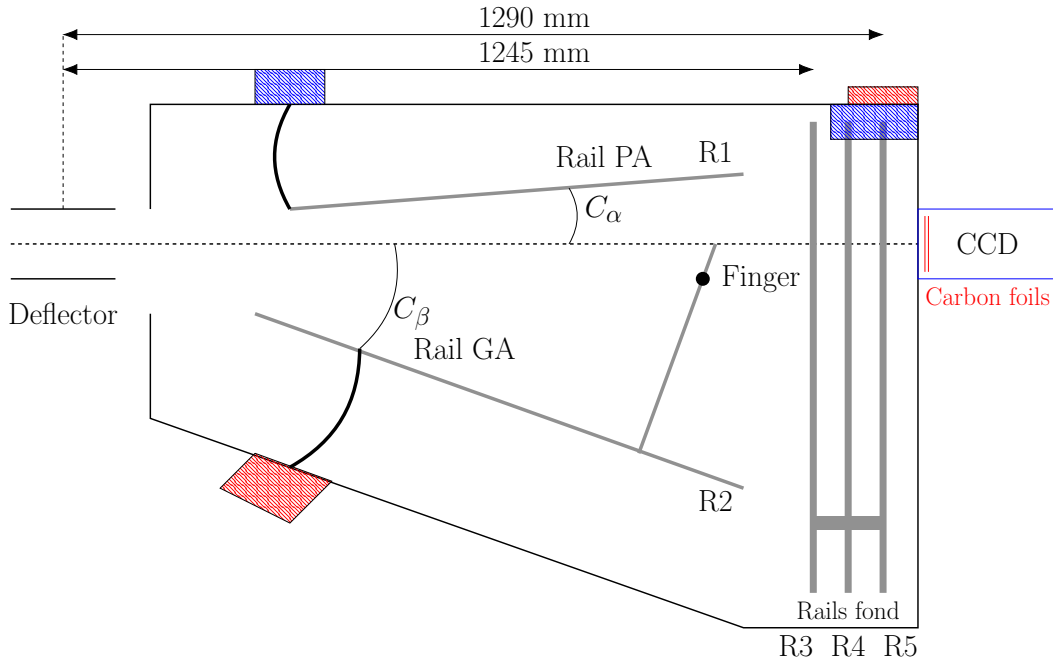


Figure 1-13: Schematic view of the interior of the detection chamber

solids. The electrons in the solid is theorized to be in either conduction band or valence band. Those in the conduction band is responsible for electrical conductivity and those in the valence band do not contribute to the conductivity. The conduction band and the valence band are further separated by a "forbidden band" of which the width of it is usually termed as the "band width" or "band gap". Note here that the "width of band" is expressed in energy. In layman terms, for an electron in a valence band to contribute for conduction, it must gain sufficient energy to "jump" across the forbidden band. In metals, the conduction band and the valence band overlap which amounts to their high conductivity. Whereas in the insulators, the band width is too large for the electrons to jump to the conduction band to contribute to conductivity. In semiconductors, the band gap is in the intermediate energy range (1.12 eV for silicon, 0.66 eV for germanium), so that it is possible for the electrons to jump across the gap by gaining energy from the ionising radiation. The semiconductor detectors are composed of two joined silicon semiconductors, the P-type and N-type. Doping a semiconductor is a process of adding impurities such that the impurities increase or

decrease the band-width. There are two types of doping:

- - N-type doping: Increasing the population of negative charge carriers (donor of electrons), e.g. adding pentavalent atoms.
- P type doping: Increasing the population of positive charge carriers (acceptor of electrons), usually by adding trivalent atoms (boron).

At the P-N junction between these two semiconductors, the electrons of the doped region N will diffuse in the doped region P. The opposite occurs for the carriers of the positive charges. There are thus no more free charge carriers at the P-N junction also called depletion zone. A potential barrier is thus formed in this zone, which prevents the free charges from crossing it. In order to increase the efficiency of the detector, an inverse electrical potential is applied at its terminals, the depletion zone is thus enlarged, as shown in Figure 1-14.

When the P-N junction is hit by a particle, its kinetic energy is transferred to the creation of electrons and holes. If the particle traverses the dead layer (which is before the depleted zone) with a small energy loss and if it is fully stopped in the depleted zone, as is in our case, the efficiency of detection is 100%. The total number of electrons n_e is proportional to the kinetic energy KE of the incoming particle.

If ϵ is the energy required to create one electron-hole pair then, the number of electrons created n_e is given by

$$n_e = \frac{KE}{\epsilon} \quad (1.9)$$

In silicon $\epsilon = 3.6$ eV. It is much greater than the energy gap (1.12 eV) because a part of the projectile kinetic energy is not used for electron-hole production (but recombinations, phonons ...). The number n_e is very large in our case and so are the fluctuations of this value (governing, with the noise level, the energy resolution of the detector). The detectors we used (except the detector of neutral fragments) were commercial ion-implanted detectors provided by ORTEC (Ultra ion-implanted detec-

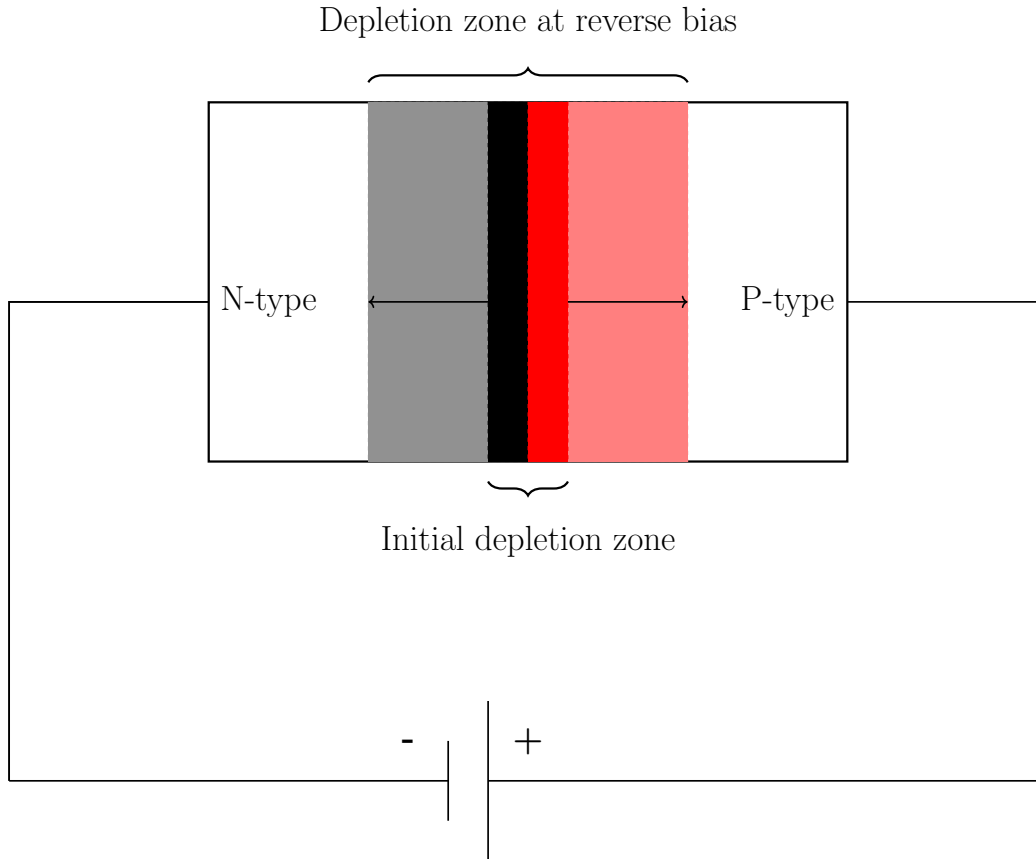


Figure 1-14: Enlargement of the depletion zone

tors) and Canberra (PIPS detector). By the ion-implantation process, the doping of the silicon is best controlled leading to better performances. The resolution of these detectors is typically 15/20 keV at 5 MeV as measured with a tri-alpha source (Plutonium 239 (5.244 MeV), Americium 241 (5.637 MeV) and Curium 244 (5.901 MeV)) before the runs (see Figure 1-15).

1.5.4.3 The detector of neutral fragments

There are two detectors for neutral species, one is a home-made silicon detector developed at IPNO and made for optimizing the current shape analysis technique (see Section 2.5). The other one is an original CCD camera developed recently in the team (Chabot et al., 2011).

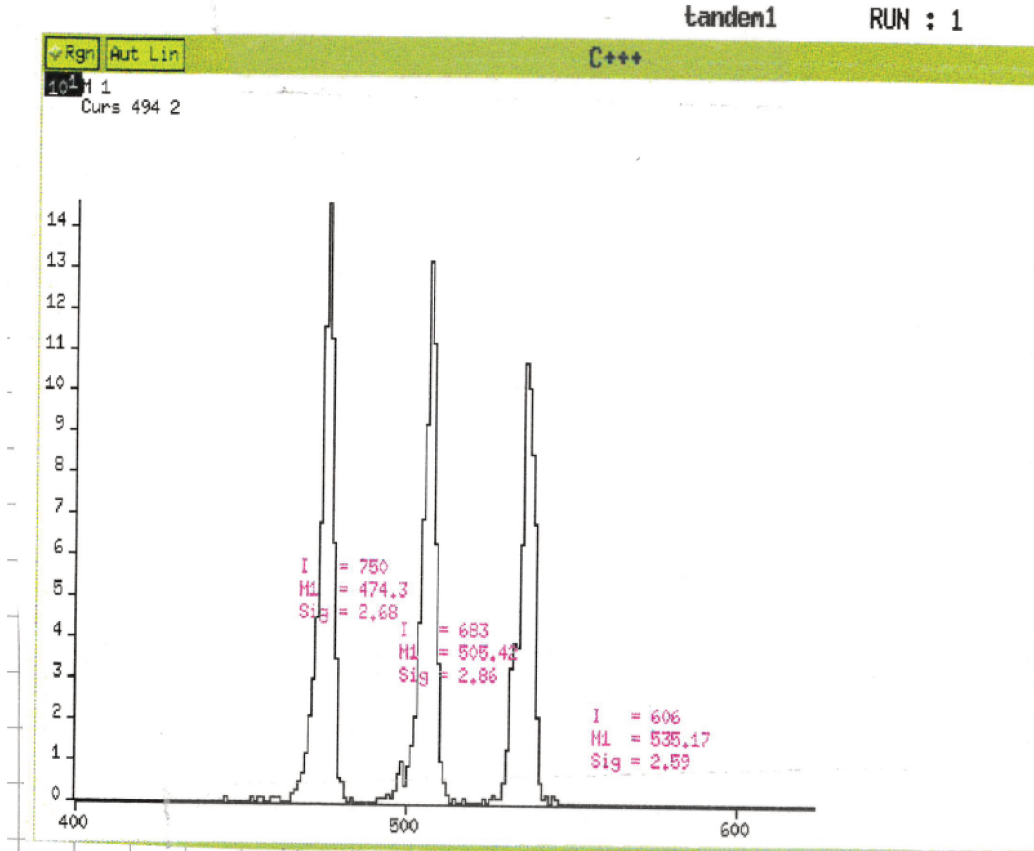


Figure 1-15: Calibration of “ C^{+++} ” detector with the tri-alpha source. Using the known energies of the peaks, we could calibrate the detector i.e. attribute an energy (then mass) to the channel of axis X.

1.5.4.3.1 The EPI for current shape analysis technique The neutral detector is a surface barrier detector (junction semiconductor-metal). The detector is made from N-type epitaxial silicon grown on a N^+ type silicon substrate. A gold entrance layer made the $P^+ - N$ junction and, together with an aluminium layer on the back, was used for electrical contacts. The silicon used for this detector is an epitaxial silicon (origin of the EPI name) of strong resistivity ($7\text{ k}\Omega\text{ cm}$) of $50\text{ }\mu\text{m}$ thickness deposited on a silicon of low resistivity. The significant resistivity of this type of silicon as well as the great homogeneity of the crystal make it possible to implement the shape recognition of the fragmentation figure during the stacking of several fragments in the same detector. The signal from this detector depends on the number of impinging fragments for the same total energy (Chabot et al., 2002). This property will be used in data analysis, finding the fragmentation branching ratios of

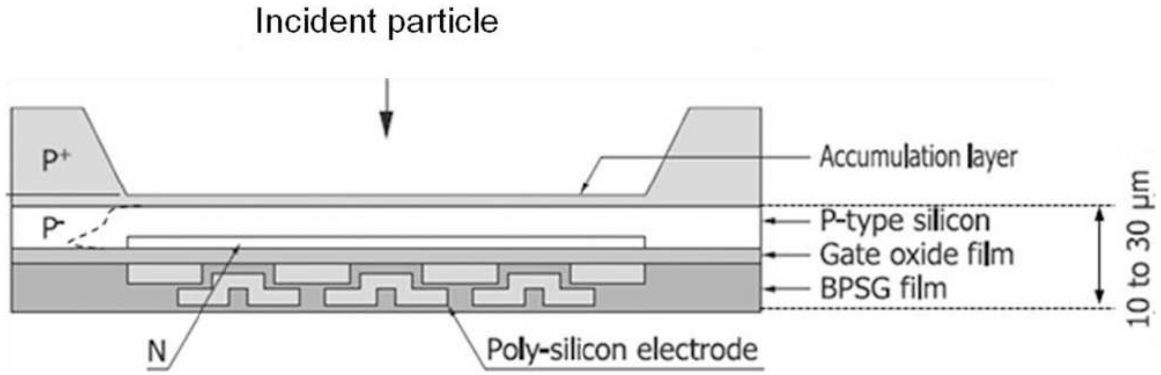


Figure 1-16: Sketch of a cross section of the CCD sensor. The structured electrode at the bottom allows to collect and transfer charges created locally at the pixel level.

C_2N and $C/C/N$ for example. But, in the experiments, we were not able to separate between C/CN and C_2/N which motivated us to use the camera for their branching ratios.

1.5.4.3.2 The CCD camera The CCD was invented in 1970 by Boyle and Smith (1970); Amelio et al. (1970). This type of detector is generally used for the detection of photons. In order to be able to integrate these detectors with spacecraft, the damage that cosmic rays can produce has been studied since the early 1990's . In recent experiments the team showed that this detector was able to detect particles and then to combine the position information with the mass information (Chabot et al., 2011). We used the C4742-98-26KADVS camera manufactured by Hamamatsu Photonics. This camera is designed for direct x-ray detection applications.

It is mechanically attached to an experimental chamber by a vacuum flange and cooled down to -55°C for reducing thermal noise. The CCD of the camera is an S7170 manufactured by Hamamatsu Photonics as well. S7170 has 512×512 pixels of $24\mu\text{m}$ pitch, leading to an active area of $12.3 \times 12.3\text{mm}^2$, (see Figure 1-16).

With the aim of extending capabilities for this experiment, this customized version benefited from an extended full well capacity (FWC) of 400 000 electrons per pixel as compared to 340 000 electrons per pixel for the "standard" version. The FWC of the CCD is defined as the amount of signal electrons that can be properly collected.

The camera functions as a pixelated silicon detector. The fragments are spatially

resolved and each of their kinetic energy is measured. The two limitations of this detector are the following: the detector needs 160 ms for treating an event; it then reduced our counting rate, normally of 300s^{-1} , to 6s^{-1} . Also the camera needs to be externally triggered, which was done by sending a signal from the MCP recoil detector as mentioned before.

1.5.4.4 The detector configurations

The configuration (number of detectors, sizes, positions) is always a delicate matter. We want to detect every fragments and to distinguish fragments impinging in the same detector. The result (detector configuration) is shown in Table 1.6 (and the corresponding Figure 1-17) for the run of March 2015 and Table 1.7 (and Figure 1-18) for the run of February 2016. In October 2016, the configuration was identical to February 2016, exception made of the neutral fragments detector replaced by a CCD camera and the corresponding EPI detector put in the PA rail in place of detector of negative species (due to the very low counting rate imposed by the CCD camera, negative species could not be detected, their abundance is about 1000 times lower than cations).

In Table 1.6 is presented the detector configuration installed in March 2015 for studies with incident CN^+ and C_2N^+ beams. The detectors for anions were both placed on the rail 1(PA) but at different distances: respectively $(\frac{L}{2} + D) = 1027\text{ mm}$ for " C^- " detector and $(\frac{L}{2} + D) = 1081\text{ mm}$ for the " CN^- " detector. In Figure 1-17 is shown the photography of this configuration.

Detector	Surface area mm ²	Type	Rail	Position on rail mm	Range of detection [min, max]	Fragments in detector
" C^- "	14×14	Canberra	R1	-35	[-42, -28]	C^-
" CN^- "	14×14	Canberra	R1	-16	[-23, -9]	C_2N^-, CN^-, C_2^-
"Neutral"	$(H = 6)x(L = 12)$	EPI L34	R3	0	[-6, 6]	All neutrals
" CN^+ "	14×14	Canberra	R3	25	[18, 32]	C_2N^{++}, CN^+, C_2^+
" C^+ "	14×14	Canberra	R5	44	[37, 51]	N^+, CN^{++}, C^+
" C^{+++} "	600	ORTEC	R5	89.1	[75.3, 102.9]	N^{++}, C^{++}
" N^{+++} "	300	ORTEC	R3	115	[105.2, 124.8]	N^{+++}
" C^{+++} "	600	ORTEC	R5	142.2	[134, 156]	C^{+++}

Table 1.6: Detector configuration of March 2015 ($\Delta V = 26\text{kV}$); range of detection may be non-symmetrical in case there is a (slight) masking by another detector.

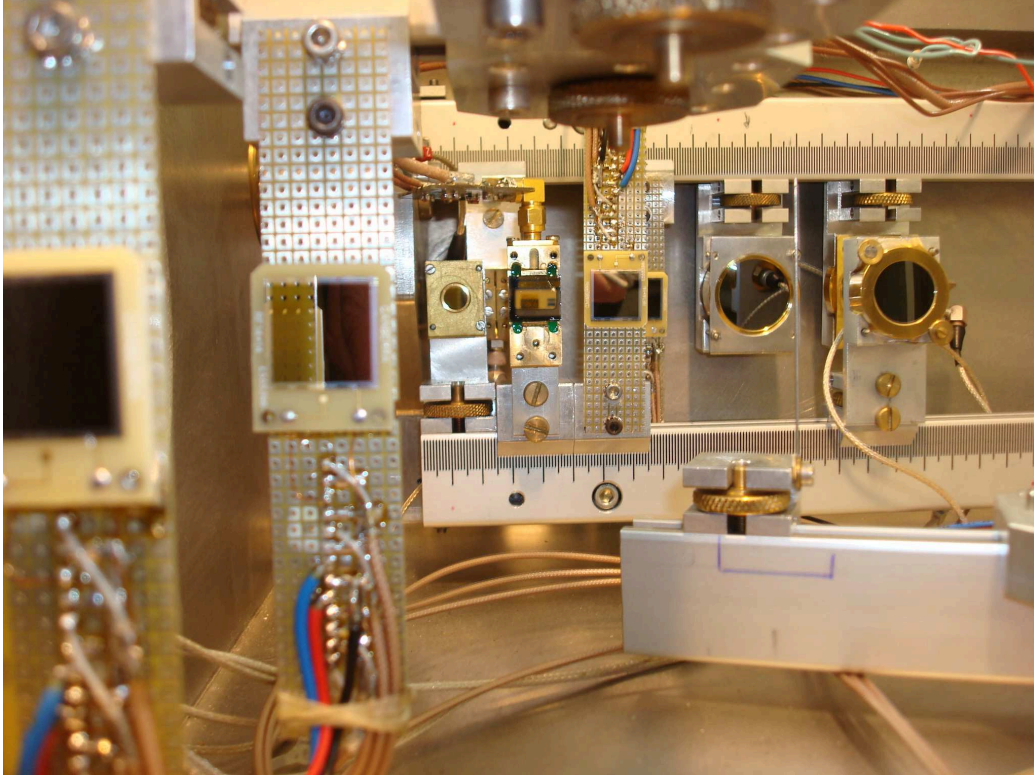


Figure 1-17: View of the detectors in runs of March 2015

The configuration of February 2016 is presented in Table 1.7 and a photograph presented in Figure 1-18. On this figure the "finger" is clearly visible in front of the "CN⁺" detector.

In order to separate C_3N^{++} from CN^+/C_2^+ we made a separate run in which we displaced by 35 mm all detectors so that these fragments were incident on the neutral detector. Now dividing the voltage by 2 we could have in the neutral detector, CN^{++} and C^+/N^+ , then resolving these two species as well.

1.6 Electronics and acquisition

1.6.1 Electronics

1.6.1.1 Electronics for all detectors but CCD camera

The Figure 1-19 presents the electronics scheme, starting with signals from detector pre-amplifiers. Two types of signals are used: a charge channel $E(Q)$, providing the

Detector	Surface area mm ²	Type	Rail	Position on rail mm	Range of detection [min, max]	Fragments in detector
"C ⁻ "	14 × 14	Canberra	R1	-49	[-56, -42]	C ⁻
"CN ⁻ "	600	ORTEC	R1	-24.6	[-38.4, -10.8]	C ₄ N ⁻ , C ₃ N ⁻ , C ₄ ⁻ , C ₂ N ⁻ , C ₃ ⁻ , CN ⁻ , C ₂ ⁻
"Neutral"	(H = 6)x(L = 12)	EPI L34	R3	0	[-6, 6]	All neutrals
"C ₃ N ⁺ "	14 × 14	Canberra	R5	22	[15, 28]	C ₃ N ⁺ , C ₄ ⁺ , C ₂ N ⁺ , C ₃ ⁺
"CN ⁺ "	300	ORTEC	R3	41.2	[31.4, 51]	C ₂ N ⁺⁺ , CN ⁺ , C ₂ ⁺ , C ₃ ⁺⁺ , C ₃ N ⁺⁺
"C ⁺ "	600	ORTEC	R5	70.5	[56.7, 84.2]	N ⁺ , CN ⁺⁺ , C ⁺
"N ⁺⁺ "	300	ORTEC	R3	123	[113.2, 132.8]	N ⁺⁺
"C ⁺⁺ "	600	ORTEC	R5	152	[143.5, 165.8]	C ⁺⁺
"N ⁺⁺⁺ "	600	ORTEC	R3	188	[174.2, 201.8]	N ⁺⁺⁺
"C ⁺⁺⁺ "	600	ORTEC	R5	228	[214.2, 241.8]	C ⁺⁺⁺

Table 1.7: Detector configuration of February 2016 ($\Delta V = 42kV$); range of detection may be non-symmetrical in case there is a (slight) masking by another detector.

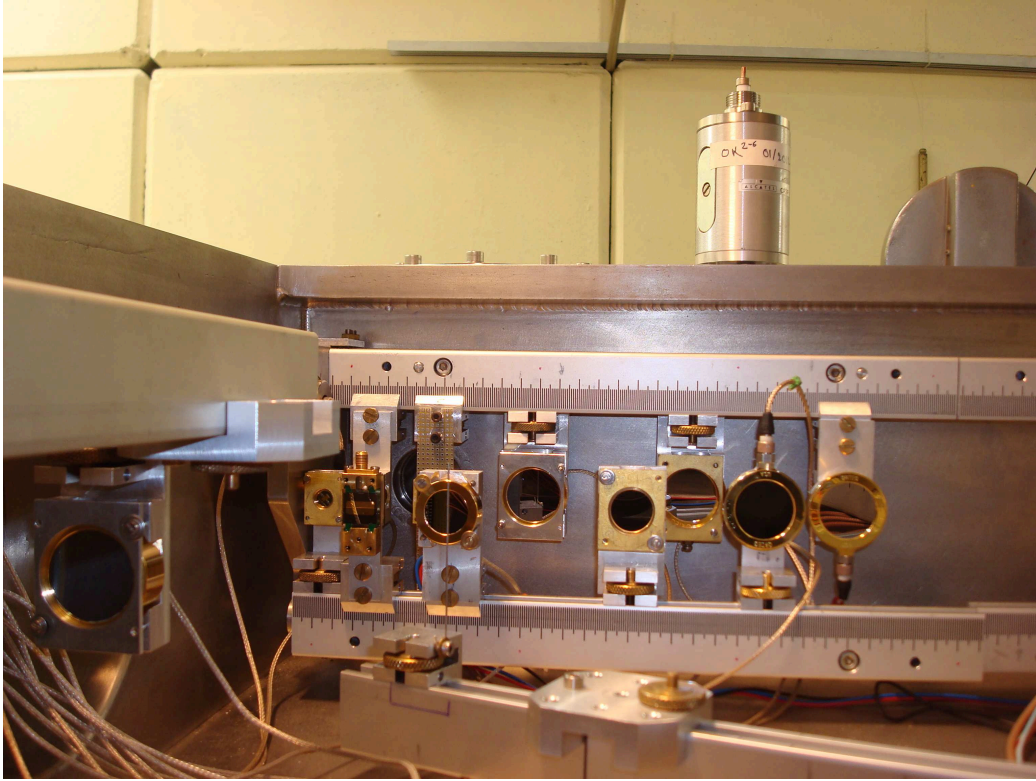


Figure 1-18: View of the detectors in runs of February 2016. The "finger" is seen in front of the detector "CN⁺".

fragments' energy (mass) with the best accuracy and a current signal $T(I)$ used for shape analysis studies. The current signal is of poor quality for commercial detectors, but of very good quality for EPI Neutral detector equipped with a pre-amplifier PACI manufactured at IPNO. With PACI, the current amplifier preserves the shape of the signal allowing shape analysis studies to be conducted.

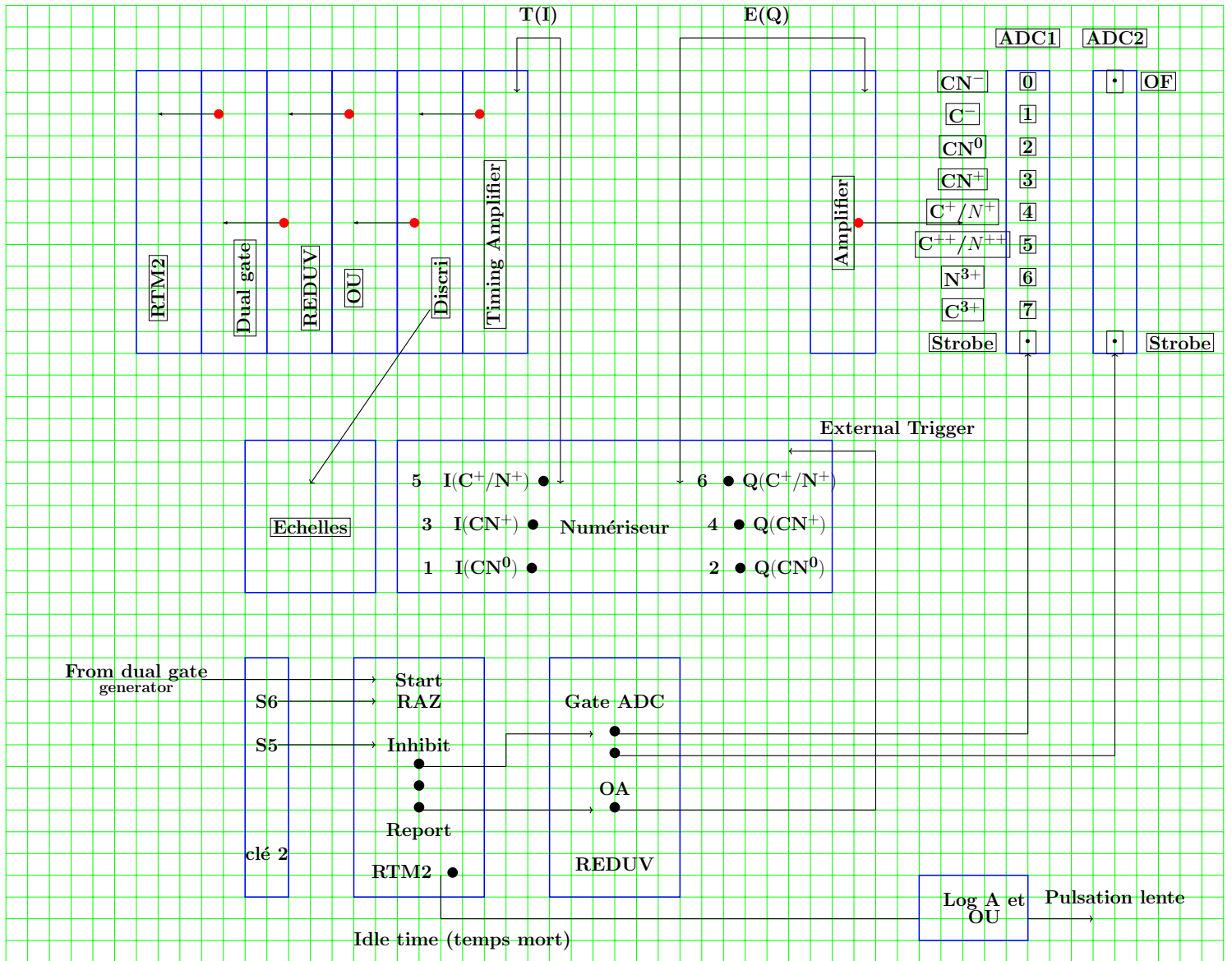


Figure 1-19: Electronics schematic diagram

Outputs of the charge pre-amplifiers $E(Q)$ are sent to a 12-bit ADC (Analog to Digital Converter) of CAMAC standard (ADC Leroy 512) via an "energy" filter-amplifier.

Outputs of the current pre-amplifiers $T(I)$ are used for triggering and identifying fragmentation patterns. These signals are on the one part digitized with the acqiris scanner ("Numériseur" in Figure 1-19) which communicates with the acquisition via a PCI bus. These signals are, on the other hand, amplified with a fast amplifier and used for triggering the acquisition (*via* a "ou" module in Figure 1-19), or used

for counting purposes ("Echelles" in Figure 1-19). The shape analysis method is operating on these digitized current signals.

1.6.1.2 The electronics of CCD camera

During a trigger call, the CCD outputs the image of the rotating buffer. The filling of the rotating buffer is fed by the ADC of 2.5 MHz frequency (0.4 μ s per pixel). The ADC works continuously when writing the output buffer. Therefore, if other impacts arrive shortly after the trigger, they may appear in the buffer image. To avoid these stacks, the beam is stopped at each event by means of the chopper located at the entrance of the accelerator.

The camera has several recording modes. We have chosen this which allows us to deal with the image during the acquisition. The image is 8 \times 8 bit coded, which corresponds to 65 535 shades of gray

1.6.2 Acquisition

The way the acquisition works is illustrated in Figure 1-20.

Three workstations control the data acquisition : IPNLINTDM6, AZ4PI and PC AGAT. They are running on Debian OS and we use NARVAL interface on all the three systems. NARVAL (Nouvelle Acquisition temps-Réel Version Avec Linux) is a software developed by Grave et al. (2005), containing the experiment parameters.

It acts as a conductor: it sends directions to modules called 'actors'. It oversees the acquisition, it routes the data in real time so that we can monitor the progress of the experiment. 'Actors' can be producers, intermediaries or consumers. Producers, as their name implies, produce the data. Intermediaries distribute these data to consumers. As for the consumers, they process the data.

We interact directly with two computers IPNLINTDM6 and PC AGAT. It is from these computers that we start, stop and order the acquisition. The acquisition is first started at the camera via PC AGAT. The camera must be initialized and cooled down to -55°C before it can start recording. Once the camera is ready, the acquisition is

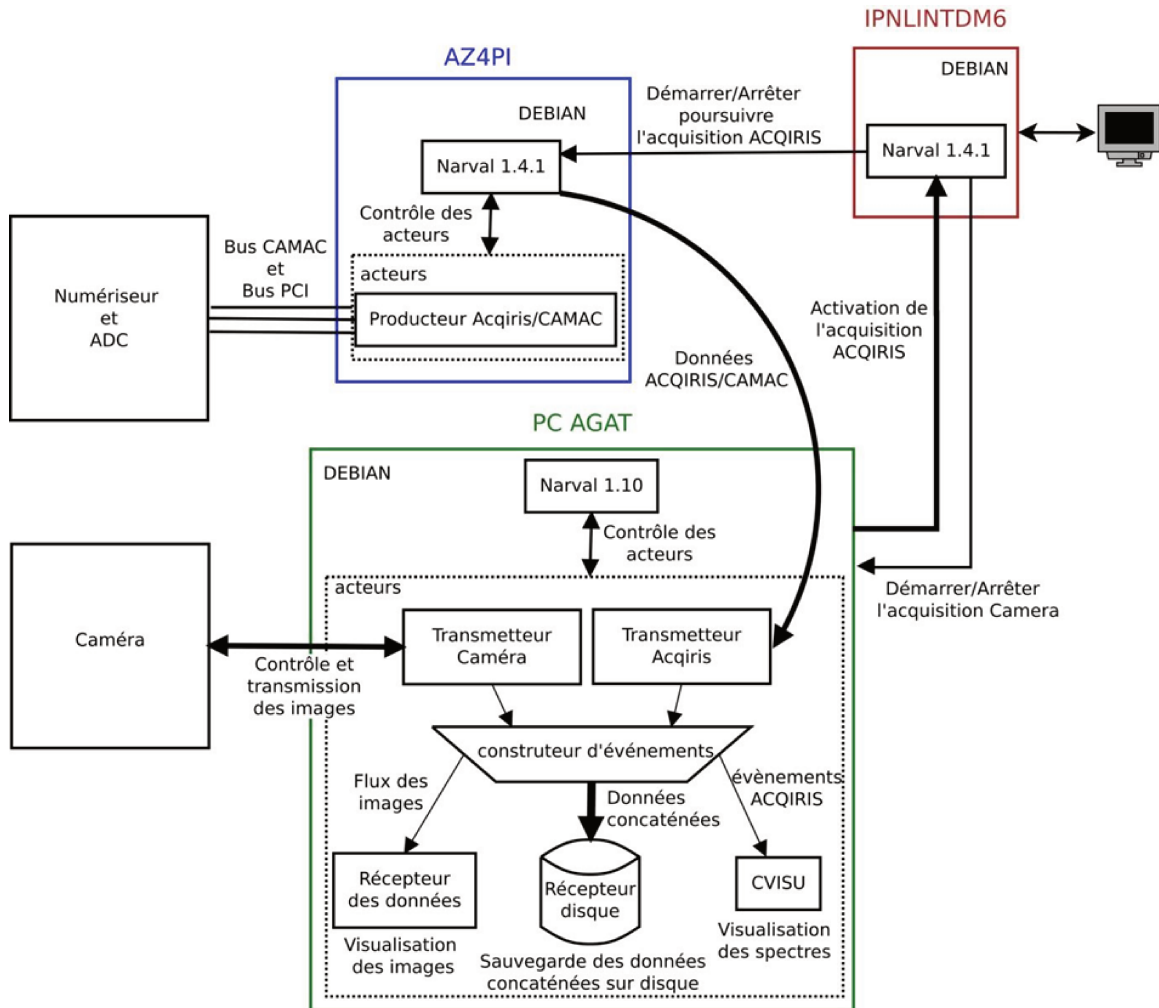


Figure 1-20: Principle of the acquisition

switched on at the detector level with IPNLINTDM6.

AZ4PI is the computer connected to semiconductor detectors and the MCP detector. It contains a producer, named acqiris producer, who collects the data from these detectors. Narval time stamps these data and then sends them to PC AGAT. The timestamp associates a date and a time with the computer data. Narval then wait for the acquisition at AZ4PI level, so PC AGAT does not receive new data until it has finished processing the old ones.

PC AGAT is the computer connected to the camera. It has two producers (Camera Transmitter and Transmitter acqiris), an intermediary (Event Builder) and three consumers (Data Receiver, Disk Receiver and CVISU). The data sent from AZ4PI by

Narval is transferred to the acquiris transmitter.

The camera transmitter generates the images from the camera. For this, it captures the image and the timestamps, that is to say, it delimits the size of the event that will include: the acquiris data, the image and the time. The event builder collects

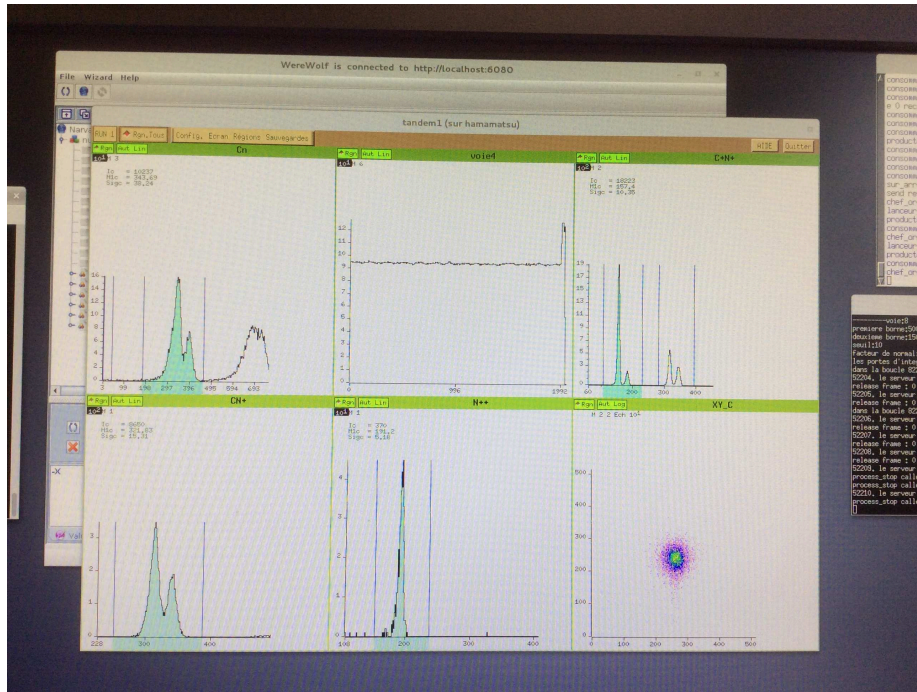


Figure 1-21: A live CVISU during the run

time stamped data from the 'acquiris transmitter' and the Camera Transmitter. Its primary role is to compare the two times, to be sure that the data of the detectors and the camera come from the same event. The event builder will then concatenate the two events that match and sent them to the three consumers that are:

- The data receiver that receives the stream of images sent by the camera and then displays the images in a window of SDL (Simple Direct media Layer) control. We can see in real time the images recorded by the camera.
- CVISU that receives the data flow from the acquiris transmitter and then generates the desired spectra. This 'actor' allows us to visualize during the experiment in real time the detector spectra (see Figure 1-21).

- The disk receiver that writes the data concatenated by the event builder on a hard disk. These are the raw data that will be analysed later.

If the detection of the neutral fragments is done with the EPI detector and not with the camera, then the operation of the acquisition is simplified. The camera transmitter and acqiris transmitter are not in operation.

Chapter 2

Data analysis

2.1 Data formatting and data treatment

The data collected from our experiments are of two types depending on whether or not the camera was used to detect neutral fragments. If the camera has not been used, then each event constitutes a word formed by the values of the sixteen Camac ADC followed by the eight traces of current signals digitized by the acqiris scanner. If the camera was used, then a table of 512×512 (number of pixels) is added to the previous word. The data will then be reduced (formatted) to a multidimensional matrix called NDB by a code written by IPNO engineers. NDB files are especially arranged as to be easily treated by a data visualization software DP2 developed by L.Tassan-Got and JF.Rabasse from IPNO. In the same code it is possible to make a basic treatment of the digitized current signals. Figure 2-1 shows a current signal from the detector. The signal treatment is done with, subtracting the background, smoothing by n -point running averages, time calculation and finding the amplitude and integral of the signal. The background is subtracted by subtracting the average of a region of no signal, for example, an interval of $[500, 900]$ in the Figure 2-1. The signals are filtered using a linear smoothing filter to reduce noise. This filter makes a running average of the signal on $n + 1$ points. Thus each sampled point of the signal is substituted by the average value of the $\frac{n}{2}$ values around. For a signal $S(k)$ that

A typical current signal.

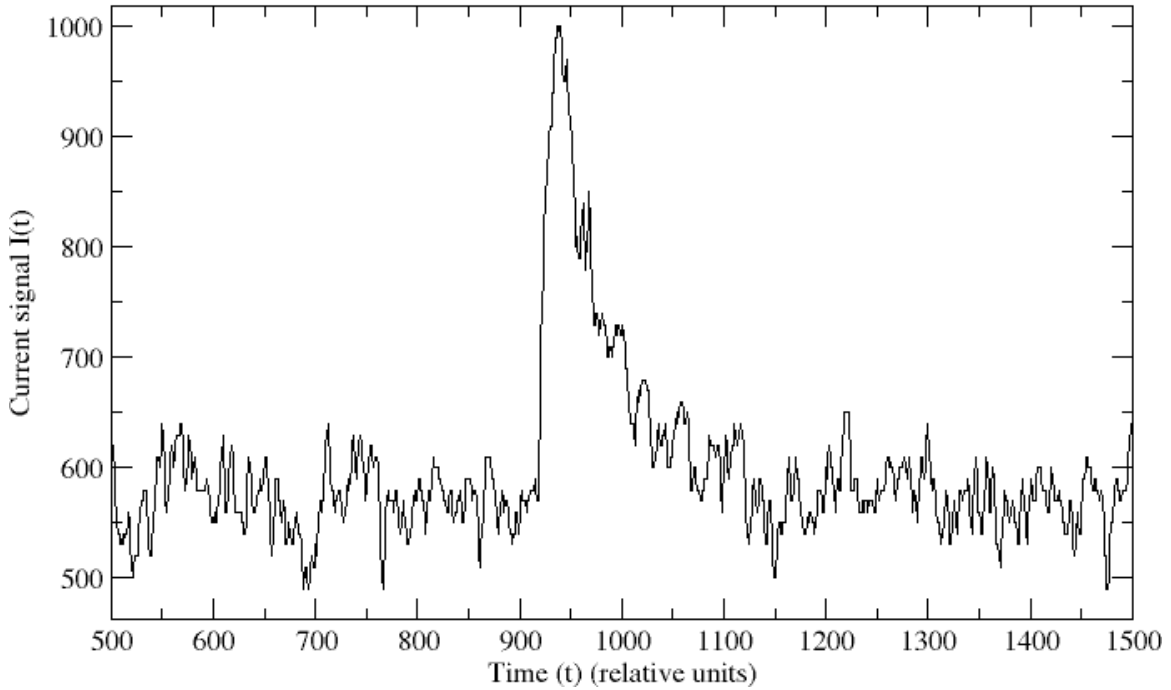


Figure 2-1: Current signal output before treatment; on x-axis, 0.5 ns per canal.

samples on n points, this filter is written as:

$$S_{av}(k) = \frac{1}{n+1} \sum_{i=-n/2}^{n/2} S(k+i) \quad (2.1)$$

The running average returns to convolute the signal $S(k)$ by a square function:

$$S_{av} = \frac{1}{n+1} S \otimes \text{rect}_n \quad (2.2)$$

$$\text{rect}_n(k) = \begin{cases} 1, & |k| < \frac{n}{2} \\ 0, & |k| > \frac{n}{2} \end{cases} \quad (2.3)$$

But the Fourier transform of the product of convolution of two functions corresponds to the product of the Fourier transforms of these functions. Consequently, the application of this linear filter amounts to multiplying the Fourier transform of the signal by the Fourier transform of the square function, that is to say by the cardinal sinus

function $\text{sinc}(x) = \frac{\sin(x)}{x}$. This linear smoothing of the signal therefore modulates its frequency spectrum by the sinc function. The higher the number of bridges chosen for running average, the lower the filter cutoff frequency. But the noise frequencies are rather in the high-end spectrum. Therefore, n is chosen judiciously to reduce the noise without deteriorating the frequencies containing the information on the signal. In the Figure 2-2 the resolution between the signals of C_2 and $2C$ are plotted with various n values. $n = 5$ is found to output the highest resolution as can be seen in the

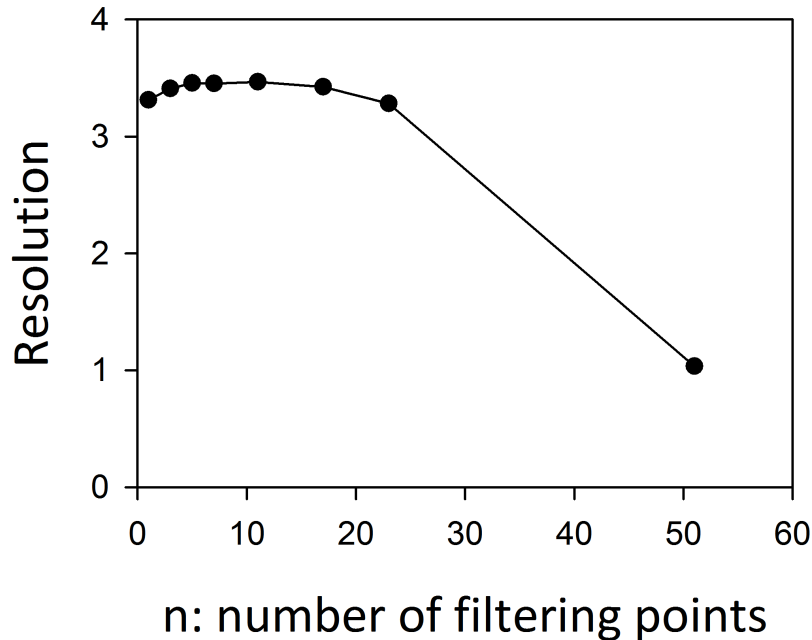


Figure 2-2: Amplitude fragmentation resolution of C_2 vs $2C$ as a function of the filtering points number of current signal.

Figure 2.2 but the improvement is rather small. Once the signals are smoothed, some signal characteristics may be extracted. The most important ones are the amplitude of the signal (for the shape analysis method) and the time of the signal (time at which it reaches a given % of its amplitude) that we used for noise removing in the case of a very noisy detector.

2.2 The DP2 software

DP2 is a 2D visualization and analysis software for multi-dimensional data, and for making grids and contours over the displayed data. The raw data is first treated as outlined before and made into a readable format called NDB compatible with DP2. NDB is a tree structure data format which is useful in working with large dataset and many parameters. The list of parameters that DP2 can treat is made of ADC values for each detector, amplitude, integral and time at which signal rises for each numerical current signal. Most of the information is extracted from ADC that provide the information energy (mass) of the fragments. Prior to looking at coincidences between ADC, an essential work consists in calibrating precisely all ADC. DP2 allows to extract monodim (1-dimension) spectra from ADC. Figure 2-3 shows the ADC spectrum of the " C^+ " detector during a $C_3N^+ + He$ run. As seen in Figure 2-3, the " C^+ " detector could detect C^+ , N^+ , CN^{++} and any combination of those. The

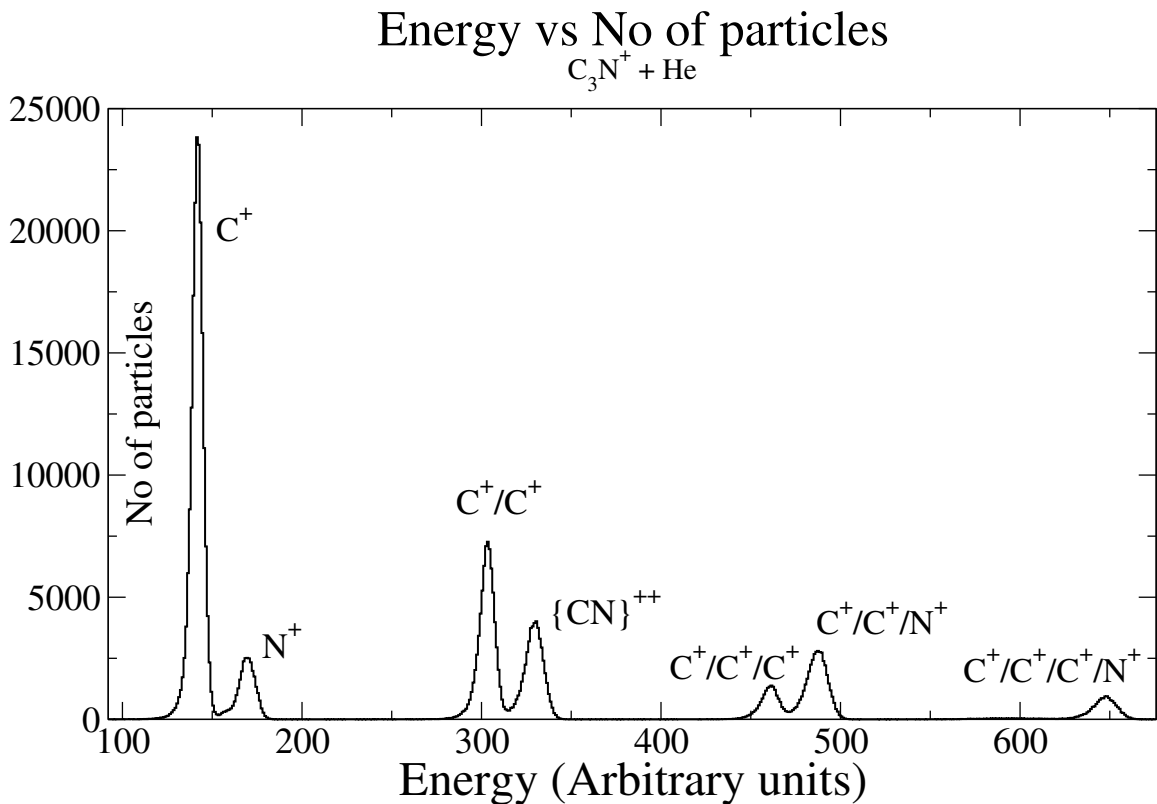


Figure 2-3: Energy response of " C^+ " detector at the impact of one or several C^+ , N^+ and CN^{++} fragments ($C_3N^+ - He$ collision)

curly brackets on $\{CN^{++}\}$ means that the molecule can be intact (CN^{++}) or broken (C^+/N^+). Using the absolute calibration between channel and energy performed before the runs with the tri-alpha source, it is easy to correlate the channel number of ADC from detector " C^+ " with the fragment's mass (see result of calibration on Figure 2-4 and in Table 2.1). The calibration curve is given below.

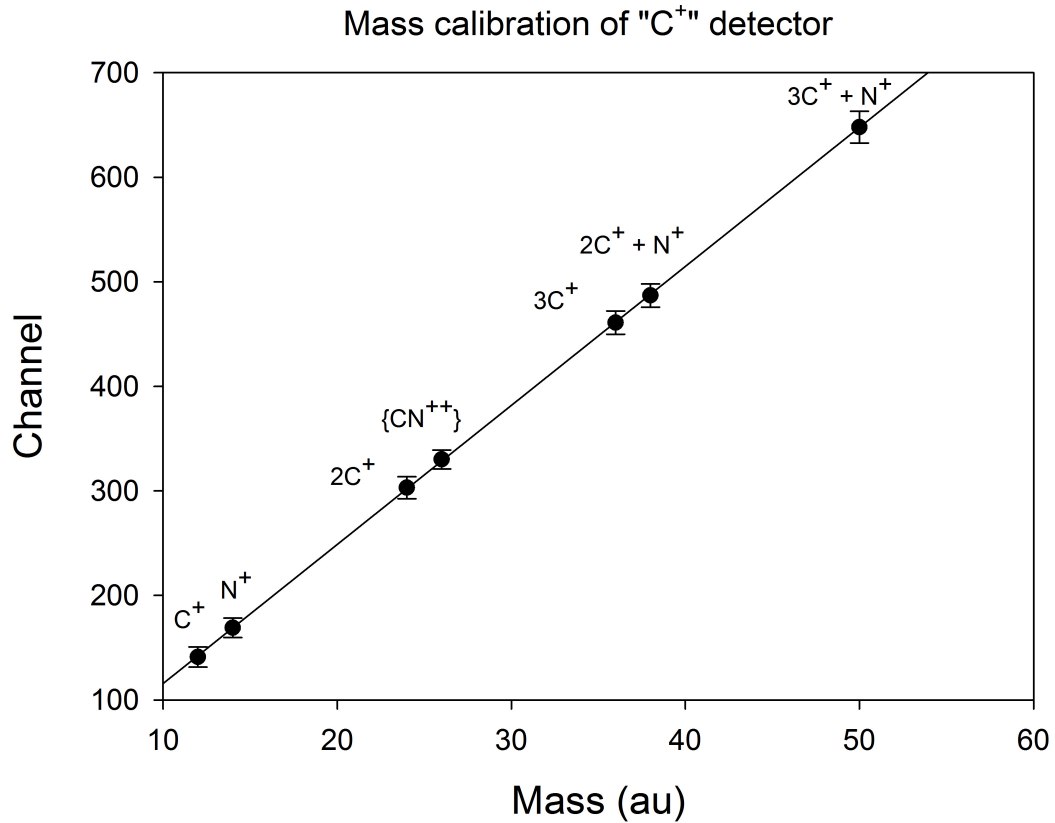


Figure 2-4: Mass calibration of " C^+ " detector in runs of February 2016 and October 2016 following Figure 2-3

On fitting with a straight line,

$$y(\text{channel}) = a \times (\text{mass}) + b$$

$$a = 13.30$$

$$b = -17.33$$

$$r^2 = 0.99$$

where r^2 is the goodness of fit.

Mass	Peak channel	Standard deviation (channel)
12	141	9.67
14	169	9.38
24	303	10.54
26	330	9.09
36	461	11.11
38	487	11.11
50	648	15.16

Table 2.1: Mass calibration of " C^+ " detector following Figure 2-3.

DP2 allows to visualize coincidences between two ADC (2D spectrum). Figure 2-5 shows such a 2D spectrum between ADC from neutral detector and ADC from " C^+ " detector. The data used here is from $C_3N^+ + He$ collisions. This 2D representation gives the coincidence between the two detectors such that each point on this 2D plane represents an event in which a fragment was detected on the neutral fragment detector and another fragment on the " C^+ " detector. Using calibrations made for each detector it is easy to identify each spot of the Figure 2-5. The notation with curly brackets (for example $\{C_2\}$, $\{CN\}$, $\{C_3\}$ or $\{C_2N\}$) means that the species may be intact or fragmented. This convention will hold in the whole manuscript. The resolution of the fragmentation for these species is discussed in section 2.5 and section 2.6. The encirclements are what we call 'grids' in DP2. It defines an area on the 2D plane. DP2 is able to do a 'contour integration', which essentially gives the total number of points inside the contour.

In the Figure 2-5 we encircled with contours complete events (a complete event is having the same mass as the incident C_3N^+ projectile). DP2 could also look for coincidences with 3 or more detectors. In the Figure 2-5, there are many peaks that are incomplete in mass, because a third (or fourth) fragment was detected on another detector. For example for the $C^+/C^+/N$ spot, since we work with incident C_3N^+ , the missing fragment should be C^- , C^{++} or C^{+++} . DP2 allows to select one of this fragment (selection of the corresponding ADC range, see the list of parameters with their range on the right vertical column of Figure 2-5) and the displayed 2D spectrum will now be coincident with this selection. Alternatively it is possible to

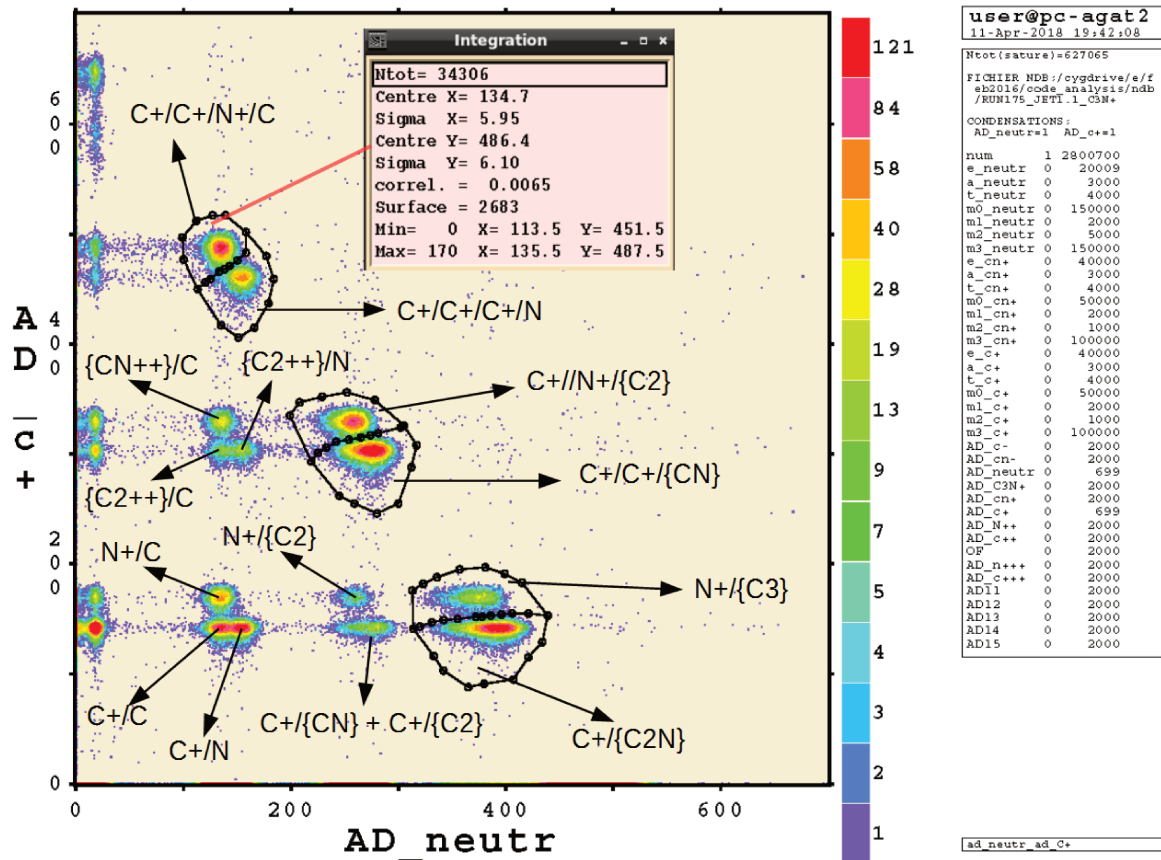


Figure 2-5: DP2 window showing a coincidence between two detectors, neutral and "C+"

select a contour (grid) on any 2D spectrum and to visualize a coincident 2D spectrum of any two other detectors.

2.3 Incomplete events

On discussing coincidence counting, it is mentioned that the particular aim of the method is to recreate the molecule after fragmentation. In a very few cases, some fragments are lost. This event is termed as an incomplete event. During the runs, it is usually a few percent of incomplete events as compared to the complete events that are measured. This contribution to the cross section of the processes is negligible and usually the incomplete events can be safely ignored (Mezdari, 2005). During the run of March 2015, of CN^+ and C_2N^+ , we found a very large rate of incomplete

events. From the CN^+ run we could rapidly suspect C^+ not to be fully detected as incomplete events with N^{q+} ($q = 0 - 3$) were detected (with a rate of 15% up to 50% depending on q) whereas no incomplete events with C^{q+} alone ($q = 0 - 3$) were measured. Such a result could be explained if the " C^+ " detector was badly positioned towards lower q/m value. We made a simulation of the fragmentation with a Fortran code for C^+/N^{q+} fragmentation channels ($q = 1 - 3$). The fragmentation energy was assumed to arise from the coulomb explosion. We took a Gaussian energy distribution centered on the coulomb point charge formula E_c (see Equation 2.4) with $R = 1.17 \text{ \AA}$ in CN^+ (Peterson, 1995) and standard deviation taken from Table 2.2:

$$E_c = \frac{14.4qq'}{R} \quad (2.4)$$

q and q' are in atomic units (au), E_c is in eV and R is in \AA .

Channel	$E_c(\text{eV})$	$\sigma(\text{eV})$	$LR(C^+)_{C^+/N^{q+}}$ for " C^+ " detector's shift $x = -2 \text{ mm}$	Experimental loss rate $LR(C^+)_{C^+/N^{q+}}$
C^+/N^+	12.3	6.2	0.25	0.34(30%)
C^+/N^{++}	24.6	8.1	0.33	0.45(20%)
C^+/N^{+++}	36.9	9.4	0.37	0.49(30%)

Table 2.2: Comparison between simulated and measured loss rates of C^+ in C^+/N^{q+} fragmentation channels

Equation 2.4 was found to be valid in similar experiments (Sampoll et al., 1992; Caraby, 1997; Béroff et al., 2011). Standard deviations were taken by assuming their ratio to the centroid value to be equal to measured values in similar systems (CO molecule ionized by highly energetic charged ion (Caraby, 1997)). We defined the loss rate of C^+ in the C^+/N^{q+} fragmentation as:

$$LR(C^+)_{C^+/N^{q+}} = \frac{N_{alone}^{q+}}{N_{alone}^{q+} + C^+/N^{q+}} \quad (2.5)$$

As seen in Table 2.2 simulated $LR(C^+)$ are close from measured ones if assuming

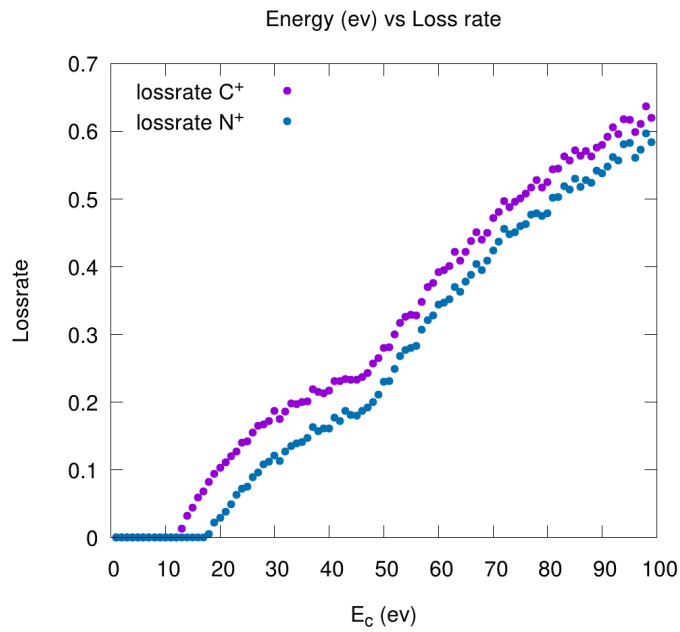


Figure 2-6: Loss rate calculation vs coulomb explosion energy E_c for C^+ and N^+ fragments.

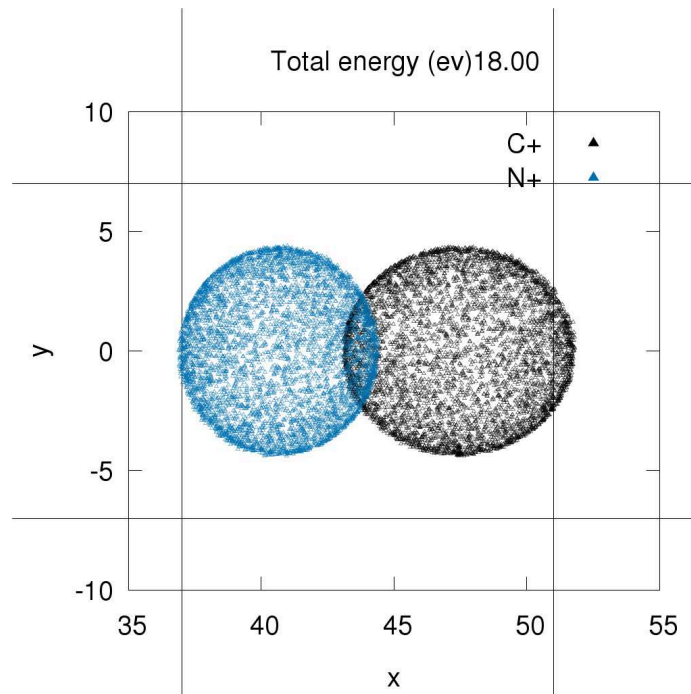


Figure 2-7: Simulating the C^+ and N^+ hits for a well centered $14 \text{ mm} \times 14 \text{ mm}$ detector and for $E_c = 18 \text{ eV}$

a shift of the C^+ detector $x = -2$ mm. In this x direction, N^+ detection is not affected and the loss of N^+ fragment was found null as in the experiment. This value $x = -2$ mm was also found in agreement with the examination of the positioning: the detector was not centered on the support by -2 mm. Note that a very small loss of events is also arising from the fact that the " C^+ " detector ($14 \text{ mm} \times 14 \text{ mm}$) is a bit too small. In Figure 2-6 we show the C^+ and N^+ loss rate for a well centered detector as a function of E_c . The loss of C^+ for a well centered detector is around 10% at $E_c = 20$ eV. Figure 2-7 shows the simulated mapping of the fragments C^+ and N^+ on the well centered " C^+ " detector for $E_c = 18$ eV. We then corrected the

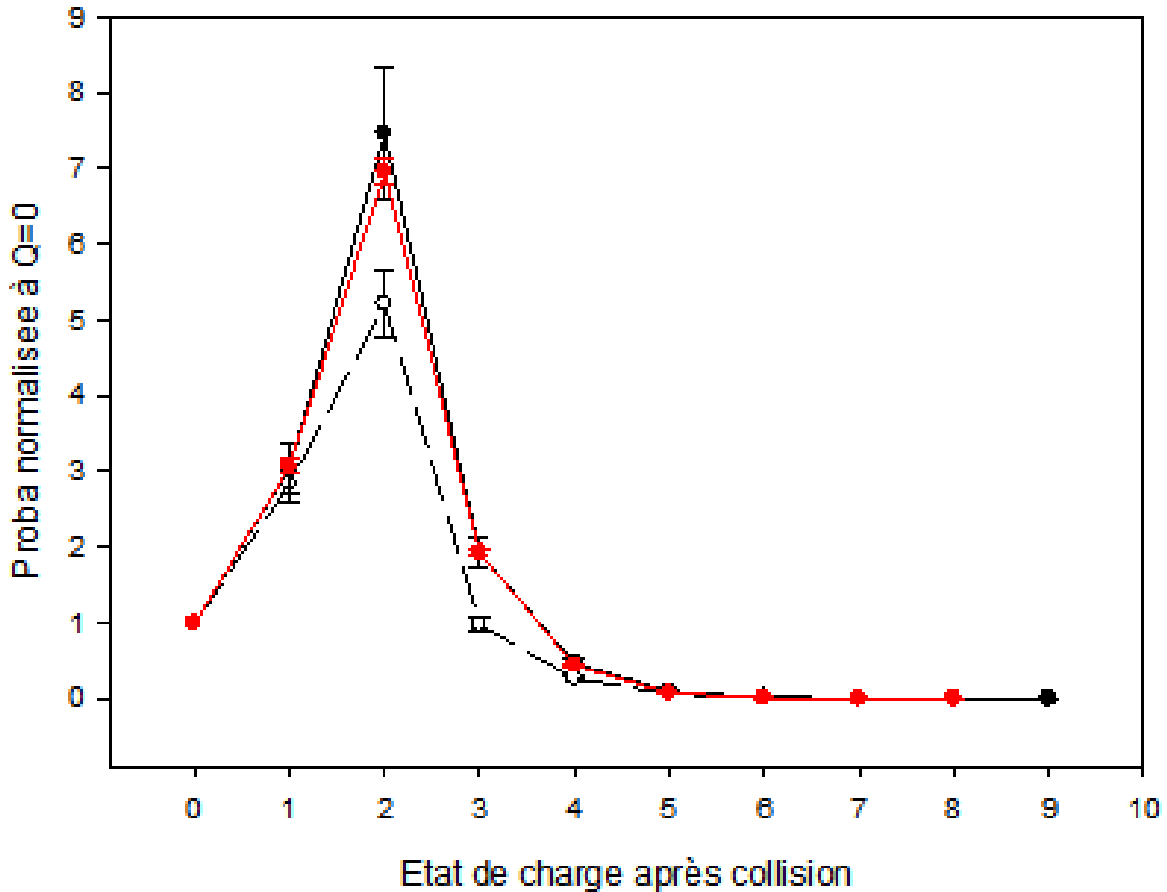


Figure 2-8: Comparison between raw (broken line and open symbols), corrected (black line and full symbols) final C_2N^{Q+} probabilities (normalized to $Q = 0$) recorded in March 2015 and results of the October 2016 run (red line and red symbols); collision $C_2N^+ - He$

number of counts in the runs of March 2015 by assuming that the whole loss was

originating from C^+ loss i.e. all incomplete events should be counted as complete events with C^+ missing. The quality of this correction was further validated because the C_2N^+ run was done again in October 2016 with a new detector configuration. In this configuration the " C^+ " detector was of 600 mm^2 surface and all C^+ fragments were detected. In Figure 2-8 we show that results of corrected C_2N^+ run of March 2015 are equal to proper results of C_2N^+ from October 2016.

2.4 Removing noise by timing selection

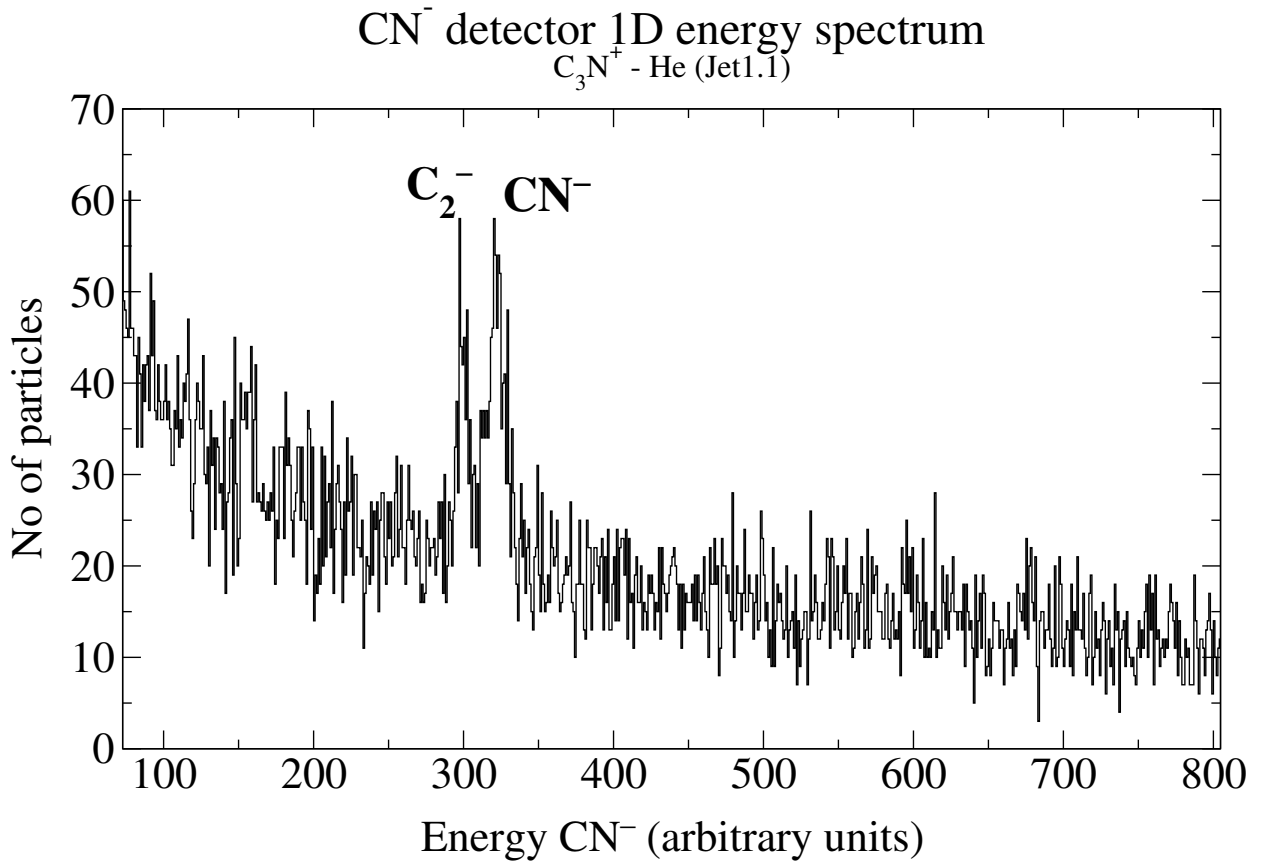


Figure 2-9: Energy spectrum of "CN⁻" detector without time selection

During the analysis of negative species produced in $C_3N^+ + He$ data, we found that the mass spectrum (1D ADC spectrum) of " CN^- " detector was full of noise, as demonstrated in the Figure 2-9. With this noise we could not see any of the expected C_3^- , C_2N^- and C_3N^- fragments. We then decided to make a time selection

for the signal issued from the " CN^- " detector. For that we followed the procedure described in section 2.1 i.e., background subtraction, filtering and search of time at which the current signal rises (defined as t_{CN^-}). This time selection allowed to keep only signals above a physical threshold i.e. eliminating all background. We show in the Figure 2-10 the mass spectrum when t_{CN^-} is selected around its physical value. Coincident spectra exhibit the same effect. In Figure 2-11 and Figure 2-12 are shown

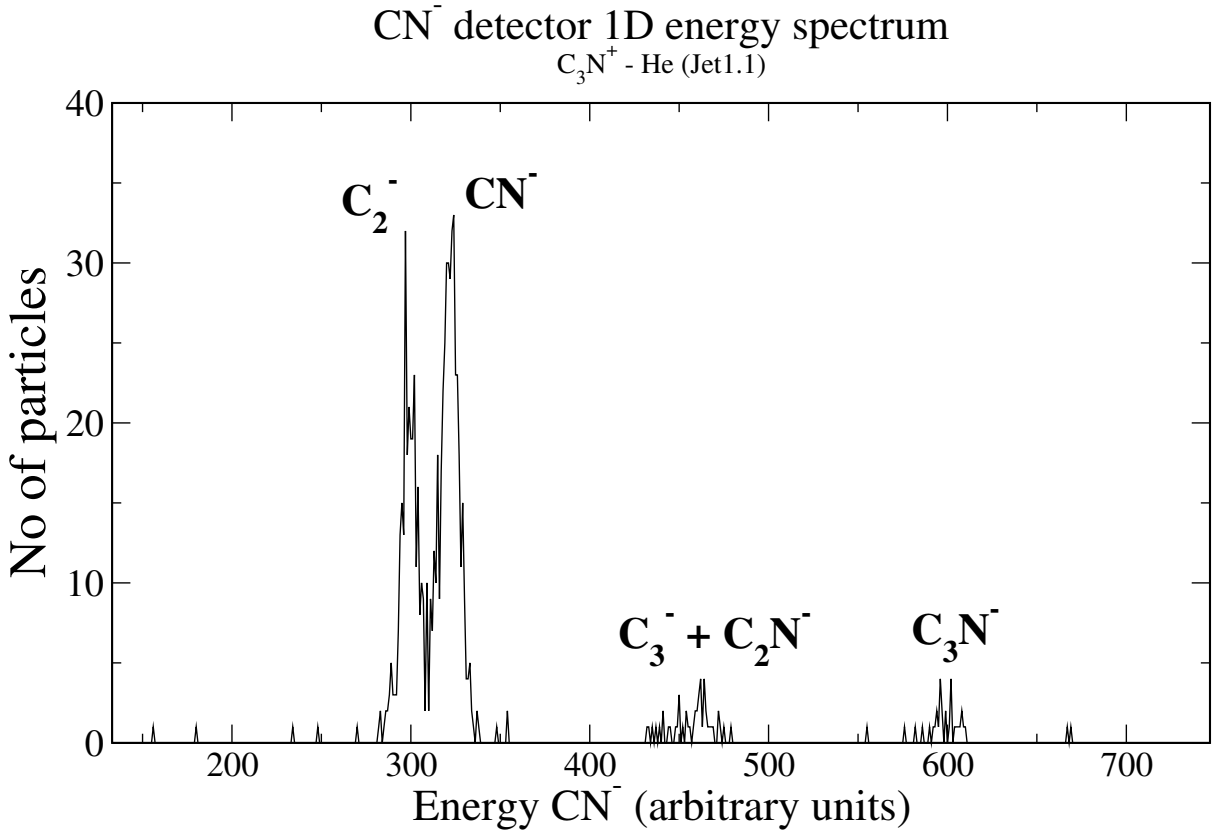


Figure 2-10: Same spectrum of Figure 2-9 with timing selection of t_{CN^-}

coincidence between ADC from " CN^- " and " C^+ " detectors without (Figure 2-11) and with (Figure 2-12) timing selection t_{CN^-} . Without time selection, $2C^+/CN^-$ and $\{CN^{++}\}/C_2^-$ can be barely identified and no other channels are visible. It will be clear on comparison with the Figure 2-12.

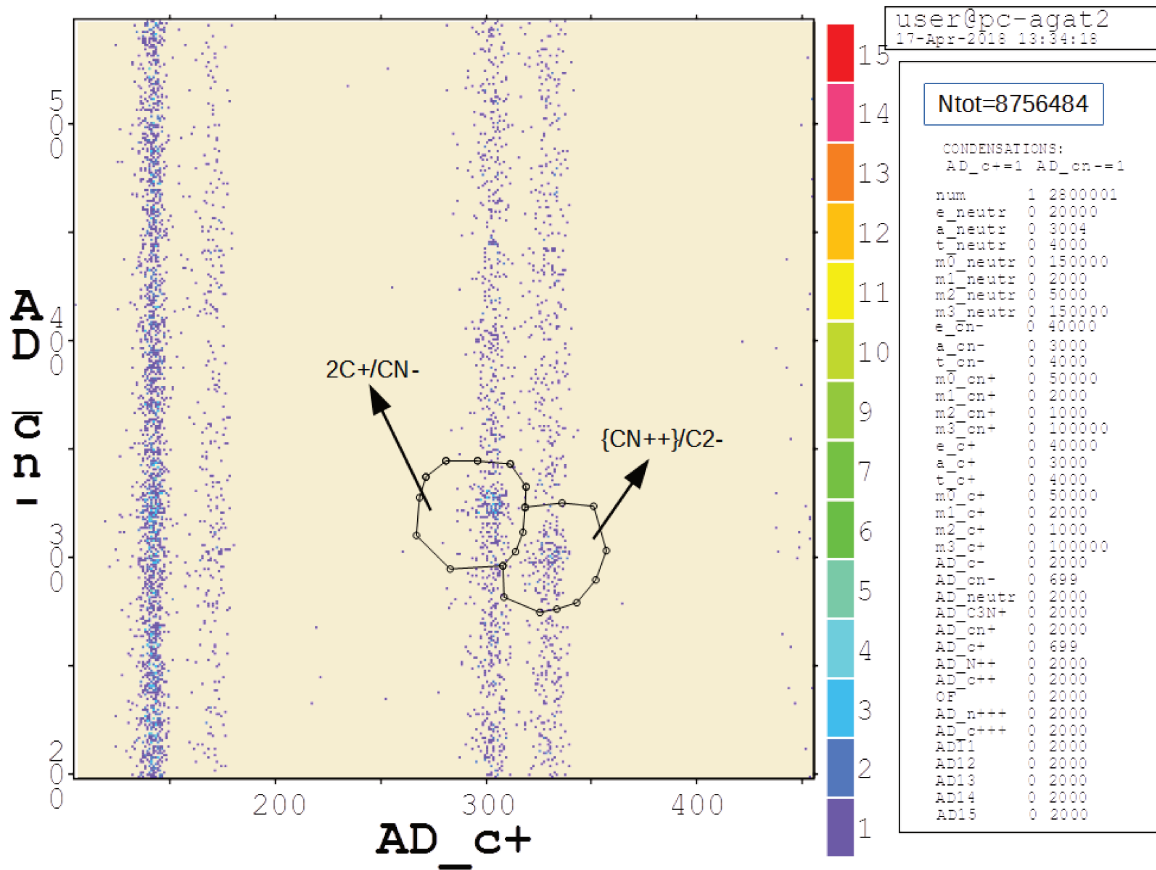


Figure 2-11: 2D coincidence between "C⁺" and "CN⁻" detectors without time selection t_{CN^-}

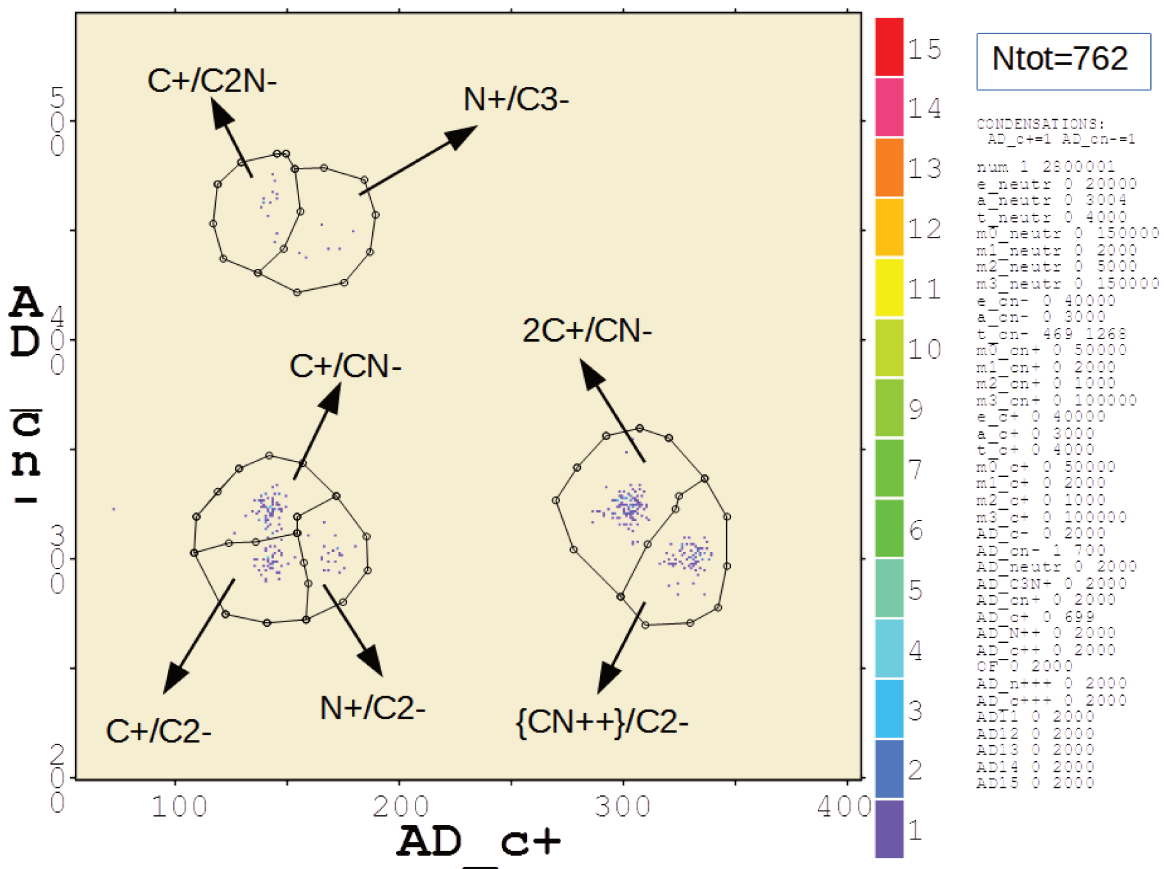


Figure 2-12: Same 2D spectrum as in Figure 2-11 with time selection

2.5 The current signal shape analysis

In our data, the numerical signals are the current outputs from the detectors. Each current signal is characteristic of the type of projectile atom, cluster or molecule. At fixed size and velocity of the projectile, the current signal shape is a characteristic of the projectile fragmentation state (Chabot et al., 2002) as illustrated schematically in the Figure 2-13. This property occurs for a special type of detector that the IPNO detector service makes for our experiments. As a results we could distinguish

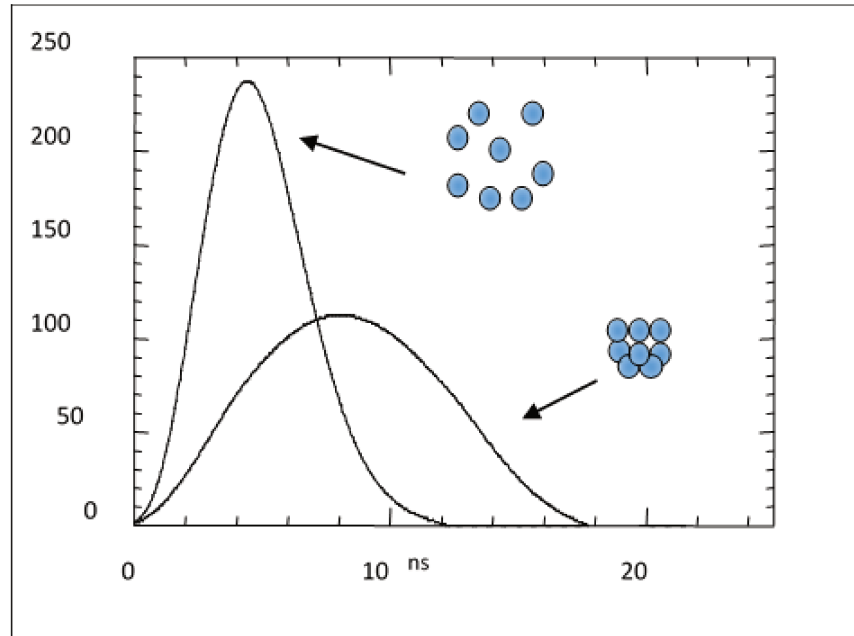


Figure 2-13: Correlation between the shape of the current signal and the fragmentation state of the projectile

in our experiments signal for C_2 of signal from $2C$. This method is demonstrated in the Figure 2-14. This is coming from $C_2N^+ + He$ collision from the neutral detector. x -axis is the ADC spectrum (mass) and y -axis is the amplitude of the current signal. The encircled region contains intact C_2 and fragmented $2C$. There is a visible separation of two regions along y and almost a single region in x . This

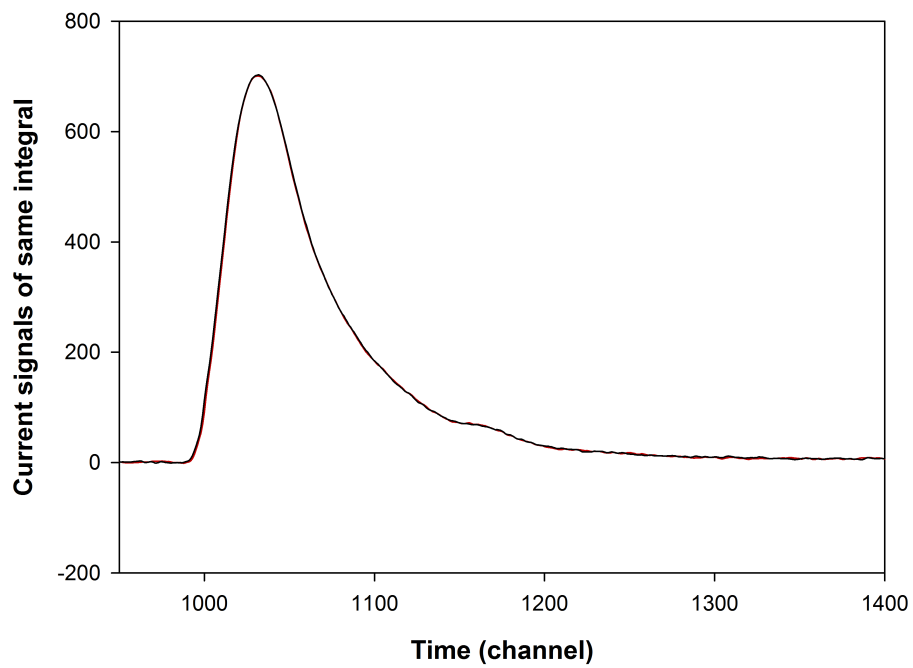
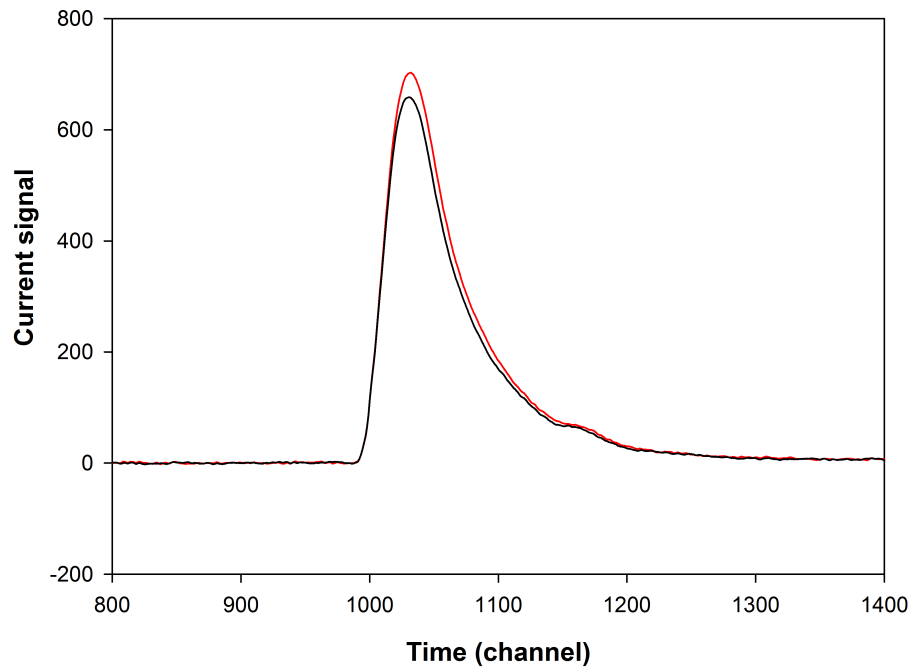


Figure 2-15: Comparison between current signals from CN (red curve) and C_2 (black curve). Top: raw results; down: normalized signals.

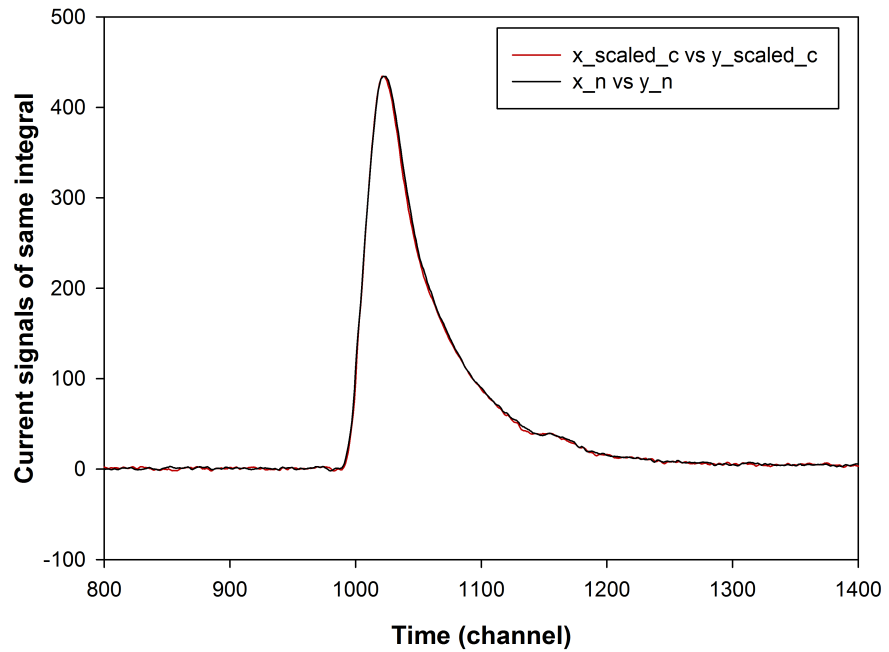
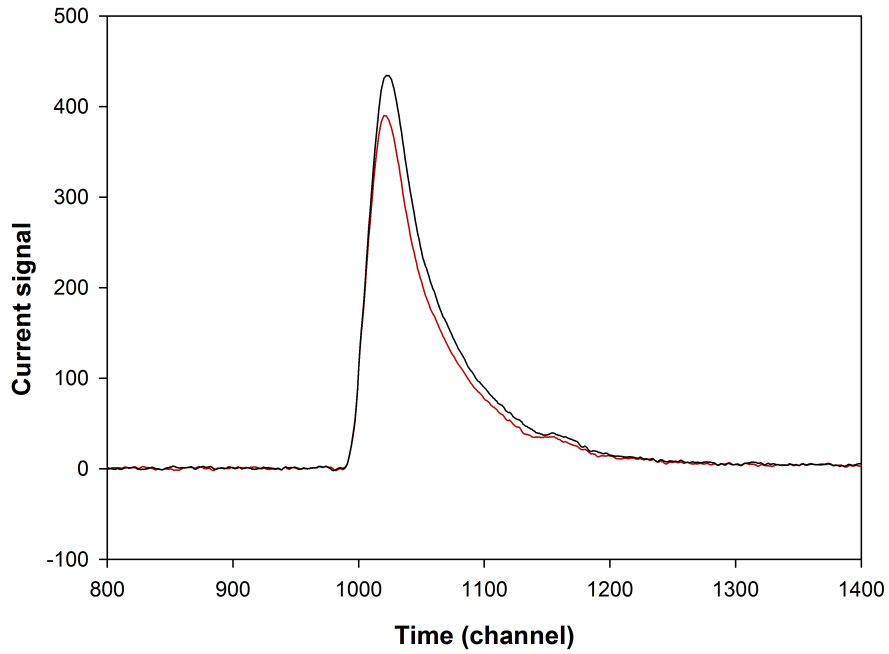


Figure 2-16: Comparison between current signals from C (red curve) and N (black curve); top: raw results; down: normalized signals.

so produced is the sum of individual current signals. For instance the output signal from CN/C is the sum of current signals due to separate CN and C and the same is

true for C_2/N whose current signal is the sum of current due to C_2 and N separately. We found that the *shapes* of CN and C_2 , as well as N and C were identical with our detector (see Figure 2-15 and Figure 2-16). Then since the energy (mass) of the sum is the same (C_2/N has the same mass as CN/C) we could not separate the two channels by the shape analysis method. This was the case for a number of channels (for instance 2 over 7 for $\{C_3N\}$, 2 over 13 for $\{C_3N^+\}$). For that reason, we used a CCD camera whose treatment is presented below.

2.6 The CCD treatment

The treatment of data from the CCD camera has been performed by Tijani IdBarkach from IPNO. The steps included: subtraction of the background, localization of fragments and identification (mass) of the fragments, evaluation of error bars. Figure 2-17

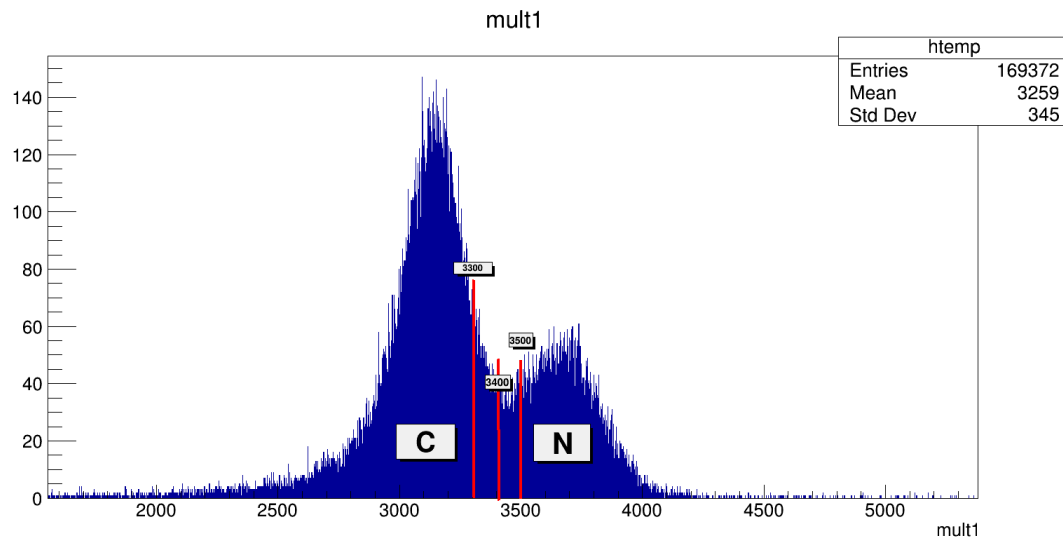


Figure 2-17: Mass resolution of the CCD camera

shows the mass identification between a C and a N fragment. The energy (mass) is obtained by summing the charges delivered by the pixels belonging to the same impact (typically 20 pixels per impact). As seen in Figure 2-17, the mass resolution of the camera is not as good as the mass resolution of commercial detectors (see for instance Figure 2-3 for the " C^+ " detector). In Figure 2-17, the cut at which a mass

separation will be performed is around channel 3400 with some errors (± 150). This will introduce error on the countings and on dissociation BRs. Another source of error is to determine whether two impacts originate from an intact impinging molecule or from a fragmented system. Due to the two carbon foils placed before the camera, all molecules are vaporized into atoms. In Figure 2-18 we show the distribution of distances between two impacts recorded during $C_2N^+ - He$ runs. The very small distances (less than 30/40 pixels, one pixel is $24\mu\text{m}$ large) are due to intact C_2N whereas the distribution of larger distances originate from C_2N fragments, as predicted by simulation of the explosion. Still, the exact limit at which to separate between intact and fragmented species is around 35 pixels, with some error (± 5), that will introduce another error on counting and branching ratios. On the whole, except some channels for which the camera is the only way of resolving the fragmentation, it was possible to compare the CCD results with the shape analysis method for a number of channels. As seen in Table 2.3 (case of $\{C_2N\}$), the agreement is pretty good.

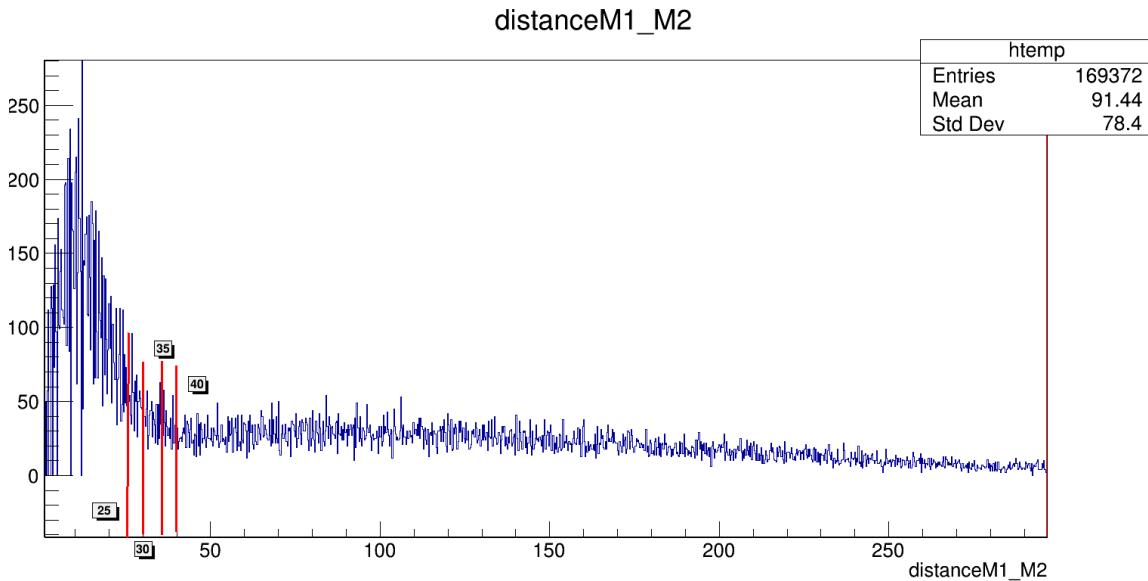


Figure 2-18: Distribution of distances between two impacts (in pixels, 1 pixel = $24\mu\text{m}$) measured in the collision $C_2N^+ - He$

Channel	BR camera (abs. err)	BR shape analysis method (abs. err)
C_2N	0.40(0.05)	0.36(0.01)
$(C_2/N) + (CN/C)$	0.48(0.04)	0.55(0.01)
$C/C/N$	0.12(0.04)	0.09(0.01)

Table 2.3: Comparison between dissociation BR measured with the CCD camera and with the shape analysis method ($C_2N^+ - He$) collision, October 2016

2.7 Probabilities and dissociation branching ratios

2.7.1 The normalisation procedure

Let N_{inc} be the number of incident particles in a run, $N_{process}$ the number of events associated to a given process. The probability for the process $P_{process}$ to happen is given by

$$P_{process} = \frac{N_{process}}{N_{inc}} \quad (2.6)$$

Recall that we use a ‘finger’ to stop the incident beam during counting runs. This effectively left us handicapped in directly measuring the incident particles without which all of the physical quantities couldn’t be found out. We use a method called ‘Normalisation’ to find the incident number of particles. For this, we perform, for each flow rate, ‘Normalisation runs’ with the finger removed. The incident beam intensity is lowered to about 150 events/sec which is about 100/200 times less than during the counting runs. The data is collected and analyzed as usual. The idea is to find a conserved quantity in the experiment of which one of the factor is N_{inc} . The conserved quantity used here is the probability of a significant channel. Significant channel here refers to a channel with high statistics in order to minimize the experimental error. Let P_{SN} be the probability of a significant channel in ‘normalisation run’ and P_S is its counterpart in a counting run. Now, since both the experiments were conducted

with the same parameters, these two probabilities must be equal. That is,

$$P_{SN} = P_S; \quad (2.7)$$

$$P_{SN} = \frac{N_{SN}}{N_{IN}} \text{ and } P_S = \frac{N_S}{N_{inc}}; \quad (2.8)$$

$$\text{it is clear from above that } N_{inc} = N_S \frac{N_{IN}}{N_{SN}}; \quad (2.9)$$

All the quantities in the right side is known and thus the incident particles.

2.7.2 Background subtraction

As mentioned in chapter 1, we do two distinct experimental runs for each flow rate apart from the normalisation run. One with the beam passing directly through the jet, one with the beam travelling unhindered by the jet, jet being introduced in a lateral direction inside the collision chamber. Probabilities are calculated ‘with jet’ (P_{jet}) and ‘without jet’ (P_{back}). The probability P of a process due to the jet only (i.e background subtracted) is then:

$$P = P_{jet} - P_{back} \quad (2.10)$$

2.7.3 Dissociation branching ratios (BRs)

For a process say, single capture, the molecule after collision may or may not be fragmented. Consider single capture,



$\{C_2N\}$ could be $C/C/N$, C_2/N , C/CN , C_2N

Branching ratio (BR) for a given channel is defined as

$$BR_{channel} = \frac{P_{channel}}{\{P_{C_2N}\}} \quad (2.11)$$

$P_{channel}$ and $P\{C_2N\}$ are occurrence probabilities of the considered channel and $\{C_2N\}$ where probabilities are calculated following Equation 3.1 *i.e.* are background subtracted.

2.8 Absolute cross sections

2.8.1 The single collision condition

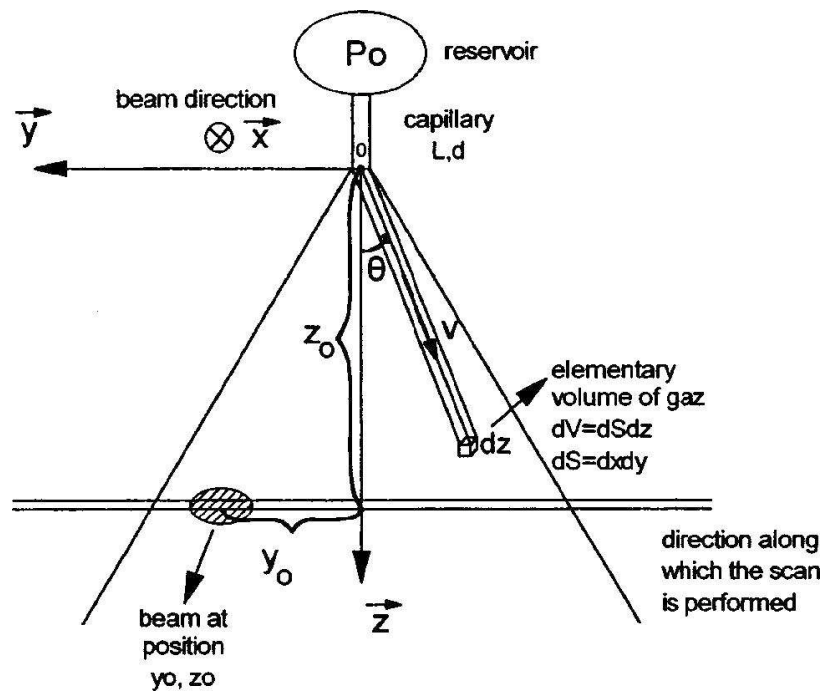


Figure 2-19: Schematic illustration of beam and jet relative positions (from Wohrer et al. (2000))

Thanks to the jet-beam overlap profile that is measured during the experiment, we will be able to extract the cross sections associated with each process. A detailed description of the method is given in Wohrer et al. (2000). A brief description is as follows. In the single collision condition the cross section (σ) of a given process is given as:

$$\sigma = \frac{P_{jet} - P_{back}}{B_{jet}} \quad (2.12)$$

Where, B_{jet} is the ‘beam-jet overlap’ (expressed in units of *atoms cm⁻²*) expressed as:

$$B_{jet} = \iiint \frac{\phi(x, y, z)}{N_0} n(x, y, z) dx dy dz \quad (2.13)$$

$\phi(x, y, z)$ is the flux of incident projectiles, N_0 is the total number of incident particles per second and $n(x, y, z)$ the density of the jet. Following Wohrer et al. (2000), B_{jet} can be written as:

$$B_{jet} = R_{exp} \frac{dN}{dt} \frac{f_\lambda}{v_{th}} \quad (2.14)$$

f_λ is a factor close from 1 depending of the flow regime of the gas in the capillary, v_{th} is the thermal velocity of the helium gas in this jet for room temperature, $\frac{dN}{dt}$ is the flow rate of atoms and R_{exp} is given by Equation 2.15.

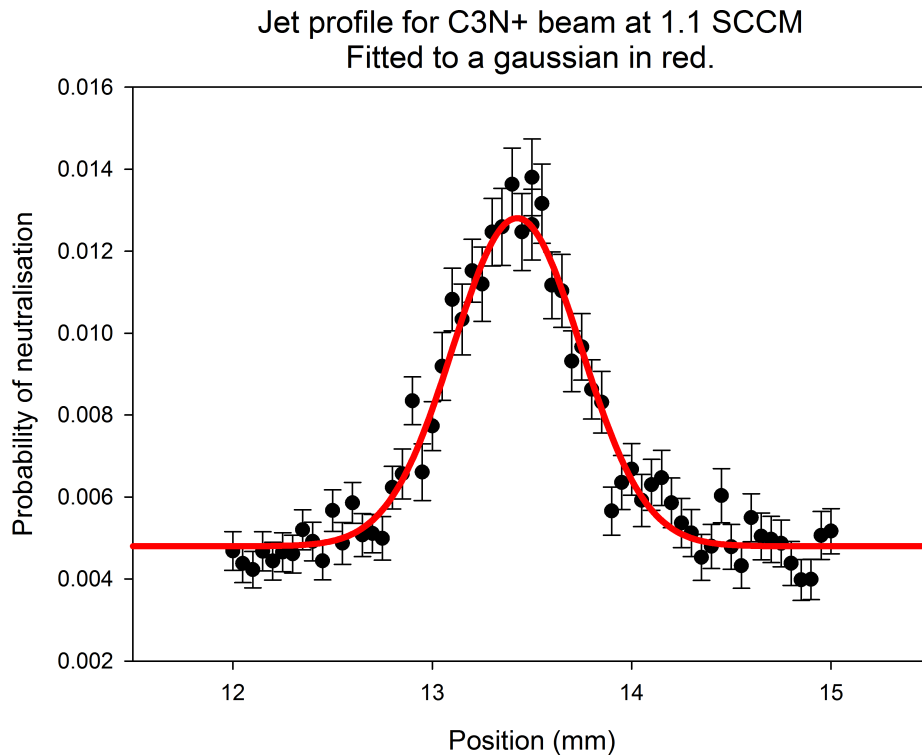


Figure 2-20: An example of beam-jet profile fitted to a Gaussian function.

$$R_{exp} = \frac{P(y_0)}{\int P(y)dy} \quad (2.15)$$

$P(y_0)$ is the probability measured at the beam position y_0 and $\int P(y)dy$ is the integral of the jet profile extracted using a Gaussian fit, see Figure 2-20. We give in Table 2.4 the values of B_{jet} we derived in the runs and that were used for extracting absolute cross sections. As the dimension of the jet is typically 1 mm we see that the density of the jet at the beam crossing is, for 3×10^{13} at/cm², of the order of 10^{-2} Torr.

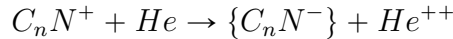
Beam	Run	Flow rate (sccm)	Flow rate corrected from offset (sccm)	B_{jet} (at/cm ²) (relative error bar)
CN^+	March 2015	0.6	0.53	2.77×10^{13} (17%)
C_2N^+	March 2015	1.1	1.03	5.30×10^{13} (14%)
C_3N^+	Feb 2016	1.1	1.03	5.28×10^{13} (11%)
C_3N^+	Feb 2016	0.25	0.18	9.23×10^{12} (14%)
N^+	Oct 2016	1.1	1.03	4.62×10^{13} (18%)

Table 2.4: Measured B_{jet} in the experiments

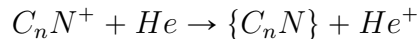
2.8.2 The special case of anions

From the dependence of anion production probabilities with B_{jet} , we could conclude that this production is partly related to double collisions. Indeed, unless Equation 2.12 predicts, we found that the anion production probability is quadratic with B_{jet} as illustrated for instance in Figure 2-21 for $C^-/C/N/C^+$. Anions are produced through the following processes.

- 1 Double electron capture (DEC) in a single collision



- 2 Ion-pair relaxation (IPR) of excited $\{C_nN^{q+}\}$ species, for example following single electron capture (SEC, Q=0) (single collision process):



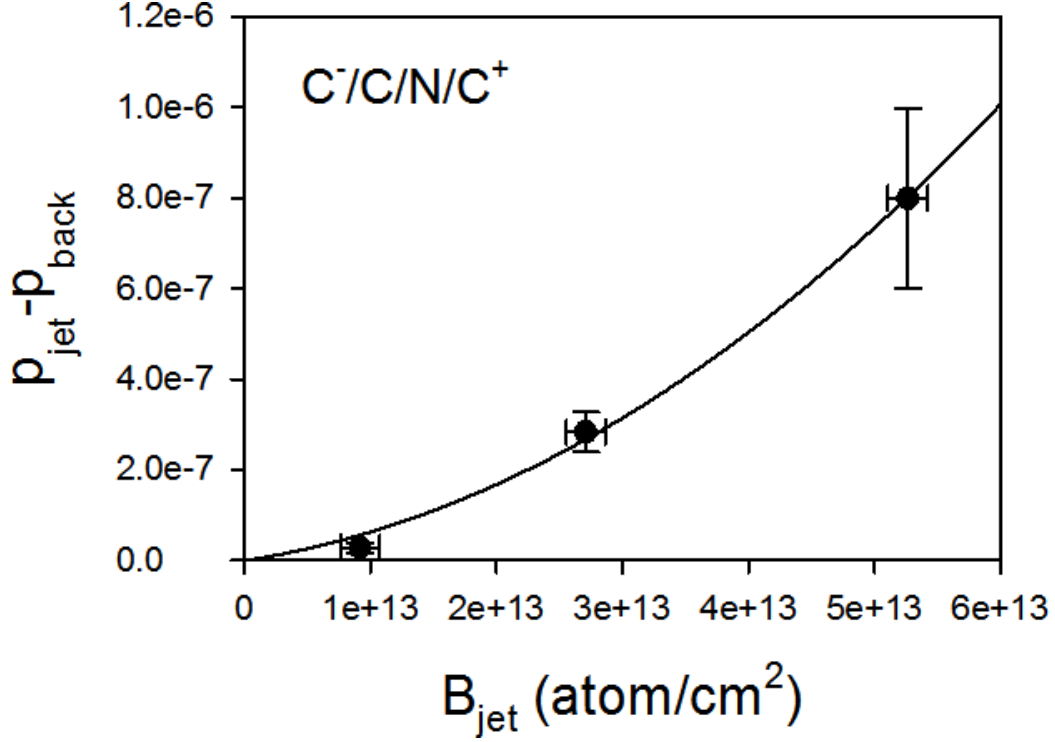
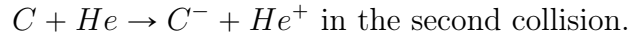


Figure 2-21: Dependence of $C^-/C/N/C^+$ probability with B_{jet}

and $\{C_n N\}$ de-exciting into $(C_p^-/C_{n-p}N^+)$

- 3 Single electron capture onto neutral fragment (SECN) in a second collision following a first excitation process, for example dissociative excitation (double collision process),



The probability of anionic production $\{C_n N^-\}$ writes:

$$P = \sigma_{DEC} B_{jet} + \sigma_{SEC} \sigma_{SECN} \frac{B_{jet}^2}{2} \quad (2.16)$$

The first term in the Equation 2.16 corresponds to single collision process whereas the second one is associated with double collisions in the jet. In order to reduce

the quadratic dependence of P with B_{jet} in the equation to a linear one, normalized probabilities P_N are introduced defined as

$$P_N = \frac{P}{P_{SUM}} \quad (2.17)$$

Where P_{SUM} refers to the sum of probabilities of ‘large’ processes (Single ionization, excitation etc.) which are directly proportional to B_{jet} . For runs with incident C_3N^+ we choose P_{SUM} to be equal to the complete channels of Figure 2-5 that are linear with B_{jet} (see Figure 2-22). We have, for the associated cross section,

$$P_{SUM} = \sigma_{SUM} B_{jet} \quad (2.18)$$

and then:

$$P_N = \frac{\sigma_{DEC}}{\sigma_{SUM}} + \frac{\sigma_{SEC}\sigma_{SECN}}{\sigma_{SUM}} \frac{B_{jet}}{2} \quad (2.19)$$

The above formula render itself to extract, from the B_{jet} dependence of P_N , $\frac{\sigma_{DEC}}{\sigma_{SUM}}$ (ordinate of the origin) and $\frac{\sigma_{DEC}\sigma_{SECN}}{\sigma_{SUM}}$ (slope of the curve) quantities as seen in Figure 2-22 (down). Since σ_{SUM} and σ_{SEC} are measured in the experiment, σ_{DEC} and σ_{SECN} cross sections can be deduced.

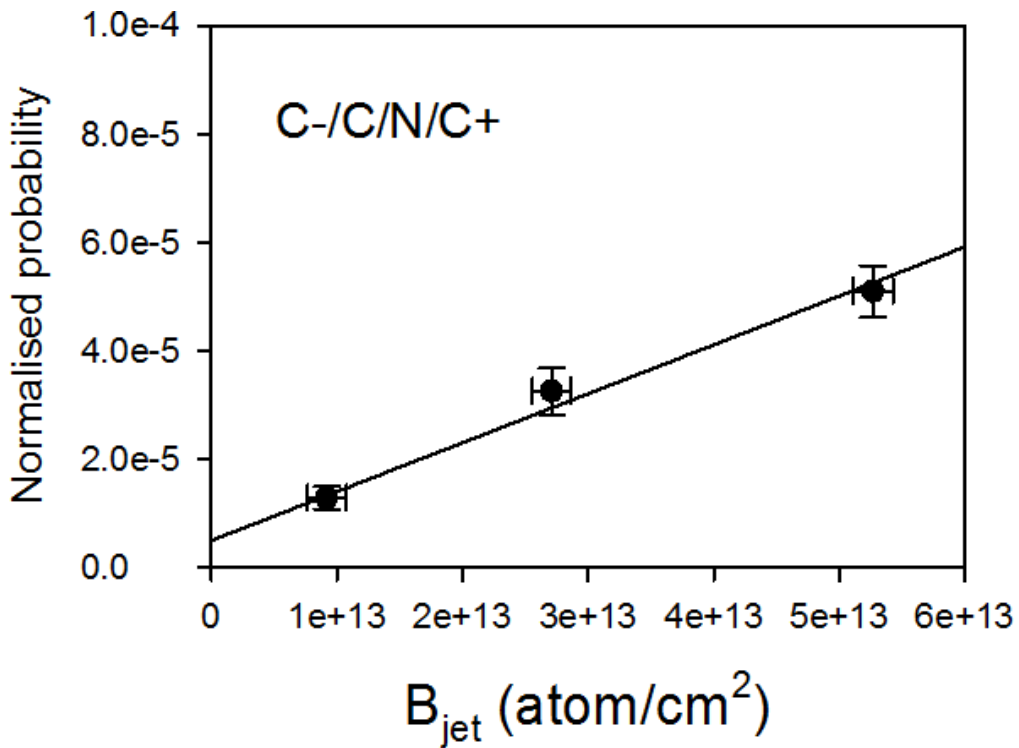
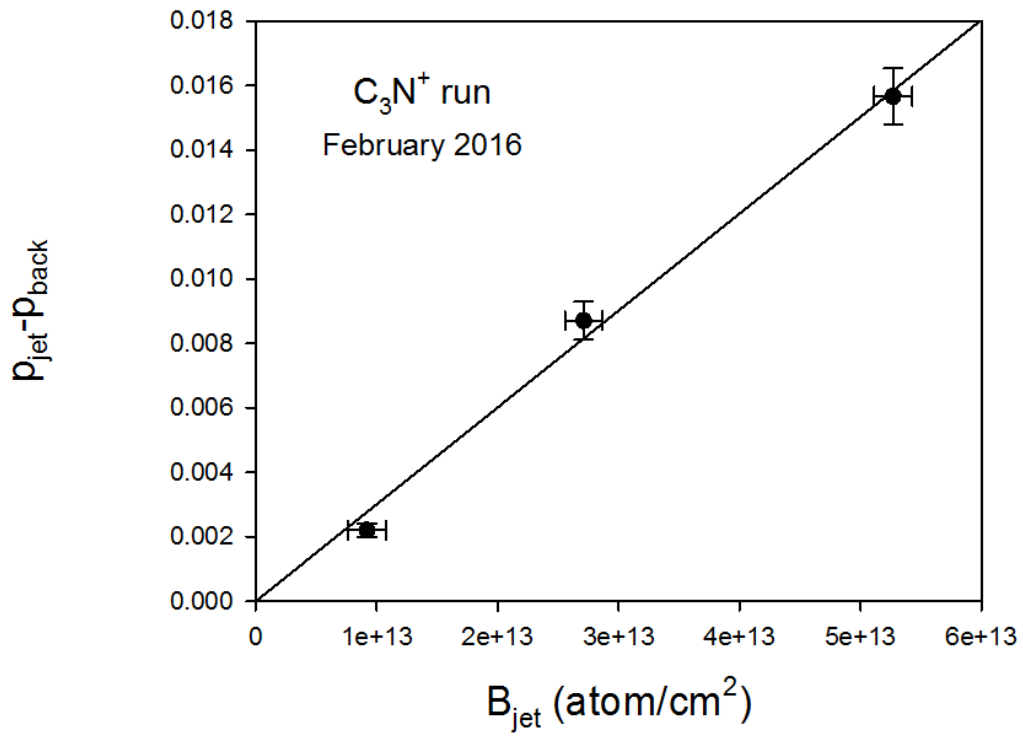


Figure 2-22: Probabilities as a function of B_{jet} . Top: for P_{sum} (Equation 2.18); bottom: for P_N where the channel studied is $C^-/C/N/C^+$ (Equation 2.19).

Chapter 3

Modelisation of the collision

3.1 Molecule-atom collisions : the Independent Atom and Electron (IAE) model

The IAE model used in this study was first introduced by Wohrer and Watson (1993) to study the effects of orientation of a diatomic molecule on the cross section for multielectron ionization in fast collisions. According to this paper, «The model was used to compare K and L-shell ionization cross sections for O_2 molecules with inter-nuclear axes oriented parallel and perpendicular to the beam». The strong predicted alignment effect was measured a few years later in He^+-N_2 collisions by Werner et al. (1997) and more recently in the He_2 and Ne_2 dimers by Kim et al. (2014). On the other hand the ability of this simple model to predict absolute cross sections is another interesting topic. In a recent work (Labaigt et al., 2015) probabilities were introduced in the IAE model without any adjustment and IAE predictions for various electronic processes (single and multiple ionization and electron capture) occurring in C_n^+-He, Ar collisions ($n = 1-5, v = 2.25$ ua) compared to the experiment. The IAE model is tested here for $C_{n=1,3}N^+-He$ collisions at the same $v = 2.25$ a u velocity.

3.1.1 Description of the IAE model

The dynamics of the molecule-atom collision is described in the framework of the impact parameter approximation (Bransden and McDowell, 1992) in which the projectile, whose centre of mass is characterized by the impact parameter \mathbf{b} with respect to the target, follows rectilinear trajectories with constant velocity \mathbf{v} (see Figure 3-1). The IAE model assumes the following :

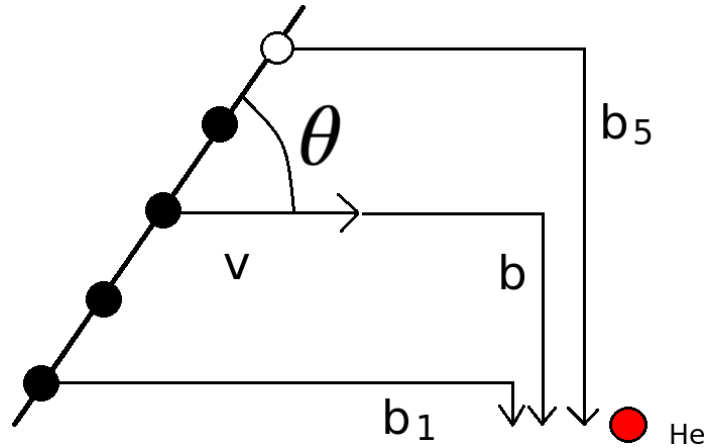


Figure 3-1: Schematic view of the molecule-atom collision

- The molecule under collision is supposed to be made of n independent atoms (ions).
- The electrons in each atom are treated independently following the so-called Independent Particle Model (IPM) (McGuire and Weaver, 1977) and (Lüdde and Dreizler, 1985) widely used in collisions physics.

The atoms are positioned at the proper molecule geometry and do not move during the fast ($\sim 10^{-16}s$) collision. For instance C_4N^+ is modelled by 4 carbon atoms (ions) shown in black in Figure 3-1 and one N atom (open circle) at the end of the chain (see precise geometries in Chapter 4). The collision between C_4N^+ and He is treated as 5 collisions (three $C-He$, one C^+-He and one $N-He$)* operating at different impact parameters. The impact parameters values depend on the inter-atom

*Due to the charge repartition in the molecule, N and not N^+ is introduced in the simulation (see chapter 4).

distances, orientation angle θ and the polar angle α of \mathbf{b} in the plane perpendicular to the page (Wohrer et al., 1996). In the independent atom approximation the IAE probabilities consist of products of atomic probabilities. For instance the He-induced neutralization probability P_{Neutr} of a C_nN^+ molecule ($C_nN^+ \rightarrow \{C_nN\}$ molecule) is expressed as:

$$\begin{aligned}
P_{Neutr}(\mathbf{b}) &= \sum_i^n P_{Capt}^{(1)}(b_i) \\
&\times \prod_{i=1}^n (1 - P_{ion}(b_i)) \prod_{j \neq i} (1 - P_{Capt}(b_j)) \\
&+ \left[\sum_{i=1}^n P_{Capt}^{(2)}(b_i) + \sum_{i=1}^n \sum_{j>i} 2P_{Capt}^{(1)}(b_i)P_{Capt}^{(1)}(b_j) \right] \\
&\times \left[\sum_{i=1}^n P_{ion}^{(1)}(b_i) \prod_{j \neq i} (1 - P_{ion}(b_j)) \right]
\end{aligned} \tag{3.1}$$

where b_i stands for the impact parameter of the i -th centre with respect to the target, $P_{Capt}^{(1)}(b_i)$, $P_{Capt}^{(2)}(b_i)$ and $P_{Capt}(b_i)$ stand for the probabilities of single-electron, double-electron and total electron capture on centre i , and $P_{ion}^{(1)}(b_i)$, $P_{ion}(b_i)$ stand for the projectile single ionization and total ionization for centre i (C , C^+ or N). The first term of Equation 3.1 represents the dominant contribution to the neutralization probability, which is from single-electron capture without projectile ionization (described in the $(1 - P_{ion})$ terms). The second term, amounting to a few per cent at most, corresponds to double-electron capture concomitant with projectile single ionization. The atomic probabilities of processes occurring in C -He, C^+ -He and N -He collisions are computed assuming independence of the electrons. Furthermore, only valence electrons of the projectile and/or the target are assumed to be active within the dynamics. The probabilities entering Equation 3.1 can thus be written as:

$$P_{capt}^{(1)}(b_i) = 2p_c(b_i)(1 - p_c(b_i)) \tag{3.2}$$

$$P_{capt}^{(2)}(b_i) = p_c(b_i)^2 \tag{3.3}$$

$$(1 - P_{capt}(b_i)) = (1 - p_c(b_i))^2 \tag{3.4}$$

while,

$$P_{ion}^{(1)}(b_i) = 2p_{ion}^{(2s)}(b_i)(1 - p_{ion}^{(2s)}(b_i))(1 - p_{ion}^{(2p)}(b_i))^a + ap_{ion}^{(2p)}(b_i)(1 - p_{ion}^{(2p)}(b_i))^{(a-1)}(1 - p_{ion}^{(2s)}(b_i))^2 \quad (3.5)$$

$$(1 - P_{ion}(b_i)) = (1 - p_{ion}^{(2s)}(b_i))^2(1 - p_{ion}^{(2p)}(b_i))^a \quad (3.6)$$

p_c is the probability for capturing an electron from He , while $p_{ion}^{(2s,2p)}$ refers to the probability of ionizing one electron from the 2s and 2p valence subshells of C (C^+ or N). Depending on the projectile (C, C^+, N), $a = 2, a = 1$ or $a = 3$ respectively. Absolute cross sections are derived by integrating over \mathbf{b} IAE probabilities such as Equation 3.1. In Figure 3-2 we show how this integral depends (at variance with the ion-atom case) not only on the modulus of \mathbf{b} but also on the polar angle of \mathbf{b} and on the orientation angles of the molecule. The integrals to be performed are then rather complicated. They were performed by a Monte Carlo procedure within a Fortran code.

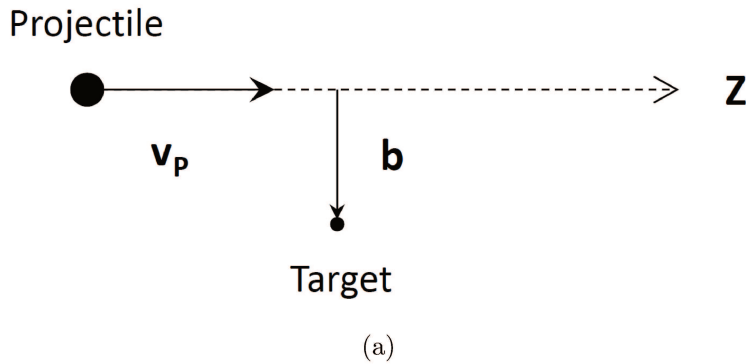
ION-ATOM COLLISION

The velocity \mathbf{v}_p and the target define the collision plane.

$\mathbf{b} = \{b, \alpha\}$, α is the polar angle of \mathbf{b} in the plane perpendicular to \mathbf{Z} .

$$\sigma_{proc} = \int \int P_{proc}(b, \alpha) b db d\alpha = 2\pi \int P_{proc}(b) b db$$

Integration over one length b .

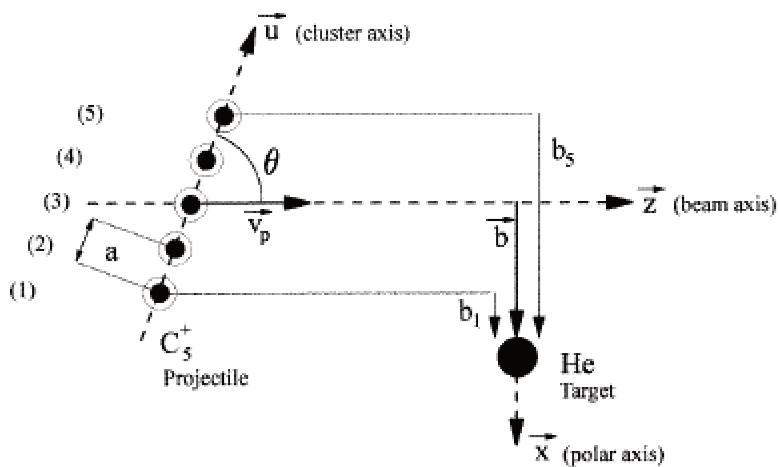


ION-LINEAR MOLECULE COLLISION

The molecule axis \mathbf{u} and \mathbf{V}_p define the collision plane.
 α is the polar angle of \mathbf{b} (target is in the plane for a given α).

$$\sigma_{proc} = \int \int \int P_{proc}(b, \theta, \alpha) b db \sin \theta d\theta d\alpha$$

Integration over two angles (θ, α) and one length (b)



(b)

ION-3D MOLECULE COLLISION

The beam axis \mathbf{u} and \mathbf{b} define the collision plane, α is the polar angle of \mathbf{b}

$$\sigma_{proc} = \frac{1}{4\pi} \int \int \sin\theta d\theta d\phi \sigma_{proc}(\mathbf{u})$$

Integration over three angles (θ, ϕ for \mathbf{u} , α for \mathbf{b}) and one length b .

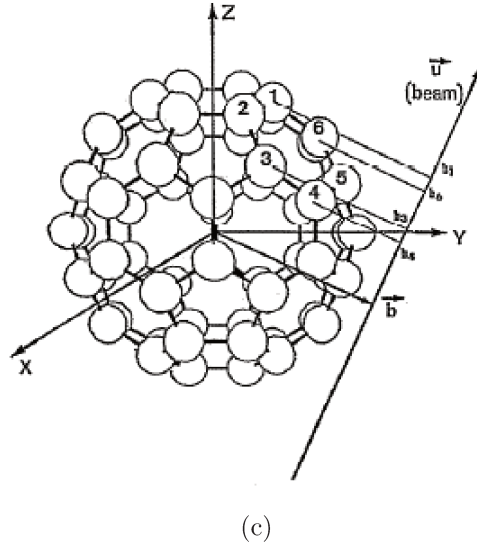


Figure 3-2: Cross section calculation, for a given process, in ion-atom (a), ion-linear molecule (b) and general ‘3D molecule-atom’ (c) configurations.

3.1.2 IAE code: Cross sections calculations and energy deposit calculations

The IAE Fortran code with integrals performed by a Monte Carlo procedure was developed by Mezdari (2005), initially to compute projectile ionization and excitation cross sections. Later on the code was extended in order to calculate the electron capture and target ionization as well (Béroff et al., 2013).

3.1.2.1 Cross sections calculations

Suppose we want to calculate the cross section whose expression is given in figure 3.2

b). To calculate the cross section we generate b, α, θ :

- α is generated with a uniform probability $P(\alpha) = \frac{1}{2\pi}$
- θ is generated with a probability $P(\theta) = \sin(\theta)$
- b is generated with a probability $P(b) = \frac{2b}{b_{max}^2}$

Where b_{max} is the maximum value of b that we generate in the code; the value of b_{max} is set when results are independent of its value (convergence of the results). Suppose we are interested in the cross section $\sigma^{(m)}$ for removing m electrons from the projectile. The cross section is calculated as :

$$\sigma^{(m)} = \pi b_{max}^2 \frac{\sum_{b \leq b_{max}} \sum_{\theta \leq \frac{\pi}{2}} \sum_{\alpha \leq 2\pi} l_{b,\theta,\alpha}^{(m)}}{N_{try}} \quad (3.7)$$

Where $l_{(b,\theta,\alpha)}^{(m)}$ is equal to 1 if m electrons have been ionized during the try (b, θ, α) and 0 otherwise. At each event (collision) we draw for each electron a random number r ($0 \leq r \leq 1$). For the electrons of the projectile the random number is compared to the probability of ionization $P_i(b_i)$ and the probability of excitation $P_{exc}(b_i)$ (b_i is the impact parameter for the atom i to which the electron belongs). These probabilities for the $C, C^+, N, N^+ - He$ collision systems have been calculated using the Classical Trajectory Monte Carlo (CTMC) method (see next section). If $r \leq P_i(b_i)$ the electron is ionized, if $P_i(b_i) < r \leq P_i(b_i) + P_{exc}(b_i)$ it is excited ; if $r > (P_i(b_i) + P_{exc}(b_i))$ it remains on its initial atomic (ionic) shell. The same is done for the electrons of the target where the random is compared to target ionization and electron capture probabilities. All electrons of all atoms are so tested and a final result of the collision is registered. This number will be divided by the number of tries (collisions), typically equal to 10^6 events, and multiplied by the geometrical cross section πb_{max}^2 following Equation 3.7.

3.1.2.2 Energy deposit by electronic excitation calculation

The probability of exciting an electron is calculated as explained above. When the collision is finished, excitation is obtained if one or more electrons have been excited whereas no projectile ionization nor electron capture has taken place. As will be seen in the next section, excitation into specific (n, l) final states are calculated with the CTMC method. By relating these final states to the corresponding excited energy E , it is possible to derive differential in energy $\frac{dp_{exc}}{dE}$ probabilities. The differential in energy excitation cross section is then obtained as (case of the linear molecule):

$$\frac{d\sigma}{dE} = \int \int \int \frac{dP_{exc}(b, \theta, \alpha)}{dE} b db \sin\theta d\theta d\alpha \quad (3.8)$$

and calculated as explained before. The variation with E of $\frac{d\sigma}{dE}$ provides the energy deposit distribution that we will present in chapter 5.

3.2 Atom(ion)-atom collisions : Classical Trajectory Monte Carlo (CTMC) calculations

3.2.1 The CTMC approach

A complete quantum mechanical calculation of the probabilities and cross sections of the various processes involved in collision is impractical because of the immense computational resources that it demands. It is also the case in semi-classical calculations where the size of the basis required to describe all elastic and inelastic channels often renders the method impractical. This is where a purely classical description of the process is called for in the case of ion-atom collisions. CTMC (Classical Trajectory Monte Carlo method) is the most widely used method which treats the ion-atom collision as purely classical. This was developed by Abrines and Percival (1966) and later used successfully by Olson and Salop (1977) to calculate the ionization and capture cross sections for positive ions colliding with H atom at intermediate energies. Many authors have since then used the CTMC method and recent developments have

concerned the application of CTMC to ion-molecule collisions (Illescas et al., 2011) or the switching method between 4-body and 3-body collisions for the treatment of two active electrons (Jorge et al., 2016).

Before moving on to the description, the validity of such a deviation from a physically ‘accurate’ (i.e, quantum-mechanical) method needed to be addressed. CTMC considers the interacting particles as classical objects in the sense that they obey classical laws of motion. Typical processes not classical are tunneling (ionization at low and high impact velocities) and interference effects (for instance for electron capture at small impact velocities). It then results that the velocity range where CTMC is valid is typically [1 a.u - 4 a.u] for electron capture and [1 a.u - 6 a.u] for ionization (Illescas, private communication). This is near the assumption of Bransden and McDowell (1992), which is $1 \leq \frac{v_p}{v_e} \leq 4$, where v_p is the velocity of the projectile and v_e is the velocity of the target electron. In our case $v_p = 2.2$ au and $v_e \sim 1.7$ au (active electron of helium). The method is outlined below.

3.2.1.1 Dynamics

The collision is treated within the impact parameter approximation (see Figure 3-3), valid at these energies (Jorge Palacios, 2017). In a purely classical framework, one introduces a phase-space distribution $\rho(\mathbf{r}, \mathbf{p}, t)$ which satisfies the Liouville equation:

$$\frac{\partial \rho}{\partial t} = -\{\rho, H_e\} = -\frac{\partial \rho}{\partial \mathbf{r}} \frac{\partial H_e}{\partial \mathbf{p}} + \frac{\partial \rho}{\partial \mathbf{p}} \frac{\partial H_e}{\partial \mathbf{r}} \quad (3.9)$$

$\{\rho, H_e\}$ is the Poisson’s bracket with H_e is the electronic Hamiltonian function.

To describe and solve the problem of an atom and an electron, a statistical collective of $N \sim 10^6$ non-interacting electrons is defined for each nuclear trajectory:

$$\rho(\mathbf{r}, \mathbf{p}, t) = \frac{1}{N} \sum_{j=1}^N \delta(\mathbf{r} - \mathbf{r}_j(t)) \delta(\mathbf{p} - \mathbf{p}_j(t)) \quad (3.10)$$

Using a ρ distribution discretized in terms of N independent trajectories allows to transform the Liouville equation into the well-known Hamilton equations monitoring

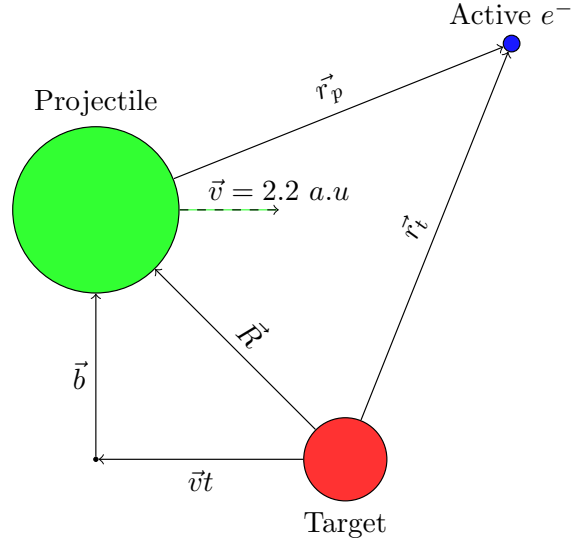


Figure 3-3: A schematic diagram showing a 3 body collision

the time evolution of each electron trajectory.

3.2.1.2 Initial conditions

Different classical initial distributions have been proposed through the years (Jorge Palacios, 2017). In the microcanonical distribution all electrons are having the same energy corresponding to the ionization potential E_i of the active electron we want to describe (Reinhold and Falcón, 1986):

$$\rho_M(\mathbf{r}, \mathbf{p}) = k\delta(E_i - \frac{p^2}{2m} - V(r)) \quad (3.11)$$

where δ is the delta function, k is the normalisation constant and $\frac{p^2}{2m} - V(r)$ is the Hamiltonian of the isolated atom. It can be shown (Reinhold and Falcón, 1986) that

r is confined between 0 and r_0 where r_0 satisfies:

$$E_i = V(r_0) \quad (3.12)$$

In order to generate an initial condition for the active electron, two transformations must be performed (Reinhold and Falc3n, 1986):

- Transforming Cartesian $(\mathbf{r}, \mathbf{p}) \rightarrow (E, r, \nu_r, \nu_p, \phi_r, \phi_p)$

The Cartesian coordinates of position-momentum phase space is related to the new coordinates as:

$$\begin{aligned} x &= r(1 - \nu_r^2)^{\frac{1}{2}} \cos \phi_r \\ y &= r(1 - \nu_r^2)^{\frac{1}{2}} \sin \phi_r \\ z &= r\nu_r \\ p_x &= [2m(E - V(r))]^{\frac{1}{2}} (1 - \nu_p^2)^{\frac{1}{2}} \cos \phi_p \\ p_y &= [2m(E - V(r))]^{\frac{1}{2}} (1 - \nu_p^2)^{\frac{1}{2}} \sin \phi_p \\ p_z &= [2m(E - V(r))]^{\frac{1}{2}} \end{aligned}$$

The intervals of the variables are given by:

$$E = E_i; \quad r \in [0, r_0]; \quad \nu_r, \nu_p \in [-1, 1]; \quad \phi_r, \phi_p \in [0, 2\pi]$$

- a second transformation is performed introducing ω by:

$$\omega(r) = \int_0^r m r'^2 (2m[E_i - V(r')])^{\frac{1}{2}} dr'$$

The variables are selected at random from the intervals:

$$\omega \in [0, \omega(r_0)], \quad \phi_r, \phi_p \in [0, 2\pi], \quad \nu_r, \nu_p \in [-1, 1]$$

A good initial distribution must reproduce as well as possible the quantum radial and momentum densities. The microcanonical distribution is known not to reproduce well the radial density as illustrated for instance in Figure 3-4. This behaviour (sharp boundary at the classical turning point) will induce limitations to a good description of processes in the low and medium velocity range (Jorge Palacios, 2017) and (Jorge et al., 2014) where dynamical processes involve electrons located at the tail of the

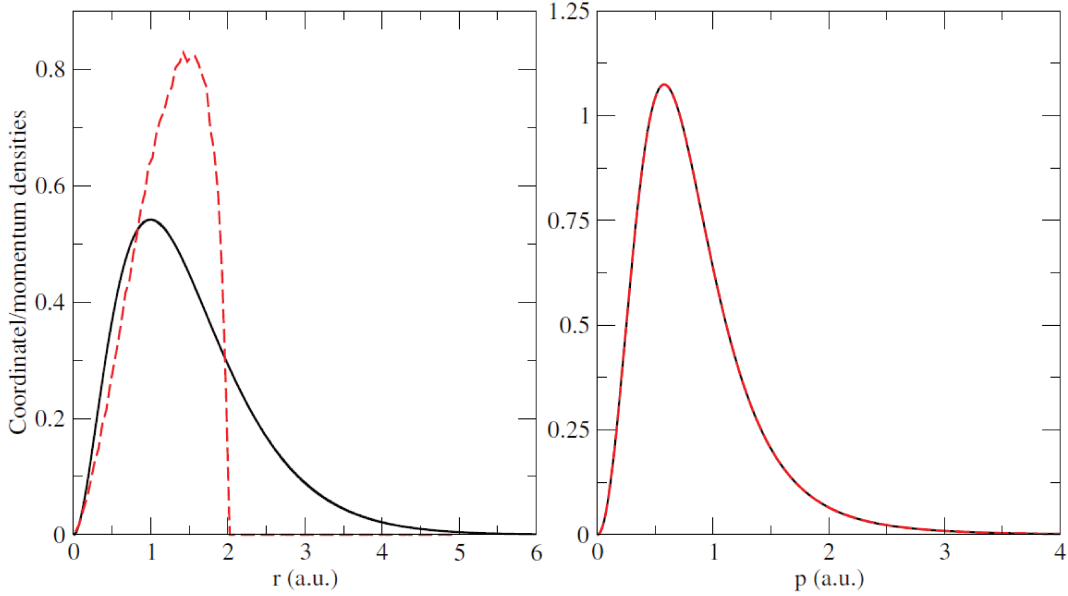


Figure 3-4: Comparison of the quantum (black line) and microcanonical (red line) distributions of $H(1s)$ in the coordinate (left) and momentum (right) spaces; extracted from Jorge Palacios (2017)

quantum-mechanical density.

Another initial condition refers to the distance R_0 of the projectile to the target at the beginning of the simulation. R_0 is chosen large enough so as it is possible to neglect the interaction of the projectile with the target. Results of the simulations must be independent of R_0 .

3.2.1.3 One electron calculations

In this method, only one electron of the target is considered active. Such calculations therefore yield probabilities for electron capture by the projectile, as well as for target excitation and ionization. The Hamiltonian is given by (atomic units are used):

For the $C\text{-He}$ collision:

$$H_{1e^-} = \frac{p^2}{2} + V_{mod}^{He^{++}+e}(r_t) + V_{mod}^{C+e}(r_p) \quad (3.13)$$

For the C^+-He (or N^+-He) collision:

$$H_{1e^-} = \frac{p^2}{2} + V_{mod}^{He^{++}e}(r_t) + V_{mod}^{C^{++}e}(r_p) \quad (3.14)$$

V_{mod} are the model potentials describing the interaction of the active electron with frozen projectile and/or target cores. They are built as explained in section 3.2.1.5. Because, N^- is not stable (Hotop and Lineberger, 1985), $1e^-$ calculations in $N-He$ cannot be performed with the active electron belonging to He, with a Hamiltonian similar to equation 3.13.

Further, with a suitable $e^- - He$ model potential (see Section 3.2.2.4.1), we could study projectile excitation and ionization in all C , C^+ , N , $N^+ - He$ systems within $1e^-$ calculations, considering active e^- on the projectile and using e.g. a Hamiltonian of the type,

For the $N-He$ collision:

$$H_{1e^-} = \frac{p^2}{2} + V_{mod}^{He^{++}e}(r_p) + V_{mod}^{N^{++}e}(r_t) \quad (3.15)$$

After a sufficiently long integration time of the Hamilton equations, $t_{max} \sim \frac{500}{v} - \frac{2000}{v}$ au , the final collision processes are selected by applying the well known energy criteria. The final energies of the electron will associate each electron trajectory to a different process. Electrons with positive energies with respect to the target ($E_T > 0$) and projectile ($E_P > 0$) will imply ionization, and the bound states will be differentiated as electron capture ($E_P < 0$ and $E_T > 0$) and elastic/excitation ($E_P > 0$ and $E_T < 0$) processes. Once this energy criteria has been applied, the probability corresponding to a process i (ionization, capture or excitation in the 1 electron scheme) will be obtained simply dividing the number of trajectories giving rise to this process, N_i , by

the total number of considered trajectories, N .

$$P_i(v, b) = \frac{N_i}{N} \quad (3.16)$$

For a given collision velocity, the integration of the opacity function $bP_i(v, b)$ over all impact parameters will lead to the associated total cross section:

$$\sigma_i = 2\pi \int_0^\infty bP_i(v, b)db \quad (3.17)$$

3.2.1.4 Two electron calculations

Here, one electron each of the projectile and the target take part in the collision.

For $X^+ - He$ collision, the Hamiltonian writes:

$$\begin{aligned} H_{2e^-} = & \frac{p_1^2}{2} + V_{mod}^{(He^++e)}(r_{1T}) + V_{mod}^{(X^{2++e})}(r_{1P}) \\ & + \frac{p_2^2}{2} + V_{mod}^{(He^++e)}(r_{2T}) + V_{mod}^{(X^{2++e})}(r_{2P}) \\ & + \frac{1}{|\mathbf{r}_{1T} - \mathbf{r}_{2T}|} \end{aligned} \quad (3.18)$$

and for $X-He$:

$$\begin{aligned} H_{2e^-} = & \frac{p_1^2}{2} + V_{mod}^{(He^++e)}(r_{1T}) + V_{mod}^{(X^++e)}(r_{1P}) \\ & + \frac{p_2^2}{2} + V_{mod}^{(He^++e)}(r_{2T}) + V_{mod}^{(X^++e)}(r_{2P}) \\ & + \frac{1}{|\mathbf{r}_{1T} - \mathbf{r}_{2T}|} \end{aligned} \quad (3.19)$$

In the case of two active electrons, the initial distribution $\rho(\mathbf{r}_1, \mathbf{r}_2, \mathbf{p}_1, \mathbf{p}_2, t \rightarrow -\infty)$ consists of the product of microcanonical sets $\rho_{He}(\mathbf{r}_1, \mathbf{p}_1)\rho_{X^+,X}(\mathbf{r}_2, \mathbf{p}_2)$ of dimension $N = N_{He}N_{X^+,X}$ (Labaigt et al., 2015). Integration of the Hamilton equations is performed for the $N_{He}N_{X^+,X}$ pairs of electrons. Main shortcomings of $2e^-$ calculations are

2 The treatment of electron capture.

Indeed in the case of electron capture, there is in the final state 2 electrons on the same atom, which is classically unstable. A recent switching method was proposed by Jorge et al. (2016) to solve this problem, but it was not applied in the present work. With two active electrons, we can distinguish between an exclusive process where the state of the two electrons is known from an inclusive process where the state of only one electron is defined (i.e consisting of a sum of at least two exclusive processes).

3.2.1.5 The model potentials

When the active electron is located in the He target, the model potential to describe the interaction of the valence electron with He^+ ionic core, is of the form:

$$V_{mod}(\text{He}^+ + e^-) = -\frac{Z - N}{r} - \frac{1 + \alpha r}{r} e^{-2\alpha r} \quad (3.20)$$

where Z , N and r are the atomic number, number of electrons in the frozen core and radial distance from the center of the atom to the active electron and α is set to its variational value, $\alpha = 1.6875$.

For the projectiles, the V_{mod} is of the form,

$$V_{mod}(r) = -\frac{Z - N}{r} - \frac{Ae^{-Br} + (N - A)e^{-Cr}}{r} \quad (3.21)$$

A , B and C are the parameters of the model potential. These parameters are optimised so as diagonalization of the $1e^-$ Hamiltonian $H = -\frac{1}{2}\nabla^2 + V_{mod}(r)$ yields bound eigenenergies in close agreement with those tabulated at NIST. This is illustrated in Tables 3.1 and 3.2 for the cases of N and N^+ respectively. Furthermore, the consistency of the V_{mod} description can be checked by comparing the radial densities of the fundamental states to those which are issued from conventional Hartree-Fock calculations. This consistency is illustrated in Figure 3.5 for the prototypical N and N^+ cases. Finally, the A , B and C parameters associated to all atoms and ions considered in the present work are listed in Table 3.3.

Orbital	<i>NIST</i>	V_{mod}
2p	-0.5345	-0.5346
3s	-0.1548	-0.1541
3p	-0.1004	-0.1009
3d	-0.0568	-0.0581
4s	-0.0621	-0.6240
4p	-0.0472	-0.0474
4d	-0.0319	-0.0326

Table 3.1: Energy levels of V_{mod} compared to *NIST* values for N atom.

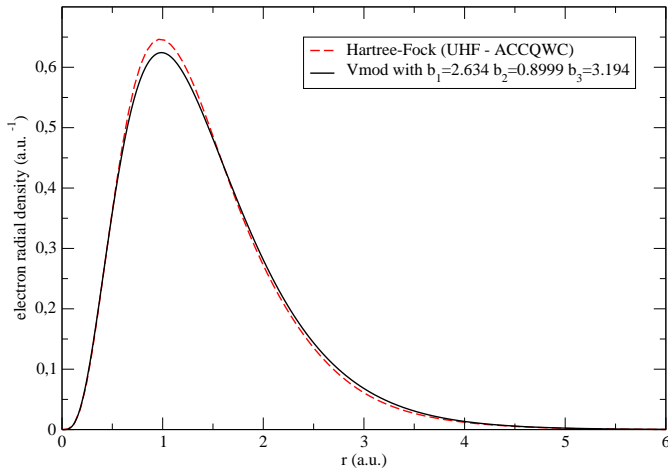
Orbital	<i>NIST</i>	V_{mod}
2p	-1.0884	-1.0888
3s	-0.4094	-0.4047
3p	-0.3219	-0.3227
3d	-0.2347	-0.2362
4s	-0.1923	-0.1906
4p	-0.1633	-0.1625
4d	-0.1310	-0.1315

Table 3.2: Energy levels of V_{mod} compared to *NIST* values for N^+ atom.

Projectile	Z	N	A	B	C
C	6	6	1.964	7.136	0.840
C^+	6	5	1.904	0.808	2.518
N^+	7	6	2.634	0.899	3.194
N^{++}	7	5	2.401	1.264	3.238
C^{++}	6	4	2.044	1.256	3.202

Table 3.3: The optimised A , B , C parameters for the projectile-electron model potential.

Comparison of 2p radial densities for N



Comparison of 2p radial densities for N^+

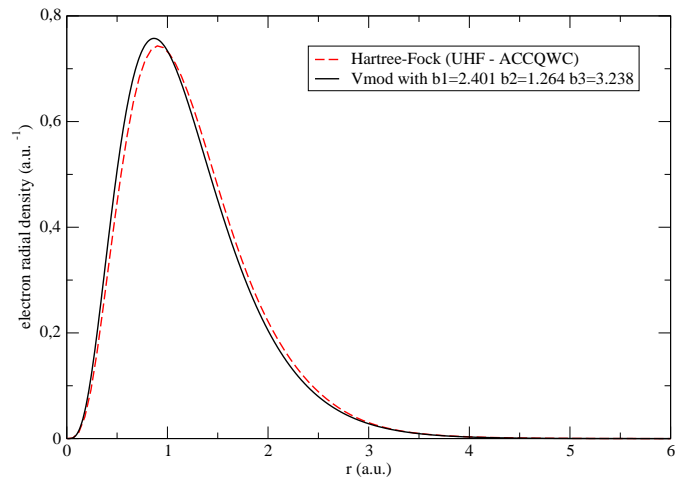


Figure 3-5: Comparison of radial densities in N and N^+ with V_{mod} (solid line) or with Hartree-Fock (broken line) potential.

3.2.2 CTMC probabilities results

In the following we will discuss some specific points, illustrated with some probabilities results. On the other hand, the whole set of CTMC probabilities used in the IAE simulation is presented in Appendix A.

3.2.2.1 Convergence of probabilities with the number of trajectories ($2e^-$ calculations)

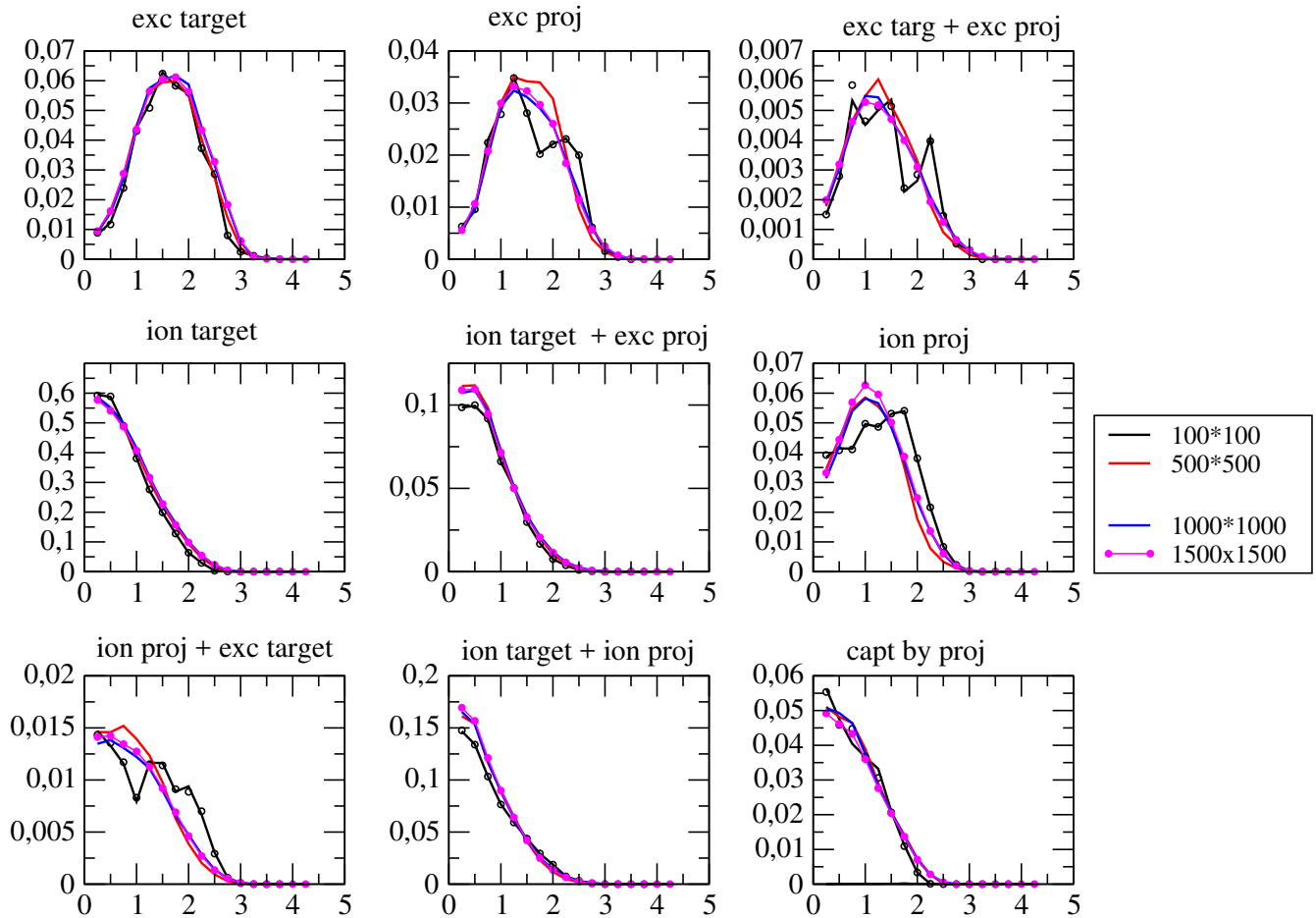


Figure 3-6: $2e^-$ exclusive probabilities as a function of the impact parameter b in $C^+ - He$, $v=2.25$ au with 100×100 , 500×500 , 1000×1000 and 1500×1500 trajectories.

While the number of electron trajectories can be easily enlarged in $1e^-$ -CTMC calculation where only 6 Hamilton equations, associated to the active electron, are

integrated, the number of trajectories in $2e^-$ -CTMC calculations has to be further controlled because of the inherent 12 coupled underlying Hamilton equations.

In Figure 3-6 we report impact parameter probabilities for various processes obtained in such $2e^-$ calculations for $C^+(2p) - He$ system as a function of the number of trajectories employed in the computations. We choose to look at exclusive processes of low probabilities. The statistics are too low, as is evident, for 100x100 trajectories and 500x500 trajectories. To be sure of the convergence with 1000x1000 trajectories, we compared it with 1500x1500 trajectories and the convergence was satisfactory. We worked with 1000x1000 trajectories for all the results presented hereafter.

3.2.2.2 Overview of process probabilities ($1e^-$ calculations)

Being in the intermediate velocity regime ($v_p \sim v_e$) we anticipate that all electronic processes will have similar importance. Indeed we find (see Appendix A) that (target and projectile) ionization is very large but not far are projectile excitation (especially 2s excitation) and electron capture. The only exception is attachment on neutral atom (C) which is very small. Note that $P(b)$ of Appendix A are given per electron. This will favor of course projectile ionization and projectile excitation over the other processes in the atom, and even more, in the molecule.

3.2.2.3 Comparison between $1e^-$ and $2e^-$ calculations (target ionization and excitation)

It is important to check the consistency of $1e^-$ and $2e^-$ CTMC calculations when both of them are able to yield probabilities for the same process. As a first example we present in Figure 3.7 a comparison between $1e^-$ and $2e^-$ CTMC calculations for target ionization in $C(2p)-He^\dagger$ collision. We see that the inclusive ionization probability predicted by the $2e^-$ calculation is very close from the $1e^-$ calculation. The situation is a little bit different in the $C^+ - He$ collision (see Figure 3.8). In the case of $C^+ - He$ collision, inclusive target ionization differs between $1e^-$ and $2e^-$

[†]Note that results with $C(2s)$ are found identical to those with $C(2p)$ for inclusive target ionization whereas exclusive components differ (in particular target ionization + projectile excitation is larger with $C(2s)$ and target ionization alone accordingly smaller).

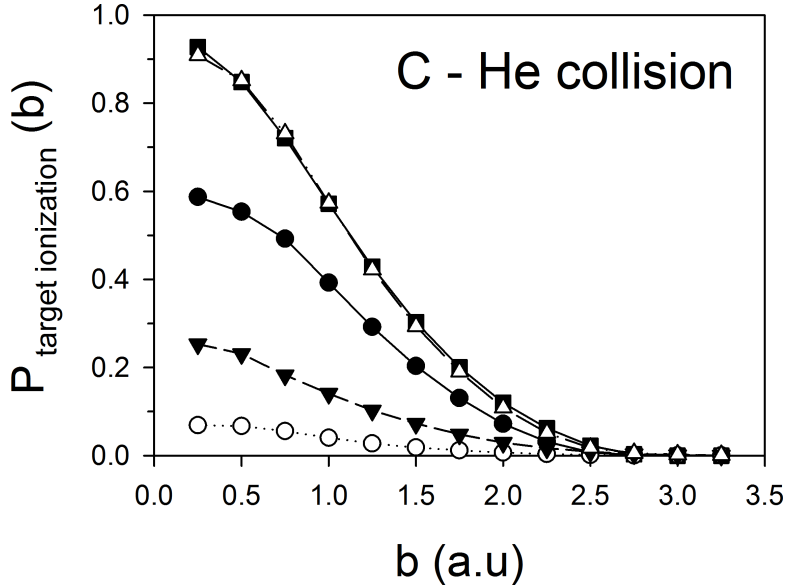


Figure 3-7: Target ionization in C(2p)-He collision. $1e^-$ calculations: black squares; $2e^-$ calculation: open triangles up. Components of target ionization in $2e^-$ calculation: target ionization alone: black circles; target ionization + projectile ionization: black triangles down; target ionization + projectile excitation: open circles.

calculations but target electron loss (target ionization + electron capture) are close (see Figure 3.8). The difference can be attributed to the smaller electron capture in $2e^-$ model as compared to $1e^-$ model. The underlying reason for this difference is the fact that the $2e^-$ -captured electron makes the system unstable due to the increased repulsive potential from the other electron. In any case, capture is not expected to be well calculated in $2e^-$ calculation so that we always used only $1e^-$ calculation in our simulations for target ionization, electron capture and attachment. For target excitation a similar behaviour to target ionization was observed between $1e^-$ and $2e^-$ calculations. But target excitation was not introduced in our simulations.

3.2.2.4 Comparison between $1e^-$ and $2e^-$ calculations (projectile ionization and excitation)

For projectile ionization and excitation $1e^-$ calculation requires to introduce a potential between an electron and the He atom. We discuss it below. Before finding this potential, we performed $2e^-$ calculations. In simulations both $1e^-$ and $2e^-$ calculations were used and compared.

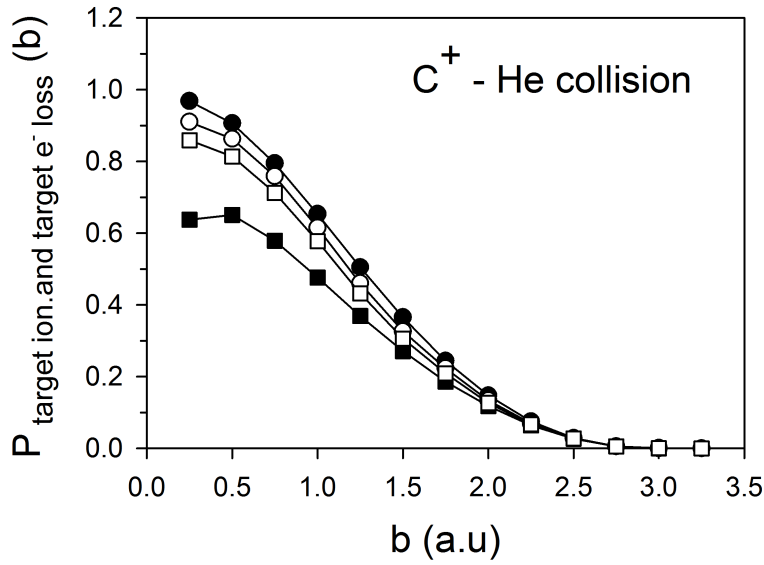


Figure 3-8: Target ionization (squares) and target electron loss (circles) in $1e^-$ calculation (black symbols) and $2e^-$ calculation (open symbols). Calculations performed with incident $C^+(2p)$.

3.2.2.4.1 The electron-He model potential for $1e^-$ calculations

A parametrized form of target potential for neutral $He - e^-$ system exists on experimental and theoretical grounds (Valiron et al., 1979). We present 3 potentials extracted from that paper in Figure 3-9 V1(red), V2(black) and V1 with null dipole polarizability α (blue). On comparing the force experienced by the electron of which the magnitude is given by the first derivative of the potential, we find a stark difference between V1 and V2, (see inset in Figure 3-9). In the latter case, there is a big bump in the force experienced by the electron in the range of distance $r \in (0.75, 1.25)\text{au}$. This is the result of the localized attractive well in V2. We chose to work with V1 potential where the dipole polarizability is not neglected ($\alpha \neq 0$), this potential giving results in good agreement with the experiment (see discussion of Figure 1 in Valiron et al. (1979)). $1e^-$ CTMC calculations, using Hamiltonians similar to that of Equation 3.15, allowed us to obtain projectile ionization and excitation of $C(2s, 2p)$, $C^+(2s, 2p)$, $N(2s, 2p)$ and $N^+(2s, 2p)$. Capture to helium has been found to be zero as expected since formation of He^- is unlikely compared to competing (ionization and excitation) processes.

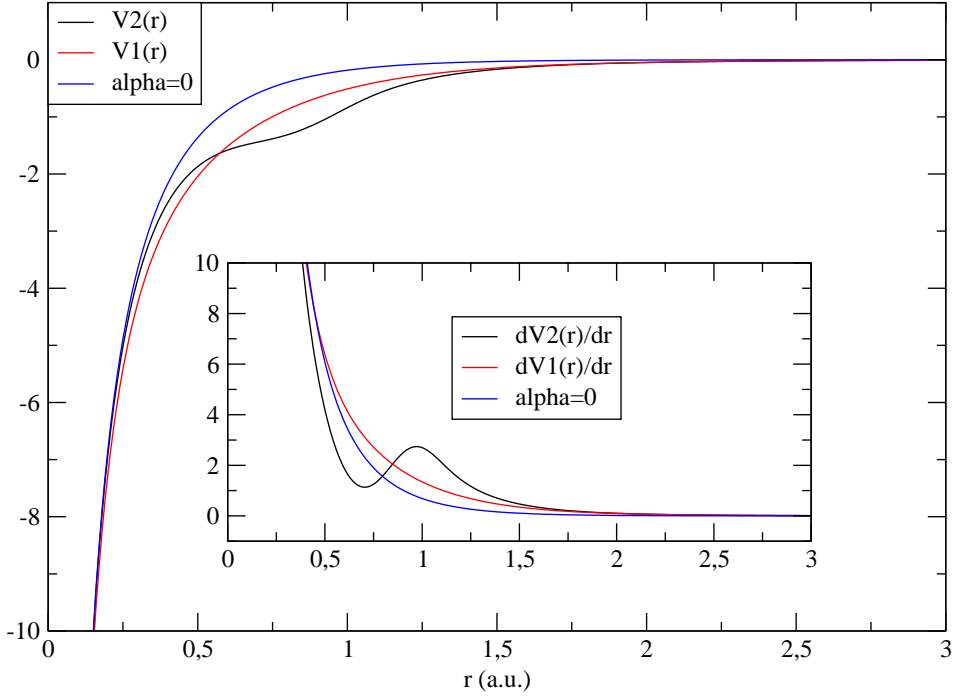


Figure 3-9: Model potentials and its derivatives for $He-e^-$ system

3.2.2.4.2 Comparison between $1e^-$ and $2e^-$ calculations

Figure 3-10 presents the projectile ionization probabilities calculated with $1e^-$ CTMC using $V1(\alpha \neq 0)$ compared to the $2e^-$ CTMC calculations for the $N - He$ collision system. Whereas the $2s$ ionization probability is always smaller than the $2p$ ones (correlated to the higher binding energy) it is seen that the ionization probability from the same shell is higher in $1e^-$ calculations. Figure 3-11 presents the projectile excitation probabilities calculated with $1e^-$ CTMC using $V1(\alpha \neq 0)$ and compared to the $2e^-$ CTMC calculations for the same system. The excitation probability from the same shell is lower in $1e^-$ calculations. This observation is in direct opposition to what had been observed in the ionization probabilities and was observed for all projectiles (see Appendix A). We will present and discuss both $1e^-$ and $2e^-$ calculations results when comparing to experiments (Table 3.5 and Table 3.6 and in chapter 4). We

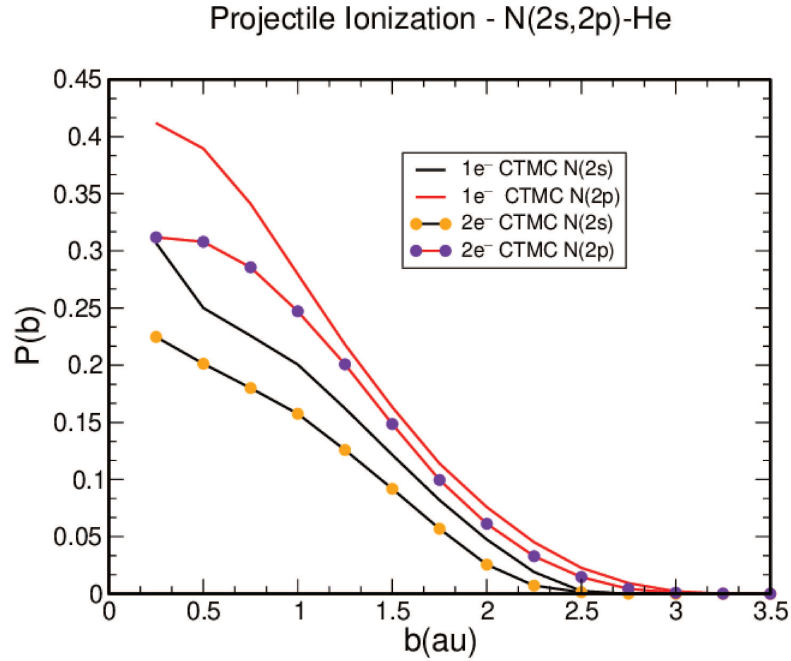


Figure 3-10: Projectile ionization in N - He system. Comparison between $1e^-$ calculation using $V1(\alpha \neq 0)$ and $2e^-$ calculations.

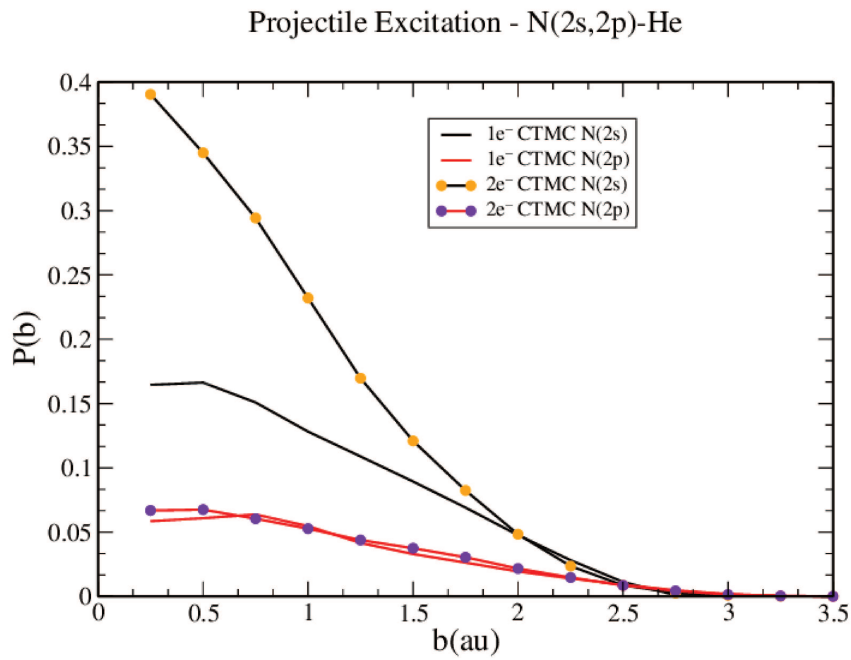


Figure 3-11: Projectile excitation in N - He system. Comparison between $1e^-$ calculation using $V1(\alpha \neq 0)$ and $2e^-$ calculations.

already note that discrepancies are bigger for small impact parameter $b \leq 1$ a.u such that these discrepancies will be somewhat washed out at the level of cross sections involving the opacity functions $bP(b)$.

3.2.2.5 (n, l) classical cross sections

Beyond total probabilities for bound states within capture and (projectile and target) excitation, CTMC is able to provide state-selective, i.e (n, l) cross sections. However, one has first to link the continuous E and $||\vec{L}|| = ||\vec{r} \wedge \vec{p}||$ classical values to the quantized n and l numbers. Concerning $||\vec{L}||$ and l , we simply state, following Rakovic et al. (2001) that all e^- trajectory ending with $l \leq ||\vec{L}|| < l + 1$ belong to l subshell. Concerning E and n , the classical-quantum correspondence is more involved, and the partition of the continuous classical phase-space must be considered.

3.2.2.5.1 The classical (r, p) to quantum (n, l) correspondence

In the CTMC calculation, the final energy E of the electron and its kinetic momentum L is known. In case the electron is bound ($E < 0$) a classical quantum number n_c is calculated by the hydrogenic formula:

$$n_c = \sqrt{\frac{-(Z - N)^2}{2E}} \quad (3.22)$$

Where $(Z - N)$ is the effective charge felt by the active electron (Z atomic number, N number of frozen electrons). A quantum counterpart to the classical n_c is

$$n_{quant} = \sqrt{\frac{-(Z - N)^2}{2E_{quant}}} \quad (3.23)$$

where E_{quant} is the energy of the quantized (n, l) subshell. If we want to keep the fact that the quantum volume occupied by a (n, l) electron is proportional to $(2l + 1)$ we must consider a domain for n_c in terms of adjacent $[n_c^{min}, n_c^{max}]$ intervals, such that

(Rakovic et al., 2001):

$$\frac{8\pi^2(Z - N)^2}{n_c^3} \int_{n_c^{min}}^{n_c^{max}} dn_c \int_l^{l+1} dLL \int dr \frac{1}{\sqrt{-\frac{Z-N}{n_c^2} - \frac{L^2}{r^2} - 2V_{mod}(r)}} = (2l + 1)(2\pi)^3 \quad (3.24)$$

where r is the distance from the electron to the nucleus where it is attached. In

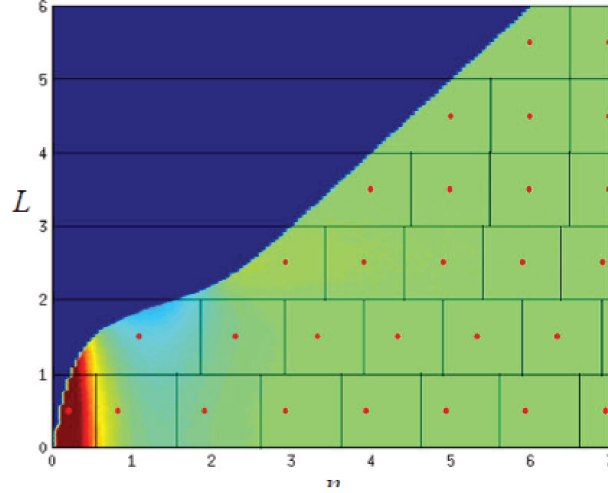


Figure 3-12: Classical domains for classical n_c values of the C electronic spectrum for different values of the classical kinetic momentum L . From bottom (from left to right) to top : $1s \rightarrow 8s$, $2p \rightarrow 7p$, $3d \rightarrow 7d$, $4f \rightarrow 7f$, $5g \rightarrow 7g$, $6h \rightarrow 7h$. Red points are quantum results.

Figure 3-12 we show the n_c^{min} and n_c^{max} values (vertical lines) for $l = 0$ to $l = 5$ states in the case of the C atom. The classical domains are adjacent, the red points correspond to the quantum n_{quant} values with E_{quant} values calculated with the model potential presented in section 3.2.1.5. A perfect classical quantum correspondence should correspond to cases where n_{quant} is located at the center of the $\{n_c^{min}, n_c^{max}\} \times \{l, l+1\}$ area. We observe that this is the case for large n and l as well known since the establishment of quantum theory. For large n and first allowed l , this is not strictly the case since a large part of the partition function (integrand of Equation 3.24) is prohibited (blue area in Figure 3.12). For small l , n_{quant} is not at the center of the classical area because of the existence of occupied inner-shells with small n , which cannot be transposed to the classical world easily in terms of V_{mod} , only optimized

for valence and unoccupied subshells. However it is clear that there is a satisfying quantum-classical correspondence which can be used to derive (n, l) -selective cross sections, using a procedure similar to Equation 3.16.

3.2.2.5.2 The $2s - 2p$ excitation process; use of quantum results

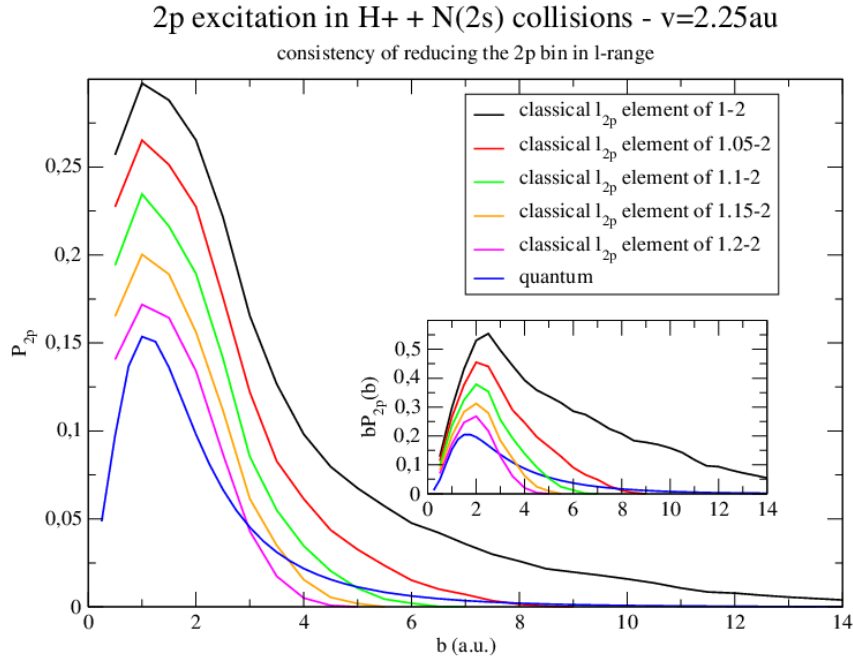


Figure 3-13: $2s$ - $2p$ excitation probability $P(b)$ as a function of b in $H^+ - N(2s)$ collision ($v = 2.25au$). Comparison between quantum calculations (blue curve) and classical calculations with different bin ranges: Black [1-2], red [1.05-2], green [1.1-2], yellow [1.15-2], pink [1.2-2]

When calculating projectile $2s$ excitation we were faced with the fact that the $2s$ $2p$ being adjacent, very large cross sections were obtained. This results from the fact that any small perturbation, induced for instance as the He target lies at infinity from the $C^+(2s)$ projectile, is classically sufficient to pass from the $2s$ bin to the $2p$ one. This is quantum mechanically prohibited since quantum trajectories are entangled, unlike the classical ones so that the whole set of $2s$ quantum trajectories remain in the $2s$ bin. To tackle this problem we checked, by comparing to quantum calculations (Errea

n	2	3	4	5	6	≥ 7
2s	82	13	2	1	0.5	1.1
2p		74	12	5	3	6

Table 3.4: Percentage (%) of projectile excitation into final n levels for 2s and 2p electron of N in N -He collision (2.25 au); $1e^-$ calculation ($V1, \alpha \neq 0$)

et al., 2006; Pons, 2000b,a), the bin range in the classical calculation and decided to enlarge the 2s one from $[0, 1[$ to $[0, l_{max}[$ with $l_{max} \in \mathbb{R}$, and correspondingly shrink the 2p one to $[l_{max}, 2[$.

Figure 3-13 shows the result for the H^+ - $N(2s)$ system and for 2s – 2p excitation. As seen on this figure a reasonable agreement between classical and quantum results is obtained when the classical bin for 2p is reduced from $[l = 1, l = 2]$ to $[l = 1.2, l = 2]$. All projectile excitation probabilities were then extracted with this latter condition.

3.2.2.5.3 CTMC predictions for (n, l) cross sections

Thanks to the classical to quantum correspondence projectile excitation into final (nl) states could be calculated. This was done up to $n = 6$ and for $n \geq 7$ and the results are shown in Appendix A (for probabilities into n final states summed over l). The (n, l) distributions are used in the energy deposit calculation that we present in chapter 5. It is noticeable that the l distributions show the importance of non dipolar transitions ($\Delta l = 0, 2$) in these medium velocity collisions.

Projectile excitation probabilities do decrease rapidly with n , especially for 2s excitation. Table 3.4 gives, for $1e^-$ calculation ($V1, \alpha \neq 0$), the percentage of excitation ($\int bP(b)db$) into the n final state for 2s and 2p excitation in $N - He$ collision ($v = 2.25$ au). The l distribution of final states is found little dependent on n . For $N(2p)$ excitation, the percentages into l levels are typically 7% for $l = 0$, 60% for $l = 1$ and 33% for $l = 2$ ($1e^-$ calculation $V1, \alpha \neq 0$), emphasizing non-dipolar (short-range) behaviour.

Process	System	Formula	σ_{calc}	Experiment
Single Capture N+ \rightarrow N	N+-He N+-He	$2p_c(1 - p_c)$ $2p_c(1 - p_c)(1 - p_{ion}^{2s})^2(1 - p_{ion}^{2p})^2$	$7.99 \cdot 10^{-17}$ $5.24 \cdot 10^{-17}$	$3.74 \cdot 10^{-17}$ (60%)
Single Capture C+ \rightarrow C	C+-He C+-He	$2p_c(1 - p_c)$ $2p_c(1 - p_c)(1 - p_{ion}^{2s})^2(1 - p_{ion}^{2p})$	$7.72 \cdot 10^{-17}$ $5.4 \cdot 10^{-17}$	$3.5 \cdot 10^{-17}$ (30%)
N+ \rightarrow N++ N+ \rightarrow N+++	N+-He N+-He	Made with code (projectile ionization without electron capture)	$0.72 \cdot 10^{-16}$ $1.13 \cdot 10^{-17}$	$1.7 \cdot 10^{-16}$ (40%) $0.99 \cdot 10^{-17}$ (50%)
C+ \rightarrow C++ C+ \rightarrow C+++	C+-He C+-He	"	$0.75 \cdot 10^{-16}$ $0.76 \cdot 10^{-17}$	$1.5 \cdot 10^{-16}$ (64%)
Single ion He Double ion He	N+-He N+-He	$2p_i(1 - p_i - p_c)$ p_i^2	$1.34 \cdot 10^{-16}$ $0.57 \cdot 10^{-16}$	
Single ion He Double ion He	C+-He C+-He	$2p_i(1 - p_i - p_c)$ p_i^2	$1.27 \cdot 10^{-16}$ $0.52 \cdot 10^{-16}$	$1.8 \cdot 10^{-16}$ (40%) $0.3 \cdot 10^{-16}$ (60%)
Single ion He Double ion He	C -He C -He	$2p_i(1 - p_i - p_c)$ p_i^2	$1.55 \cdot 10^{-16}$ $0.78 \cdot 10^{-16}$	$1.4 \cdot 10^{-16}$ (30%)* $0.14 \cdot 10^{-16}$ (30%)*
Single cap C C \rightarrow C-	C -He C -He	$2p_c(1 - p_c)$ $2p_c(1 - p_c)(1 - p_{ion}^{2s})^2(1 - p_{ion}^{2p})^2$	$0.41 \cdot 10^{-17}$ $0.2 \cdot 10^{-17}$	$0.55 \cdot 10^{-17}$ (30%)
C+ \rightarrow C-	C+-He	$(p_c^{c+})^2(1 - p_{ion}^{2s})^2(1 - p_{ion}^{2p})$	$4.79 \cdot 10^{-18}$	$8.0 \cdot 10^{-20}$ (40%)

Table 3.5: Comparison between measured and calculated cross sections with $2e^-$ calculation for projectile ionization. All experiments are done at AGAT except * DuBois and Toburen (1988)

Process	System	Formula	σ_{calc}	Experiment
N \rightarrow N	N+-He	$2p_c(1-p_c)(1-p_{ion}^{2s})^2(1-p_{ion}^{2p})^2$	$4.38 \cdot 10^{-17}$	$3.74 \cdot 10^{-17}$ (60%)
C \rightarrow C	C+-He	$2p_c(1-p_c)(1-p_{ion}^{2s})^2(1-p_{ion}^{2p})$	$4.73 \cdot 10^{-17}$	$3.5 \cdot 10^{-17}$ (30%)
C \rightarrow C-	C-He	$2p_c(1-p_c)(1-p_{ion}^{2s})^2(1-p_{ion}^{2p})^2$	$0.17 \cdot 10^{-17}$	$0.55 \cdot 10^{-17}$ (40%)
C \rightarrow C-	C+-He	$(p_c^{c+})^2(1-p_{ion}^{2s})^2(1-p_{ion}^{2p})$	$3.98 \cdot 10^{-18}$	$8.0 \cdot 10^{-20}$ (40%)
N \rightarrow N++	N+-He	Made in the code	$0.94 \cdot 10^{-16}$	$1.7 \cdot 10^{-16}$ (40%)
N \rightarrow N+++	N+-He	(projectile ionization without electron capture)	$2.10 \cdot 10^{-17}$	$0.99 \cdot 10^{-17}$ (50%)
C \rightarrow C++	C+-He	”	$0.98 \cdot 10^{-16}$	$1.5 \cdot 10^{-16}$ (64%)
C \rightarrow C+++	C+-He	”	$1.33 \cdot 10^{-17}$	
C \rightarrow C+	C-He	$2p_{2s}(1-p_{2s})(1-p_{2p})^2 + 2p_{2p}(1-p_{2p})(1-p_{2s})^2$	$1.89 \cdot 10^{-16}$	$1.77 \cdot 10^{-16}$ (0.36)*
C \rightarrow C++	C-He	$p_{2s}^2(1-p_{2p})^2 + p_{2p}^2(1-p_{2s})^2 + 4p_{2s}p_{2p}(1-p_{2s})(1-p_{2p})$	$5.39 \cdot 10^{-17}$	$2.99 \cdot 10^{-17}$ (0.60)*

Table 3.6: Comparison between measured and calculated cross sections with $1e^-$ calculation for projectile ionization. All experiments were performed at AGAT except (*) by Nakai and Sataka (1991)

3.2.2.6 Comparison between CTMC and experiment for total cross sections (C , C^+ , N^+ – He collisions)

In Table 3.5 and Table 3.6 is presented a comparison between measured cross sections and CTMC calculated cross sections. Experimental error bars are given at “2 sigma” i.e with a 95% confidence. The two Tables differ by the type of calculation for projectile ionization : $2e^-$ calculation for Table 3.5 and $1e^-$ calculation (V1, $\alpha \neq 0$) for Table 3.6.

Looking at Table 3.5 and Table 3.6 we see that projectile ionization cross sections are higher in $1e^-$ calculations than in $2e^-$ calculations. The difference is of the order of 20% for single ionization but amounts to 80% for double ionization. We see that the larger $p(b)$ at small impact parameters for $1e^-$ calculations are having a larger effect on double ionization than on single ionization, as expected. According to the large error bars, both calculations are compatible with the experimental results, with the exception of single ionization of N^+ ($2e^-$ calculation) and double ionization of N^+ ($1e^-$ calculation).

Target (He) ionization is well reproduced by the CTMC calculations (always $1e^-$ calculations) with the exception of double ionization in the $C-He$ collision (experiment of DuBois and Toburen (1988)) where the calculation is 4 times too high. The IPM may be questionable. A new experiment would also be desirable.

Experimental neutralisation (single electron capture without projectile ionization) cross sections in C^+-He and N^+-He collisions are well reproduced by both $1e^-$ and $2e^-$ projectile ionization CTMC calculations . It is much better than what we found in C^+-Ar collision (Labaigt et al., 2015). Note that the reduction of single electron capture by the “no projectile ionization” was larger in the C^+-Ar collision ($\sim 60\%$) than in the present systems ($\sim 35\%$ in C^+-He and $\sim 40\%$ in N^+-He). In the case of attachment without projectile ionization $C \rightarrow C^-$ both CTMC calculations ($1e^-$ and $2e^-$) are providing a cross section roughly two times smaller than experiment. We believe CTMC to be too small in its prediction for that process. Looking now to anionic production cross sections $C^+ \rightarrow C^-$ (double electron capture without

projectile ionization) we find that both $1e^-$ and $2e^-$ CTMC calculations predict cross sections that are too large roughly by a factor 50. This is an equivalent result to what was obtained in $C^+ - Ar$ collisions (Labaigt et al., 2015). The IPM may be incorrect, but may not be the only cause of discrepancy (see chapter 4).

In conclusion, there is an overall reasonable agreement between experiment and CTMC calculations in C , C^+ , $N^+ - He$ collision systems, especially for one electron processes i.e with the exception of some double ionization processes ($N^+ \rightarrow N^{+++}$ and $He \rightarrow He^{++}$) and exception made of the peculiar $C^+ \rightarrow C^-$ process leading to a final anion.

Chapter 4

Results on cross sections

4.1 Experimental results on cross sections

The experimental results for the cross sections will be presented in this chapter. To recall the experimental conditions, the collision velocity is 2.2 a.u with the projectiles being C_nN^+ ($n=1,2,3$) molecules with the target He atom.

In Tables 4.1 to 4.3 are presented experimental cross sections for various electronic processes measured in $CN^+ - He$, $C_2N^+ - He$ and $C_3N^+ - He$ collisions. Also reported from Chapter 3 the results obtained with the atomic ions C^+ and N^+ in Table 4.4. The considered processes are projectile ionization, projectile dissociative excitation, neutralization and projectile anionic production. What is measured in the experiment is the projectile charge after the collision. This observable covers in fact multi-electron processes (for instance neutralization is electron capture without projectile ionization; projectile excitation is without projectile ionization but includes electron capture with single projectile ionization) that are estimated within the IAE/CTMC model. In order to compare to this modelling we give in Tables 4.1 to 4.3 experimental error bars “at two sigma” (i.e with 95% confidence).

The single ionization (SI) cross sections are of the order of a few 10^{-16} cm^2 which is the dominant process. The cross sections show an increasing trend in their absolute value as the size of the molecule increases. This can be attributed to the increase in the individual atomic centres, each contributing to the process. This trend is not

as dominant if C_2N^+ and C_3N^+ cross sections are compared. This saturation of SI cross sections is compensated by the increase of multi-ionization cross sections (see for instance the relative triple over single ionization cross sections in the last column of the Tables 4.1 to 4.3). The second more probable process is dissociative excitation amounting roughly to 40% of the single ionization whatever the molecule. This ratio of excitation over ionization is typical of this velocity range (Vernhet et al., 1996). As mentioned before multi-ionization cross sections increase relatively to SI cross sections when the molecule size increases. By contrast neutralization cross sections, of the order of a few 10^{-17} cm^2 , decrease relatively to SI when the projectile size increases. The cross sections for anionic production (C_nN^+ becoming C_nN^-) have orders of magnitude of 10^{-20} cm^2 . Two electrons are captured by the projectile and we expect small cross sections. In fact we find results very close from what we get with incident carbon clusters C_n^+ of the same velocity in collision with He (see Figure 8 in Béroff et al. (2013)) i.e a decrease of the anionic production cross section with the molecule size.

Process (final Q)	Cross section $\sigma \text{ cm}^2$ (rel err)	σ_{norm} to proj. single ionization (rel. err)
Projectile single ionization (Q=2)	$2.29 \cdot 10^{-16}$ (38%)	1
Projectile double ionization (Q=3)	$5.44 \cdot 10^{-17}$ (38%)	0.24(26%)
Projectile triple ionization (Q=4)	$8.28 \cdot 10^{-18}$ (36%)	0.04(26%)
Projectile quadruple ionization (Q=5)	$6.52 \cdot 10^{-19}$ (38%)	$2.8 \cdot 10^{-3}$ (34%)
Projectile quintuple ionization (Q=6)	$\leq 3.10 \cdot 10^{-20}$ (38%)	$\leq 1.3 \cdot 10^{-4}$
Projectile dissociative excitation (Q=1)	$9.44 \cdot 10^{-17}$ (36%)	0.41(26%)
Neutralization (Q=0)	$4.15 \cdot 10^{-17}$ (34%)	0.18(22%)
Anionic production (Q=-1)	$2.51 \cdot 10^{-20}$ (42%)	$1.10 \cdot 10^{-4}$ (46%)

Table 4.1: Measured cross sections for various electronic processes in the $CN^+ - He$ ($v = 2.2 \text{ au}$) collision; confidence in error bars: 95%.

Process (final Q)	Cross section σ cm^2 (rel err)	σ_{norm} to proj. single ionization (rel. err)
Projectile single ionization (Q=2)	$4.35 \cdot 10^{-16}$ (32%)	1
Projectile double ionization (Q=3)	$1.13 \cdot 10^{-16}$ (32%)	0.26(18%)
Projectile triple ionization (Q=4)	$2.74 \cdot 10^{-17}$ (34%)	0.06(22%)
Projectile quadruple ionization (Q=5)	$5.51 \cdot 10^{-18}$ (36%)	$1.3 \cdot 10^{-2}$ (24%)
Projectile quintuple ionization (Q=6)	$9.74 \cdot 10^{-19}$ (46%)	$2.21 \cdot 10^{-3}$ (36%)
Projectile sextuple ionization (Q=7)	$1.52 \cdot 10^{-19}$ (74%)	$3.5 \cdot 10^{-4}$ (70%)
Projectile seven ionization (Q=8)	$\leq 1.90 \cdot 10^{-20}$	$\leq 4.4 \cdot 10^{-5}$
Projectile eight ionization (Q=9)	$\leq 3.30 \cdot 10^{-21}$	$\leq 7.4 \cdot 10^{-6}$
Projectile dissociative excitation (Q=1)	$1.78 \cdot 10^{-16}$ (32%)	0.41(18%)
Neutralization (Q=0)	$5.83 \cdot 10^{-17}$ (30%)	0.13(16%)
Anionic production (Q=-1)	$4.94 \cdot 10^{-20}$ (40%)	$1.10 \cdot 10^{-4}$ (38%)

Table 4.2: Measured cross sections for various electronic processes in the $C_2N^+ - He$ ($v = 2.2$ au) collision; confidence in error bars: 95%.

Process (final Q)	Cross section σ cm^2 (rel err)	σ_{norm} to proj. single ionization (rel. err)
Projectile single ionization (Q=2)	$4.43 \cdot 10^{-16}$ (26%)	1
Projectile double ionization (Q=3)	$1.36 \cdot 10^{-16}$ (26%)	0.31(22%)
Projectile triple ionization (Q=4)	$4.35 \cdot 10^{-17}$ (32%)	0.10(28%)
Projectile quadruple ionization (Q=5)	$1.09 \cdot 10^{-17}$ (42%)	0.025(38%)
Projectile quintuple ionization (Q=6)	$2.36 \cdot 10^{-18}$ (48%)	$5.3 \cdot 10^{-3}$ (44%)
Projectile sextuple ionization (Q=7)	$4.83 \cdot 10^{-19}$ (50%)	$1.1 \cdot 10^{-3}$ (48%)
Projectile seven ionization (Q=8)	$8.70 \cdot 10^{-20}$ (72%)	$2.0 \cdot 10^{-4}$ (70%)
Projectile dissociative excitation (Q=1)	$1.69 \cdot 10^{-16}$ (26%)	0.38(20%)
Neutralization (Q=0)	$5.05 \cdot 10^{-17}$ (26%)	0.11(20%)
Anionic production (Q=-1)	$3.00 \cdot 10^{-20}$ (40%)	$6.80 \cdot 10^{-5}$ (34%)

Table 4.3: Measured cross sections for various electronic processes in the $C_3N^+ - He$ ($v = 2.2$ au) collision; confidence in error bars: 95%.

Process	$C^+ - He$ collision	$N^+ - He$ collision
Proj. single ionization cross section (SI) cm^2 (rel. err)	$1.5 \cdot 10^{-16}$ (64%)	$1.7 \cdot 10^{-16}$ (40%)
Proj. double ionization cross section (DI) cm^2		$0.99 \cdot 10^{-17}$ (50%)
Ratio DI/SI (rel. err)		0.06 (28%)
Neutralization cross section cm^2 (rel. err)	$3.5 \cdot 10^{-17}$ (30%)	$3.74 \cdot 10^{-17}$ (60%)
Anionic production cross section cm^2 (rel. err)	$8.0 \cdot 10^{-20}$ (40%)	

Table 4.4: Measured cross sections for various electronic processes in the $C^+ - He$ (second column) and $N^+ - He$ (third column) collision ($v=2.2$ au); confidence in error bars: 95%. Partial report from Table 3.6 of Chapter 3.

4.2 Comparison with IAE/CTMC predictions

4.2.1 Geometries of C_nN^+ molecules

In the IAE model the geometry of the incident C_nN^+ molecule is needed. We used the calculations performed by N. Aguirre and S. Diaz-Tendero from the Universidad Autonoma de Madrid. Geometry optimization and harmonic frequencies have been obtained at the DFT-B3LYP/6-311++G(3df,2p) level of theory. More accurate electronic energies were computed over the geometry previously optimized at the DFT level by using single (S) and double (D) excitations, adding triple (T) excitations in a perturbative way, with the same basis set: CCSD(T)/6-311++G(3df,2p). For each molecule, several geometrical conformations and the two lowest spin state isomers have been considered (singlet/triplet and quadruplet/doublet). These calculations were carried out with the Gaussian09 package. The same type of calculations has been previously performed on C_nH_m hydrocarbon molecules by the same authors (Sánchez et al., 2016). In Figure 4.1 is presented a general view of the geometries for the lowest energy and excited isomers of C_nN^+ molecules (CnN.q1) and C_nN^{++} molecules (CnN.q2). In the calculations the linear lowest energy isomers were introduced but the shape effect (variation of the results with the molecule shape) is discussed in Section 4.2.3 by comparing the results obtained with a linear molecule

Molecule (isomer)	Atom	X (au)	Y (au)	Z(au)	Mulliken charge
CN^+ iso1 (linear)	C	-1.11	0	0	0.995
	N	1.11	0	0	0.005
C_2N^+ iso1 (linear)	C1	2.35	-0.245	0	0.46
	C2	-2.35	0.245	0	0.46
	N	$6 \cdot 10^{-5}$	$5 \cdot 10^{-4}$	0	0.08
C_2N^+ iso3 (cyclic)	C1	0.79	-1.25	0	0.53
	C2	0.62	1.34	0	0.53
	N	-1.40	$5 \cdot 10^{-4}$	0	0.08
C_3N^+ iso1 (linear)	C1	$2.5 \cdot 10^{-3}$	-1.29	0	0.26
	C2	-0.39	1.17	0	1.17
	C3	0.08	3.64	0	0.17
	N	0.30	-3.52	0	-0.60
C_3N^+ iso5 (cyclic)	C1	-0.061	1.48	$2 \cdot 10^{-3}$	0.29
	C2	2.15	0.088	-0.038	0.59
	C3	0.061	-1.48	$-2 \cdot 10^{-3}$	0.29
	N	-2.15	-0.088	0.038	-0.17

Table 4.5: Position of the atoms in the barycentre of the molecules and Mulliken charges.

with those obtained with a cyclic (compact) molecule. Precise results concerning the positions of the atoms are given in Table 4.5 and Figures 4.2 to 4.6. Also reported in this Table and Figures are the charges on each atom calculated by the Mulliken procedure and provided by the Gaussian package. Whereas the Mulliken procedure is not expected to be very accurate (Wiberg and Rablen, 1993) we will only retain from these calculations that the positive charge of the cation is essentially shared between carbon atoms. Because we need it for the calculation of the dissociation energies in Chapter 5 we also present in Table 4.6 the total energies calculated by N.Aguirre and S.Diaz-Tendero for various atoms and molecules of use in this work. The ZPE (zero point energy) is calculated as:

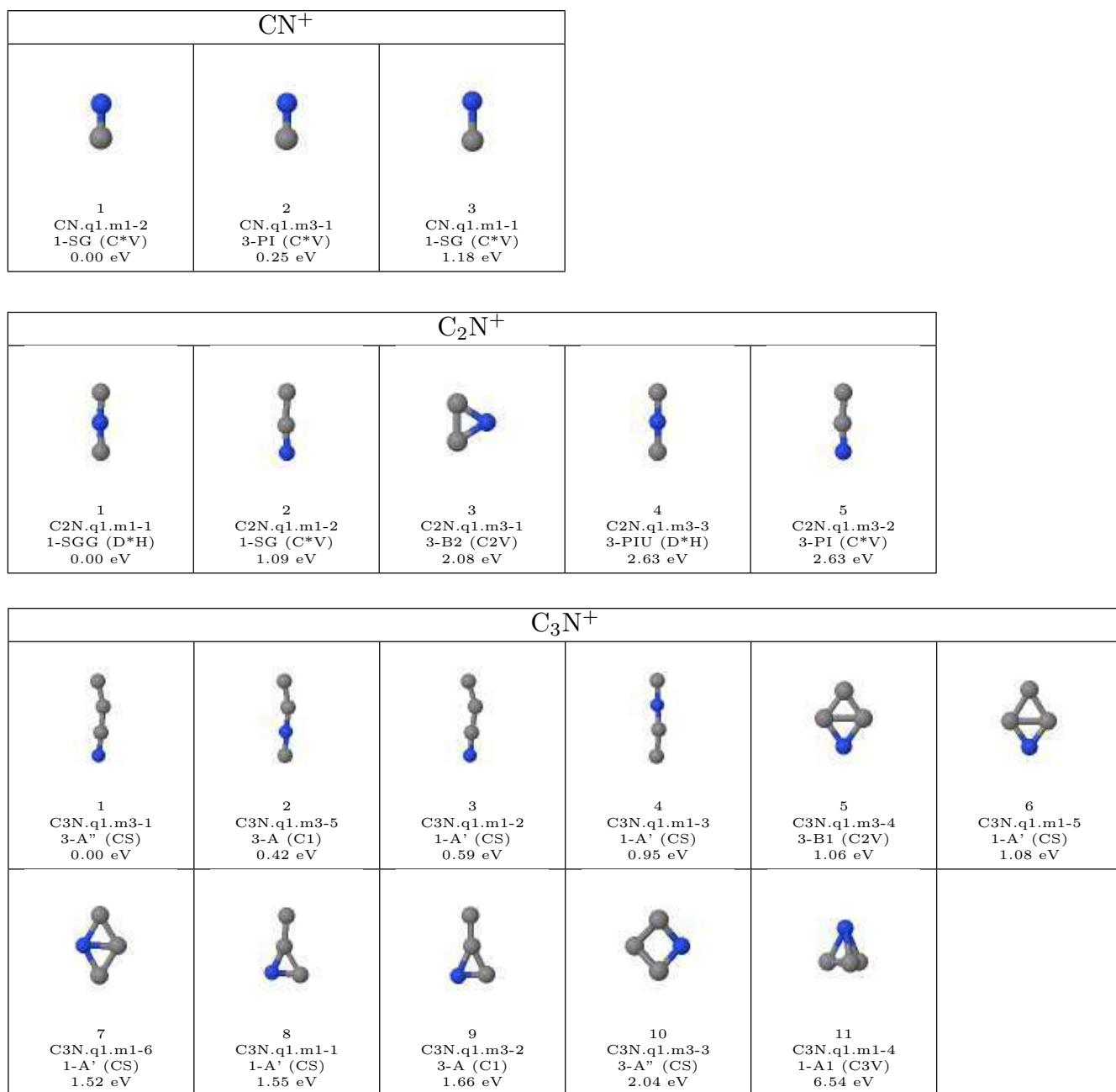


Figure 4-1: General view of the geometries of the first isomers of C_nN^+ ($n=1-3$). In blue, the Nitrogen atom. Calculations by Nestor Aguirre and Sergio Díaz-Tendero (private communications).

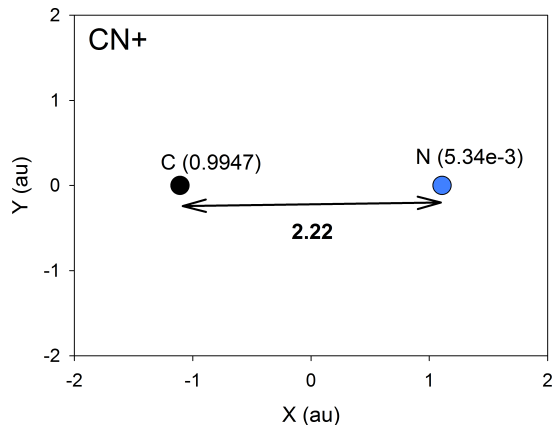


Figure 4-2: Geometry of the lowest energy isomer of CN^+ molecule. Distances are given in atomic units. Nitrogen in blue. Mulliken charges in parenthesis.

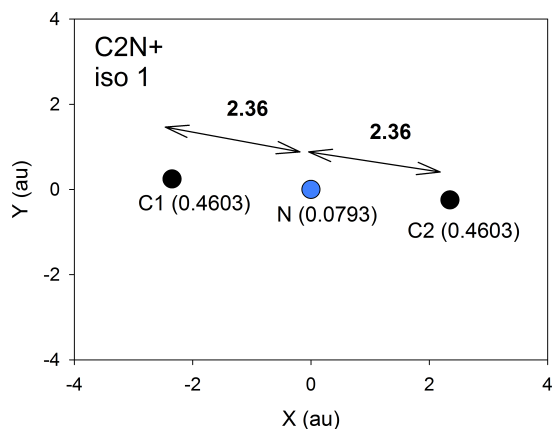


Figure 4-3: Geometry of the lowest energy isomer of C_2N^+ molecule. Distances are given in atomic units. Nitrogen in blue. Mulliken charges in parenthesis.

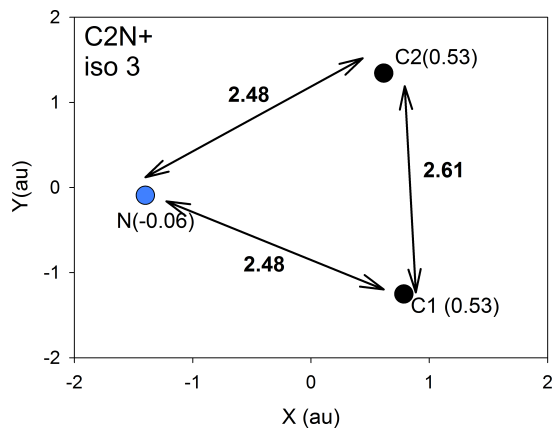


Figure 4-4: Geometry of the lowest energy isomer of C_2N^+ molecule in cyclic configuration. Distances are given in atomic units. Nitrogen in blue. Mulliken charges in parenthesis.

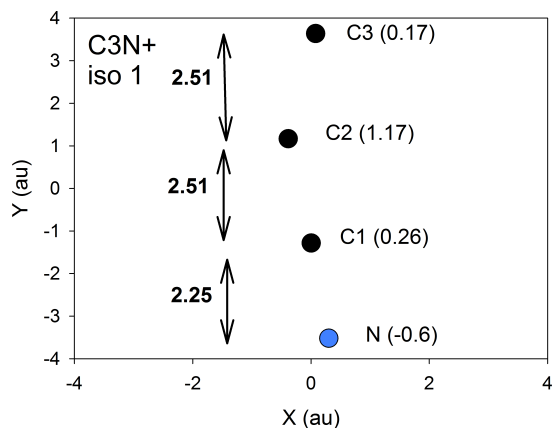


Figure 4-5: Geometry of the lowest energy isomer of C_3N^+ molecule. Distances are given in atomic units. Nitrogen in blue. Mulliken charges in parenthesis.

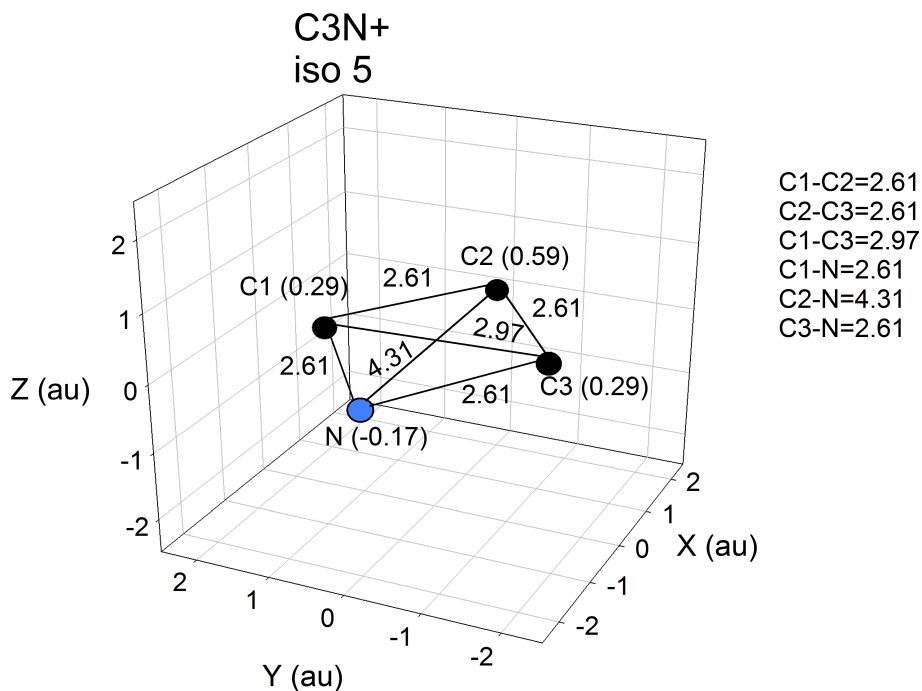


Figure 4-6: Geometry of the lowest energy isomer of C_3N^+ molecule in cyclic configuration. Distances are given in atomic units. Nitrogen in blue. Mulliken charges in parenthesis.

Atom/Molecule (lowest energy isomer)	Electronic state (symmetry)	E(au)	ZPE (au)	E+ZPE (au)
C	3P_g (atom)	-37.77917		-37.77917
N	4S_u (atom)	-54.512703		-54.512703
C_2	$^1\Sigma_g^+$ ($D\infty h$)	-75.78264	$4.3 \cdot 10^{-3}$	-75.77834
CN	$^2\Sigma_g^+$ ($C\infty v$)	-92.5659	$4.9 \cdot 10^{-3}$	-92.561
C_3	$^1\Sigma_g^+$ ($D\infty h$)	-113.83237	$8.15 \cdot 10^{-3}$	-113.82422
CNC	$^2\Pi_g$ ($D\infty h$)	-130.5269	$7.9 \cdot 10^{-3}$	-130.519
C_3N	$^2A'$ (Cs)	-168.5547	0.013	-168.5417
C^+	2P_u (atom)	-37.36834		-37.36834
N^+	3P_g (atom)	-53.98072		-53.98072
C_2^+	$^4\Sigma_g^-$ ($D\infty h$)	-75.35179	$3.05 \cdot 10^{-3}$	-75.34874
CN^+	$^1\Sigma_g^+$ ($C\infty v$)	-92.0639	$4.7 \cdot 10^{-3}$	-92.0592
C_3^+	2B_2 (C_2v)	-113.40504	$8.9 \cdot 10^{-3}$	-113.39614
CNC^+	$^1\Sigma_g$ ($D\infty h$)	-130.17236	$8.3 \cdot 10^{-3}$	-130.16406
C_3N^+	$^3A''$ (Cs)	-168.1215	0.012	-168.1095
C^{++}	1S_g (atom)	-36.51295		-36.51295
N^{++}	4S_u (atom)	-52.892701		-52.892701
CN^{++}	$^4\Sigma$ ($C\infty v$)	-91.187118	$1.84 \cdot 10^{-3}$	-91.185278
C_3^{++}	$^3\Sigma_u^+$ ($D\infty h$)	-112.66201	$8.92 \cdot 10^{-3}$	-112.65309
CNC^{++}	2S ($C\infty v$)	-129.39711	$7.45 \cdot 10^{-3}$	-129.38966
C_3N^{++}	$^4A''$ (Cs)	-167.43507	0.0127	-167.42237

Table 4.6: Total energies of atomic and molecular systems of interest here. Calculations by N. Aguirre and S. Diaz-Tendero (see text).

$$ZPE = \sum_i \frac{h\nu_i}{2} \quad (4.1)$$

Where ν_i are the vibrational frequencies in the molecule.

4.2.2 The role of the charge position

In the IAE code, only integers can be introduced for the charges carried out by the atoms. In the C_nN^+ atomic representation of the molecule, the Nitrogen atom has been taken as neutral and the positive charge carried out by one of the carbon atom. We looked at the effect of the charge position on the results of the IAE/CTMC predicted cross sections. In Table 4.7 are presented cross sections predictions as a

Process	Charge on C1	Charge on C2	Charge on C3	Average
Single proj. ion. *	$3.87 \cdot 10^{-16}$	$3.82 \cdot 10^{-16}$	$3.57 \cdot 10^{-16}$	$3.75 \cdot 10^{-16}$
Double proj. ion.*	$1.46 \cdot 10^{-16}$	$1.44 \cdot 10^{-16}$	$1.45 \cdot 10^{-16}$	$1.45 \cdot 10^{-16}$
Triple proj. ion.*	$4.37 \cdot 10^{-17}$	$4.52 \cdot 10^{-17}$	$5.08 \cdot 10^{-17}$	$4.66 \cdot 10^{-17}$
Total proj. Exc.*	$2.20 \cdot 10^{-16}$	$2.20 \cdot 10^{-16}$	$2.20 \cdot 10^{-16}$	$2.20 \cdot 10^{-16}$
Single electron capture (SC)	$7.79 \cdot 10^{-17}$	$7.76 \cdot 10^{-17}$	$7.82 \cdot 10^{-17}$	$7.79 \cdot 10^{-17}$
SC without proj.ion.	$2.77 \cdot 10^{-17}$	$2.99 \cdot 10^{-17}$	$4.04 \cdot 10^{-17}$	$3.27 \cdot 10^{-17}$
Attachment	$8.06 \cdot 10^{-18}$	$8.26 \cdot 10^{-18}$	$8.37 \cdot 10^{-18}$	$8.23 \cdot 10^{-18}$
Attachment without proj. ion	$2.70 \cdot 10^{-18}$	$2.79 \cdot 10^{-18}$	$2.31 \cdot 10^{-18}$	$2.60 \cdot 10^{-18}$
Gain (SC + Attach.)	$8.54 \cdot 10^{-17}$	$8.50 \cdot 10^{-17}$	$8.60 \cdot 10^{-17}$	$8.55 \cdot 10^{-17}$
Gain without proj. ion. (Neutralization)*	$3.02 \cdot 10^{-17}$	$3.24 \cdot 10^{-17}$	$4.26 \cdot 10^{-17}$	$3.51 \cdot 10^{-17}$
Double electron capture (DC)	$7.89 \cdot 10^{-18}$	$8.04 \cdot 10^{-18}$	$7.85 \cdot 10^{-18}$	$7.79 \cdot 10^{-18}$
DC without proj. ion. (Anionic production)*	$2.48 \cdot 10^{-18}$	$2.75 \cdot 10^{-18}$	$3.61 \cdot 10^{-18}$	$2.95 \cdot 10^{-18}$

Table 4.7: Role of the charge position on predicted cross sections; case of linear C_3N^+ with CTMC $2e^-$ calculations. Processes with a star are directly comparable to the experiment.

function of the charge position for linear C_3N^+ and for $2e^-$ CTMC calculations. It is seen that the charge position has a sizeable effect when it is positioned on C3 i.e at the end of the chain (see Figure 4.5). These results (also obtained with the $1e^-$ CTMC calculations) are understandable: when the charge is on C3 the projectile multi-ionization is increased (taking into account the fact that passing between two neutrals is more efficient than passing between a neutral and an ion) and the projectile single ionization is accordingly reduced. Then, whereas single electron capture onto the ion does not depend on the charge position, the single electron capture without projectile ionization, dominated by single electron capture without projectile single ionization, is larger when the charge is on C3. A similar effect is observed on Neutralization and Anionic production cross sections. As a consequence, an average of predicted cross sections with the charge positioned in C1, C2 and C3 was performed before comparing to experiment.

4.2.3 The role of the molecule shape

As already noticed (Chabot et al., 2001) the shape of the molecule has some effects on the results. Whereas predicted cross sections are not sensitive to a little modification of the interatomic distances, the compactness of the molecule (i.e linear versus cyclic) may induce sizeable modifications on multi-ionization cross sections. In Table 4.8 we present IAE/CTMC predicted cross sections when considering the cyclic isomer of C_3N^+ (Figure 4.6). This cyclic isomer is situated 1.1 eV above the lowest energy isomer according to N.Aguirre calculations. Since the internal energy of C_3N^+ is estimated to be around 2 eV (see Table 1.2 in Chapter 1) it is likely to be populated in the experiment. It is interesting to note that the charge position does not matter in the cyclic case, which makes sense. In the last column of Table 4.8 is reported the ratio between predicted cross sections (averaged over the charge position) for the cyclic isomer divided by results with the linear isomer. As expected the projectile triple ionization is larger with the cyclic isomer and the projectile single ionization accordingly smaller but the effect is modest ($\sim 10 - 15\%$) on this small molecule. An effect of the same order of magnitude is observed for the cyclic C_2N^+ as compared to the linear C_2N^+ . Nevertheless, the first cyclic C_2N^+ , situated 2 eV above the linear ones is not expected to be very much populated since the internal energy of C_2N^+ is around 1 eV. Since this is difficult to estimate the quantitative contribution of the cyclic isomers in the experiment and since the effect is rather small we compare in sections 4.2.5 to 4.2.8 the experiment to the IAE/CTMC calculations performed with the lowest energy isomers.

4.2.4 The role of inner shells

In the preceding chapters we presented CTMC impact parameters probabilities for processes affecting only the valence shells of the C, C^+ , N and N^+ atoms (ions). This is because, at this velocity, the probability of ionising inner-shells is about 100 times smaller. We show in Figure 4.7 the carbon K-shell ionization cross sections measured in C^+ -He collisions as a function of the projectile energy (collision velocity)

Process	Charge on C1	Charge on C2	Charge on C3	Average	Cyclic/linear
Single proj. ion. *	$3.37 \cdot 10^{-16}$	$3.25 \cdot 10^{-16}$	$3.38 \cdot 10^{-16}$	$3.33 \cdot 10^{-16}$	0.89
Double proj. ion.*	$1.43 \cdot 10^{-16}$	$1.41 \cdot 10^{-16}$	$1.42 \cdot 10^{-16}$	$1.42 \cdot 10^{-16}$	0.98
Triple proj. ion.*	$5.19 \cdot 10^{-17}$	$5.42 \cdot 10^{-17}$	$5.21 \cdot 10^{-17}$	$5.27 \cdot 10^{-17}$	1.13
Total proj. Exc.*	$1.90 \cdot 10^{-16}$	$1.91 \cdot 10^{-16}$	$1.90 \cdot 10^{-16}$	$1.90 \cdot 10^{-16}$	0.86
Single electron capture (SC)	$7.81 \cdot 10^{-17}$	$7.78 \cdot 10^{-17}$	$7.77 \cdot 10^{-17}$	$7.79 \cdot 10^{-17}$	1.00
SC without proj.ion.	$2.72 \cdot 10^{-17}$	$3.20 \cdot 10^{-17}$	$2.70 \cdot 10^{-17}$	$2.87 \cdot 10^{-17}$	0.88
Attachment	$7.95 \cdot 10^{-18}$	$8.22 \cdot 10^{-18}$	$8.35 \cdot 10^{-18}$	$8.17 \cdot 10^{-18}$	0.99
Attachment without proj. ion	$2.33 \cdot 10^{-18}$	$2.24 \cdot 10^{-18}$	$2.41 \cdot 10^{-18}$	$2.33 \cdot 10^{-18}$	0.89
Gain (SC + Attach.)	$8.54 \cdot 10^{-17}$	$8.52 \cdot 10^{-17}$	$8.53 \cdot 10^{-17}$	$8.53 \cdot 10^{-17}$	1.00
Gain without proj. ion. (Neutralization)*	$2.94 \cdot 10^{-17}$	$3.41 \cdot 10^{-17}$	$2.93 \cdot 10^{-17}$	$3.09 \cdot 10^{-17}$	0.88
Double electron capture (DC)	$7.93 \cdot 10^{-18}$	$7.91 \cdot 10^{-18}$	$8.01 \cdot 10^{-18}$	$7.95 \cdot 10^{-18}$	1.00
DC without proj. ion. (Anionic production)*	$2.50 \cdot 10^{-18}$	$2.78 \cdot 10^{-18}$	$2.43 \cdot 10^{-18}$	$2.57 \cdot 10^{-18}$	0.87

Table 4.8: Role of the molecular shape on predicted cross sections; Predicted cross sections for cyclic C_3N^+ and CTMC $2e^-$ calculations. In the last column, ratio between cross section with cyclic isomer divided by the cross section with linear C_3N^+ .

by Toburen et al. (1990). At 0.12 MeV/u ($v=2.2$ a.u) the cross section is about 10^{-18} cm^2 (i.e $0.5 \cdot 10^{-18} \text{ cm}^2$ per electron) as compared to $0.5 \cdot 10^{-16} \text{ cm}^2$ per valence shell electron ($1.5 \cdot 10^{-16} \text{ cm}^2$ for total ionization in the valence shell, see Table 4.4).

Still, if now interested in multiple ionization, it appears that inner shell ionization, followed by Auger de-excitation, becomes more and more important and competitive with valence shell ionization as illustrated in Figure 4.8. In this Figure 4.8 it is seen that inner-shell ionization amounts about to 10% of the triple ionization in $C_3H^+ - He$ collisions at $v= 4.5$ a.u. Since the K shell ionization is larger at $v=4.5$ a.u as compared to $v=2.2$ a.u (see Figure 4.7) and valence shell smaller, we can safely assume that inner-shell ionization will contribute negligibly to projectile ionization up to triple ionization. As a consequence comparison of experimental projectile ionization cross sections with IAE/CTMC predictions will be restricted to projectile ionization up to triple. Inner shell ionization can be included easily in the IAE code and this is only by a lack of time that it has not been done in the present work.

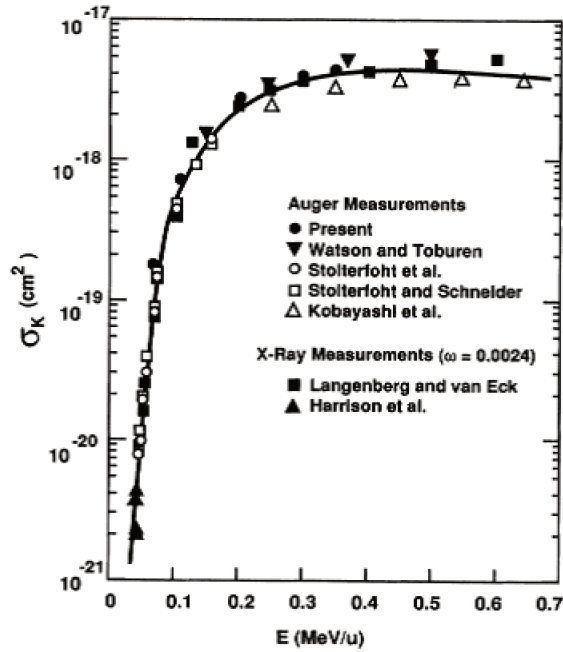


Figure 4-7: Measured Carbon K shell ionization cross sections in $C^+ - He$ collisions as a function of the projectile energy E (MeV/u). From Toburen et al. (1990).

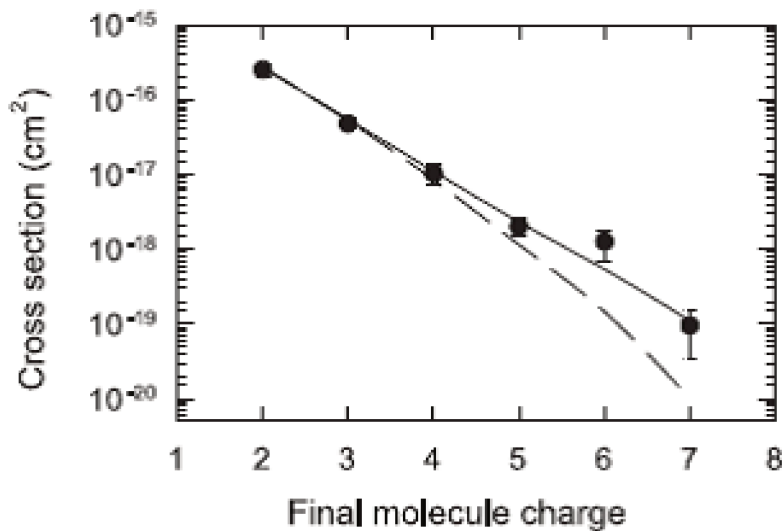


Figure 4-8: Measured projectile ionization cross sections in $C_3H^+ - He$ collisions at $v=4.5$ au. Solid line: IAE including inner shell ionization; dashed line: IAE without inner shell ionization. Extracted from Béroff et al. (2011).

4.2.5 Comparison between experiment and IAE/CTMC model for projectile ionization

We now compare, process by process, the experimental and theoretical cross sections. In Figure 4.9 and 4.10 is presented the case of projectile ionization. In order to visualise the results obtained in the different systems, cross sections of Tables 4.1 to 4.4 are presented as a function of the number of atoms in the projectile n_{atom} , putting arbitrarily for visualisation purposes the N^+ projectile at $n_{\text{atom}}=1.2$. We see that pre-

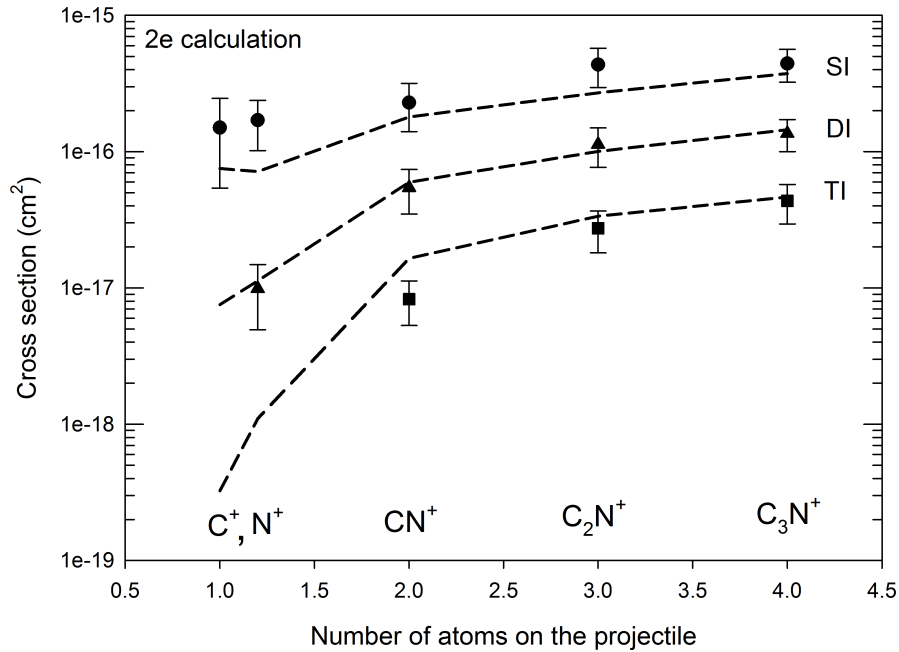


Figure 4-9: Comparison between experimental cross sections and IAE/CTMC predictions for projectile ionization; SI (circles), DI (triangles up), TI (squares) refer to single, double, triple ionization respectively; CTMC calculations performed with two active electrons (CTMC $2e^-$ calculation).

dictions are in rather good agreement with the experimental results, especially when using the CTMC $2e^-$ calculation for atomic ionization. The strong increase of double ionization when going from the atom to the diatomics, observed experimentally, is well reproduced by the IAE model and explained by the possibility for the helium atom to ionise the two components of the molecule when passing between, their half separation (~ 1.1 a.u) corresponding roughly to the impact parameters where probabilities are at their maximum. The saturation of ionization cross sections with the

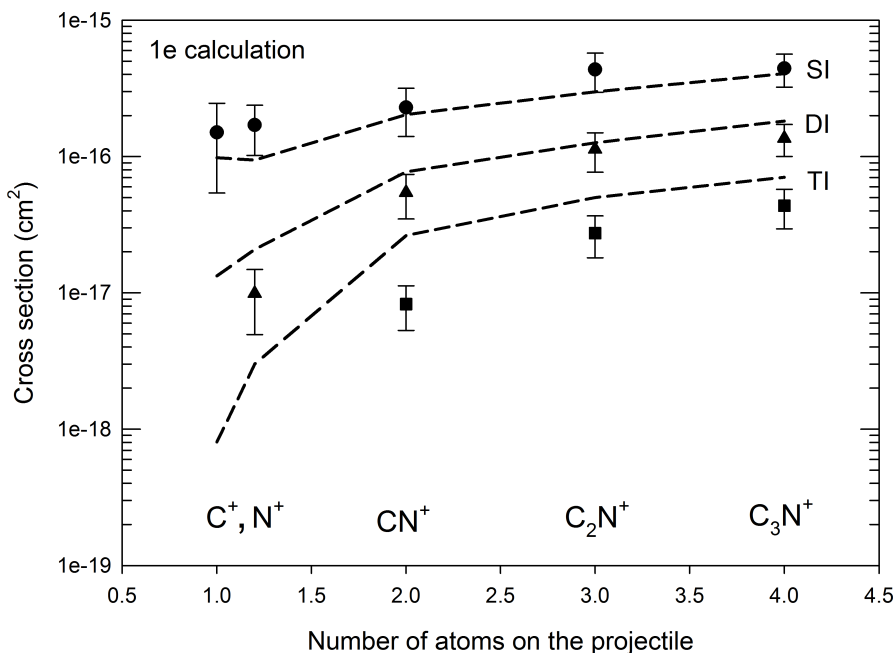


Figure 4-10: Comparison between experimental cross sections and IAE/CTMC predictions for projectile ionization; SI (circles), DI (triangles up), TI (squares) refer to single, double, triple ionization respectively; CTMC calculations performed with one active electron (CTMC $1e^-$ calculation).

molecule size is also reproduced by the model. It is found that a small difference of single ionization cross sections in the atoms ($1e^-$ predicting roughly a cross section 30% higher than the $2e^-$ calculation) is having a large effect on the multi-ionization cross sections, especially for the small systems. It would be interesting to measure the triple ionization of the atoms to constrain more the model.

4.2.6 Comparison between experiment and IAE/CTMC model for projectile excitation

In Figure 4.11 is presented the comparison between experiment and IAE/CTMC model for projectile excitation cross sections. In the experiment, the dissociative excitation only is measured whereas in the model the total excitation (single and multiple), calculated on the basis of atomic excitation, is considered. In atomic C, C^+ , N the first spin allowed transitions begin above 7.5, 9.3 and 10.3 eV respectively (see Tables 5.20, 5.21 and 5.22 in Chapter 5), then depositing enough energy for

dissociation (dissociation energy is around 5/6 eV for C_nN^+ molecules, see Chapter 5). In order to be comparable to the experiment (no change of the projectile charge state) the calculation has to be for excitation without projectile ionization.

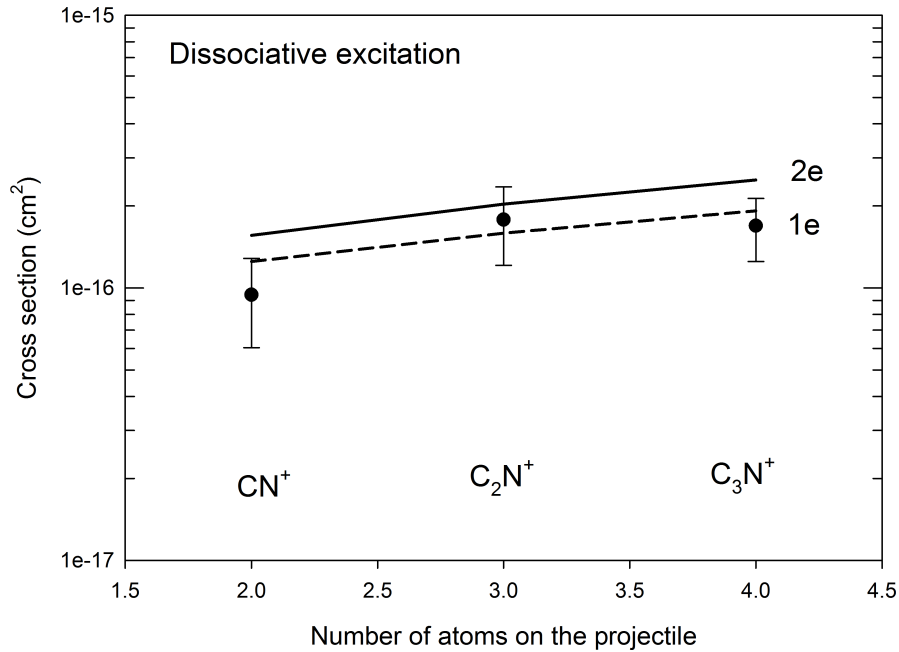


Figure 4-11: Comparison between measured dissociative excitation cross sections and projectile excitation cross sections predicted by the IAE/CTMC model.

This correction is large, reducing the inclusive excitation cross sections by roughly 60% (an almost constant reduction with the molecule size, slightly larger with the $1e^-$ CTMC calculation as compared to the $2e^-$ calculation). Also the double process of single projectile ionization together with electron capture has to be (and was) added. This last “correction” is much smaller, giving rise to an increase of the cross sections between 13% and 26% depending on the molecule and type of calculation. In the end, the very good agreement between experiment and model is remarkable. We will test in more detail this atomic approach to the excitation process with the use of measured dissociation branching ratios.

4.2.7 Comparison between experiment and IAE/CTMC model for projectile neutralization

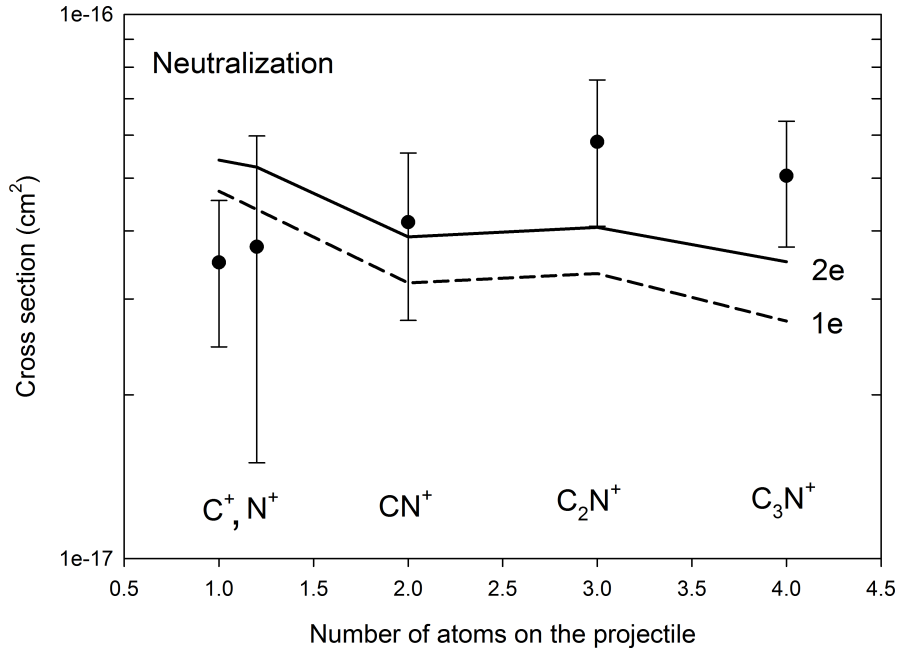


Figure 4-12: Comparison between experiment and IAE/CTMC model for projectile neutralization cross sections.

In Figure 4.12 are compared measured and predicted cross sections for projectile neutralization. This process (change of the projectile charge from +1 to 0) is due to electron capture without projectile ionization. Again this last restriction (no ionization) leads to very large reductions of electron capture cross sections: from 30% for $C^+ 2e^-$ calculation up to 73% for $C_3N^+ 1e^-$ calculation. As expected the reduction is larger with $1e^-$ calculation (larger projectile ionization probabilities) and for largest sizes (since projectile ionization increases with the size). Altogether the agreement between the experiment and the model for projectile neutralization is satisfactory.

4.2.8 Comparison between experiment and IAE/CTMC model for projectile anionic production

In Figure 4.13 are compared measured and predicted cross sections for anionic production cross sections. This process (change of the projectile charge from +1 to -1) is

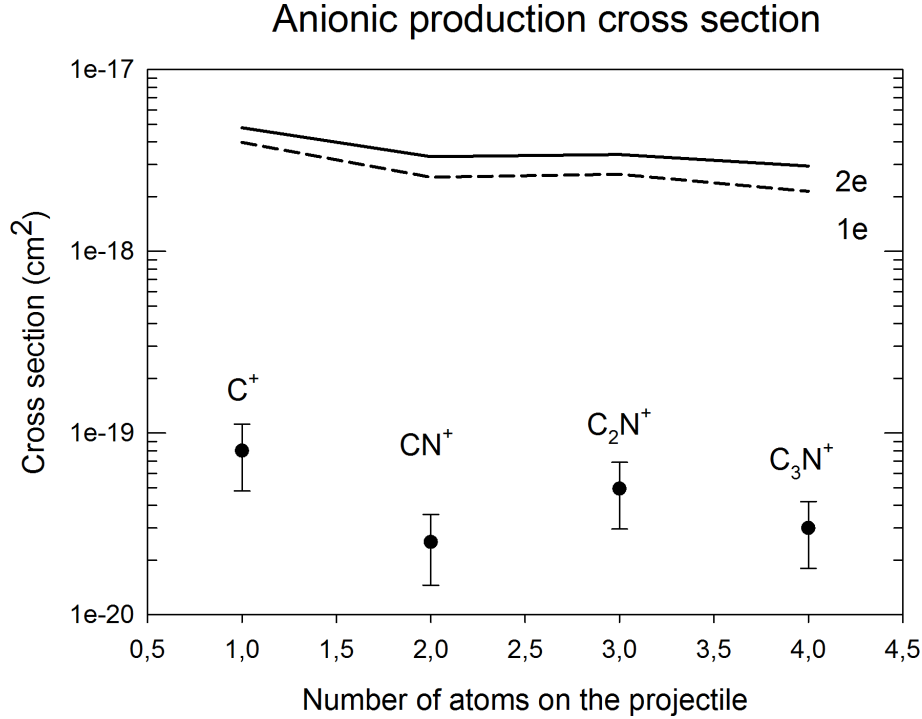


Figure 4-13: Comparison between experiment and IAE/CTMC model for anionic production cross sections.

due to double electron capture without projectile ionization. This last restriction (no ionization) leads to reductions of cross sections of the order of 60%-70% for C_2N^+ and C_3N^+ and 40%-50% for C^+ (depending on $1e^-$ or $2e^-$ CTMC calculation for projectile ionization). As seen in this figure there is a strong overestimation of IAE/CTMC predictions as compared to the experiment (a factor 50 to 100), as already obtained in CN^+-Ar collisions (Labaigt et al., 2015).

One point to discuss is the fact that, with the exception of CN^+ , all double electron capture processes are spin forbidden for ground state to ground state (GS to GS) double transfer. Indeed, since GS of Helium is singlet, it is found that a spin allowed process requires the spin of C_nN^+ to be equal to the spin of C_nN^- , which is not the case except for CN^+ (compare Table 4.6 and Table 5.19). On the other hand, there are close in energy states in C_nN^- allowing to perform the double electron transfer such as the final 1A_1 states, situated respectively at 0.04eV (C_2N^-) and 0.2 eV (C_3N^-) above the GS (Pascoli and Lavendy, 1999) . Whether these states are stable or not is not discussed by the authors. Note that in CN^- only

the GS is stable (Khamesian et al., 2016) whereas in C^- there exists, apart from the 4S GS, a 2D loosely bound (33 meV) state (Andersen, 2004). In this last case, calculations of double electron transfer towards this excited 2D state using a semi-classical atomic orbital close coupling (SCAOCC) calculations taking into account electron correlations (static and dynamic) gave good results (Labaigt et al., 2015). Such a calculation for double electron capture towards the GS of CN^- would be instructive.

Indeed, another source of disagreement between experiment and model could be related to the fact that the outer electron is captured in a non stable state and is ejected before entering in the analysis chamber (i.e within 80 ns). There are indeed some indications in the experiments of spurious trajectories for anions that could be explained by the loss of the outer electron during the path within the electrostatic analyser. An extensive and careful analysis of this phenomenon has to be done.

4.2.9 Conclusions and future

In conclusion, comparisons of experimental single, double and triple projectile ionization as well as dissociative excitation and neutralization with the IAE/CTMC model showed a very reasonable agreement. For projectile ionization, the $2e^-$ CTMC calculations give better results. We recall that there are no adjustable parameters in the theoretical modelization, apart from the basic approximations of IAE. By contrast, the anionic production cross sections are overestimated by the theory by such a factor that we suspect some incomplete detection of the anions in the experiment.

In the future various points should be investigated:

- Introduction of inner shell ionization in the model and interpretation of multi-ionization cross sections (quadruple ionization and above).
- Calculation of double electron capture in CN^+ with SCAOCC including electron correlations
- Search in the data of electron ejection signature in case of anionic fragments

- Beyond the IAE model : a new approach is developed in the group of Bernard Pons in Bordeaux in order to introduce the molecule and the stable propagation of electrons in molecular orbitals.

Chapter 5

Dissociation Branching Ratios

5.1 Experimental results on dissociation Branching Ratios (BR)

5.1.1 Neutral molecules C_nN ($n = 1 - 3$)

Measured dissociation BR of neutral species, produced by electron capture in $CN^+ - He$, $C_2N^+ - He$ and $C_3N^+ - He$ collisions, are reported in Tables 5.1, Table 5.2 and Table 5.3 respectively. Also reported in these Tables are: the channel dissociation energy (column 3) i.e the energetical cost of the channel starting from the ground state of C_nN species calculated using total energies of Table 4.6 ; the number of fragments N_f of the considered channel (column 4); $BR(N_f)$, the branching ratio in number of emitted fragments, obtained by summing all BR corresponding to the same value of N_f (column 5). The $BR(N_f)$ distribution is a good indicator of the species internal energy. Indeed (see Table 5.3) two-fragments channels all require around 6 eV of internal energy for being open whereas three-fragments and four-fragments channels require around 12 eV and 18 eV respectively. Then the knowledge of $BR(N_f)$ could in principle allow to extract the species internal energy $f(E)$. In Figure 5.1 are presented the $f(E)$ distributions that were found to match measured BR of Tables 5.2 and 5.3 respectively. Details of the procedure may be found in IdBarach et al. (2018) (see

chapter 6).

Channel	BR (abs.err)	Dissociation Energy (eV)	N_f	BR(N_f) (abs.err)
CN	0.43(0.02)		1	0.43(0.02)
C +N	0.57(0.02)	7.32	2	0.57(0.02)

Table 5.1: Measured dissociation BR of excited CN species produced by electron capture in CN^+ -He collisions; the first line refers to the BR for non fragmented (intact) species

Channel	BR (abs.err)	Dissociation Energy (eV)	N_f	BR(N_f) (abs.err)
C_2N	0.36(0.02)		1	0.36(0.02)
CN +C	0.45(0.02)	4.89	2	0.55(0.03)
C_2 +N	0.10(0.01)	6.23		
C+C+N	0.09(0.02)	12.21	3	0.09(0.02)

Table 5.2: Measured dissociation BR of excited C_2N species produced by electron capture in C_2N^+ -He collisions; the first line refers to the BR for non fragmented (intact) species

Channel	BR (abs.err)	Dissociation Energy (eV)	N_f	BR(N_f) (abs.err)
C_3N	0.22(0.02)		1	0.22(0.02)
C_3 +N	0.04(0.01)	5.57	2	0.46(0.05)
C_2N +C	0.12(0.02)	6.60		
C_2 +CN	0.30(0.02)	5.51		
CN+C+C	0.17(0.03)	11.49	3	0.29(0.05)
C_2 +N+C	0.12(0.02)	12.82		
N+C+C+C	0.03(0.01)	18.82	4	0.03(0.01)

Table 5.3: Measured dissociation BR of excited C_3N species produced by electron capture in C_3N^+ -He collisions; the first line refers to the BR for non fragmented (intact) species.

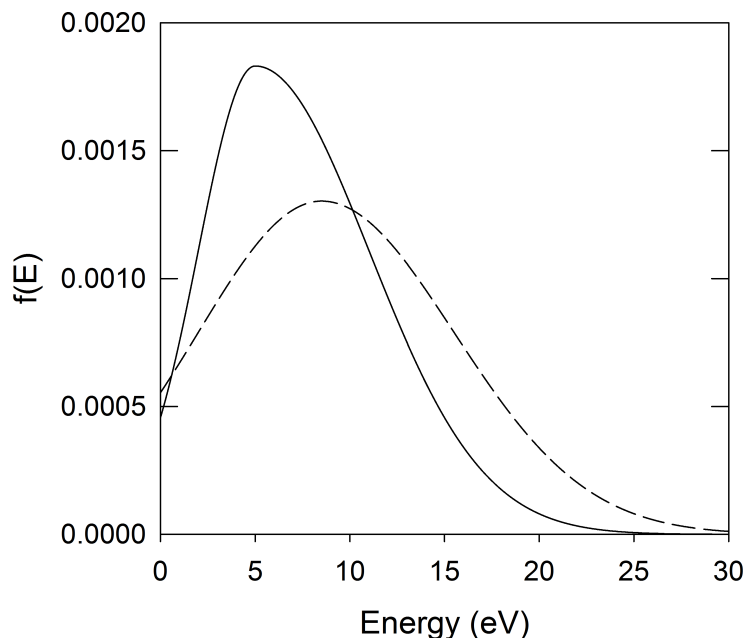


Figure 5-1: Internal energy distribution of C_2N (solid line) and C_3N (dashed line) extracted from measured $BR(N_f)$

Within a given N_f , the higher dissociation BR corresponds to the channel having the smaller energetical cost (smaller dissociation energy). This result is typical of a statistical fragmentation behaviour. It will be interesting to compare these BR to calculations performed within such approach, for instance, Microcanonical Metropolis Monte Carlo method (M3C, (Aguirre et al., 2017)) that are presently underway by the collaborators from Madrid.

5.1.2 Singly charged molecules C_nN^+ ($n=1-3$)

Measured dissociation BR of singly charged species, produced by projectile electronic excitation in $CN^+ - He$, $C_2N^+ - He$ and $C_3N^+ - He$ collisions, are reported in Tables 5.4, Table 5.5 and Table 5.6 respectively. As indicated before, the BR of intact C_nN^+ species are not measured in the experiment. As in the case of neutrals, $BR(N_f)$ may be used to extract the species internal energy. We anticipate distributions shifted towards higher energies as compared to neutrals since $BR(N_f)$ are the largest for $N_f=3$, at variance with neutrals where that was for $N_f=2$. This is what is obtained as shown in figure 5.2. In the section 5.2 we will compare these distributions to energy

deposit calculations performed within the IAE/CTMC model.

Channel	BR (abs.err)	Dissociation Energy (eV)	N_f	BR(N_f) (abs.err)
$C^+ + N$	0.53(0.05)	4.85	2	1(0)
$C + N^+$	0.47(0.05)	8.14		

Table 5.4: Measured dissociation BR of excited CN^+ species produced by projectile electronic excitation in CN^+ -He collisions

Channel	BR (abs.err)	Dissociation Energy (eV)	N_f	BR(N_f) (abs.err)
$CN+C^+$	0.218(0.015)	6.39	2	0.47(0.03)
$C+CN^+$	0.145(0.007)	8.86		
C_2+N^+	0.025(0.002)	11.02		
$N+C_2^+$	0.086(0.004)	8.24		
$C+C+N^+$	0.112(0.005)	17.01	3	0.53(0.03)
$C+N+C^+$	0.414(0.03)	13.71		

Table 5.5: Measured dissociation BR of excited C_2N^+ species produced by projectile electronic excitation in C_2N^+ -He collisions

Channel	BR (abs.err)	Dissociation Energy (eV)	N_f	BR(N_f) (abs.err)
$C_2N^+ + C$	0.148(0.003)	4.52	2	0.40(0.03)
$C_2^+ + CN$	0.086(0.007)	5.43		
$C^+ + C_2N$	0.064(0.005)	6.02		
$C_3^+ + N$	0.052(0.002)	5.45		
$CN^+ + C_2$	0.033(0.003)	7.40		
$N^+ + C_3$	0.012(0.0015)	8.28		
$C^+ + CN + C$	0.14(0.01)	10.91	3	0.41(0.03)
$C^+ + C_2 + N$	0.076(0.006)	12.25		
$C_2^+ + N + C$	0.108(0.008)	12.76		
$CN^+ + C + C$	0.053(0.005)	13.38		
$N^+ + C_2 + C$	0.038(0.003)	15.54		
$C^+ + N + C + C$	0.155(0.011)	18.23	4	0.19(0.02)
$N^+ + C + C + C$	0.03(0.003)	21.53		

Table 5.6: Measured dissociation BR of excited C_3N^+ species produced by projectile electronic excitation in C_3N^+ -He collisions

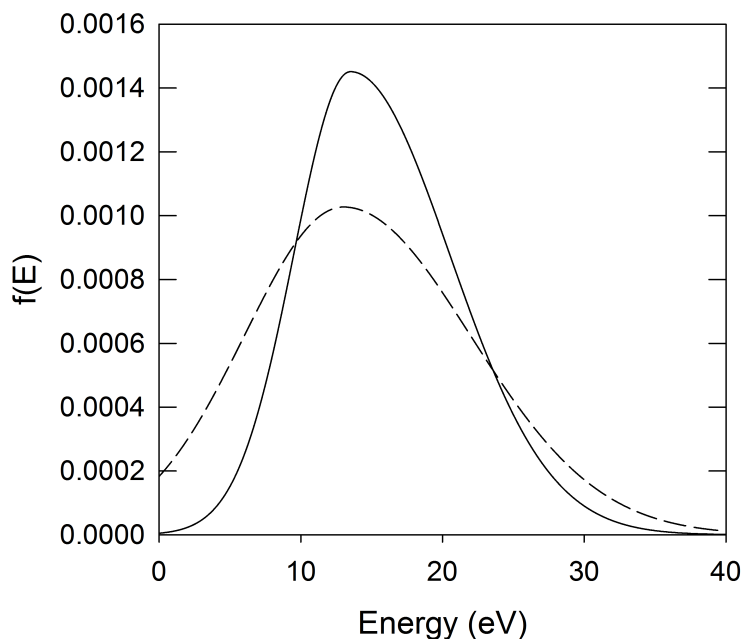


Figure 5-2: Internal energy distribution of C_2N^+ (solid line) and C_3N^+ (dashed line) extracted from measured $BR(N_f)$

As in the case of neutrals, within a given N_f , the higher dissociation BR corresponds to the channel having the smaller energetical cost (smaller dissociation energy). Calculations within the statistical fragmentation model M3C (Aguirre et al., 2017) are under study.

5.1.3 Doubly charged molecules C_nN^{++} (n=1-3)

Measured dissociation BR of doubly charged species (dications), produced by projectile single ionisation in CN^+ -He, C_2N^+ -He and C_3N^+ -He collisions, are reported in Tables 5.7, Table 5.8 and Table 5.9 respectively. Due to the coulombic repulsion between the two charges, C_nN^{++} states are not stable i.e do have exothermic dissociation channels: $C^+ + N^+$ for CN^{++} (-4.5 eV), $CN^+ + C^+$ for C_2N^{++} (-1.03 eV) and $C_2N^+ + C^+$ for C_3N^{++} (-3.0 eV). The CN^{++} dication has been theoretically studied and its ground state found to be metastable due to a barrier of 0.84 eV (Fiser and Polák, 2012). We were not able to distinguish CN^{++} from $C^+ + N^+$ in the CN^+ -He collisions but we managed, in the C_3N^+ -He collisions, to do a separate configuration

with a detector at current shape recognition: no CN^{++} fragment was detected.

Channel	BR (abs.err)	Dissociation Energy (eV)	N_f	BR(N_f) (abs.err)
CN^{++}	Not measured		1	
$C^+ + N^+(+CN^{++})$	0.91(0.02)	-4.5	2(1)*	
$C^{++} + N$	0.052(0.015)	4.3		
$C + N^{++}$	0.024(0.005)	14.0		

Table 5.7: Measured dissociation BR of excited CN^{++} species produced by projectile single ionisation in CN^+ -He collisions; the first line refers to the BR for non fragmented (intact) species; negative dissociation energies correspond to exothermic channels.*: the sum of BR for $C^+ + N^+$ and CN^{++} dissociation is measured.

Channel	BR (abs.err)	Dissociation Energy (eV)	N_f	BR(N_f) (abs.err)
C_2N^{++}	0.082(0.004)		1	0.082(0.004)
$CN^+ + C^+$	0.476(0.046)	-1.03	2	0.52(0.05)
$C_2^+ + N^+$	0.041(0.002)	1.64		
$CN + C^{++}$	8.6	1.15e-3(1.3e-4)		
$C_2 + N^{++}$	2e-4(6e-5)	19.5		
$C + C^+ + N^+$	0.216(0.033)	7.11	3	0.40(0.04)
$N + C^+ + C^+$	0.174(0.010)	3.82		
$C + N + C^{++}$	7.7e-3(3.9e-4)	15.92		
$C + C + N^{++}$	1.2e-3(9.3e-5)			

Table 5.8: Measured dissociation BR of excited C_2N^{++} species produced by projectile single ionisation in C_2N^+ -He collisions; the first line refers to the BR for non fragmented (intact) species; negative dissociation energies correspond to exothermic channels.

Channel	BR (abs.err)	Dissociation Energy (eV)	N_f	BR(N_f) (abs.err)
C_3N^{++}	0.03(3 e-3)		1	0.03(3 e-3)
$C_2N^+ + C^+$	0.378(0.026)	-3.0	2	0.46(0.03)
$C_2^+ + CN^+$	0.05810(6 e-3)	0.4		
$C_3^+ + N^+$	0.026(1.8 e-3)	1.24		
$C_3^{++} + N$	1.145 e-3(1.14 e-4)	7.0		
$C_2N^{++} + C$	6.574 e-4(6.6 e-5)	6.9		
$C^{++} + C_2N$	7.413 e-5(7.4 e-6)	10.6		
$N^{++} + C_3$	3.97 e-5(6 e-6)	19.2		
$2C^+ + CN$	0.075 (6 e-3)	3.5	3	0.28(0.02)
$C^+ + C_2^+ + N$	0.072 (5 e-3)	5.2		
$C^+ + CN^+ + C$	0.057 (4.6 e-3)	5.9		
$C_2^+ + N^+ + C$	0.041(3 e-3)	8.5		
$C^+ + N^+ + C_2$	0.03(2.4 e-3)	8.1		
$(C^{++} + C_2 + N) +$				
$(C^{++} + CN + C)$	8.4e-4(7 e-5)			
$N^{++} + C_2 + C$	1.85 e-4(1.8 e-5)	26.4		
$2C^+ + C + N$	0.133(0.011)	10.8	4	0.23(0.02)
$C^+ + N^+ + 2C$	0.095(8 e-3)	14.0		
$C^{++} + 2C + N$	1.56 e-3(1.2 e-4)	23.9		
$N^{++} + 3C$	2.16 e-4(2.2 e-5)	30.4		

Table 5.9: Measured dissociation BR of excited C_3N^{++} species produced by projectile single ionisation in C_3N^+ -He collisions; the first line refers to the BR for non fragmented (intact) species; negative dissociation energies correspond to exothermic channels.

In the experiments, C_2N^{++} and C_3N^{++} were detected with non negligible BR (8% and 3% respectively), meaning that a part of this population was surviving the 80ns separating the collision from the fragment analyser. Sizeable barriers to the dissociation are then highly probable in these molecules but we could not find any theoretical study on these systems, to the best of our knowledge. As a general behaviour on these dissociation BR of dications, we note the preference towards an equal sharing of the charge between the fragments, which is indeed less costly in energy.

5.1.4 Highly charged molecules C_nN^{q+} ($n=1-3$, $q>2$)

Measured dissociation BR of highly charged species ($q>2$), produced by projectile multiple ionisation in CN^+ -He, C_2N^+ -He and C_3N^+ -He collisions, are reported in

Tables 5.10, Table 5.11 and Table 5.12 for $q=3$ and Tables 5.13, Table 5.14 and Table 5.15 for $q=4$.

For $q \geq 3$ no intact species were detected. It is found that vaporisation prevails, where the number of emitted fragments is equal to the number of atoms in the molecule. In fact the criterium for vaporisation depends qualitatively on q/n , in agreement to what was quantitatively obtained on carbon clusters (Chabot et al., 2010). As in the case of the dications, the sharing of the charge is preferred in the

Channel	BR (abs.err)	N_f	BR(N_f) (abs.err)
$C^{++} + N^+$	0.60(0.05)	2	1(0)
$C^+ + N^{++}$	0.39(0.05)		
$C^{+++} + N$	4 e-3(5 e-4)		
$C + N^{+++}$	8.4 e-4(7 e-4)		

Table 5.10: Measured dissociation BR of excited CN^{+++} species produced by projectile double ionisation in CN^+ -He collisions.

Channel	BR (abs.err)	N_f	BR(N_f) (abs.err)
$CN^+ + C^{++}$	0.023(0.002)	2	0.03 (0.003)
$C_2^+ + N^{++}$	1.7 e-3(1.2 e-4)		
$CN + C^{+++}$	5.6 e-5 (1.7 e-5)		
$C^+ + C^+ + N^+$	0.792(0.045)	3	0.97 (0.06)
$N + C^+ + C^{++}$	0.083(8 e-3)		
$C + N^+ + C^{++}$	0.061 (3 e-3)		
$C + C^+ + N^{++}$	0.037 (4.2 e-3)		
$C + N + C^{+++}$	1.4 e-4 (4.4 e-5)		
$C + C + N^{+++}$	8.3 e-5 (2.6 e-5)		

Table 5.11: Measured dissociation BR of excited C_2N^{+++} species produced by projectile double ionisation in C_2N^+ -He collisions.

dissociation. When the sharing leads to unequal charges on the different atoms, the charge onto C is preferred as compared to the charge onto N, for energetical reasons.

5.1.5 Anionic molecules C_nN^- ($n=1-3$)

Measured dissociation BR of anionic species, produced by double electron capture in CN^+ -He, C_2N^+ -He and C_3N^+ -He collisions, are reported in Tables 5.16, Table 5.17 and Table 5.18 respectively. Dissociation energies, reported in the columns 3, were

Channel	BR (abs.err)	N_f	BR(N_f) (abs.err)
$C_2N^{++} + C^+$	0.018(1.3 e-3)	2	0.031(4 e-3)
$C_2N^+ + C^{++}$	6.63e-3(1.6 e-3)		
$C_3^{++} + N^+$	6.00e-3(5 e-4)		
$C_3^+ + N^{++}$	6.85e-4(9 e-5)		
$2C^+ + CN^+$	0.147(0.010)	3	0.304(0.03)
$C_2^+ + C^+ + N^+$	0.142(0.010)		
$C^{++} + C^+ + CN$	3.9e-3(1 e-3)		
$C_2^+ + N + C^{++}$	3.38e-3(1.20 e-3)		
$CN^+ + C^{++} + C$	2.93e-3(1 e-3)		
$C^{++} + N^+ + C_2$	1.57e-3(4 e-4)		
$C_2^+ + N^{++} + C$	1.48e-3(1.5 e-4)		
$N^{++} + C^+ + C_2$	1.42e-3(1.4 e-4)		
$(C^{+++} + C_2 + N) + (C^{+++} + CN + C)$	1.41e-4(3 e-5)	4	0.665(0.06)
$2C^+ + N^+ + C$	0.425(0.03)		
$3C^+ + N$	0.184(0.013)		
$C^{++} + C^+ + C + N$	0.035(9 e-3)		
$C^{++} + N^+ + 2C$	0.014(4 e-3)		
$N^{++} + C^+ + 2C$	6.93e-3(7 e-4)		
$C^{+++} + 2C + N$	5.22e-5(2 e-5)		
$N^{+++} + C_3$	3.65e-5(2 e-5)		

Table 5.12: Measured dissociation BR of excited C_3N^{+++} species produced by projectile double ionisation in C_3N^+ -He collisions.

Channel	BR (abs.err)	N_f	BR(N_f) (abs.err)
$C^{++} + N^{++}$	0.83(0.02)	2	1(0)
$C^{+++} + N^+$	0.10(0.02)		
$C^+ + N^{+++}$	0.07(0.03)		

Table 5.13: Measured dissociation BR of excited CN^{++++} species produced by projectile triple ionisation in CN^+ -He collisions.

Channel	BR (abs.err)	N_f	BR(N_f) (abs.err)
$CN^+ + C^{+++}$	1 e-3 (2 e-4)	2	1.3 e-3 (3 e-4)
$C_2^+ + N^{+++}$	3 e-4 (8. e-5)		
$C^+ + N^+ + C^{++}$	0.745(0.02)	3	0.999 (3 e-4)
$C^+ + C^+ + N^{++}$	0.195(0.02)		
$N + C^{++} + C^{++}$	0.033 (2 e-3)		
$C + N^{++} + C^{++}$	0.017 (2 e-3)		
$C^+ + C^{+++} + N$	4 e-3 (1 e-3)		
$C + N^+ + C^{+++}$	3 e-3 (2 e-4)		
$C + C^+ + N^{+++}$	2 e-3 (5 e-4)		

Table 5.14: Measured dissociation BR of excited C_2N^{++++} species produced by projectile triple ionisation in C_2N^+ -He collisions.

Channel	BR (abs.err)	N_f	BR(N_f)(abs. err)
$C_2N^{++} + C^{++}$	2.06e-4(2 e-4)	2	3.84 e-4(4 e-4)
$C_2N^+ + C^{+++}$	8.50e-5(9 e-5)		
$C_3^{++} + N^{++}$	5.01e-5(5 e-5)		
$C_3^+ + N^{+++}$	4.25e-5(4 e-5)		
$C^+ + CN^+ + C^{++}$	0.015(4 e-3)	3	0.03(9 e-3)
$N^+ + C_2^+ + C^{++}$	0.011(3 e-3)		
$C^+ + C_2^+ + N^{++}$	5.52e-3(1 e-3)		
$C^+ + C^{+++} + CN$	4.67e-4(2 e-4)		
$C + C_2^+ + N^{+++}$	3.51e-4(2 e-4)		
$2C^{++} + CN$	3.08e-4(1.5 e-4)		
$C + CN^+ + C^{+++}$	2.55e-4(9 e-5)		
$C^+ + N^{+++} + C_2$	2.43e-4(1 e-4)		
$C^{++} + N^{++} + C_2$	1.64e-4(4 e-5)		
$N + C_2^+ + C^{+++}$	1.62e-4(8 e-5)		
$N^+ + C^{+++} + C_2$	2.23e-5(1 e-5)		
$3C^+ + N^+$	0.641(0.045)	4	0.97(0.12)
$C + C^+ + N^+ + C^{++}$	0.175(0.044)		
$N + 2C^+ + C^{++}$	0.098(0.025)		
$C + 2C^+ + N^{++}$	0.044(4 e-3)		
$2C^{++} + C + N$	4.82e-3(2 e-3)		
$C^{++} + N^{++} + 2C$	2.57e-3(7 e-4)		
$C^+ + C^{+++} + C + N$	6.20e-4(3 e-4)		
$C^+ + N^{+++} + 2C$	4.93e-4(2 e-4)		
$N^+ + C^{+++} + 2C$	2.57e-4(1.2 e-4)		

Table 5.15: Measured dissociation BR of excited C_3N^{++++} species produced by projectile triple ionisation in C_3N^+ -He collisions.

obtained using energies of Table 4.6 (chapter 4) and experimental electron affinities (see Table 5.19).

Channel	BR (abs.err)	Dissociation Energy (eV)	N_f	BR(N_f) (abs.err)
CN^-	≥ 0.97		1	≥ 0.97
$C^- + N$	≤ 0.03	9.92	2	≤ 0.03

Table 5.16: Measured dissociation BR of excited CN^- species produced by double electron capture in CN^+ -He collisions; the first line refers to the BR for non fragmented (intact) species.

Channel	BR (abs.err)	Dissociation Energy (eV)	N_f	BR(N_f) (abs.err)
C_2N^-	0.40(0.04)		1	0.40(0.04)
$CN^- + C$	0.51(0.06)	3.8	2	0.58(0.09)
$CN + C^-$	6.34	0.07(0.02)		
$C_2^- + N$	≤ 0.02	4.24		
$C^- + C + N$	0.02(0.01)	14.3	3	0.02(0.01)

Table 5.17: Measured dissociation BR of excited C_2N^- species produced by double electron capture in C_2N^+ -He collisions; the first line refers to the BR for non fragmented (intact) species.

Channel	BR (abs.err)	Dissociation Energy (eV)	N_f	BR(N_f) (abs.err)
C_3N^-	0.09(0.01)		1	0.09(0.01)
$CN^- + C_2$	0.69(0.06)	6.24	2	0.90(0.03)
$C_2^- + CN$	0.16(0.06)	6.83		
$C_2N^- + C$	0.05(1e-3)	8.44		
$(C^- + C + CN) + (C^- + N + C_2)$	≤ 0.02	14.82 and 16.5	3	≤ 0.02

Table 5.18: Measured dissociation BR of excited C_3N^- species produced by double electron capture in C_3N^+ -He collisions; the first line refers to the BR for non fragmented (intact) species.

Species	Electron affinity (abs.err) eV	Reference	Ground state anion
CN	3.862 (0.004)	Bradforth et al. (1993)	$1 \Sigma^+$
C_2N	2.749 (0.001)	Garand et al. (2009)	$3 \Sigma^-$
C_3N	4.59 (0.25)	Graupner et al. (2006)	$1 \Sigma^+$
C_4N	3.1113 (0.001)	Garand et al. (2009)	$3 \Sigma^-$
C	1.262119 (2 e-5)	Rienstra-Kiracofe et al. (2002)	$4S$
C_2	3.269 (0.006)	Rienstra-Kiracofe et al. (2002)	$2 \Sigma_g^+$
C_3	1.995 (0.025)	Rienstra-Kiracofe et al. (2002)	$2 \Pi_g$
C_4	3.882 (0.010)	Rienstra-Kiracofe et al. (2002)	2Π

Table 5.19: Experimental electron affinities used in the calculation of channel dissociation energies of C_nN^- anionic species.

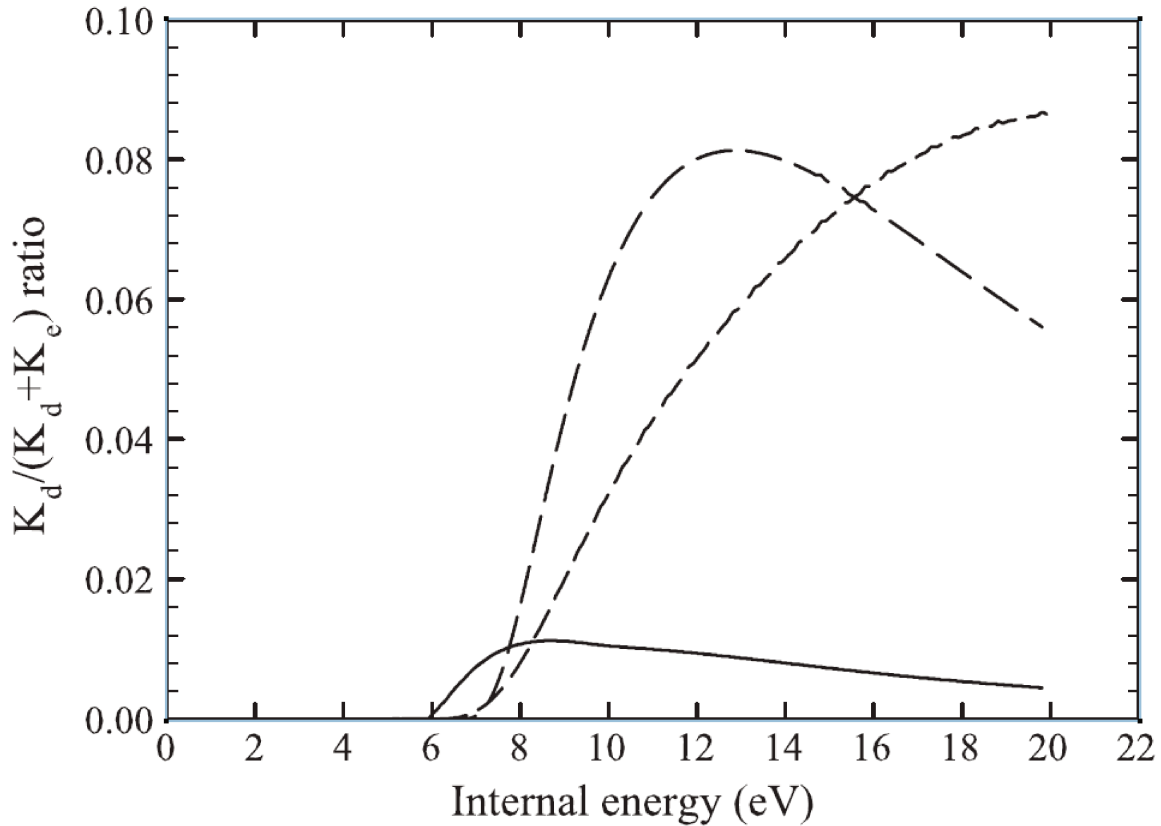


Figure 5-3: Calculated $K_d/(K_d + K_e)$ ratios as a function of C_n^- internal energy where K_d and K_e are calculated rates for dissociation and electron emission respectively; Solid, long dashed and short dashed lines correspond to $n=3, 4, 5$ respectively (From Béroff et al. (2013))

The $BR(N_f)$ cannot be here converted easily in $f(E)$ distributions because one important channel is not measured in the experiment: the electron emission. Indeed,

if the internal energy exceeds the neutral electron affinity (EA), the electron will be emitted. In Béroff et al (2013) we evaluated this so-called thermionic emission (statistical emission) within the Weisskopf formalism and found the rate to be very large (typical 10^{11} s^{-1} at $E^*=5 \text{ eV}$), much larger than dissociation as illustrated in Figure 5.3 where the ratio of dissociation over (dissociation + electron emission) is reported (case of C_n^- clusters). The relaxation following double capture can then be summarized as follows, as a function of the internal energy E :

- for $E \leq EA$, $C_n N^-$ stays intact
- for $EA < E < E_{diss}$ (E_{diss} dissociation energy of the anion) 100% of the relaxation occurs by electron emission
- for $E \geq E_{diss}$ a few % of the relaxation occurs by dissociation, and the rest by electron emission

On the other hand we cannot prove from results of Tables 5.16-5.18 that this electron emission is taking place. We see for instance that $BR(N_f)$ are rather close from those obtained for neutrals (see Table 5.1 to 5.3), exception made of CN/CN^- but the difference could be explained by the fact that E_{diss} is equal to 10 eV in CN^- and only 7 eV in CN . An experimental study of electron emission is then mandatory for concluding.

Looking now at specific channels we note that, whereas C_2^- was a populated fragment in the dissociation of C_n^- clusters, this is here CN^- that appears dominant. We have a very large BR for intact CN^- (more than 97%), and channels with CN^- fragment are by far dominant: the $CN^- + C$ channel for relaxation of C_2N^- (BR=51%) and channel $CN^- + C_2$ for relaxation of C_3N^- (69%). Its strong stability (dissociation energy of $\sim 10 \text{ eV}$) may explain it.

5.2 Interpretation of dissociation of C_nN^+ molecules using the energy deposit calculation performed within IAE/CTMC model.

The principle of the calculation is the following: we introduce in the IAE code the excitation into final (n,l) states on each atom (n, l principal and orbital angular momentum quantum numbers), using the probabilities P_{exc} calculated with CTMC (only 1e calculation of P_{exc} will be presented here). Because $P_{n,l}(b)$ are noisy and not so easy to fit, we calculated in the code the probability of excitation into a n level, $P_n(b)$, then used relative $\sigma(n,l)$ cross sections to determine in which (n,l) state is the electron excited. This approximation is valid if the shapes of the $P_{n,l}(b)$ do not depend much on l, which is approximately the case. At each final state (n,l) is associated a given energy E (see below) so that we have the $\frac{dP_{exc}}{dE}$ to be introduced in the formula 3.8 of chapter 3.

5.2.1 Correspondence between the final (n,l) state and the energy of the transition

The energies of the transitions have been taken from the NIST database. We present only final states that may be populated according to the following selection rules :

$$\Delta S = 0; \Delta L = 0, 1, 2; \Delta J = 0, 1, 2$$

Where S, L, J are respectively the spin, orbital angular momentum and total angular momentum of the considered state. In Tables 5.20, 5.21 and 5.22 are presented the states that may be populated according to these selection rules in the case of C, C^+ and N respectively. When many terms $2^{S+1}L_J$ contribute to a same one-electron transition, the energy of each term is introduced in the code that contributes with a weight (2J+1).

Final configuration	Transition	Term (Energy in eV)
2s ² 2p 3s	2p →3s	³ P(7.48)
2s 2p 4s	2p →4s	³ P (9.68)
2s ² 2p 5s	2p →5s	³ P (10.38)
2s ² 2p 6s	2p →6s	³ P (10.70)
2s 2p 7s	2p →7s	³ P (10.87)
2s ² 2p 3p	2p →3p	³ D (8.64), 3S (8.77), ³ P (8.84)
2s 2p 4p	2p →4p	³ D (10.01), 3S (10.05), ³ P (10.08)
2s ² 2p 5p	2p →5p	³ D (10.53), ³ P (10.55)
2s ² 2p 6p	2p →6p	³ D (10.78), ³ P (10.79)
2s 2p 7p	2p →7p	³ D (10.92), ³ P (10.93)
2s ² 2p 3d	2p →3d	³ F (9.69), ³ D (9.70), ³ P (9.83)
2s 2p 4d	2p →4d	³ F (10.38), ³ D (10.39), ³ P (10.42)
2s ² 2p 5d	2p →5d	³ F (10.70), ³ D (10.70), ³ P (10.72)
2s ² 2p 6d	2p →6d	³ F (10.87), ³ D (10.87), ³ P (10.88)
2s 2p 7d	2p →7d	³ F (10.97), ³ D (10.97), ³ P (10.98)
2s 2p ³	2s →2p	³ D(7.94), ³ P(9.33), 3S(13.11)*
2s 2p ² 3p	2s →3p	³ D(14.27)*
2s 2p ² 4p	2s →4p	³ D(15.44)*
2s 2p ² 5p	2s →5p	³ D(15.90)*
2s 2p ² 6p	2s →6p	³ D(16.12)*
2s 2p ² 7p	2s →7p	³ D(16.26)*

Table 5.20: Energies of reachable states in carbon atom starting from the ground state 2s² 2p² ³P₀. Ionisation potential of C is 11.26 eV; states with a star are autoionizing. From NIST database.

Final configuration	Transition	Term (Energy in eV)
$2s^2 3s$	$2p \rightarrow 3s$	$^2S (14.44)$
$2s 4s$	$2p \rightarrow 4s$	$^2S (19.49)$
$2s^2 5s$	$2p \rightarrow 5s$	$^2S (21.49)$
$2s^2 6s$	$2p \rightarrow 6s$	$^2S (22.47)$
$2s 7s$	$2p \rightarrow 7s$	$^2S (23.02)$
$2s^2 3p$	$2p \rightarrow 3p$	$^2P (16.33)$
$2s 4p$	$2p \rightarrow 4p$	$^2P (20.14)$
$2s^2 5p$	$2p \rightarrow 5p$	$^2P (21.73)$
$2s^2 6p$	$2p \rightarrow 6p$	$^2P (22.68)$
$2s 7p$	$2p \rightarrow 7p$	$^2P (23.15)$
$2s^2 3d$	$2p \rightarrow 3d$	$^2D (18.04)$
$2s 4d$	$2p \rightarrow 4d$	$^2D (20.84)$
$2s^2 5d$	$2p \rightarrow 5d$	$^2D (22.13)$
$2s^2 6d$	$2p \rightarrow 6d$	$^2D (22.82)$
$2s 7d$	$2p \rightarrow 7d$	$^2D (23.22)$
$2s 2p^2$	$2s \rightarrow 2p$	$^2D(9.29), ^2S(11.96), ^2P(13.71)$
$2s 2p 3s$	$2s \rightarrow 3s$	$^2P(22.04)$
$2s 2p 3p$	$2s \rightarrow 3p$	$^2P(22.56), ^2D(23.38)$
$2s 2p 4p$	$2s \rightarrow 4p$	$^2P(26.58)^*, ^2D(26.89)^*$
$2s 2p 5p$	$2s \rightarrow 5p$	$^2P(28.25)^*$
$2s 2p 3d$	$2s \rightarrow 3d$	$^2D(24.60)^*, ^2F(24.78)^*, ^2P(25.07)^*$
$2s 2p 4d$	$2s \rightarrow 4d$	$^2D(27.35)^*, ^2F(27.45)^*, ^2P(27.55)^*$

Table 5.21: Energies of reachable states in the C^+ ion starting from the ground state $2s^2 2p \ ^2P_{1/2}$. Ionisation potential of C^+ is 24.38 eV; states with a star are autoionizing. From NIST database.

Final configuration	Transition	Term (Energy in eV)
$2s^2 2p^2 3s$	$2p \rightarrow 3s$	4P (10.32)
$2s 2p^2 4s$	$2p \rightarrow 4s$	4P (12.84)
$2s^2 2p^2 5s$	$2p \rightarrow 5s$	4P (13.61)
$2s^2 2p^2 6s$	$2p \rightarrow 6s$	4P (13.95)
$2s 2p^2 7s$	$2p \rightarrow 7s$	4P (14.13)
$2s^2 2p^2 3p$	$2p \rightarrow 3p$	4D (11.75), 4P (11.83), 4S (11.99)
$2s 2p^2 4p$	$2p \rightarrow 4p$	4D (13.23), 4P (13.26), 4S (13.32)
$2s^2 2p^2 5p$	$2p \rightarrow 5p$	4D (13.78), 4P (13.79), 4S (13.32)
$2s^2 2p^2 6p$	$2p \rightarrow 6p$	4D (14.04), 4P (14.05)
$2s 2p^2 7p$	$2p \rightarrow 7p$	4D (14.20)
$2s^2 2p^2 3d$	$2p \rightarrow 3d$	4P (12.99), 4D (13.01)
$2s 2p^2 4d$	$2p \rightarrow 4d$	4P (13.67), 4D (13.68)
$2s^2 2p^2 5d$	$2p \rightarrow 5d$	4P (13.98), 4D (13.99)
$2s^2 2p^2 6d$	$2p \rightarrow 6d$	4P (14.15), 4D (14.16)
$2s 2p^2 7d$	$2p \rightarrow 7d$	4P (14.25), 4D (14.26)
$2s 2p4$	$2s \rightarrow 2p$	4P (10.92)
$2s 2p^3 3p$	$2s \rightarrow 3p$	4P (17.89)*
$2s 2p^3 4p$	$2s \rightarrow 4p$	4P (19.14)*
$2s 2p^3 5p$	$2s \rightarrow 5p$	4P (19.62)*
$2s 2p^3 6p$	$2s \rightarrow 6p$	4P (19.86)*
$2s 2p^3 7p$	$2s \rightarrow 7p$	4P (20.00)*

Table 5.22: Energies of reachable states in Nitrogen atom starting from the ground state $2s^2 2p^3 \ ^4S_{3/2}$. Ionisation potential of N is 14.53 eV; states with a star are autoionizing. From NIST database.

5.2.2 Discrete spectra

Having introduced the energies associated to the (n,l) final state in the code, we obtain a spectrum for the energy deposit which is composed of discrete lines. In Figure 5.4 we show such a spectrum (with an interval between the points of 0.2 eV) obtained in the case of excitation of C_2N^+ where single excitation has been selected and autoionizing states are not included. The highest peaks correspond to 2s-2p excitation into C atom (8 eV, 9.3eV), C^+ ion (9.3 eV, 13.7eV) and N(11 eV). The spectrum stops before the IP of C^+ (24.4 eV). In figure 5.5 the energy deposit associated to single and multiple excitation into C_2N^+ is presented. It is seen that new peaks appear after 15 eV up to 40 eV (and above). The intensities of the peaks are small because the multiple excitation (roughly 10% of single excitation in C_2N^+) is shared between many different energies.

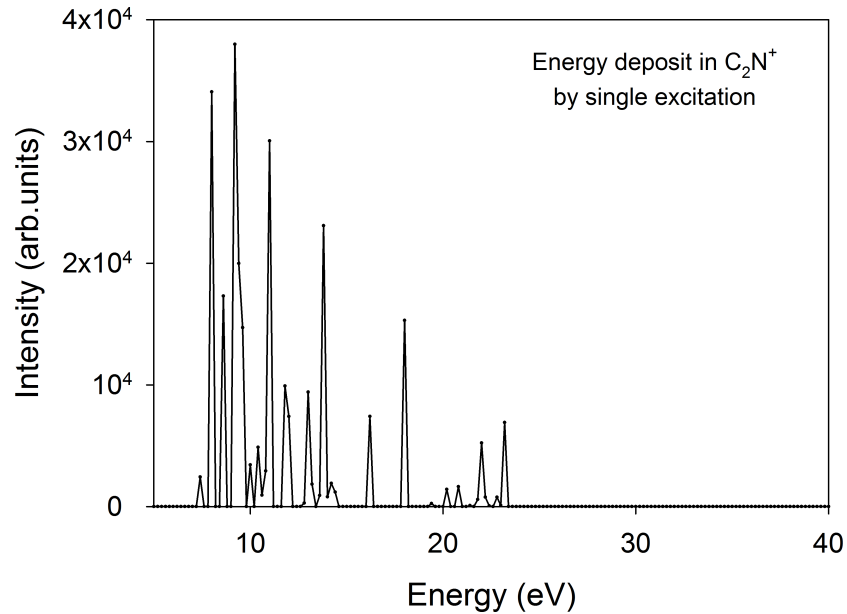


Figure 5-4: Internal energy deposit in C_2N^+ by single electron excitation calculated by IAE/CTMC

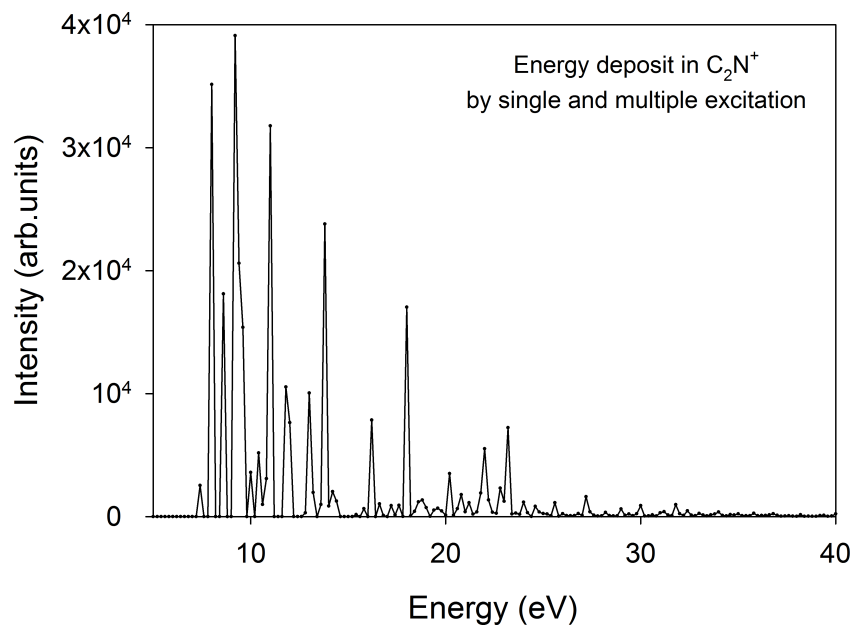


Figure 5-5: Internal energy deposit in C_2N^+ by single and multiple electron excitation calculated by IAE/CTMC

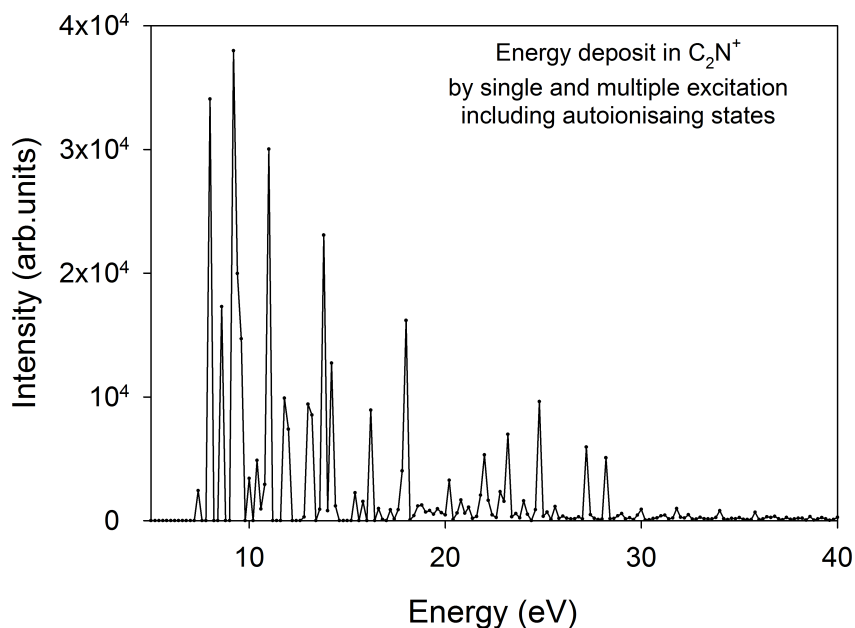


Figure 5-6: Internal energy deposit in C_2N^+ by single and multiple electron excitation and including excitation to autoionizing states calculated by IAE/CTMC

In figure 5.6 the single and multiple excitation of C_2N^+ include the lines which are above the IPs of atoms (i.e autoionizing lines). If autoionization is fast (as compared to dissociation) , the lines should not be included because the molecule would change

its charge and would not be selected as excited molecule. On the other hand, fragmentation could occur before autoionization, especially when the molecule is excited into repulsive states as for instance in double excitation. This is why we present both case. In this situation new lines appear (around 28 eV) but the modification of the spectrum is modest.

5.2.3 Convolved spectra

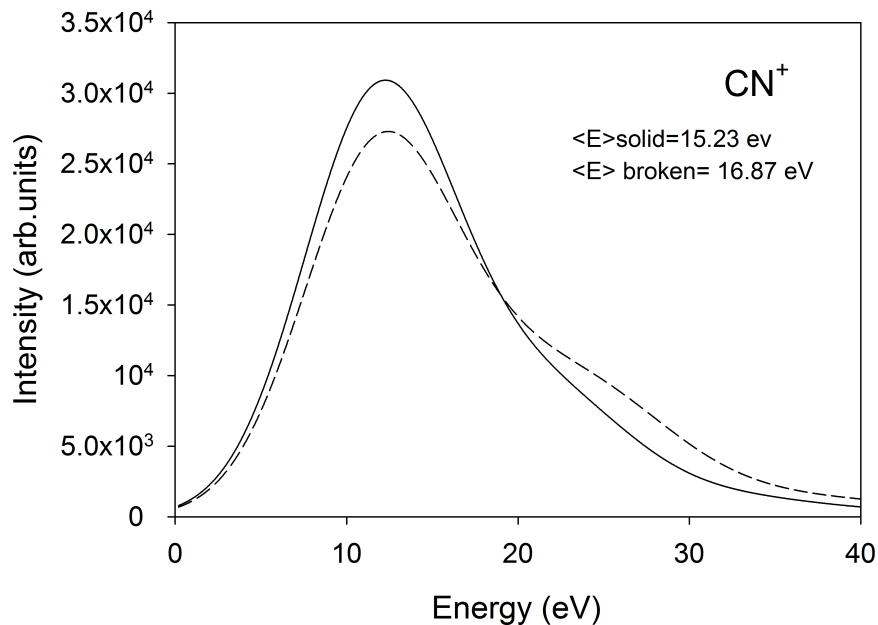


Figure 5-7: Calculated energy deposit in CN^+ without (solid line) and with (broken line) inclusion of the autoionizing states following single and multiple excitation in CN^+ -He collisions. The two curves have the same integral.

In order to compare to the internal energy distribution extracted with $BR(N_f)$ (see figures 5.1 and 5.2), we have to degrade seriously the resolution. We made a convolution between the discrete spectrum and a gaussian curve of 4 eV of standard deviation placed at the position of the peaks. In fact, because the molecules are having already some internal energy before the collision, we shifted all the peaks by the mean energy of the projectile i.e 0.3 eV for CN^+ , 1.2 eV for C_2N^+ and 2.1 eV for C_3N^+ (see Table 1.2 in chapter 1).

Results of convoluted spectra for CN^+ , C_2N^+ and C_3N^+ are shown in figures 5.7,

5.8 and 5.9 respectively where two spectra with or without contribution of the autoionizing states are reported, both including the total single and multiple excitation.

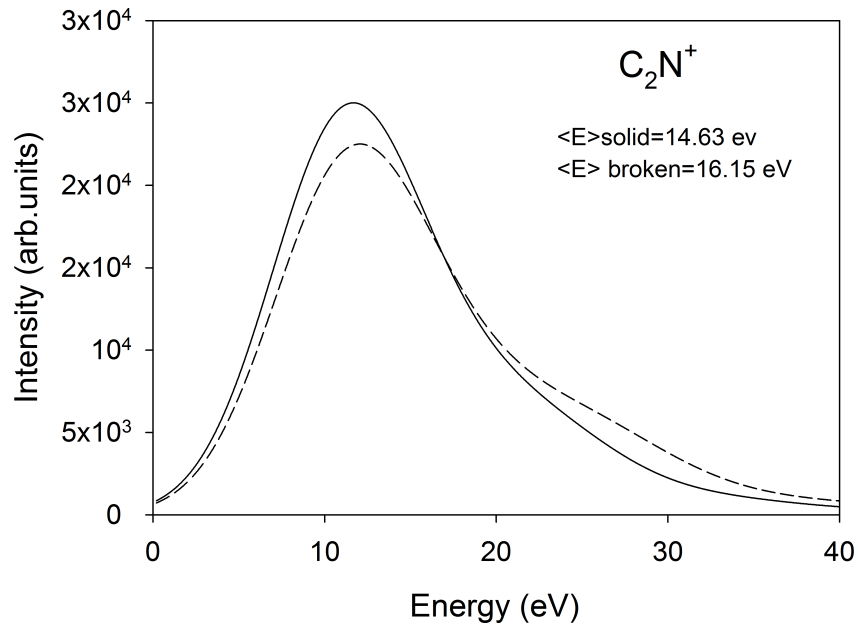


Figure 5-8: Calculated energy deposit in C_2N^+ without (solid line) and with (broken line) inclusion of the autoionizing states following single and multiple excitation in C_2N^+ -He collisions. The two curves have the same integral.

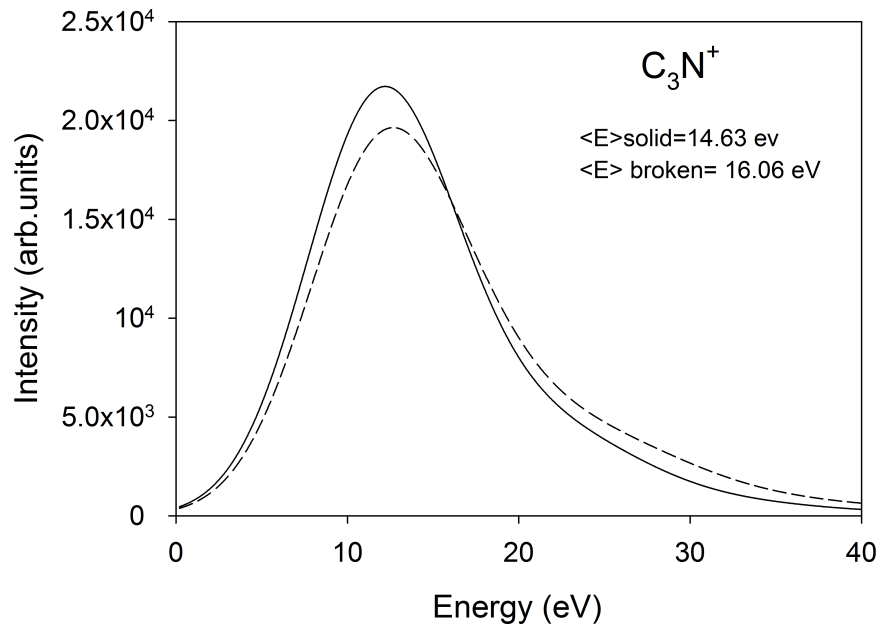


Figure 5-9: Calculated energy deposit in C_3N^+ without (solid line) and with (broken line) inclusion of the autoionizing states following single and multiple excitation in C_3N^+ -He collisions. The two curves have the same integral.

5.2.4 Comparison with the internal energy distribution deduced from experimental branching ratios

In this section we compare the internal energy distributions calculated with IAE/CTMC with the distributions extracted with the use of the measured dissociation branching ratios $BR(N_f)$. The associated energy distributions (semiempirical distributions) are extracted as explained in the paper of IdBarkach et al. (2018) (see chapter 6). They are presented with solid lines, superimposed to the calculated distributions in Figure 5.10 and 5.11 for C_2N^+ and C_3N^+ respectively.

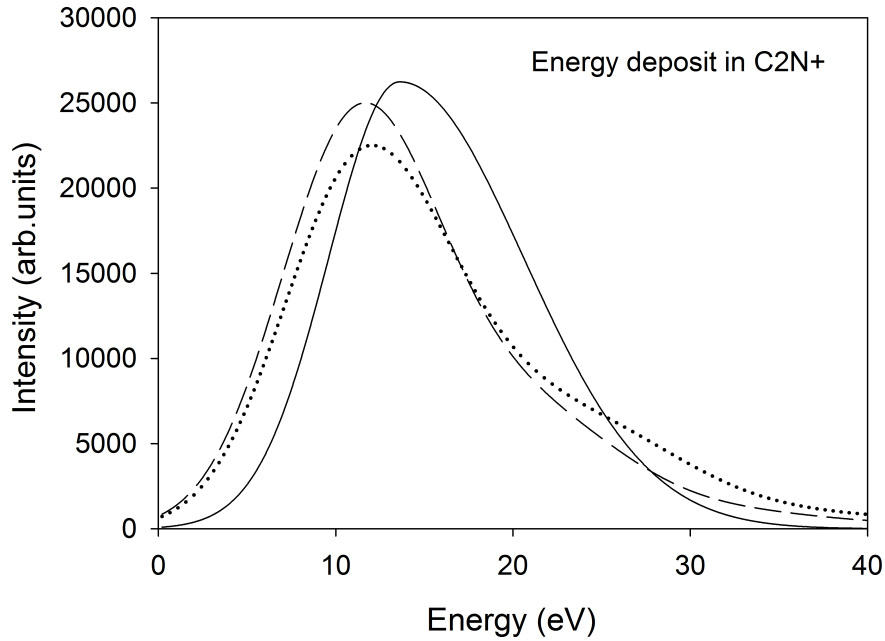


Figure 5-10: Comparison between calculated (long dashed without and dotted with autoionizing states) and semiempirical (solid) internal energy deposits due to single and multiple excitation of C_2N^+ in C_2N^+ -He collisions. The three curves have the same integral.

In figure 5.10 the semiempirical distribution (solid line) is peaked at higher energy than the calculated ones but, being narrower, the mean internal energy is close (15.9 eV as compared to 14.6 eV and 16.1 eV for calculated long dashed and dotted distributions). The opposite is observed in Figure 5.11. Here the semiempirical distribution (solid line) peaks near the calculated ones but, being broader, includes lower energies than the calculated ones. The mean energy, 15.04 eV, is close from the calculated

ones (14.6 eV and 16.1 eV for calculated long dashed and dotted distributions). The calculated distributions are very close between C_2N^+ and C_3N^+ , which is normal since the only difference comes from difference in multiple excitation, which is small in any case. Nevertheless, the agreement between the semiempirical distributions and the calculated ones is rather good taking into account the errors on the semiempirical distribution (1 eV for centroid, 2 eV for the width); it provides a qualitative explanation for the semiempirical distributions and the dissociation branching ratios of C_2N^+ and C_3N^+ measured in the experiment.

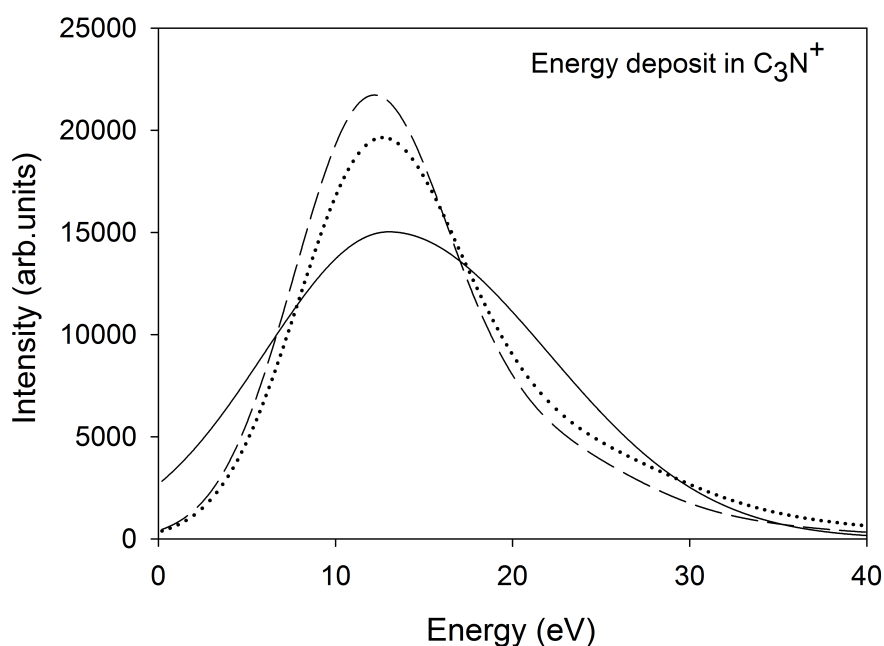


Figure 5-11: Comparison between calculated (long dashed without and dotted with autoionizing states) and semiempirical (solid) internal energy deposits due to single and multiple excitation of C_3N^+ in C_3N^+ -He collisions. The three curves have the same integral.

5.3 Ion Pair dissociation

Ion pair dissociation (IPD) is a relaxation process of highly excited molecules proceeding through emission of an anionic and one (or several) cationic fragments. Due to the energetical cost of the process and the very few density of final states, it is a process with a very small probability as compared to the “normal” dissociation (i.e

without emission of anions). In a recent work (Launoy et al., 2017) the AGAT team showed that the branching ratio for IPD is roughly constant with the species charge and size. We have measured IPD BR for numerous channels in C_nN^{Q+} species and reported the results, not yet interpreted, in Appendix B. We only present in Figure 5.12 the sum of these BR (sum over all channels of same Q value) as a function of the molecule size and charge. We obtain results that are close to those obtained on C_n^{q+} clusters (see Figure 5.13) i.e showing a weak dependence as a function of the size and charge except for C_2N^{Q+} Q=2-3. In this latter case, as N does not carry an extra electron, the other fragments must be multicharged which is energetically costly, then less favorable.

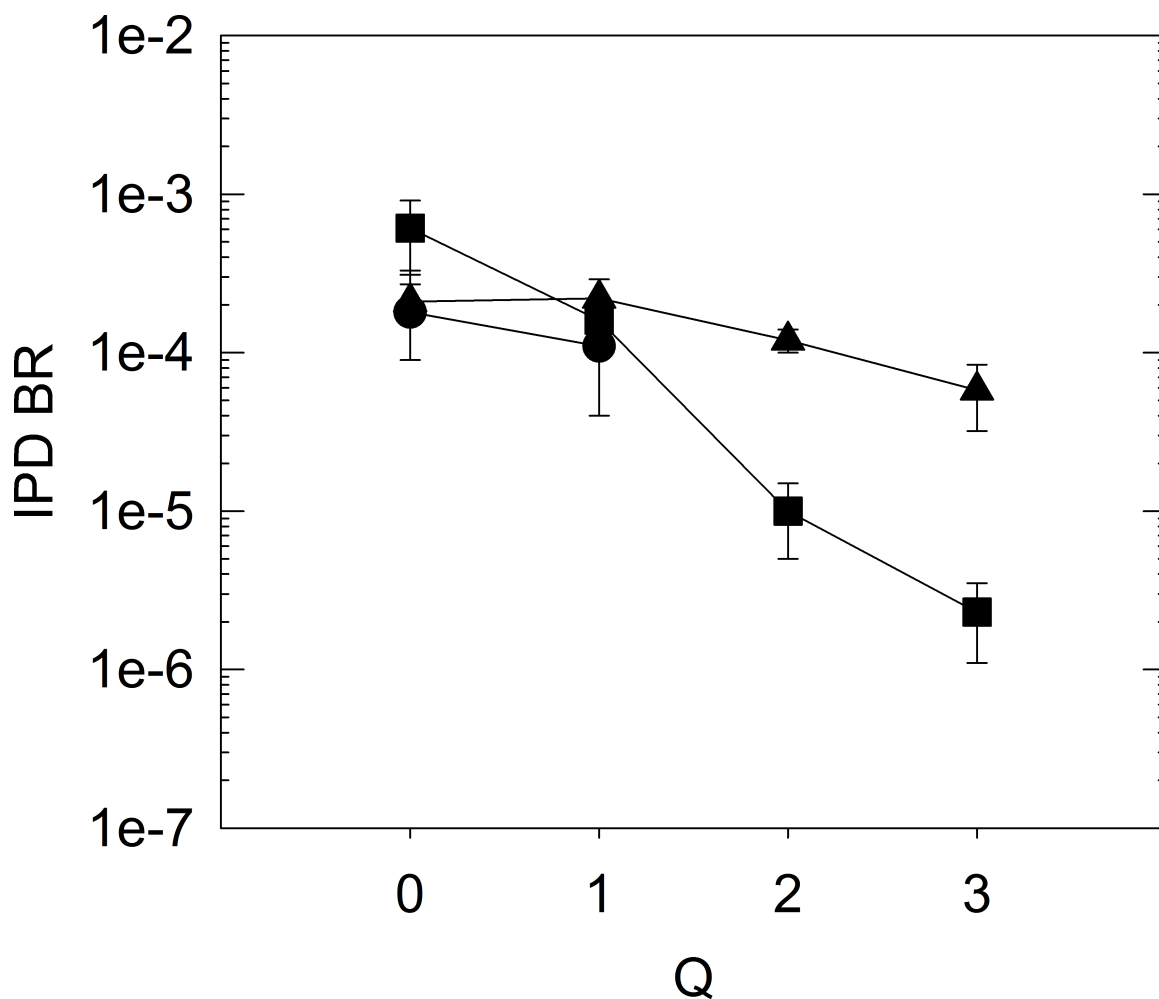


Figure 5-12: Measured BR for IPD dissociation of C_nN^{Q+} species as a function of Q for different species: CN^{Q+} (circles), C_2N^{Q+} (squares) and C_3N^{Q+} (triangles).

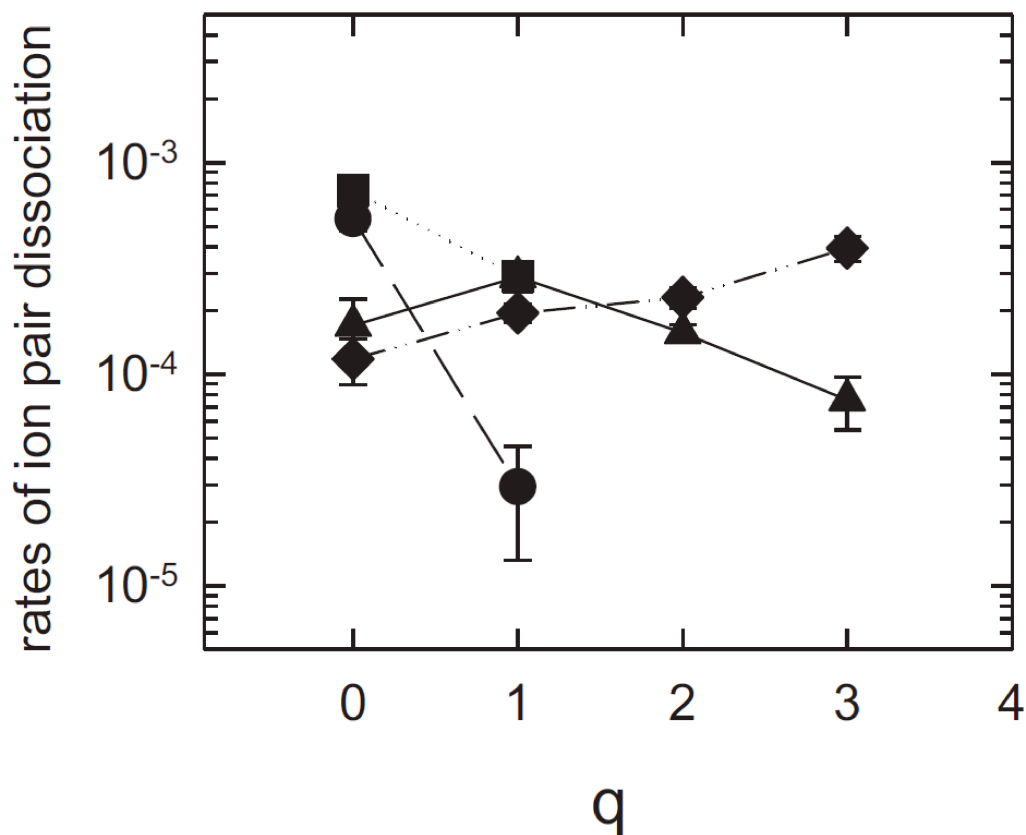


Figure 5-13: Measured BR for IPD dissociation of C_n^{q+} species as a function of q and n . $n=2$: circles; $n=3$: squares; $n=4$: triangles; $n=5$: diamonds. From Launoy et al. (2017)

5.4 Conclusions and future

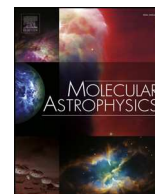
In conclusion we have presented measured dissociation branching ratios for various charges of $C_n N^{Q+}$ species ($Q=-1,0,1,2,3,4$). The BRs in number of fragments $BR(N_f)$ were used to extract the internal energy distribution of the species. For cations ($Q=1$) we found that the obtained distribution could reasonably be well understood on the basis of electronic excitation of the atoms constituting the molecule using the IAE/CTMC model. This procedure cannot be applied to fragmentation of anions, due to the competitive relaxation process by electron ejection. We found that the CN^- fragment was prominent in relaxation of anions. The BR of ion pair dissociation

channels were measured for all species and for various charges ($Q=0-3$). IPD as compared to “normal” dissociation was found to be equally probable whatever the size and the charge of the species, except when the IPD dissociation involves doubly charged fragments. In the future it would be interesting to:

- Compare the BRs of neutral C_nN and cations C_nN^+ with M3C statistical fragmentation predictions.
- Interpret the BR of multicharged species , and stimulate M3C calculations.
- For anions C_nN^- , look at electron emission in data and stimulate M3C calculations including the process of electron ejection.
- Interpret IPD dissociation.

Chapter 6

Application to astrochemistry (paper)



Semiempirical breakdown curves of $C_2N^{(+)}$ and $C_3N^{(+)}$ molecules; application to products branching ratios predictions of physical and chemical processes involving these adducts

Tijani IdBarkach^a, Thejus Mahajan^b, Marin Chabot^a, Karine Béroff^{b,*}, Néstor F. Aguirre^c, Sergio Diaz-Tendero^d, Thibaut Launoy^e, Arnaud Le Padellec^f, Luc Perrot^a, Maëlle A. Bonnin^b, Kim Cuong Le^{b,1}, Florian Geslin^a, Nicolas de Sérerville^a, Fairouz Hammache^a, Aurélie Jallat^a, Anne Meyer^a, Emeline Charon^{g,2}, Thomas Pino^b, Thibault Hamelin^a, Valentine Wakelam^h

^a Institut de Physique Nucléaire d'Orsay, IN2P3-CNRS and Université Paris-Sud, F-91406 Orsay Cedex, France

^b Institut des Sciences Moléculaires d'Orsay, INP-CNRS and Université Paris-Sud, F-91405 Orsay Cedex, France

^c Theoretical Division, Los Alamos National Laboratory, Los Alamos, NM 87545, United States

^d Departamento de Química, Universidad Autónoma de Madrid, 28049 Madrid, Spain

^e Laboratoire de Chimie Quantique et Photophysique, Université Libre de Bruxelles, 1050 Bruxelles, Belgium

^f Institut de Recherche en Astrophysique et Planétologie INP-CNRS Univ. Toulouse 3, F-31028 Toulouse, France

^g Centre de Sciences Nucléaires et de Sciences de la Matière, 91400 Orsay Cedex, France

^h Laboratoire d'Astrophysique de Bordeaux, Université de Bordeaux CNRS, F-33615 Pessac, France

ARTICLE INFO

Keywords:

Carbon and nitrogen-based molecules
Dissociation branching ratios
Breakdown curves
Astrochemistry
KIDA database
Cold cores

ABSTRACT

We constructed semiempirical breakdown curves (BDC) for C_2N , C_3N , C_2N^+ and C_3N^+ molecules. These BDC, which are energy dependent dissociation branching ratios (BR) curves, were used to predict products branching ratios for various processes leading to the formation of $C_2N^{(+)}$ and $C_3N^{(+)}$ excited adducts. These processes, of astrochemical interest, are neutral-neutral and ion-molecule reactions, dissociative recombination and charge transfer reactions with He^+ . Model predictions of BR are compared to the literature data and to reported values in the kinetic database for astrochemistry KIDA. With the new BR values, the C_nN abundances in cold cores were simulated.

1. Introduction

Breakdown curves are energy dependent dissociation branching ratios of an excited molecule (Vekey, 1996). BDCs are specific to the molecule, its size, charge (see below), then constitute a kind of identity card of the molecule that reflects its intimate electronic structure. The usefulness of BDC resides in the fact that, based on their knowledge, it is possible to predict dissociation branching ratios of the molecule following any physical or chemical process if the associated energy deposit is known. In a recent work (Chabot et al. 2013) we showed how it was possible to construct, on both experimental and theoretical grounds, semiempirical BDC for carbon and hydrocarbon molecules and to use those to predict product branching ratios for reactions of astrochemical interest. Whereas the method has its own limitations, it allows to go

beyond the usual first order prediction consisting to affect a BR equal to 1 to the most exothermic reaction. This approximation is common in astrochemical databases involving thousands of reactions that should somehow be given a value. With a more realistic estimate, the improvement may be substantial. Indeed, not only is the number of products much larger than 1 in most cases but the main channel is not always the most exothermic one as will be seen below.

In this paper we intend to pursue the work presented in Chabot et al. (2013) whose aim is to furnish product branching ratios to the astrochemical databases, in particular the recent KIDA database dedicated to the interstellar chemistry (Wakelam et al. 2012; Wakelam et al. 2015). In place of carbon and hydrocarbon molecules we focused on this paper on C_nN radicals and their cations C_nN^+ ($n = 2-3$). Some of them have been detected in the interstellar medium (ISM) : CGN in

* Corresponding author.

E-mail addresses: karine.beroff@u-psud.fr (K. Béroff), valentine.wakelam@u-bordeaux.fr (V. Wakelam).

¹ Present address : Division of Combustion Physics, Department of Physics, Lund University, Sweden.

² Present address : NIMBE, CEA CNRS, Université Paris Saclay, CEA Saclay 91191 Gif sur Yvette, France.

IRC + 10216 Nebula (Anderson and Ziurys, 2014), CCCN in the Taurus dark cloud (Friberg et al. 1980). Despite the large number of molecules containing both carbon and nitrogen in the ISM, the chemistry of nitrogen containing molecules is not well documented, exception made of the chemistry relevant to Titan's atmosphere (Dutuit et al. 2013). In Loison et al. (2014a) the chemistry in dark cloud chemical models of carbon chains containing H, O, N atoms was reviewed, amongst them the $C_nN^{(+)}$ families. For the latter ones, reported values of products BR are based on calculations or estimates but not on experiments. Generally speaking the numerous works on $C_nN^{(+)}$, mostly theoretical, refer to structure calculations in the ground (Ding et al. 1998; Maclean et al. 2007) or excited (Sadlej and Roos, 1991; Zhang et al. 2014) electronic states but very few on the stability and dissociation BR of these species. This is why the experimental dissociation branching ratios we present in Section 2.2 for excited $C_2N^{(+)}$ and $C_3N^{(+)}$ may be of fundamental interest as well.

The plan of the paper is as follows :

In Section 2 the method of construction of semiempirical BDC is presented. It covers the general principle of the method which is summarised from Chabot et al. (2013), the description of the experiments with the associated results and the presentation of semiempirical BDC. In Section 3 we use the obtained BDC to predict product BR for various processes leading to the formation of $C_2N^{(+)}$ or $C_3N^{(+)}$ adducts. It includes some neutral-neutral, ion-molecule reactions, dissociative recombination (DR) process and charge exchange with He^+ process. In each case we will compare the model predictions with the literature and what is presently reported in KIDA. In Section 4 we comment the effect these new BR could have in cold cores environments and conclude.

2. Semiempirical method

2.1. Principle and validity

The principle of the method has been detailed previously (Chabot et al. 2013) and only a brief summary will be given here. The semiempirical method is based on both experimental and theoretical ingredients. From the experimental point of view, we measured all fragmentation branching ratios of $C_2N^{(+)}$ and $C_3N^{(+)}$ molecules excited in high velocity collisions with Helium atoms (see Section 2.2). From the theoretical side, we assumed that this fragmentation was of statistical nature, i.e. only depending on the molecule internal energy. This assumption was found valid for carbon C_n (Martinet et al. 2004) and hydrocarbon C_nH (Aguirre et al. 2018) molecules. This allowed to express the fragmentation branching ratio along channel j , BR_j as :

$$BR_j = \int_0^{\infty} BDC_j(E) f(E) dE \quad (1)$$

where $f(E)$ is the normalised internal energy distribution of the excited molecule and $BDC_j(E)$ the energy dependent dissociation branching ratio along channel j , also referred as to breakdown curve for channel j (Vekey, 1996). As branching ratios, BDC_j verify, at each energy :

$$\sum_j BDC_j(E) = 1 \quad (2)$$

Since we measured in the experiments BR_j for all channels j and since $f(E)$ was also determined following the procedure recalled in Section 2.2, we could extract $BDC_j(E)$ for all channels j by inversion of Eq. (1). As explained in Chabot et al. (2013), the BDC_j curve was taken the following form :

$$BDC_j(E) = \frac{a_j G_j(E)}{\sum_j a_j G_j(E)} \quad (3)$$

where G_j has the generic form depicted in Fig. 1.

The significance of the G_j form is the following : the probability of decaying along channel j opens at E_{diss} (which is the minimum required

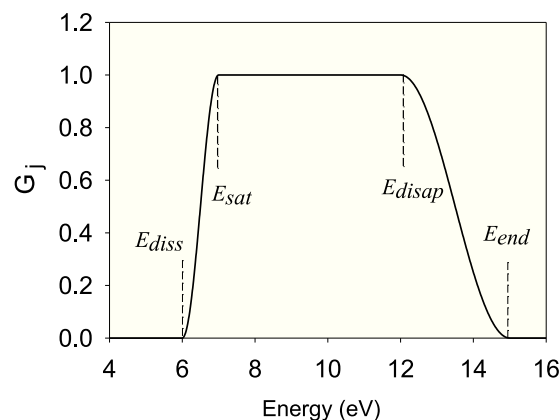


Fig. 1. Generic form of the G_j function.

energy), reaches its maximum at E_{sat} and then start to disappear at E_{disap} when further dissociation of one of the fragments opens. E_{diss} and E_{disap} quantities have been calculated using the Coupled cluster CCSD(T)/6-311++G(3df,2d) method for the molecule whose geometry was optimised at the DFT B3LYP/6-311++G(3df, 2d) level. Vibrational energies, entering in the zero-point energy correction, were performed at the same DFT level. A large number of isomers and spin states was investigated. Electronic ground states of the atoms and molecules together with symmetry of the lowest energy isomers of molecules of interest here are presented in Table 1. Similar calculations have been recently reported for hydrocarbon molecules (Sanchez et al. 2016).

The $(E_{sat}-E_{diss})$ and $(E_{disap}-E_{end})$ differences, which provide the steepness of the ascent and descent of the G_j curve, were estimated also on theoretical grounds. We used BDC calculations performed by some of the authors using the Microcanonical Metropolis Monte Carlo (MMMC) (Diaz-Tendero et al. 2006) and M_3C (Aguirre et al. 2017) statistical fragmentation theories as a guide to estimate these differences. Typical values are 1 to a few eV depending on the number of emitted fragments of the considered channel (Chabot et al. 2013). Values of E_{diss} , E_{sat} , E_{disap} and E_{end} that enter in the construction of the G_j functions are given in the appendix (Table A-1) for all channels j of each molecule.

Having constructed the $G_j(E)$ functions, the a_j scaling factors were extracted by minimization between measured and predicted BR_j using the j coupled Eqs. (1)–(3). By this manner semiempirical BDCs were obtained. The errors come from experimental error bars on BR measurements, $f(E)$ distributions and error bars on the $(E_{sat}-E_{diss})$ and $(E_{disap}-E_{end})$ values. In the Tables of Section 3, we give the error bars for all channels calculated by running the minimization code with slightly different inputs : within experimental error bars for measured BRs, with different $f(E)$ distributions compatible with the measurements and with 25% uncertainties for $(E_{sat}-E_{diss})$ and $(E_{disap}-E_{end})$ quantities.

In all cases where a comparison between experiment and model predictions was possible, a good agreement was found for products branching ratios (Chabot et al. 2013). This was the case for dissociative recombination (DR) of C_4^+ , C_2H^+ and $C_3H_2^+$ measured nearby storage rings. Also the semiempirical BDC were found in very good agreement with BDC calculations performed within the more sophisticated Microcanonical Metropolis Monte Carlo (MMMC) method for the C_n carbon clusters (see the case of C_7 in Chabot et al. 2013).

The statistical approach is expected to work when many states contribute to the studied process. According to Herbst (1978) this is the case in Dissociative Recombination and in chemical reactions already in very small systems (triatomic) when concerned with integrated properties such as products branching ratios irrespectively of their internal state. A statistical approach appears meaningful also in the case of photodissociation by a broad photon energy range. By contrast, photodissociation at specific energy may exhibit some strong dynamical

Table 1

Electronic ground states (GS) and symmetry point groups (Sym.) of atoms and molecules studied in this work. Reported results are for the lowest energy isomers except CCN which is 0.08 eV above CNC and CCN^+ which is 1.09 eV above CNC^+ .

Species	C	N	C_2	CN	CNC	CCN	C_3	C_3N
GS Sym.	$^3\text{P}_g$ atom	$^4\text{S}_u$ atom	$^1\Sigma_g^+ \text{D}\infty\text{h}$	$^2\Sigma^+ \text{C}\infty\text{v}$	$^2\Pi_g \text{D}\infty\text{h}$	$^2\Pi \text{C}\infty\text{v}$	$^1\Sigma_g^+ \text{D}\infty\text{h}$	$^2\text{A}' \text{Cs}$
Species	C^+	N^+	C_2^+	CN^+	CNC^+	CCN^+	C_3^+	C_3N^+
GS Sym.	$^2\text{P}_u$ atom	$^3\text{P}_g$ atom	$^4\Sigma_g^- \text{D}\infty\text{h}$	$^1\Sigma^+ \text{C}\infty\text{v}$	$^1\Sigma_g^+ \text{D}\infty\text{h}$	$^1\Sigma \text{C}\infty\text{v}$	$^2\text{B}_2 \text{C}2\text{v}$	$^3\text{A}' \text{Cs}$

response (see for instance the photodissociation of CH_4 near the Lyman- α in Gans et al. 2011) that the model, as all other dynamical processes, is unable to treat.

2.2. Experiments : dissociation BR, internal energy distribution of $\text{C}_2\text{N}^{(+)}$ and $\text{C}_3\text{N}^{(+)}$

Experiments have been performed at the Tandem accelerator in Orsay with beams of C_nN^+ molecules of, respectively, 4.6 MeV ($n = 2$) and 6.0 MeV ($n = 3$) kinetic energy colliding with helium atoms. Both projectiles have the same impact velocity $v = 2.2$ a.u. (120 keV/amu). The exact value of v does not matter much, the main goal being to produce in the collision excited molecular species of known internal energy and to measure the associated dissociation branching ratios. It was found that dissociation branching ratios of C_n ($n \leq 5$) were not dependent on v , within experimental error bars, over the [2–4] a.u. velocity range (Wohrer et al. 2000). It reflects the fact that there is little change of internal energy with v in this velocity domain. In the collision, excited C_nN^+ and C_nN species were produced by electronic excitation and charge transfer processes respectively. The associated fragmentation was recorded using the dedicated AGAT spectrometer (Launoy et al. 2017). Briefly, AGAT consists of a collision chamber hosting the helium jet, an electrostatic analyser for deflecting fragments according to their charge over mass ratio and a detection chamber where 10 solid-state silicon detectors, suitably positioned, intercepted the fragments. The time window for detection of fragments was [0–150 ns], long enough so as to record the total fragmentation. It was theoretically checked (Diaz-Tendero, 2005) for the dissociation of a C_5 cluster excited in similar conditions and analysed with the same setup. On the other hand, the evolution with n of C_n dissociative branching ratios let us deduce that it is the case at least up to sizes $n = 10$ (Mezdari 2005). The current signals issued from the detectors were used to extract the masses of the fragments. Because the current signal shapes for N and C were very close, some of the channels could not be resolved by the shape analysis method (Chabot et al. 2002). In order to get all channels resolved, we used for detection of neutrals an original CCD position sensitive detector associating the position and mass information (Chabot et al. 2011).

In Tables 2–5 are presented measured dissociation branching ratios for C_2N , C_3N , C_2N^+ and C_3N^+ excited in HVC. Dissociation branching ratios for all channels j have been measured and reported. Their

Table 2

Measured dissociation branching ratios BR_j of the excited C_2N molecule along channel j (second column) and as a function of the number of fragments N_f (last column). The BR_j for intact (non fragmented) molecule is given in the first line. In the third column is reported the calculated dissociation energy of channel j i.e. the minimum energetical cost for dissociation along this channel.

Channel j	BR_j (abs.err)	Dissociation energy (eV)	N_f	$\text{BR}(N_f)$ (abs.err)
C_2N	0.36(0.02)		1	0.36(0.02)
$\text{CN} + \text{C}$	0.45(0.02)	4.89	2	0.55(0.03)
$\text{C}_2 + \text{N}$	0.10(0.01)	6.23		
$\text{C} + \text{C} + \text{N}$	0.09(0.02)	12.21	3	0.09(0.02)

Table 3

Same legend as Table 2 for the excited C_3N molecule.

Channel j	BR_j (abs.err)	Dissociation energy (eV)	N_f	$\text{BR}(N_f)$ (abs.err)
C_3N	0.22(0.02)		1	0.22(0.02)
$\text{C}_3 + \text{N}$	0.04(0.01)	5.57	2	0.46(0.05)
$\text{C}_2\text{N} + \text{C}$	0.12(0.02)	6.6		
$\text{C}_2 + \text{CN}$	0.30(0.02)	5.51		
$\text{CN} + \text{C} + \text{C}$	0.17(0.03)	11.49	3	0.29(0.05)
$\text{C}_2 + \text{N} + \text{C}$	0.12(0.02)	12.82		
$\text{N} + \text{C} + \text{C} + \text{C}$	0.03(0.01)	18.82	4	0.03(0.01)

Table 4

Measured dissociation branching ratios BR_j of the excited C_2N^+ molecule along channel j (second column) and as a function of the number of fragments N_f (last column). In the third column is reported the calculated dissociation energy of channel j i.e. the minimum energetical cost for dissociation along this channel.

Channel j	BR_j (abs.err)	Dissociation energy (eV)	N_f	$\text{BR}(N_f)$ (abs.err)
$\text{CN} + \text{C}^+$	0.218(0.015)	6.39	2	0.47(0.03)
$\text{C} + \text{CN}^+$	0.145(0.007)	8.86		
$\text{C}_2 + \text{N}^+$	0.025(0.002)	11.02		
$\text{N} + \text{C}_2^+$	0.086(0.004)	8.24		
$\text{C} + \text{C} + \text{N}^+$	0.112(0.005)	17.01	3	0.53(0.03)
$\text{C} + \text{N} + \text{C}^+$	0.414(0.03)	13.71		

Table 5

Same legend as Table 4 for the excited C_3N^+ molecule.

Channel j	BR_j (abs.err)	Dissociation energy (eV)	N_f	$\text{BR}(N_f)$ (abs.err)
$\text{C}_2\text{N}^+ + \text{C}$	0.148(0.003)	4.52	2	0.40(0.03)
$\text{C}_2^+ + \text{CN}$	0.086(0.007)	5.43		
$\text{C}^+ + \text{C}_2\text{N}$	0.064(0.005)	6.02		
$\text{C}_3^+ + \text{N}$	0.052(0.002)	5.45		
$\text{CN}^+ + \text{C}_2$	0.033(0.003)	7.4		
$\text{N}^+ + \text{C}_3$	0.012(0.0015)	8.28		
$\text{C}^+ + \text{CN} + \text{C}$	0.14(0.01)	10.91	3	0.41(0.03)
$\text{C}^+ + \text{C}_2 + \text{N}$	0.076(0.006)	12.25		
$\text{C}_2^+ + \text{N} + \text{C}$	0.108(0.008)	12.76		
$\text{CN}^+ + \text{C} + \text{C}$	0.053(0.005)	13.38		
$\text{N}^+ + \text{C}_2 + \text{C}$	0.038(0.003)	15.54		
$\text{C}^+ + \text{N} + \text{C} + \text{C}$	0.155(0.011)	18.23	4	0.19(0.02)
$\text{N}^+ + \text{C} + \text{C} + \text{C}$	0.035(0.003)	21.53		

number is increasing with the size and the charge of the molecule. The rate of intact cations is not measured in the experiment. Being reported in the third columns of Tables 2–5 are the dissociation energies calculated as explained in Section 2.1. These dissociation energies are computed for the lowest energy isomers of both the parent and the fragments. This is a kind of approximation since the isomer state of the fragment is not known in these experiments. Accordingly the channel notations of Tables 2–5 should be understood as isomer unresolved notations.

An instructive information comes from the number of fragments N_f of the dissociation channel, reported in columns 4 of Tables 2–5. Indeed this number strongly correlates with the internal energy of the species

Table 6

Parameters of the internal energy distributions (see text) of C_2N , C_3N , C_2N^+ and C_3N^+ molecules fragmenting along Tables 2–5.

	E_0 (abs.err) eV	σ_L (abs.err) eV	σ_H (abs.err) eV
C_2N	5(0.5)	3(1)	6(0.5)
C_3N	8.5(0.5)	6.5(1)	7(1)
C_2N^+	13.5(1)	4(1)	7(1)
C_3N^+	13(1)	7(1)	9(1)

since channels with two fragments ($N_f = 2$) typically require 6 eV whereas channels with $N_f = 3$ and $N_f = 4$ require around 12 eV and 18 eV respectively (with the exception of C_2N^+ for which all energies are shifted by 3 eV towards higher values). Experimental $BR(N_f)$, obtained by summing experimental BR_j associated to the same value of N_f (see columns 5 in Tables 2–5), were used to extract the internal energy distribution of the species $f(E)$. This was done by using Eq. (1) in which BR_j is replaced by $BR(N_f)$ and $BDC_j(E)$ replaced by $BDC_{N_f}(E)$ ($BDC_{N_f}(E)$ is the sum of $BDC_j(E)$ for channels j having the same N_f value).

An analytical form for $f(E)$ was assumed, made of two half Gaussian distributions centered and joining at E_0 and having standard deviation σ_L (low energy side) and σ_H (high energy side). This form is flexible enough to reproduce all possible shapes and physically meaningful distributions (in particular the decrease of the distribution at high energy). The values we found for E_0 , σ_L and σ_H in the case of the four studied molecules are reported in Table 6. They show quite broad energy distributions peaking around 5/8 eV for neutral molecules, 13/14 eV for cationic molecules and extending up to 25 eV (neutrals) and 40 eV (cations). Note that the distributions obtained with cations are perfectly explained by the excitation process of atoms composing the molecule (Mahajan et al. 2018). This distribution is not expected to change more with the collision velocity, especially in the high velocity range ($v \geq 2-3$ a.u.). Indeed, in ion-atom collisions, probabilities of excitation processes decrease with v but the relative populations of $\{n, l\}$ final states (n, l principal and orbital angular momentum quantum numbers respectively) are basically unchanged (Kirchner et al. 2000).

As a general remark on these results of Tables 2–5 we note that, within a given number of emitted fragments, channels requiring the lowest energy are having the larger BR. Exception arises for the $C_3 + N$ channel which is having a very small BR although the dissociation energy is close to the lowest energy one (see Table 3). In fact the existence of a barrier along the $C_3 + N$ reaction coordinate has already been invoked in the literature (Loison et al. 2014a) and estimated to be about 1 eV in KIDA (Smith and Loison, 2011). We checked the height of this barrier by calculating the energy profile of the $C_3N(^4A'') \rightarrow C_3(^1\Sigma_g^+) + N(^4S_u)$ reaction. Results are shown in Fig. 2. Relative energy as a function of the reaction coordinate (a.u) computed at the B3LYP/6-311++G(3df,2p) level of theory is shown in black. The blue points in Fig. 2 correspond to relative energies at the critical points in the reaction (reactant, transition state and products) computed at the CCSD(T)/6-311++G(3df,2p) level over the B3LYP geometry. The CCSD(T) calculations provide a barrier height of 0.4 eV for the reverse reaction, smaller than previously estimated. In any case this barrier is likely to reduce the $C_3 + N$ outgoing channel reported in Table 3 since the required energy is not 5.57 eV but 5.97 eV.

2.3. Breakdown curves of C_2N , C_3N , C_2N^+ and C_3N^+ molecules

In the Fig. 3 are presented semiempirical breakdown curves for C_2N , C_3N , C_2N^+ and C_3N^+ . The way these BDC are constructed was explained in Section 2.1. For C_3N the existence of a barrier of 0.4 eV along the $C_3 + N$ reaction coordinate was taken into account by replacing the dissociation energy E_{diss} of Fig. 1 by $E_{diss} + 0.4$ eV. For cationic species the BDC curves start above the dissociation energy because, as mentioned before, the rate of intact cations is not measured in the

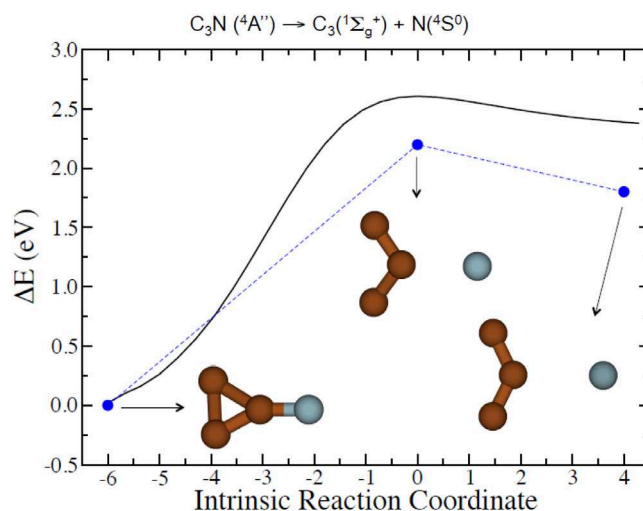


Fig. 2. Energy profile of the $C_3N(^4A'') \rightarrow C_3(^1\Sigma_g^+) + N(^4S_u)$ reaction. Relative energy (eV) as a function of the reaction coordinate (a.u.) is computed at the B3LYP/6-311++G(3df,2p) level of theory and shown in black. The blue circles correspond to relative energies at the critical points in the reaction (reactant, transition state and products) computed at the CCSD(T)/6-311++G(3df,2p) level over the B3LYP geometry.

experiment.

It is seen in Fig. 3 that BDCs exhibit well separated energy domains associated to a different number of fragments. This justifies the procedure used for extracting the internal energy distribution described previously. It is important to recall here that this energy is from electronic origin (electron capture and electron excitation) and is centered on quite large values (see Table 6). Accordingly, the constructed BDCs are presumably applicable to any type of energy deposit, electronic or vibrational (part of the electronic energy being rapidly converted into vibrational energy, especially in large systems).

The BDC are specific to each molecule, size and charge. If the internal energy of the adduct is taken as a delta function (case of the processes considered in Section 3, the energy is called E_a), it is easy to predict the products branching ratios by placing E_a on the x-axis of Fig. 3. Obviously the accuracy of the predictions will be better if this energy is in a «flat domain» and far from curve crossings. In case there is an internal energy distribution $f(E_a)$ associated to the studied process, BR are obtained using Eq. (1).

3. Semiempirical products branching ratios

Using BDCs of Fig. 3, products branching ratios for physical and chemical processes leading to excited adducts $C_2N^{(+)}$ and $C_3N^{(+)}$ of known internal energy E_a were predicted. The processes we considered below are neutral-neutral reactions, ion-molecule reactions, dissociative recombination (DR) and charge exchange reaction with He^+ .

In the calculation of the internal energy of the adduct E_a , we supposed that the reaction occurred between reactants in their electronic ground states towards the adduct in its electronic ground state. This energy is equal to the dissociation energy of the adduct in its electronic ground state towards reactants in their electronic ground states (reverse pathway, see Eq. (4)). The E_a energies are reported in bold in Tables 7–10. Similarly, the exothermicity ΔE of the reaction (reactants to products) was calculated by supposing that the products were in their electronic ground states. ΔE has been calculated by difference between the adduct internal energy and the dissociation energy of the adduct towards the considered outgoing channel (or the dissociation energy increased by a barrier height when pertinent), see Eq. (5). Exothermicities are reported in the last column of Tables 7–10; positive values correspond to exothermic reactions.

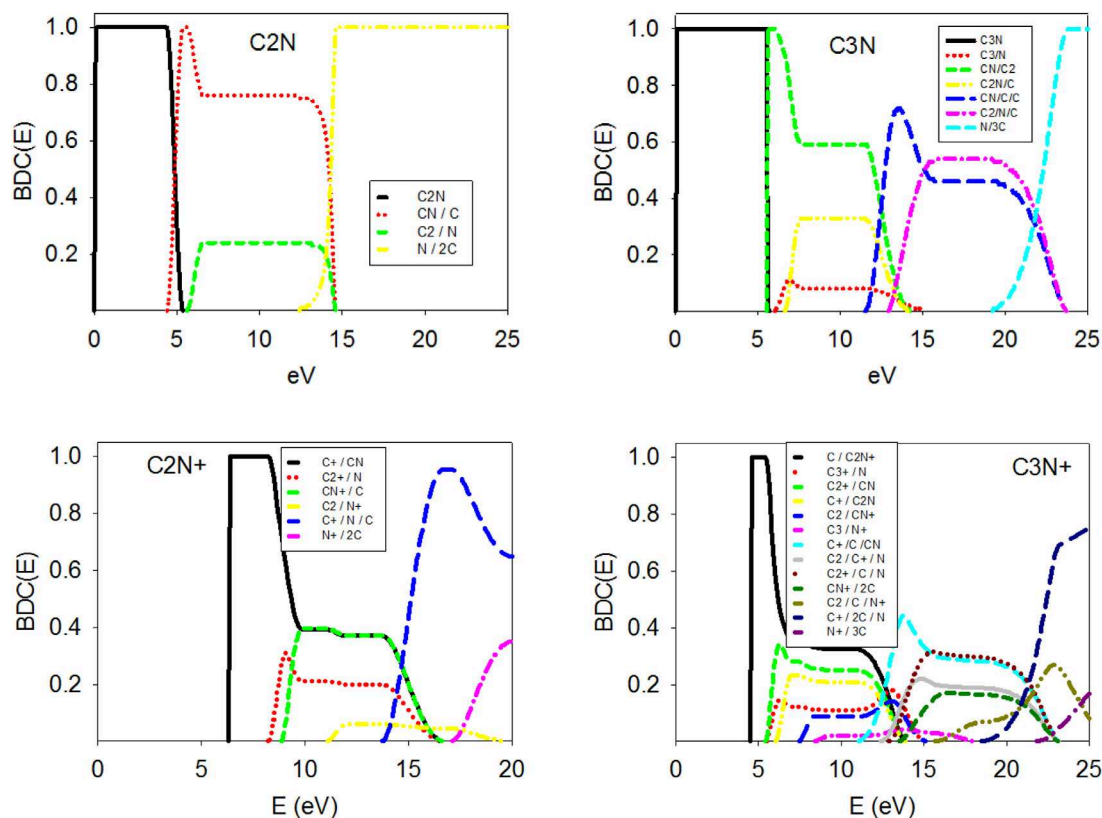


Fig. 3. Semiempirical BDC for C_2N , C_3N , C_2N^+ and C_3N^+ molecules.

Table 7

Branching ratios (BR) for Neutral-Neutral reactions. E_a represents the internal energy of the neutral adduct and ΔE the exothermicity of the reaction. *: the reaction cannot proceed through the electronic ground state of the adduct lowest energy isomer.

Reactants	Products	Model BR (abs.err)	KIDA BR	E_a (eV)	ΔE (eV)
$C_2 + N$	$C + CN^*$	1	1	6.23	1.34
$CNC + C$	$C_2 + CN$	0.90(0.05)		6.6	1.09
	$C_3 + N^*$	0.10(0.05)			0.63
$CCN + C$	$C_2 + CN$	0.90(0.05)	1	6.68	1.17
	$C_3 + N^*$	0.10(0.05)			0.71

$$E_a = E_{\text{diss}}(\text{adduct} \rightarrow \text{reactants}) \quad (4)$$

$$\Delta E = E_a - E_{\text{diss}}(\text{adduct} \rightarrow \text{products}) \quad (5)$$

These assumptions are not always valid. Ground state to ground state reaction is sometimes forbidden, for spin conservation violation or symmetry breaking reasons. We checked, for all reactions, whether the reaction between reactants and products was spin allowed and whether the adduct was possibly the lowest energy isomer of the molecule in its electronic ground state. For that, we used the electronic ground states characteristics of atoms and molecules involved in the processes (presented in Table 1) and the known selection rules (see appendix B of Chabot et al. 2013). We indicate in the legend of Tables 7–10 when the reaction is spin forbidden (\ddagger) and also when spin and/or symmetry considerations preclude the formation as an adduct of the lowest energy isomer of the molecule in its electronic ground state (*). In the first case (\ddagger), since the model is not able to predict whether a spin forbidden reaction will be closed, slowed down or will occur with a normal rate (Schwarz, 2004) we introduced this uncertainty in the error bars of the predicted values. We recommend to use in chemical models the predicted values with the associated large unsymmetrical error bars given in Tables 7–10. When the adduct cannot be the lowest energy isomer in

Table 8

Branching ratios (BR) for Ion-molecule reactions. E_a represents the internal energy of the ionic adduct and ΔE the exothermicity of the reaction. \ddagger : this value corresponds to the sum of the two isomers CNC^+ and CCN^+ . *: the reaction cannot proceed through the electronic ground state of the adduct lowest energy isomer; \ddagger : the reaction is spin forbidden for ground state reactants towards ground state products.

Reactants	Products	Model BR (abs.err)	KIDA BR	E_a (eV)	ΔE (eV)
$C_2^+ + N$	$C^+ + CN$	1	1	8.24	1.85
$CN^+ + C$	$C^+ + CN^*$	0.72(+ 0.07/− 0.05)	1	8.86	2.47
	$C_2^+ + N^*$	0.28(+ 0.05/− 0.07)			0.62
$N^+ + C_2$	$CN^+ + C^*$	0.40(0.05)		11.02	2.16
	$C^+ + CN^*$	0.39(0.05)			4.63
	$C_2^+ + N^*$	0.21(0.04)	1		2.78
$C_3^+ + N$	$[C_2N^+] + C$	1		5.45	0.93
$C_2^+ + CN$	$[C_2N^+] + C$	1		5.43	0.91
$C^+ + CNC$	$[C_2N^+] + C$	0.58(0.06)		6.02	1.5
	$C_2^+ + CN$	0.30(0.06)			0.59
	$C_3^+ + N$	0.12(0.04)			0.57
$C^+ + CCN$	$[C_2N^+] + C$	0.58(0.06)	0.7 \ddagger	6.1	1.58
	$C_2^+ + CN$	0.30(0.06)	0.3		0.67
	$C_3^+ + N$	0.12(0.04)			0.65
$CN^+ + C_2$	$[C_2N^+] + C^\ddagger$	0.35(+ 0.03/− 0.35)		7.4	2.88
	$C_2^+ + CN^\ddagger$	0.28(+ 0.03/− 0.28)	1		1.97
	$C^+ + [C_2N]^*$	0.23(+ 0.77/− 0.03)			1.38
	$C_3^+ + N^\ddagger$	0.12(+ 0.02/− 0.12)			1.95
$N^+ + C_3$	$[C_2N^+] + C$	0.33(+ 0.15/− 0.04)		8.28	3.76
	$C_2^+ + CN$	0.25[+ 0.15/− 0.03]			2.85
	$C^+ + [C_2N]$	0.22(+ 0.14/− 0.03)			2.26
	$C_3^+ + N$	0.11(+ 0.13/− 0.02)			2.83
	$CN^+ + C_2^\ddagger$	0.09(+ 0.02/− 0.09)			0.88

its electronic ground state, we checked whether the adduct could possibly be a close-in-energy isomer of the molecule in its electronic ground state (calculations of many isomers were performed as indicated before). In all cases an excited isomer of the adduct was found to be

Table 9

Branching ratios (BR) for dissociative recombination. E_a represents the internal energy of the neutral adduct and ΔE the exothermicity of the reaction. ¶ : the reaction is spin forbidden for ground state reactants towards ground state products.

Reactants	Products	Model BR (abs.err)	KIDA BR	E_a (eV)	ΔE (eV)
CNC ⁺ + e ⁻	C + CN	0.77(+ 0.23/-0.03)	0.95	9.66	4.77
	C ₂ + N [¶]	0.23(+ 0.03/-0.23)	0.05		3.43
CCN ⁺ + e ⁻	C + CN	0.77(+ 0.23/-0.03)	0.95	10.67	5.78
	C ₂ + N [¶]	0.23(+ 0.03/-0.23)	0.05		4.44
C ₃ N ⁺ + e ⁻	C ₂ + CN	0.56(0.05)	1	11.76	6.25
	C + [C ₂ N]	0.32(0.03)			5.16
	C ₃ + N	0.09(0.02)			5.79
	C + C + CN	0.03(0.02)			0.27

Table 10

Branching ratios (BR) following charge exchange reactions in collisions of CNC, CCN and C₃N with He⁺. E_a values give the internal energies of the adducts CNC⁺, CCN⁺ and C₃N⁺ after charge exchange and ΔE are the exothermicities of the reactions.

Reactants	Products (+ He)	Model BR (abs.err)	KIDA BR	E_a (eV)	ΔE (eV)
CNC + He ⁺	C ⁺ + C + N	0.30(0.15)		14.93	1.22
	C ⁺ + CN	0.25(0.10)			8.54
	CN ⁺ + C	0.25(0.07)			6.07
	C ₂ ⁺ + N	0.15(0.05)			6.69
	N ⁺ + C ₂	0.05(0.02)			3.91
CCN + He ⁺	C ⁺ + C + N	0		13.92	0.21
	C ⁺ + CN	0.38(0.05)	1		7.53
	CN ⁺ + C	0.38(0.05)			5.06
	C ₂ ⁺ + N	0.20(0.03)			5.68
	N ⁺ + C ₂	0.04(0.02)			2.9
C ₃ N + He ⁺	C ⁺ + C + CN	0.25(0.04)		12.81	1.9
	C ₃ ⁺ + N	0.18(0.04)			7.36
	[C ₂ N ⁺] + C	0.15(0.07)			8.29
	CN ⁺ + C ₂	0.14(0.03)			5.41
	C ₂ ⁺ + CN	0.12(0.06)	1		7.38
	C ⁺ + [C ₂ N]	0.09(0.05)			6.79
	N ⁺ + C ₃	0.03(0.01)			4.53
	C ⁺ + C ₂ + N	0.02(0.01)			0.56

compatible with spin and symmetry considerations. Then, symmetry considerations never precluded strictly the reaction to occur. We recommend to use the predicted branching ratios for these reactions identified with the * sign.

3.1. Neutral-neutral reactions

Reactions between neutral reactants leading to intermediate C₂N and C₃N adducts are reported in Table 7. In addition to the adduct internal energy E_a and reaction exothermicities ΔE , given in column 5 and 6 respectively, we present in column 3 semiempirical product branching ratios predicted by the model and in column 4 values found in the KIDA database.

Considering reaction with C₂ + N reactants we note that a single outgoing channel different from the entrance one, C + CN, is open so that the BR of this one has to be 1. For this reaction the adduct cannot be C₂N in the lowest energy isomer and in its electronic ground state for spin and symmetry reasons. According to our calculations of isomers, there exists an isomer having a ⁴A'(Cs) ground electronic state, situated 1.107 eV above the lowest energy one (CNC in the ²Π_g state), through which the reaction could occur. The complete pathway of this reaction has been recently elucidated (Loison et al. 2014b).

We consider next the CNC + C and CCN + C reactions because CCN + C is the reaction treated in KIDA. It is possible to treat different reactants isomers within the model since, depending on the isomer, we may get different E_a values and then different model predictions. By

contrast, because the experimental results of Section 2.2 are isomer unresolved, we have generally no access to the products isomers. Model predictions are identical between the two reactions and give C₂ + CN as very dominant, in accordance with KIDA. Prediction for C₃ + N is associated with a large error bar so that it is difficult to estimate the role of the barrier height of 0.4 eV in this reaction. Note that without barrier the model prediction for C₃ + N is 0.11 (0.03). Although a minor channel we may mention that the reaction leading to C₃ + N products cannot occur through the electronic ground state of the C₃N lowest energy isomer for spin and symmetry considerations. But the reaction can proceed through the ⁴A'(Cs) state of an excited C₃N isomer situated, according to our calculations, 3.90 eV above the lowest energy one. The C₃ + N → C₂ + CN reaction has not been reported in the Table 7 because this spin forbidden reaction is unlikely to occur due to the barrier of 0.4 eV preventing the addition of N to C₃.

3.2. Ion-molecule reactions

In Table 8 are reported model predictions for ion molecule reactions leading to intermediate C₂N⁺ and C₃N⁺ adducts. As mentioned before the isomer state of the products cannot be derived from the model; unresolved isomer product is indicated in brackets (for instance [C₂N⁺]). We note that, for a given couple of reactants, many outgoing channels with significant branching ratios are predicted by the model, at variance with KIDA where often one channel only, corresponding to the largest exothermicity, is supposed to be populated. This channel is sometimes corresponding to our main outgoing channel (case of CN⁺ + C reactants for instance) but sometimes not (cases of C₂ + N⁺ and CN⁺ + C₂ reactants). The C⁺ + CCN reaction is of interest because predictions for two products channels are reported in KIDA, based on the work of Loison et al. (2014a). In this work, DFT calculations showed no barrier for CCCN⁺ and CCNC⁺ formation. Calculated branching ratios are in good agreement with the model predictions for [C₂N⁺] + C and C₂⁺ + CN products. The reaction leading to C₃⁺ + N products, of rather small branching ratio (~10% as predicted by the model), is not considered in Loison et al. (2014a).

For a few cases in Table 8 (identified by the sign ¶), reaction from reactants in their electronic ground states towards products in their electronic ground states is spin forbidden. As explained before uncertainties on these reactions are completely included in the error bars.

As in the case of neutral-neutral reactions, the intermediate complex involved in the reaction could sometimes not be the adduct of Table 1. This concerned six channels, identified by the * sign. In all cases an adduct satisfying spin and symmetry considerations was found. Those adducts were : ³B₂(C2v), situated 2 eV above the adduct of Table 1, for the five first reactions stamped with * leading to a C₂N⁺ adduct ; ¹A'(Cs), situated 0.6 eV above the adduct of Table 1, for the last reaction stamped with * leading to a C₃N⁺ adduct.

3.3. Dissociative recombination (DR)

In Table 9 are reported branching ratios predictions following DR in electron – CNC⁺, electron – CCN⁺ and electron – C₃N⁺ collisions. The internal energy of the neutral adduct E_a has been taken equal to its ionization potential (IP), assuming that the DR process proceeds mainly with electron kinetic energy small as compared to IP (Mitchell, 2015).

Although the internal energy of the neutral adduct differs in CNC⁺ + e⁻ and CCN⁺ + e⁻ reactions, it is seen from Fig. 3 that both reactions lead to equal model predictions for BR. This is in agreement with estimations of Loison et al. (2014a) reported in KIDA. The model predicts a strong dominance of the C + CN products channel, as reported in KIDA.

For C₃N⁺ + e⁻, the main products are found to be C₂ + CN as predicted by the model and reported in KIDA. The role of the barrier along the C₃ + N outgoing channel is found rather small since, without barrier, the predicted BR is 0.07 (0.02). It is in any case a small

outgoing channel as compared to the $C + [C_2N]$ of near exothermicity. This last reaction has a BR far from being negligible and should then be considered in databases.

3.4. Charge exchange reactions with He^+

In Table 10 products of charge exchange between CNC, CCN, C_3N and He^+ are reported. As well known from ion-atom collisions, charge exchange at low velocity occurs between electronic states of equal energy (energy matching) (Olson, 1981). The same is found for ion-molecule collision as shown for instance in a recent investigation of the charge exchange reaction between He^+ and dimethyl ether (Cernuto et al. 2017). Helium, which has a large IP (24.6 eV), captures then an electron from an inner valence shell of the molecule, resulting in a large internal energy of the molecular ion $\Delta IP = IP(He) - IP(\text{molecule})$ (Chabot et al. 2010). The adducts of interest here are the excited molecular ions CNC^+ , CCN^+ and C_3N^+ after charge exchange and not the intermediate complexes $[C_2NHe^+]$ or $[C_3NHe^+]$ that are formed during the collision. Accordingly we have for those $E_a = \Delta IP$. We used our calculated IP of CNC, CCN and C_3N (equal to 9.66 eV, 10.67 eV and 11.76 eV respectively^{footnote 1}) in order to extract E_a values, reported in bold in column 5 of Table 10. Exothermicities of the reactions ΔE were calculated with Eq. (5) as before.

Due to the large internal energies of the molecular ions, fragmentation into three fragments is rather important, exception made of CCN^+ whose internal energy (13.92 eV) is close from the opening of the first three-fragment channel ($C^+ + C + N$ that requires 13.71 eV). That was already noted in C_n , C_nH and $C_3H_2 + He^+$ reactions (Chabot et al. 2013) whereas, from mass spectra and the abundance of HCO^+ , authors from (Cernuto et al. 2017) could estimate a very large contribution of channels with three or four fragments as well. Fragmentation along channels with three fragments has a large energetical cost. Accordingly the corresponding exothermicity of the reaction is rather small. This behavior is apparently non statistical. In fact within a pure statistical fragmentation process it is found that the system prefers to spend the internal energy for breaking chemical bonds (producing more fragments) rather than by dissipating the energy in fragment's internal energy or fragments kinetic energy (Diaz-Tendero et al. 2006). In that respect channels reported in KIDA as main products and corresponding to maximum exothermicities (two-fragments channels) are out of the game. The database should be updated for these charge exchange reactions.

4. Discussion about the astrophysical implications and conclusions

Using the Nautilus astrochemical model, we simulated the expected abundances of C_nN molecules in cold cores conditions. Nautilus is a gas-grain astrochemical model. Based on micro-physical parameters (such as rate coefficients for gas-phase reactions), this numerical model computes the species abundances in interstellar conditions as a function of time by solving a set of kinetic differential equations. The model includes a large number of chemical processes in the gas-phase. It also takes into account the interactions with the interstellar grains (adsorption on the surfaces and desorption from the surfaces) and the reactions at the surface of the grains (treated with the Langmuir–Hinselwood approach). The model is described in details in Ruaud et al. (2016) while the chemical parameters are described in Loison et al. (2017). For this work, the gas-phase network has been updated with the new branching ratios presented in this paper. We have run the model for typical cold core conditions, i.e. a gas and dust temperature of 10 K, a proton density of $2 \times 10^5 \text{ cm}^{-3}$, and a high visual extinction preventing any direct photochemistry. Fig. 4 presents

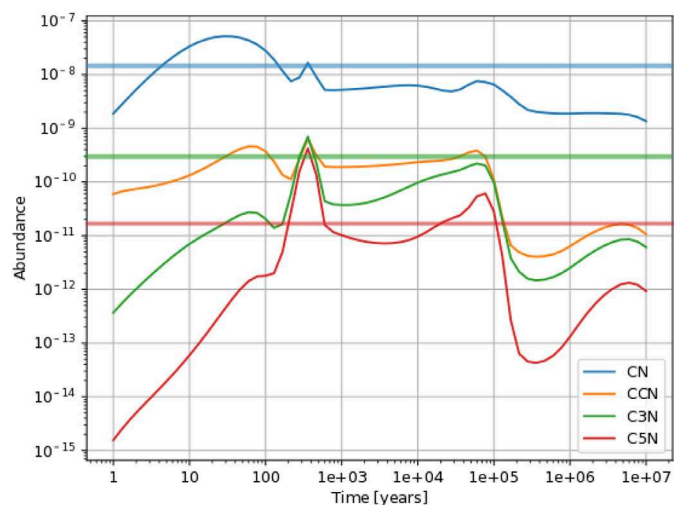


Fig. 4. Species abundances computed by our astrochemical model as a function of time for cold core conditions. The horizontal lines are the observed values in the cold core TMC-1 (Cyanopolymne Peak) (refs : Crutcher et al. 1984 for CN, Ohishi and Kaifu, 1998 for C_3N , Guélin et al. 1998 for C_5N).

the results of our simulations for CN, CCN, C_3N , and C_5N . In fact, under cold core conditions, the model results are not affected by the chemical updates. Indeed, species having an abundance of more than 10^{-12} (with respect to H) were modified by less than 5% at all times, which is not significant. One interesting point however is that the CCN predicted abundance is the same or higher as the ones of the two other detected species (i.e. C_3N and C_5N). This molecule has been detected in the circumstellar envelop of IRC + 10216 (Anderson and Ziurys, 2014) where the conditions are different from cold cores but, as far as we know, not in cold cores. We however could not find any published upper limits. In our model, CCN is formed by the dissociative recombination of CH_2CN^+ and CH_3CN^+ , and the neutral-neutral reaction $N + CCH \rightarrow H + CCN$. Note that errors on the predicted abundances of Fig. 4 may be important due to uncertainties on the rates of contributing processes. Their estimates would require an extensive work, that goes beyond the scope of this paper. On the other hand, observational constraints on CCN abundance in cold cores would be of great help to constrain the model.

In this paper, we have presented new branching ratios for a number of reactions involved in the chemistry of the interstellar molecules C_nN . Despite the fact that the new values do not significantly change the model results, they will be included in the KIDA databases and should be included in current astrochemical models. In fact, because of the non-linear behavior of these models, the importance of the reactions depends on the specific network used and the physical conditions (Wakelam et al. 2010).

Footnotes 1 : Recent measurements give 9.78 (0.04) eV and 10.82 (0.03) eV for CNC and CCN molecules respectively (Garcia et al. 2017).

Acknowledgements

VW research is funded by an ERC Starting Grant (3DICE, grant agreement 336474). The authors acknowledge the support of the CNRS program Physique et Chimie du Milieu Interstellaire (PCMI) co-funded by the Centre National d'Etudes Spatiales (CNES) and of the P2IO LabEx (ANR-10-LABX-0038) within the framework of the emblematic program «Evolution de la matière du milieu interstellaire aux exoplanètes avec le JWST». TL is funded by a fellowship of the Fonds pour la Formation à la Recherche dans l'Industrie et dans l'Agriculture-FRIA.

Appendix

In this appendix, we give in the Table A-1 the values of E_{diss} , E_{sat} , E_{disap} and E_{end} used for the construction of the G_j functions for all j channels of each molecule. These quantities are calculated or derived from theoretical work (see text).

Table A.1

Values of the E_{diss} , E_{sat} , E_{disap} and E_{end} quantities entering in the G_j functions for all channels j of each molecule.

Molecule	Channel j	E_{diss} (eV)	E_{sat} (eV)	E_{disap} (eV)	E_{end} (eV)
C ₂ N	C ₂ N	0	0.01	4.89	5.39
	CN + C	4.89	5.39	12.21	13.71
	C ₂ + N	6.23	6.73	12.21	13.71
	C + C + N	12.21	13.71	40	42.5
C ₃ N	C ₃ N	0	0.005	5.51	5.515
	C ₃ + N	5.97	6.47	12.82	14.32
	C ₂ + CN	5.51	6.01	11.49	12.99
	C ₂ N + C	6.6	7.1	11.49	12.99
	CN + C + C	11.49	12.99	18.82	21.32
	C ₂ + N + C	12.82	14.32	18.82	21.32
	N + C + C + C	18.82	21.32	40	42.5
C ₂ N ⁺	CN + C ⁺	6.39	6.89	13.71	15.21
	N + C ₂ ⁺	8.24	8.74	13.71	15.21
	C + CN ⁺	8.86	9.36	13.71	15.21
	C ₂ + N ⁺	11.02	11.52	17.01	18.51
	C + N + C ⁺	13.71	15.21	40	42.5
	C + N ⁺ + C	17.01	18.51	40	42.5
C ₃ N ⁺	C ₂ N ⁺ + C	4.52	4.57	10.91	12.41
	C ₃ ⁺ + N	5.45	5.95	12.25	13.75
	C ₂ ⁺ + CN	5.43	5.93	10.91	12.41
	C ⁺ + C ₂ N	6.02	6.52	10.91	12.41
	CN ⁺ + C ₂	7.4	7.9	12.25	13.75
	N ⁺ + C ₃	8.28	8.78	15.54	17.04
	C ⁺ + C + CN	10.91	12.41	18.23	20.73
	C ⁺ + C ₂ + N	12.25	13.75	18.23	20.73
	C ₂ ⁺ + N + C	12.76	14.26	18.23	20.73
	CN ⁺ + C + C	13.38	14.88	18.23	20.73
	N ⁺ + C ₂ + C	15.54	17.04	21.53	24.03
	C ⁺ + N + C + C	18.23	20.73	40	43.5
	N ⁺ + C + C + C	21.53	24.03	40	43.5

References

- Aguirre, et al., 2017. *J. Chem.Theory Comput.* 13, 992. <https://doi.org/10.1021/acs.jctc.6b00984>.
- Aguirre, et al. (2018) to be submitted.
- Anderson, Ziurys, 2014. <https://doi.org/10.1088/2041-8205/795/1/L1>.
- Cernuto, et al., 2017. <https://doi.org/10.1039/c7cp00827a>.
- Chabot, et al., 2002. *Nucl. Inst. Methods B* 197, 155.
- Chabot, et al., 2010. *A&A* 524, A39. <https://doi.org/10.1051/0004-6361/201015010>.
- Chabot, et al., 2011. *Rev. Sci. Instrum.* 82, 103301. <https://doi.org/10.1063/1.3640411>.
- Chabot, et al., 2013. *ApJ* 771, 90. <https://doi.org/10.1088/0004-637X/771/2/90>.
- Crutcher, et al., 1984. *ApJ* 283, 668. <https://doi.org/10.1086/162352>.
- Diaz-Tendero, et al., 2005. *PRA* 71, 033202. <https://doi.org/10.1103/PhysRevA.71.033302>.
- Diaz-Tendero, et al., 2006. *Int. J. Mass Spectrom.* 252, 126. <https://doi.org/10.1016/j.ijms.2005.12.055>.
- Ding, et al., 1998. *Chem. Phys. Lett.* 284, 325. [https://doi.org/10.1016/S0009-2614\(97\)01424-3](https://doi.org/10.1016/S0009-2614(97)01424-3).
- Dutuit, et al., 2013. *ApJS* 204, 20. <https://doi.org/10.1088/0067-0049/204/2/20>.
- Friberg, et al., 1980. *ApJ* 241, L99. <https://doi.org/10.1086/183369>.
- Gans, et al., 2011. (2011) *PCCP* 13 (18), 8053. n. <https://doi.org/10.1039/c0cp02627a>.
- Garcia, et al., 2017. *JCP* 147, 013908. <https://doi.org/10.1063/1.4978336>.
- Guélin, et al., 1998. *A&A* 335, L1.
- Herbst, 1978. *ApJ* 222, 508. <https://doi.org/10.1086/156163>.
- Kirchner, et al., 2000. *PRA* 61, 052710. <https://doi.org/10.1103/PhysRevA.61.052710>.
- Launoy, et al., 2017. *Phys. Rev. A* 95, 022711 and references therein. <https://doi.org/10.1103/PhysRevA.95.022711>.
- Loison, et al., 2014a. *MNRAS* 437, 930. <https://doi.org/10.1093/mnras/stt1956>.
- Loison, et al., 2014b. *PCCP* 16, 14212. <https://doi.org/10.1039/c4cp01801j>.
- Loison, et al., 2017. *MNRAS* 470, 4075. <https://doi.org/10.1093/mnras/stx1265>.
- Maclean, et al., 2007. *J. Phys. Chem. A* 111, 2932. <https://doi.org/10.1021/jp076315j>.
- Mahajan et al. (2018) to be published.
- Martinet, et al., 2004. *PRL* 93, 063401. <https://doi.org/10.1103/PhysRevLett.93.063401>.
- Mitchell, 2015. *J. Phys. Conf. Series* 576, 012006. <https://doi.org/10.1088/1742-6596/576/1/012006>.
- Mezdari, PHD thesis, University Paris VI, 2005 (unpublished).
- Ohishi, Kaifu, 1998. *Faraday Discuss* 109, 205. <https://doi.org/10.1039/a801058g>.
- Olson, 1981. *Phys. Rev. A* 24 (4), 1726.
- Ruaud, et al., 2016. *MNRAS* 459, 3756. <https://doi.org/10.1093/mnras/stw887>.
- Sadlej, Roos, 1991. *Chem. Phys. Lett.* 180 (1,2), 81 n.
- Sanchez, et al., 2016. *J. Phys. Chem. A* 120, 588. <https://doi.org/10.1021/acs.jpca.5b10143>.
- Schwarz, 2004. *Int. J. Mass Spectrom.* 237, 75. <https://doi.org/10.1016/j.ijms.2004.06.006>.
- Smith and Loison (2011) <http://kida.obs.u-bordeaux1.fr/datasheet/datasheet142N+C3V3.pdf>.
- Vekey, 1996. *Int. J. Mass Spectrom.* 31, 445.
- Wakelam, et al., 2010. *Space Sci. Rev.* 156, 13. <https://doi.org/10.1007/s11214-010-9712-5>.
- Wakelam, et al., 2012. *APJS* 199, 21. <https://doi.org/10.1088/0067-0049/199/1/21>.
- Wakelam, et al., 2015. *APJS* 217, 20. <https://doi.org/10.1088/0067-0049/217/2/20>.
- Wohrer, et al., 2000. *J. Phys. B* 33, 4469. <https://doi.org/10.1088/0953-4075/33/20/319>.
- Zhang, et al., 2014. *Theor. Chem. Acc.* 133, 1420. <https://doi.org/10.1007/s00214-013-1420-2>.

Chapter 7

Conclusion

In conclusion we studied collisions between C_nN^+ projectiles ($n=0,1,2,3$) and He atoms in the intermediate velocity regime ($v=2.25$ a.u), focusing on both the collisional aspect (cross sections for various electronic processes) and molecular relaxation (fragmentation) aspect. In addition, some application of these experiments to astrochemistry was performed.

The experimental tools have been described in chapter 1 and 2: The Tandem accelerator of Orsay was used to provide the molecular ions at the given velocity. A dedicated setup, AGAT, was used to perform and analyse the collision, in particular through the recording of all projectile fragments of known charge and mass including negative, neutral and positively charged ones. In chapter 2 were described the analyzing tools for identification, counting, background subtraction, normalization and extraction of absolute cross sections and absolute dissociation branching ratios.

Chapter 3 was devoted to the collision modeling, using the IAE/CTMC model based on a representation of the molecule in terms of independent atoms and using the independent electron approximation. For this, extensive calculations of impact parameter probabilities for electronic processes in C, C^+ , N, N^+ -He collisions were performed within the classical CTMC approach and presented. This included (target and projectile) ionization, electron capture and projectile excitation in (n,l) states. Comparison between measured and CTMC cross sections in these systems showed a reasonable agreement, validating its use in the IAE calculation, with the exception of

double electron capture giving rise to anionic C^- .

In chapter 4, experimental cross sections for projectile ionization, dissociative excitation, projectile neutralization and projectile anionic production cross sections were presented and compared to predictions of the IAE/CTMC model. A good agreement was generally observed, which is notable as no adjustment parameter exists in the calculation, apart from the basic approximations. On the other hand, as is the case for C^- , anionic production cross sections were grossly overestimated by the model.

In chapter 5 dissociation branching ratios of excited C_nN^{q+} species ($q = -1, 0, 1, 2, 3, 4$) were presented and discussed. Branching ratios in number of fragments were used to estimate the internal energy distribution (simulated with two half gaussians) for the case of C_nN and C_nN^+ species, using theoretical dissociation energies. In the C_nN^+ case, the distributions were compared to predictions of the IAE/CTMC model, using the CTMC probabilities for excitation into (n, l) states and the energy levels of excited C, C^+ , N atoms (ion) from the NIST. A good agreement was observed, furnishing a qualitative interpretation for the internal energy of C_nN^+ molecules following electronic excitation and measured dissociation branching ratios.

Chapter 6 (paper to appear in "Molecular Astrophysics") is describing some application of our experiments to astrochemistry, namely, the construction of breakdown curves (energy dependent dissociation branching ratios curves) for C_2N , C_3N , C_2N^+ and C_3N^+ molecules and their use for predictions of products branching ratios of some physical and chemical processes involving these excited adducts. This included some neutral-neutral reactions, ion-molecule reactions, dissociative recombination and electron transfer in collisions with He^+ processes. For those, recommendations for new products branching ratios to include in databases, in particular the KIDA database, were done. Nevertheless, inclusion of the new products branching ratios in a cold core astrochemical model did not change the model predictions significantly.

In the future various aspects should be investigated. From the collisional point of view, understanding the disagreement between experiment and model for anionic production cross section is an important point. This would require experimental

(check if some electron is lost before or during the pass through the electrostatic analyser) and theoretical (two active electron calculation) works. Also, it would be interesting to introduce the molecular character of the projectile, for instance by doing CTMC calculations with a multi-center potential. From the fragmentation point of view, we expect our measurements to be soon compared to calculations performed within the statistical fragmentation model M3C (Aguirre et al., 2017). Also, we measured all branching ratios for Ion Pair Dissociation of C_nN^{q+} species ($q=0,1,2,3$), not yet interpreted.

From the astrochemical point of view it would be interesting to construct BDC for more strategic molecules for which the potential impact on interstellar chemistry has been demonstrated. Thanks to the development of a versatile new source of cations at the terminal of the Tandem accelerator in Orsay, we should be able to work on more pertinent candidates in the future.

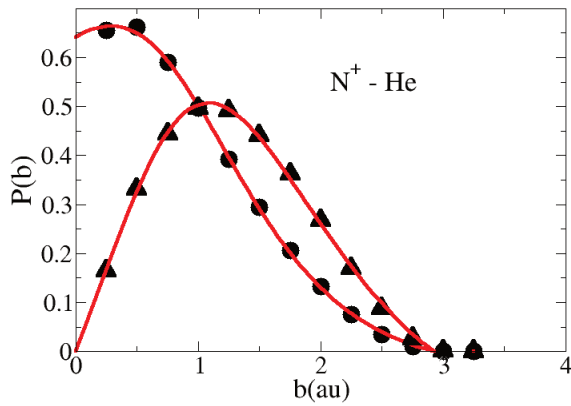
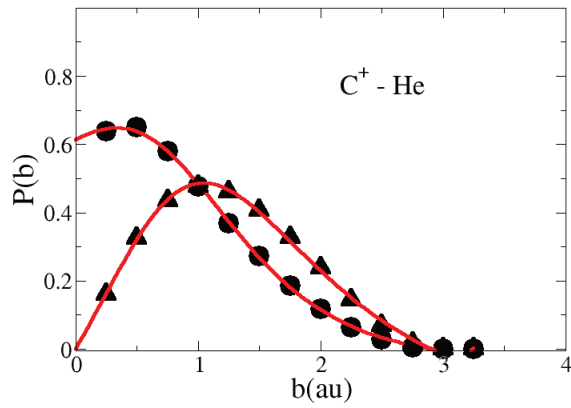
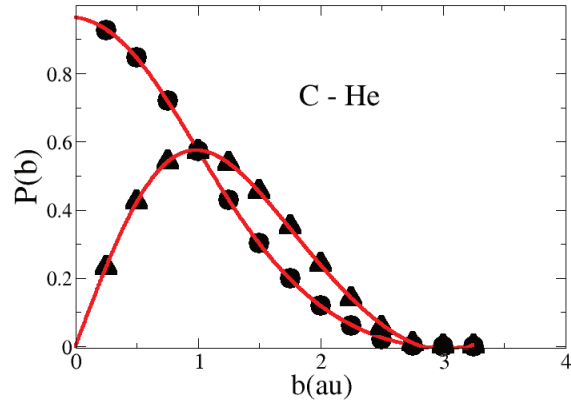
Appendix A

CTMC probabilities in C , C^+ , N , N^+ , - He collisions ($v=2.25$ a.u)

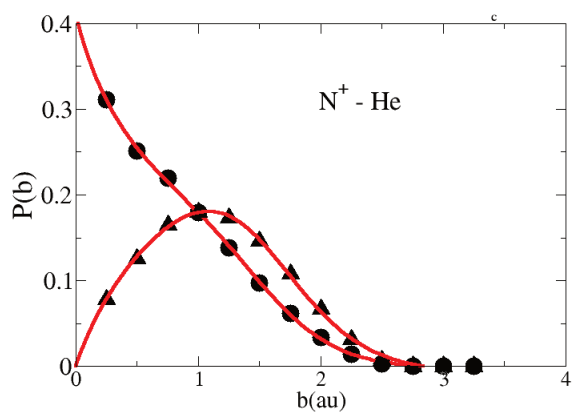
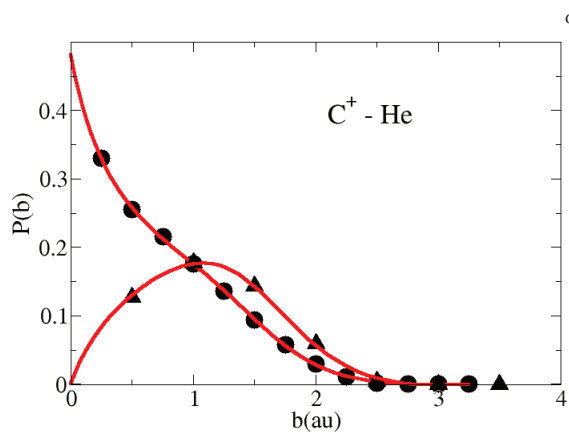
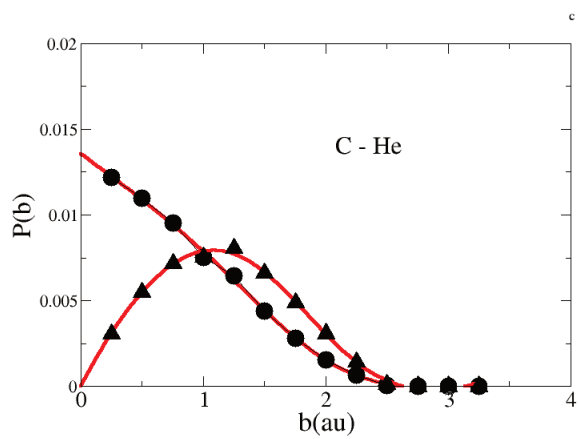
In this appendix, we present the CTMC probabilities used in the IAE model for extracting cross sections of Chapter 4. All probabilities are given by electron. On the same figure $bP(b)$ is also reported. In red are presented analytical fits used in the code.

A.1 $1e^-$ calculation

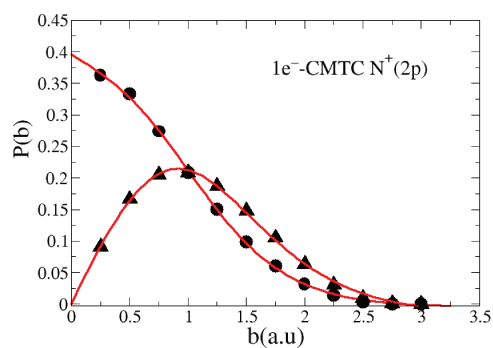
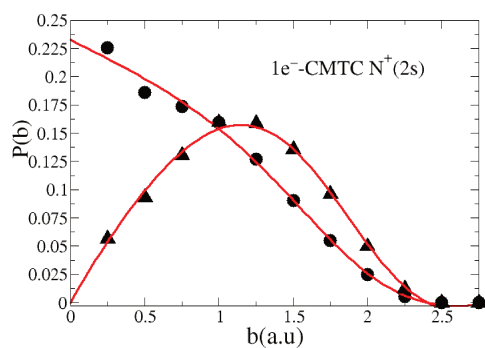
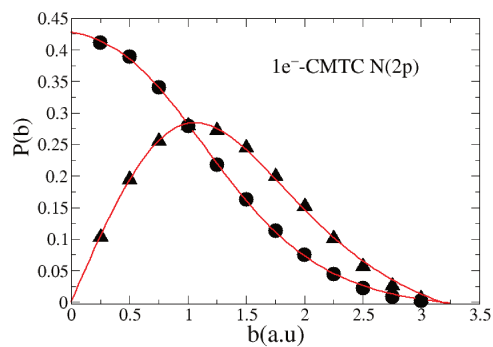
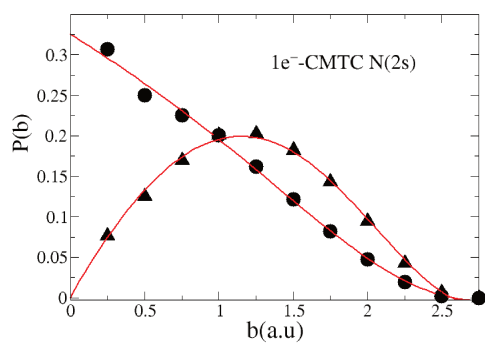
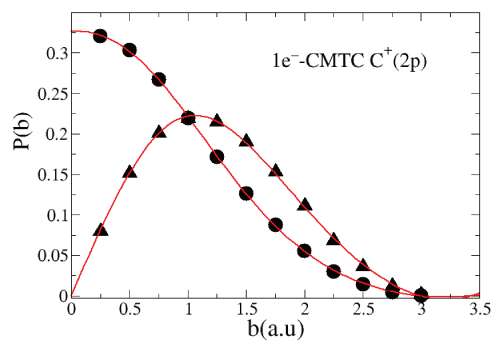
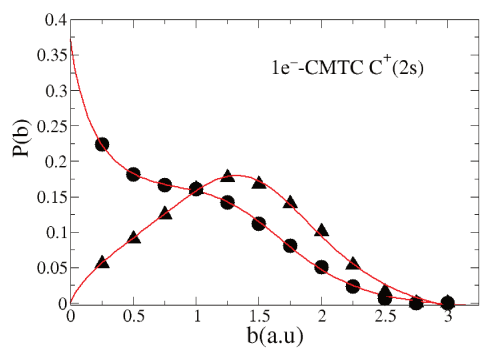
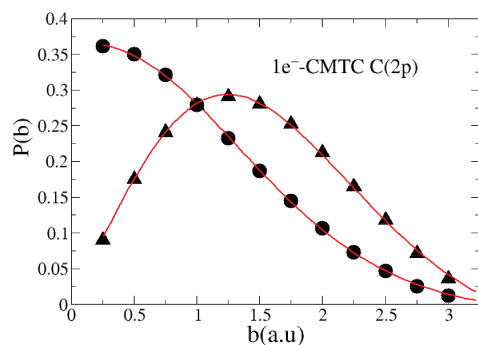
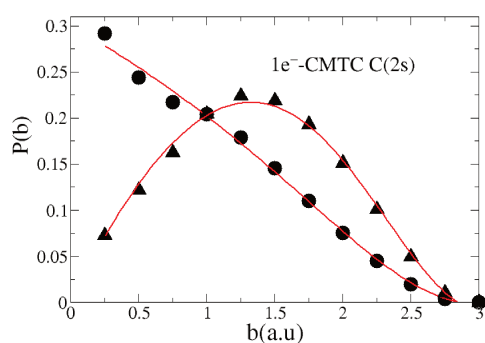
A.1.1 Target ionization



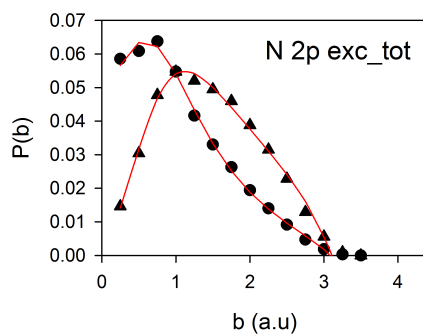
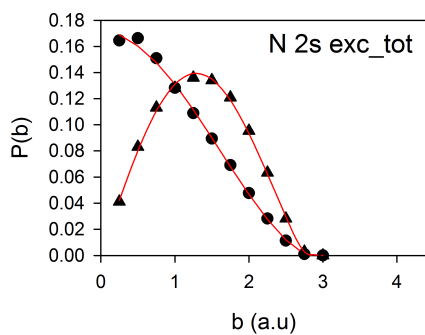
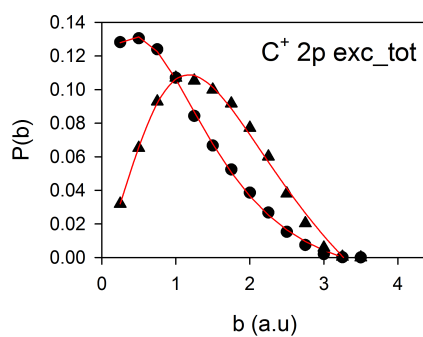
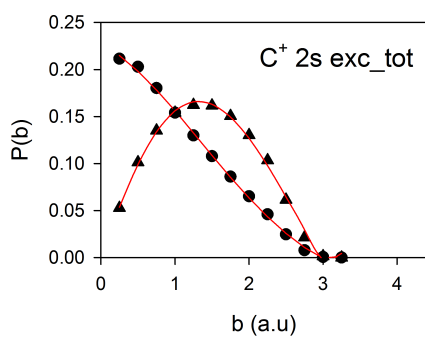
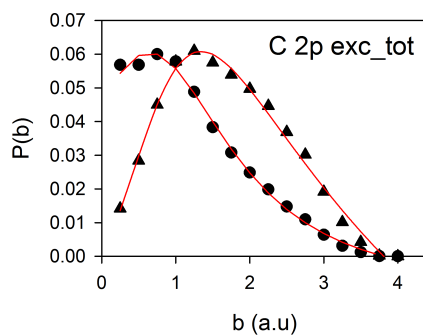
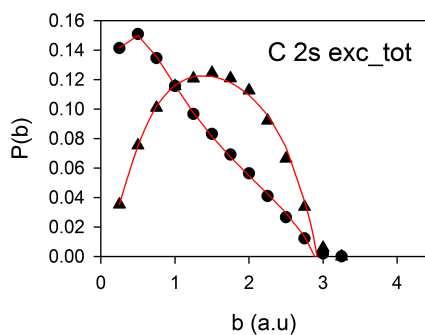
A.1.2 Electron capture and attachment.



A.1.3 Projectile ionization ($V1, \alpha \neq 0$)

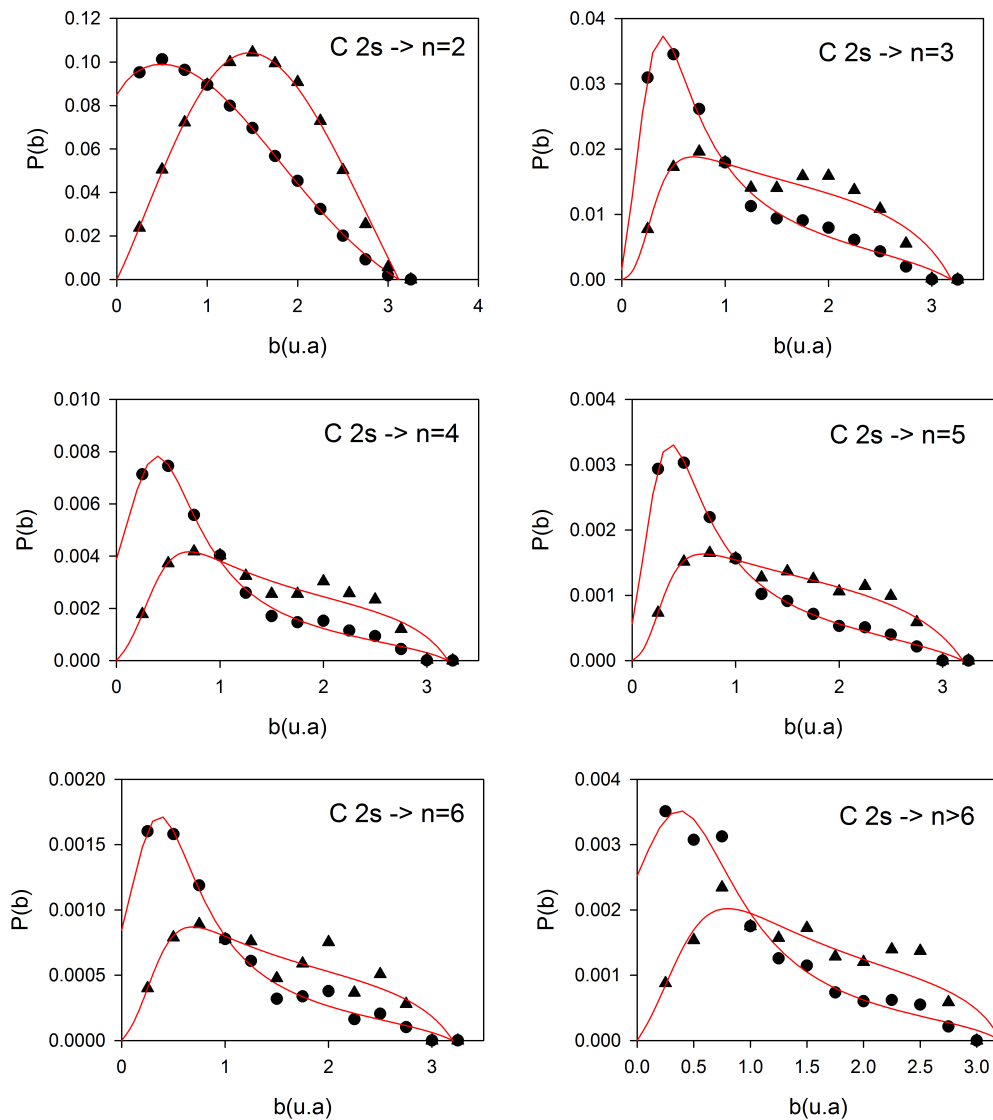


A.1.4 Projectile excitation total ($V1, \alpha \neq 0$)

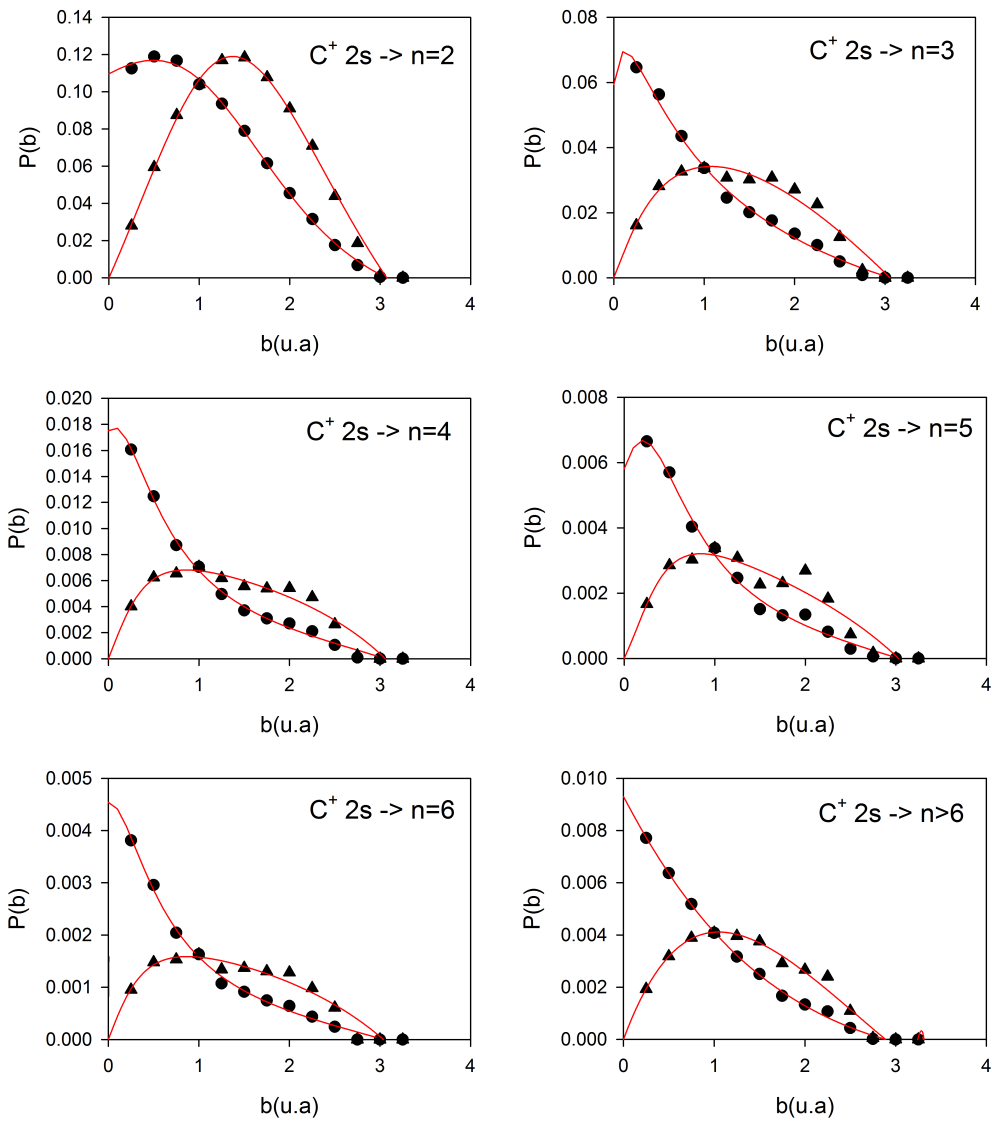


A.1.5 Projectile excitation into final (n, l) states $V1, \alpha \neq 0$

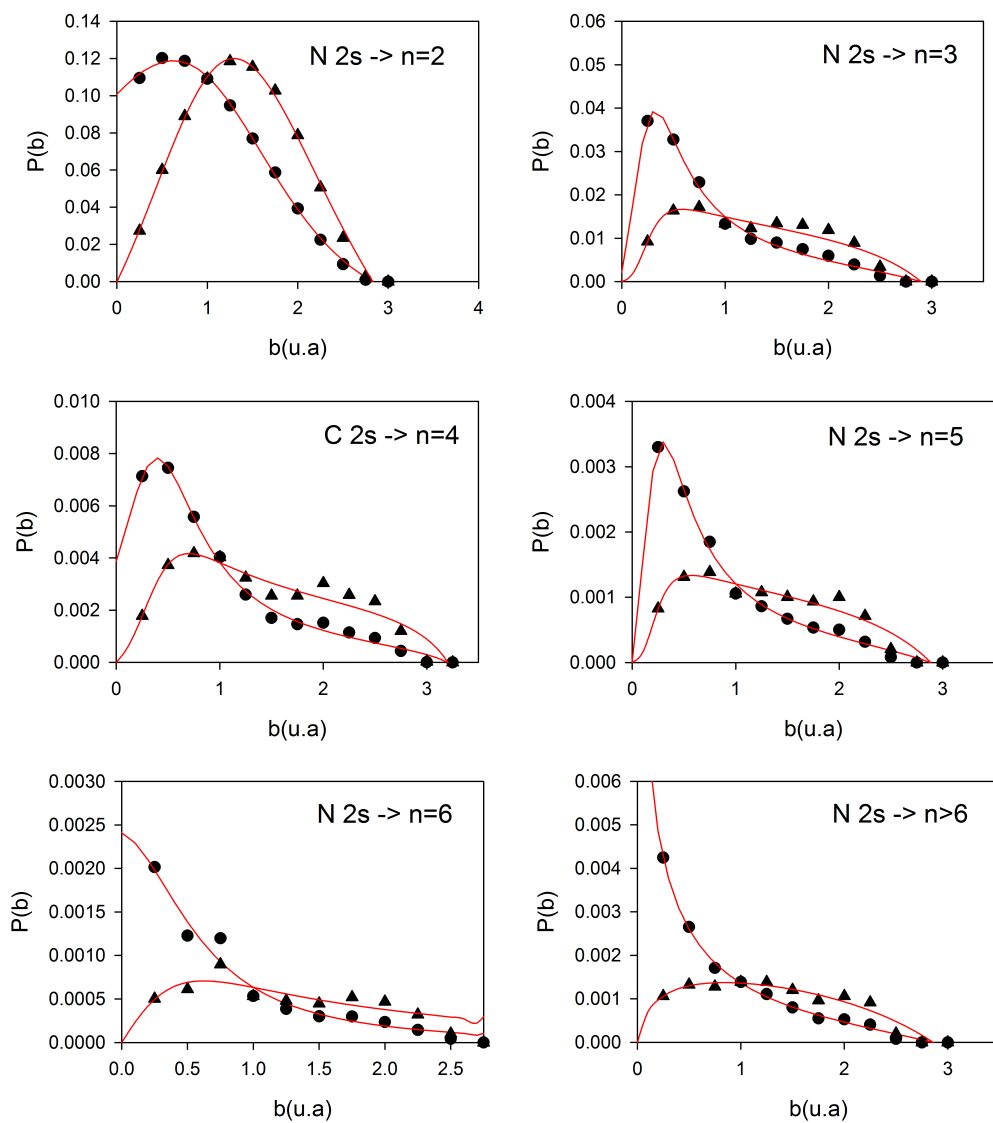
A.1.5.1 $C2s$ excitation into final n levels, $1e^-$ calculation ($V1, \alpha \neq 0$)



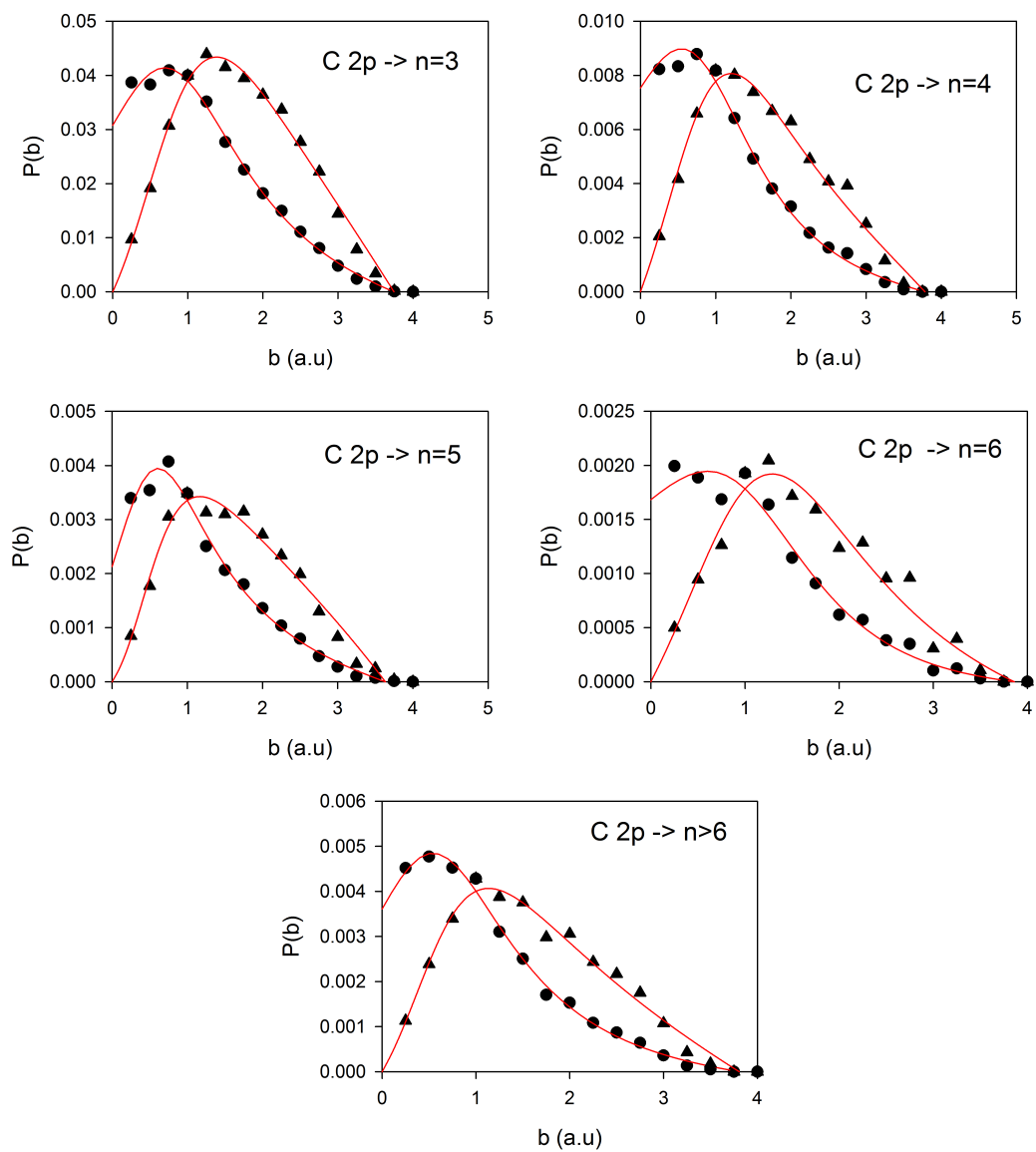
A.1.5.2 $C^+ 2s$ excitation into final n levels, $1e^-$ calculation ($V1, \alpha \neq 0$)



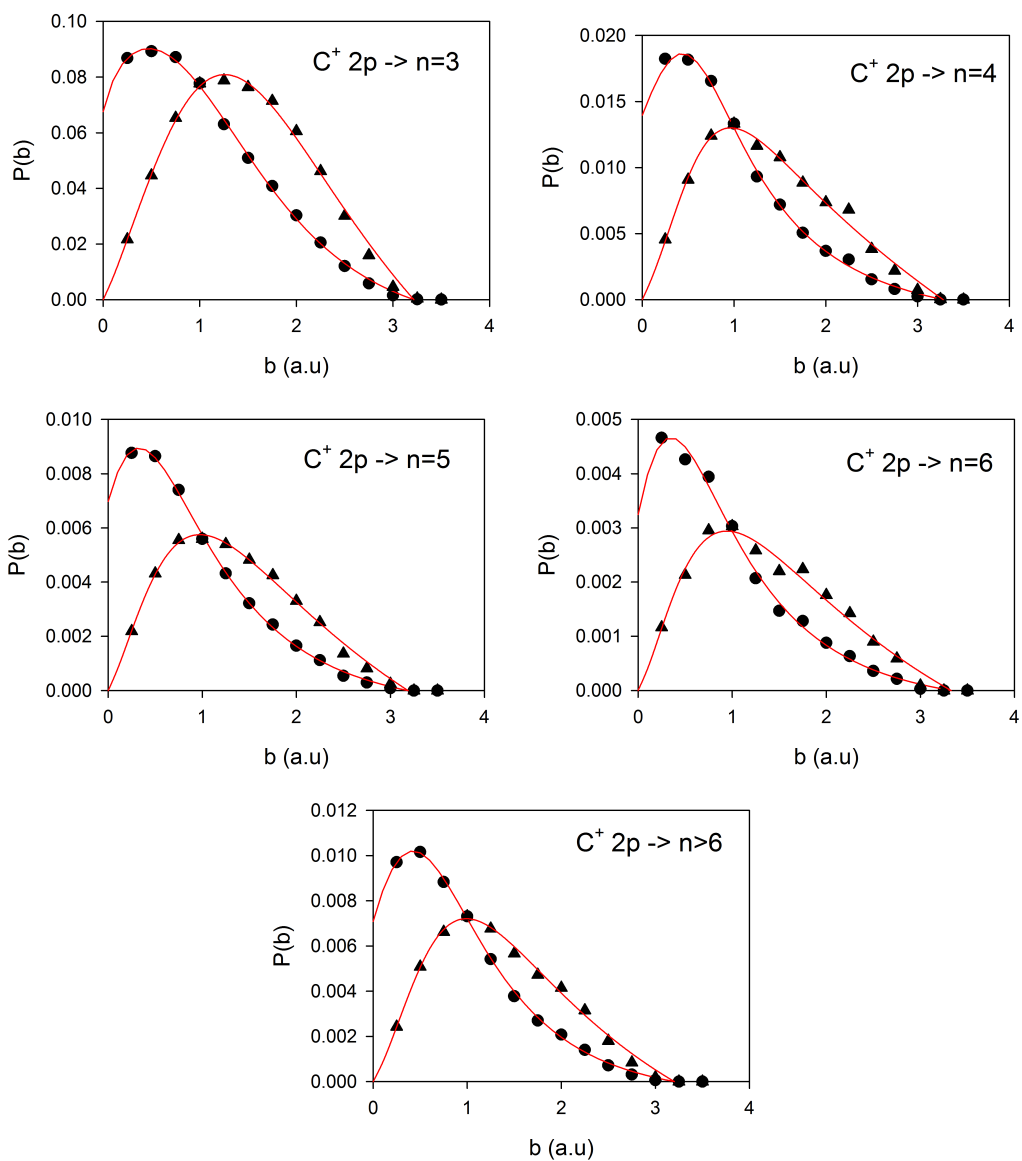
A.1.5.3 N2s excitation into final n levels, $1e^-$ calculation ($V1, \alpha \neq 0$)



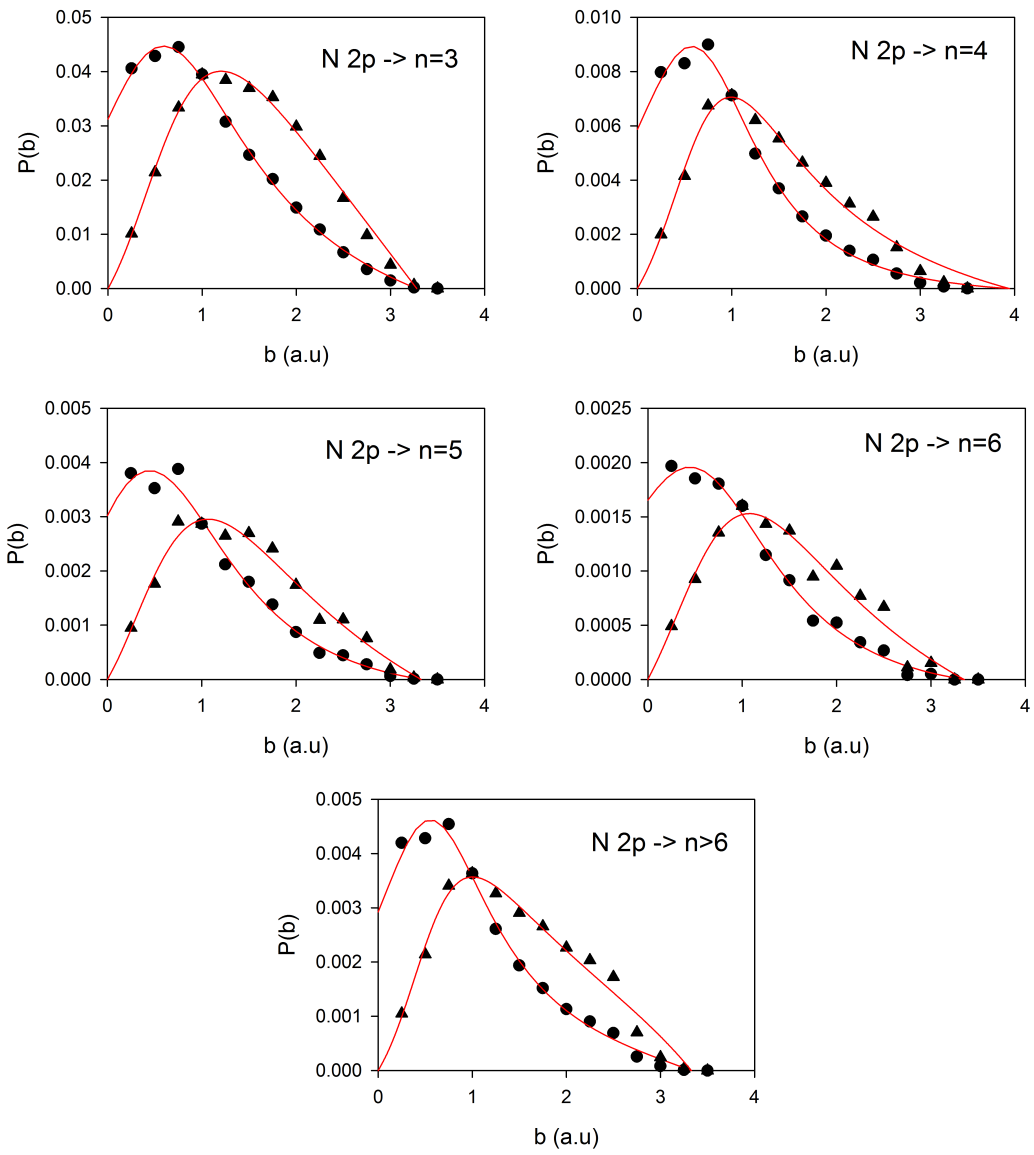
A.1.5.4 C2p excitation into final n levels, $1e^-$ calculation ($V1, \alpha \neq 0$)



A.1.5.5 $C^+ 2p$ excitation into final n levels, $1e^-$ calculation (V1, $\alpha \neq 0$)

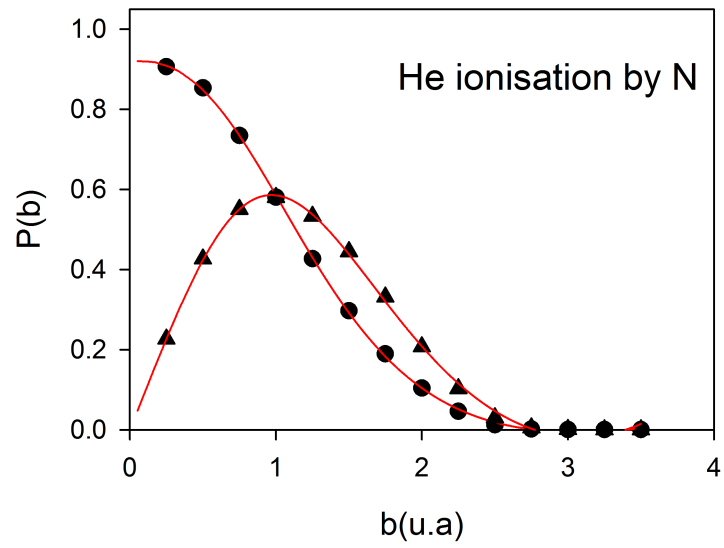


A.1.5.6 N2p excitation into final n levels, $1e^-$ calculation (V1, $\alpha \neq 0$)

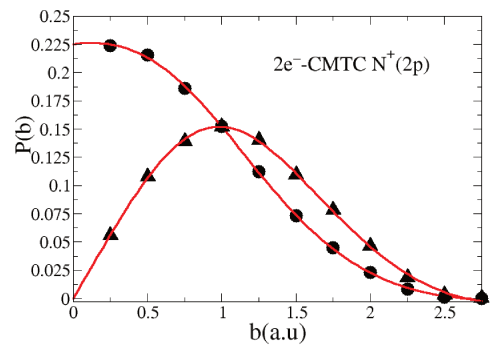
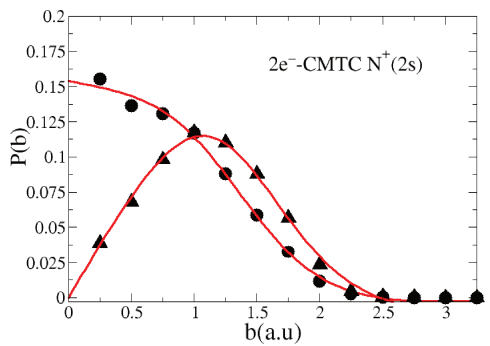
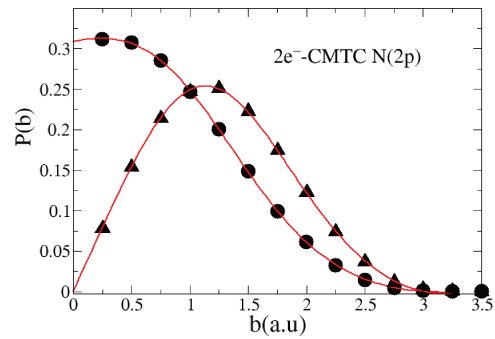
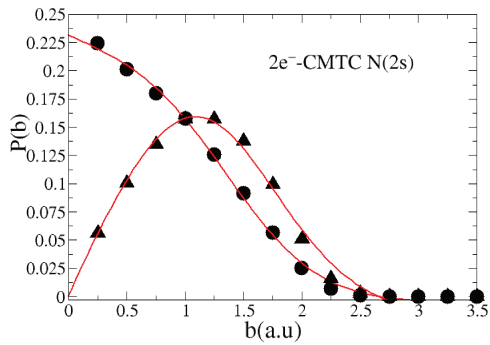
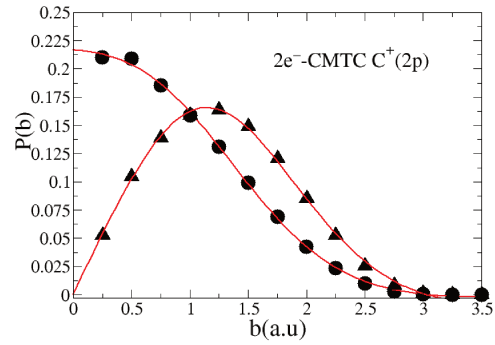
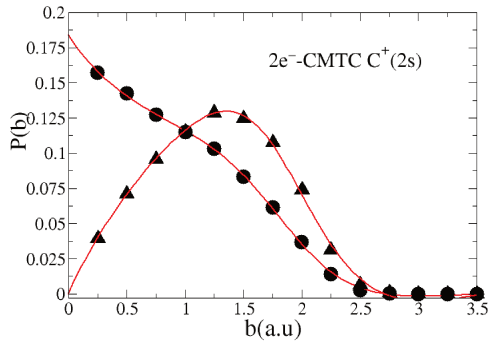
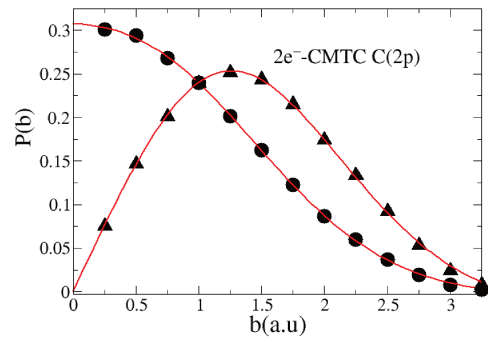
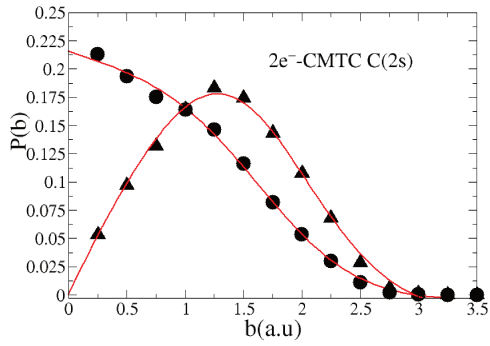


A.2 $2e^-$ calculation

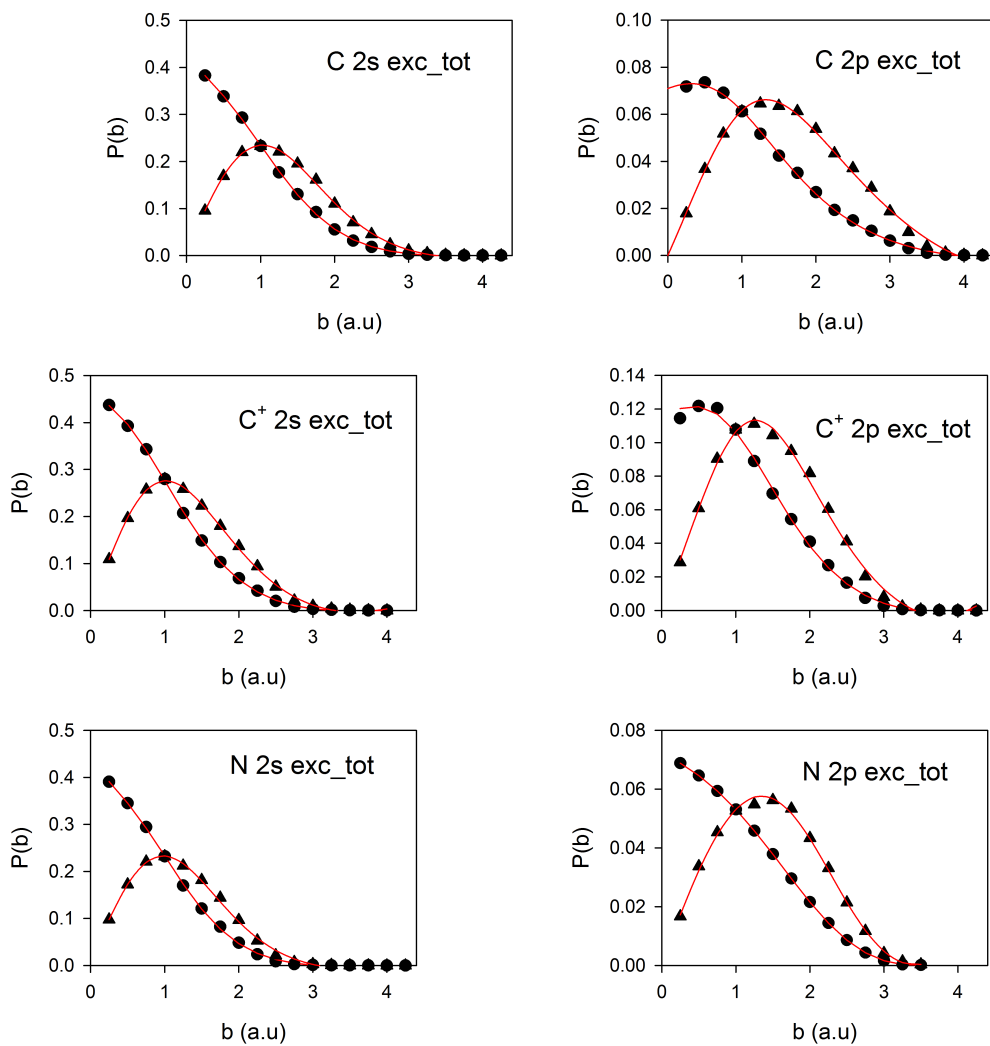
A.2.1 Target ionization



A.2.2 Projectile ionization

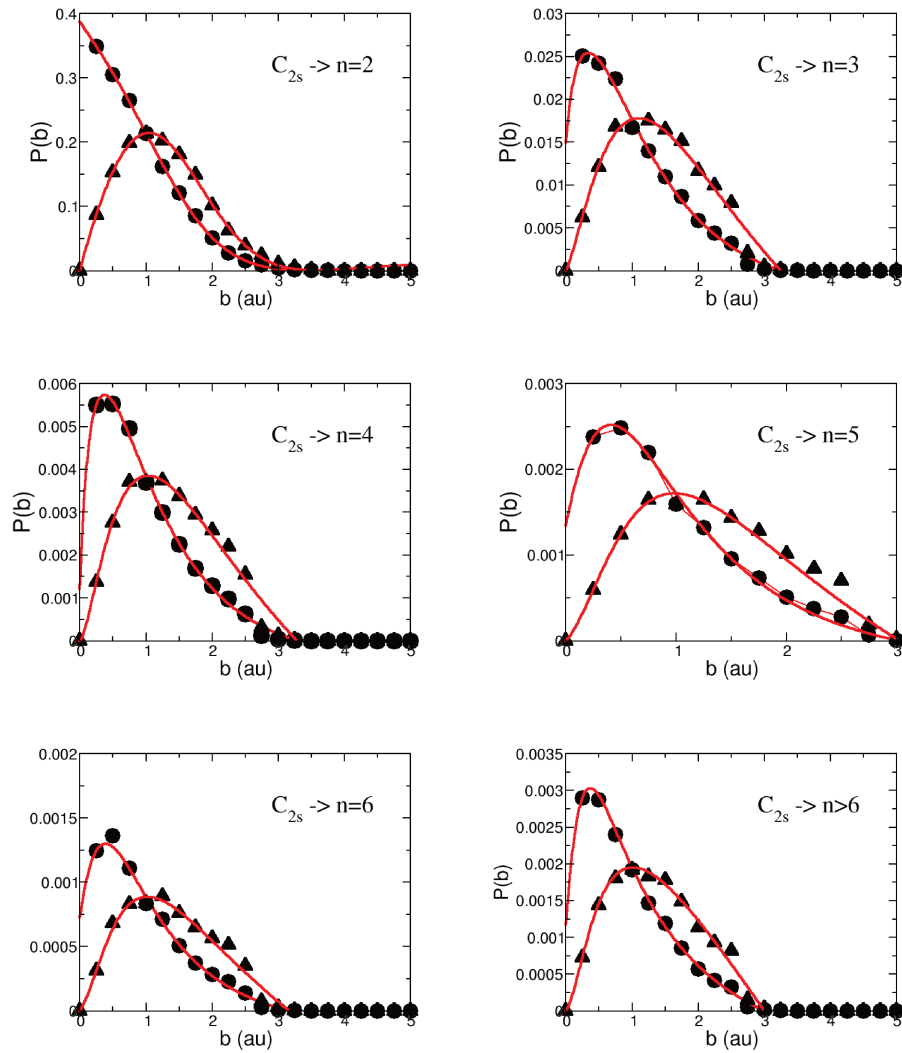


A.2.3 Projectile excitation total

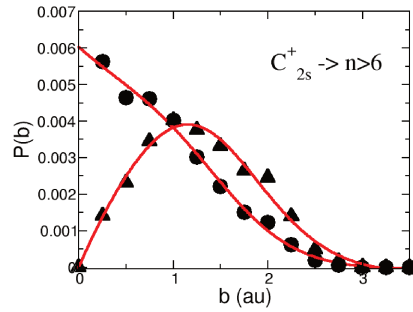
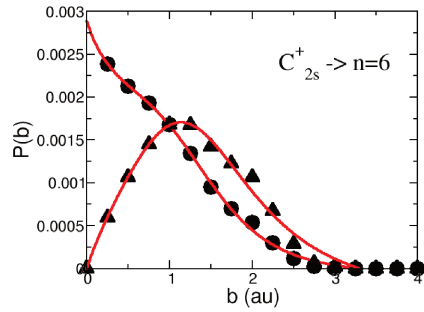
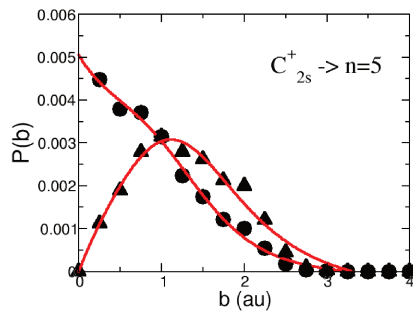
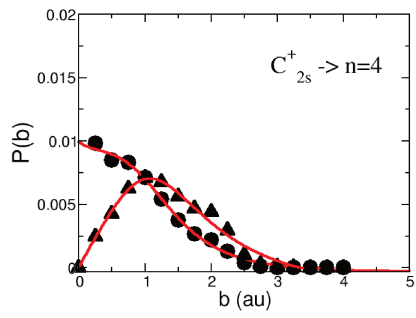
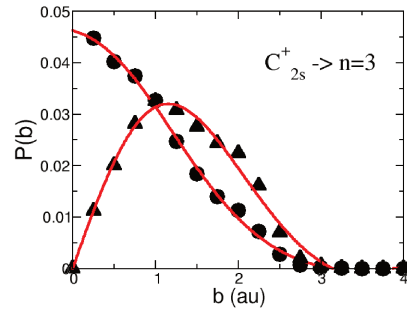
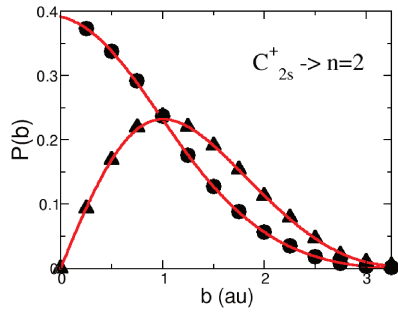


A.2.4 Projectile excitation into final (n, l) states

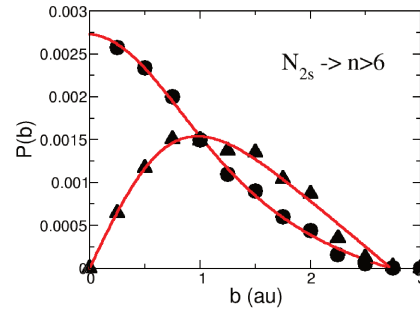
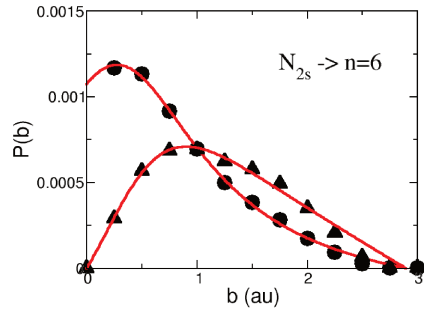
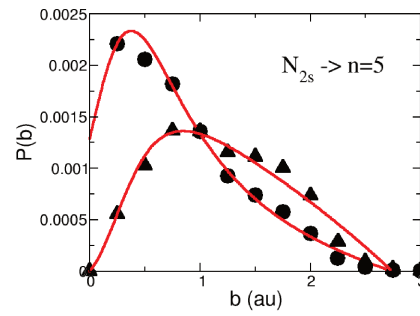
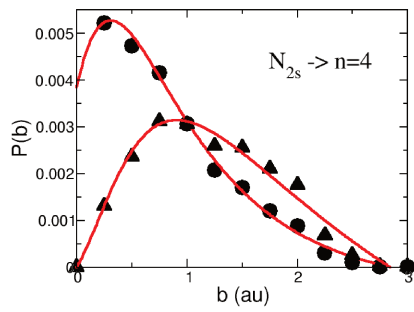
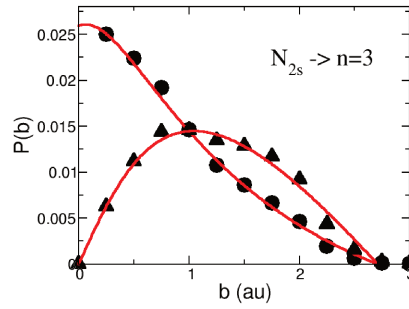
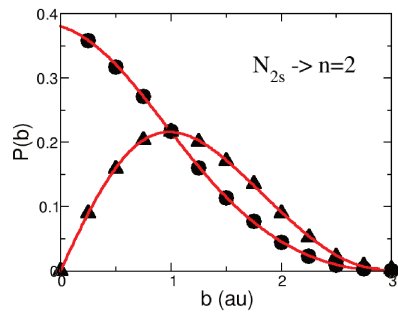
A.2.4.1 C_{2s} excitation into final n levels, $2e^-$ calculation



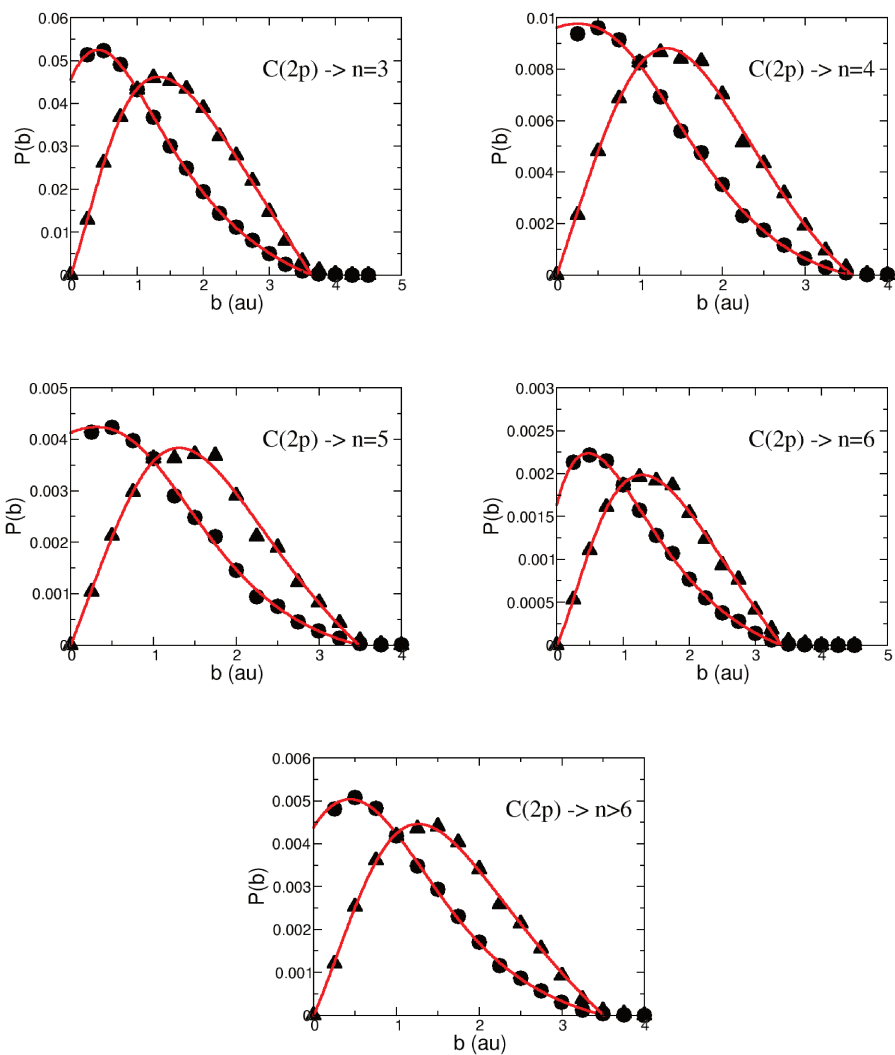
A.2.4.2 C^+2s excitation into final n levels, $2e^-$ calculation



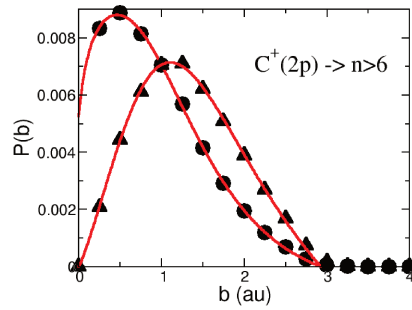
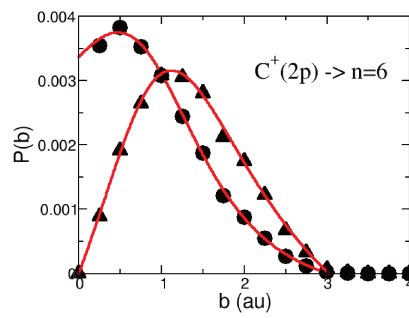
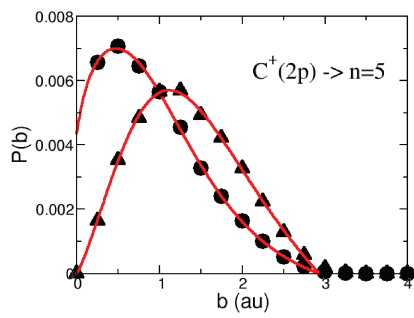
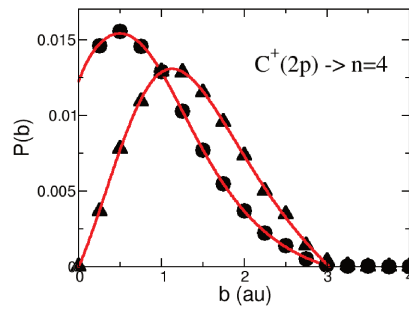
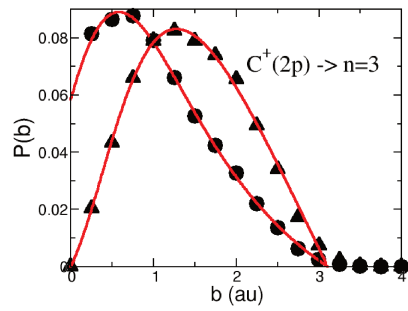
A.2.4.3 N_{2s} excitation into final n levels, $2e^-$ calculation



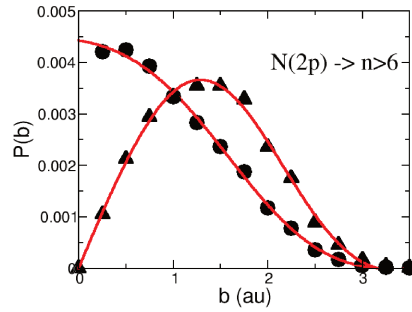
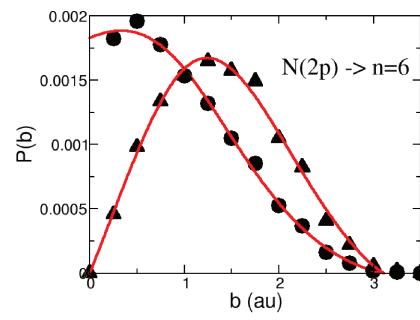
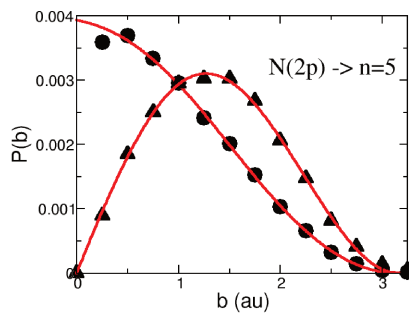
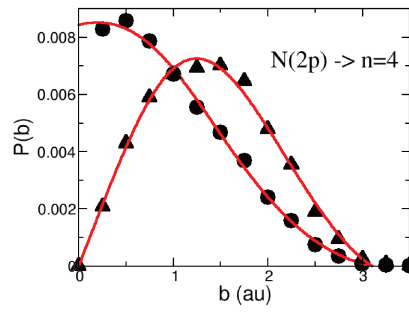
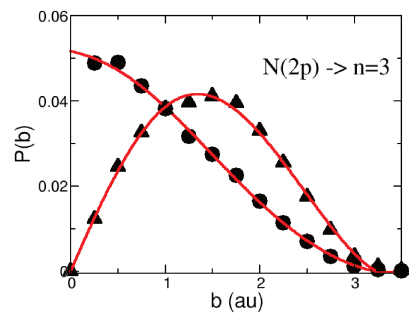
A.2.4.4 C2p excitation into final n levels, $2e^-$ calculation



A.2.4.5 C^+2p excitation into final n levels, $2e^-$ calculation



A.2.4.6 N2p excitation into final n levels, $2e^-$ calculation



Appendix B

Ion pair dissociation (IPD) branching ratios

B.1 Relaxation by IPD of $\{CN^{Q+}\}$ species (Q=0,1)

IPD dissociation of CN gives C^-/N^+ only. The BR with respect to total dissociation of CN is 1.8×10^{-4} (0.9×10^{-4}). The required energy of CN is 20.6 eV.

IPD dissociation of CN^+ gives C^-/N^{++} only. The BR with respect to total dissociation of CN^+ is 1.1×10^{-5} (0.7×10^{-5}). The required energy of CN^+ is 36.5 eV.

B.2 Relaxation by IPD of $\{C_2N^{Q+}\}$ species ($Q=0,1,2,3$)

Channel	Experimental BR (abs. err)	Required energy of C_2N (eV)
$CN^- + C^+$	0.77(0.22)	12.3
$C^- + C + N^+$	0.08(0.07)	25.5
$C^- + CN^+$	≤ 0.08	17.3
$C^- + N + C^+$	≤ 0.12	22.2
$C_2^- + N^+$	0.04(0.004)	17.5

Table B.1: Measured branching ratios within ion pair dissociation of C_2N excited species. For IPD branching ratios within $Q=0$ total dissociation, multiply all values by $6.1e-4$ ($3e-4$).

Channel	Experimental BR (abs. err)	Required energy of C_2N^+ (eV)
$C^- + \{CN^{++}\}$	0.96(-0.06/+0.04)	27.01/31.4*
$C^- + C + N^{++}$	0.018 (0.002)	45.3
$CN^- + C^{++}$	0.016 (0.015)	26.9
$C^- + N + C^{++}$	≤ 0.008	36.8

Table B.2: Measured branching ratios within ion pair dissociation of C_2N^+ excited species. For IPD branching ratios within $Q=1$ total dissociation, multiply all values by $1.6e-4$ ($0.3e-4$). * the energetical cost is 27.01 eV for $C^- + C^+ + N^+$ and 31.4 eV for $C^- + CN^{++}$

Channel	Experimental BR (abs. err)	Required energy of C_2N^{++} (eV)
$C^- + N^+ + C^{++}$	0.73(0.27)	29.2
$C^- + C^+ + N^{++}$	0.27(0.27)	35.4

Table B.3: Measured branching ratios within ion pair dissociation of C_2N^{++} excited species. For IPD branching ratios within $Q=2$ total dissociation, multiply all values by $1e-5$ ($0.5e-5$).

Channel	Experimental BR (abs. err)
$C^- + N^{++} + C^{++}$	1(0)

Table B.4: Measured branching ratios within ion pair dissociation of C_2N^{+++} excited species. For IPD branching ratios within $Q=3$ total dissociation, multiply all values by $2.3e-6$ ($1.2e-6$).

B.3 Relaxation by IPD of $\{C_3N^{Q+}\}$ species ($Q=0,1,2,3$)

Channel	Experimental BR (abs. err)	Required energy of C_3N (eV)
$CN^- + C + C^+$	0.27(0.01)	18.81
$C^- + C + N + C^+$	0.19(0.08)	28.74
$C_2^- + N + C^+$	0.12(0.01)	20.73
$C_2^- + C + N^+$	0.03(0.02)	24.02
$C^- + C_2N^+$	≤ 0.27	15.0
$C^- + CN + C^+$	≤ 0.19	21.41
$C^- + C + CN^+$	≤ 0.11	23.88
$C^- + N + C_2^+$	≤ 0.10	23.24
$C^- + 2C + N^+$	≤ 0.10	32.03
$CN^- + C_2^+$	≤ 0.01	13.33

Table B.5: Measured branching ratios within ion pair dissociation of C_3N excited species. For IPD branching ratios within $Q=0$ total dissociation, multiply all values by $2.1e-4$ ($1.2e-4$).

Channel	Experimental BR (abs. err)	Required energy of C_3N^+ (eV)
$C^- + C + C^+ + N^+$	0.40(0.07)	31.4
$C^- + N + 2C^+$	0.28(0.07)	28.1
$C_2^- + C^+ + N^+$	0.15(0.02)	23.4
$CN^- + 2C^+$	0.08(0.03)	18.2
$C^- + C_2^+ + N^+$	0.05(0.01)	26.0
$C^- + C^+ + CN^+$	≤ 0.08	23.3

Table B.6: Measured branching ratios within ion pair dissociation of C_3N^+ excited species. For IPD branching ratios within $Q=1$ total dissociation, multiply all values by $2.2e-4$ ($0.7e-4$).

Channel	Experimental BR (abs. err)	Required energy of C_3N^{++} (eV)
$C^- + 2C^+ + N^+$	0.96(0.03)	23.9
$C^- + N + C^+ + C^{++}$	0.02(0.01)	33.8
$C^- + C + C^+ + N^{++}$	0.01(6e-3)	42.3
$C^- + C + N^+ + C^{++}$	≤ 0.01	37.1

Table B.7: Measured branching ratios within ion pair dissociation of C_3N^{++} excited species. For IPD branching ratios within $Q=2$ total dissociation, multiply all values by $1.2e-4$ ($0.2e-4$).

Channel	Experimental BR (abs. err)
$C^- + C^+ + N^+ + C^{++}$	0.84(0.20)
$C^- + 2C^+ + N^{++}$	0.16(0.14)

Table B.8: Measured branching ratios within ion pair dissociation of C_3N^{+++} excited species. For IPD branching ratios within $Q=3$ total dissociation, multiply all values by $5.8e-5$ ($2.6e-5$).

Bibliography

- Abrines, R. and Percival, I. C. (1966). Classical theory of charge transfer and ionization of hydrogen atoms by protons. *Proceedings of the Physical Society*, 88(4):861, doi:10.1088/0370-1328/88/4/306.
- Adoui, L., Caraby, C., Cassimi, A., Lelièvre, D., Grandin, J. P., and Dubois, A. (1999). Fast ion-induced CO molecule fragmentation in the strong interaction regime. *Journal of Physics B: Atomic, Molecular and Optical Physics*, 32(3):631, doi:10.1088/0953-4075/32/3/008.
- Aguirre, N. F., Díaz-Tendero, S., Hervieux, P.-A., Alcamí, M., and Martín, F. (2017). M3C: A computational approach to describe statistical fragmentation of excited molecules and clusters. *Journal of Chemical Theory and Computation*, 13(3):992–1009, doi:10.1021/acs.jctc.6b00984. PMID: 28005371.
- Amelio, G. F., Tompsett, M. F., and Smith, G. E. (1970). Experimental verification of the charge coupled device concept. *The Bell System Technical Journal*, 49(4):593–600, doi:10.1002/j.1538-7305.1970.tb01791.x.
- Andersen, J. U., Bonderup, E., and Hansen, K. (2001). On the concept of temperature for a small isolated system. *The Journal of Chemical Physics*, 114(15):6518–6525, doi:10.1063/1.1357794.
- Andersen, T. (2004). Atomic negative ions: structure, dynamics and collisions. *Physics Reports*, 394(4):157 – 313, doi:10.1016/j.physrep.2004.01.001.
- Béroff, K., Chabot, M., Martinet, G., Pino, T., Bouneau, S., Padellec, A. L., Féraud, G., Thi, N. D., Calvo, F., Bordas, C., and Lépine, F. (2013). Anion production in high-velocity cluster-atom collisions; the electron capture process revisited. *Journal of Physics B: Atomic, Molecular and Optical Physics*, 46(1):015201, doi:10.1088/0953-4075/46/1/015201.
- Béroff, K., Van-Oanh, N. T., Chabot, M., Tuna, T., Pino, T., Martinet, G., Le Padellec, A., Carpentier, Y., and Lavergne, L. (2011). Fragmentation of multiply charged hydrocarbon molecules C_nH^{q+} ($n \leq 4$, $q \leq 9$) produced in high-velocity collisions: Branching ratios and kinetic energy release of the H^+ fragment. *Phys. Rev. A*, 84:032705, doi:10.1103/PhysRevA.84.032705.
- Bordenave-Montesquieu, D., Moretto-Capelle, P., Bordenave-Montesquieu, A., and

- Rentenier, A. (2001). Scaling of C_{60} ionization and fragmentation with the energy deposited in collisions with H^+ , H_2^+ , H_3^+ and He^+ ions (2-130 keV). *Journal of Physics B: Atomic, Molecular and Optical Physics*, 34(5):L137, doi:10.1088/0953-4075/34/5/103.
- Boyle, W. S. and Smith, G. E. (1970). Charge coupled semiconductor devices. *The Bell System Technical Journal*, 49(4):587–593, doi:10.1002/j.1538-7305.1970.tb01790.x.
- Bradforth, S. E., Kim, E. H., Arnold, D. W., and Neumark, D. M. (1993). Photoelectron spectroscopy of CN^- , NCO^- , and NCS^- . *The Journal of Chemical Physics*, 98(2):800–810, doi:10.1063/1.464244.
- Bransden, B. H. and McDowell, M. R. C. (1992). *Charge Exchange and the Theory of Ion-Atom Collisions*. Oxford Science.
- Caraby, Christophe; Grandin, J.-P. (1997). *Ionisation et dissociation de la molécule de monoxyde de carbone par impact d'ion lourd rapide multicharge*. PhD thesis, Université de Caen Normandie. Thèse de doctorat Physique Caen 1997.
- Chabot, M., Béroff, K., Gratier, P., Jallat, A., and Wakelam, V. (2013). Reactions forming $C_{n=2,10}^{(0,+)}$, $C_{n=2,4}H^{(0,+)}$, and $C_3H_2^{(0,+)}$ in the gas phase: Semiempirical branching ratios. *The Astrophysical Journal*, 771(2):90, doi:10.1088/0004-637X/771/2/90.
- Chabot, M., Fossé, R., Wohrer, K., Gardès, D., Maynard, G., Rabilloud, F., and Spiegelman, F. (2001). Multi-ionization cross-sections of small ionic carbon clusters by particle impact as a tool to investigate their shapes. *The European Physical Journal D - Atomic, Molecular, Optical and Plasma Physics*, 14(1):5–8, doi:10.1007/s100530170226.
- Chabot, M., Martinet, G., Béroff, K., Pino, T., Bouneau, S., Genolini, B., Grave, X., Nguyen, K., le Gailliard, C., Rosier, P., Féraud, G., Friha, H., and Villier, B. (2011). Detection of atomic and molecular mega-electron-volt projectiles using an x-ray charged coupled device camera. *Review of Scientific Instruments*, 82(10):103301, doi:10.1063/1.3640411.
- Chabot, M., Mezdari, F., Béroff, K., Martinet, G., and Hervieux, P.-A. (2010). Scaling Law for the Partitioning of Energy in Fragmenting Multicharged Carbon Clusters. *Phys. Rev. Lett.*, 104:043401, doi:10.1103/PhysRevLett.104.043401.
- Chabot, M., Negra, S. D., Lavergne, L., Martinet, G., Wohrer-Béroff, K., Sellem, R., Daniel, R., Bris, J. L., Lalu, G., Gardès, D., Scarpaci, J., Désesquelle, P., and Lima, V. (2002). Shape analysis of current pulses delivered by semiconductor detectors: A new tool for fragmentation studies of high velocity atomic clusters and molecules. *Nuclear Instruments and Methods in Physics Research Section B: Beam Interactions with Materials and Atoms*, 197(1):155 – 164, doi:10.1016/S0168-583X(02)01309-5.

- DuBois, R. D. and Toburen, L. H. (1988). Single and double ionization of helium by neutral-particle to fully stripped ion impact. *Phys. Rev. A*, 38:3960–3968, doi:10.1103/PhysRevA.38.3960.
- Errea, L. F., Méndez, L., Pons, B., Riera, A., Sevilla, I., and Suárez, J. (2006). Semiclassical treatment of excitation and electron loss in $A^{q+} + H(1s)$ collisions using spherical bessel functions. *Phys. Rev. A*, 74:012722, doi:10.1103/PhysRevA.74.012722.
- Fiser, J. and Polák, R. (2012). A theoretical study of spectroscopy and metastability of the CN^{2+} dication. *Chemical Physics*, 392(1):55 – 62, doi:10.1016/j.chemphys.2011.09.028.
- Garand, E., Yacovitch, T. I., and Neumark, D. M. (2009). Slow photoelectron velocity-map imaging spectroscopy of C_2N^- , C_4N^- , and C_6N^- . *The Journal of Chemical Physics*, 130(6):064304, doi:10.1063/1.3076320.
- Graupner, K., Merrigan, T. L., Field, T. A., Youngs, T. G. A., and Marr, P. C. (2006). Dissociative electron attachment to HCCCN. *New Journal of Physics*, 8(7):117, doi:10.1088/1367-2630/8/7/117.
- Grave, X., Canedo, R., Clavelin, J. F., Du, S., and Legay, E. (2005). Narval a modular distributed data acquisition system with ada 95 and rtai. In *14th IEEE-NPSS Real Time Conference, 2005.*, pages 5 pp.–. doi:10.1109/RTC.2005.1547454.
- Hotop, H. and Lineberger, W. C. (1985). Binding energies in atomic negative ions: II. *Journal of Physical and Chemical Reference Data*, 14(3):731–750, doi:10.1063/1.555735.
- IdBarkach, T., Mahajan, T., Chabot, M., Béroff, K., Aguirre, N. F., Diaz-Tendero, S., Launoy, T., Padellec, A. L., Perrot, L., and Ma (2018). Semiempirical breakdown curves of $c_2n^{(+)}$ and $c_3n^{(+)}$ molecules; application to products branching ratios predictions of physical and chemical processes involving these adducts. *Molecular Astrophysics*, pages –, doi:https://doi.org/10.1016/j.molap.2018.06.003.
- Illescas, C., Errea, L. F., Méndez, L., Pons, B., Rabadán, I., and Riera, A. (2011). Classical treatment of ion- H_2O collisions with a three-center model potential. *Phys. Rev. A*, 83:052704, doi:10.1103/PhysRevA.83.052704.
- Jallat, A. (2015). *Fragmentation de molécules carbonées d'intérêt astrophysique auprès des accélérateurs*. PhD thesis, Université Paris-Sud.
- Jorge, A., Errea, L. F., Illescas, C., and Méndez, L. (2014). Calculation of ionization and total and partial charge exchange cross sections for collisions of C_6^+ and N_7^+ with H. *The European Physical Journal D*, 68(8):227, doi:10.1140/epjd/e2014-50109-4.
- Jorge, A., Illescas, C., Méndez, L., and Pons, B. (2016). Switching classical trajectory monte carlo method to describe two-active-electron collisions. *Phys. Rev. A*, 94:022710, doi:10.1103/PhysRevA.94.022710.

- Jorge Palacios, A. M. (2017). *Theoretical treatment of inelastic processes in atomic collisions involving one and many electron systems*. Theses, UAM. Departamento de Química. Illescas Rojas, Clara (dir.).
- Khamesian, M., Douguet, N., Fonseca dos Santos, S., Dulieu, O., Raoult, M., Brigg, W. J., and Kokoouline, V. (2016). Formation of CN^- , C_3N^- , and C_5N^- molecules by radiative electron attachment and their destruction by photodetachment. *Phys. Rev. Lett.*, 117:123001, doi:10.1103/PhysRevLett.117.123001.
- Kim, H.-K., Gassert, H., Titze, J. N., Waitz, M., Voigtsberger, J., Trinter, F., Becht, J., Kalinin, A., Neumann, N., Zhou, C., Schmidt, L. P. H., Jagutzki, O., Czasch, A., Schöffler, M., Merabet, H., Schmidt-Böcking, H., Jahnke, T., Lüdde, H. J., Cassimi, A., and Dörner, R. (2014). Orientation dependence in multiple ionization of He_2 and Ne_2 induced by fast, highly charged ions: Probing the impact-parameter-dependent ionization probability in 11.37-MeV/u S^{14+} collisions with He and Ne. *Phys. Rev. A*, 89:022704, doi:10.1103/PhysRevA.89.022704.
- Labat, G., Jorge, A., Illescas, C., Béroff, K., Dubois, A., Pons, B., and Chabot, M. (2015). Electron capture and ionization processes in high-velocity C_n^+ , C – Ar and C_n^+ , C – He collisions. *Journal of Physics B: Atomic, Molecular and Optical Physics*, 48(7):075201, doi:10.1088/0953-4075/48/7/075201.
- Launoy, T., Béroff, K., Chabot, M., Martinet, G., Le Padellec, A., Pino, T., Bouneau, S., Vaeck, N., Liévin, J., Féraud, G., Loreau, J., and Mahajan, T. (2017). Ion-pair dissociation of highly excited carbon clusters: Size and charge effects. *Phys. Rev. A*, 95:022711, doi:10.1103/PhysRevA.95.022711.
- LeBrun, T., Berry, H. G., Cheng, S., Dunford, R. W., Esbensen, H., Gemmell, D. S., Kanter, E. P., and Bauer, W. (1994). Ionization and multifragmentation of C_{60} by high-energy, highly charged Xe ions. *Phys. Rev. Lett.*, 72:3965–3968, doi:10.1103/PhysRevLett.72.3965.
- Lüdde, H. J. and Dreizler, R. M. (1985). Comment on inclusive cross sections. *Journal of Physics B: Atomic and Molecular Physics*, 18(1):107, doi:10.1088/0022-3700/18/1/012.
- Lüdde, H. J., Spranger, T., Horbatsch, M., and Kirchner, T. (2009). Nonperturbative, quantum-mechanical approach to ion collisions from molecular targets. *Phys. Rev. A*, 80:060702, doi:10.1103/PhysRevA.80.060702.
- McGuire, J. H. and Weaver, L. (1977). Independent electron approximation for atomic scattering by heavy particles. *Phys. Rev. A*, 16:41–47, doi:10.1103/PhysRevA.16.41.
- Mezdari, F. (2005). *Fragmentation of (multi) charged carbon clusters produced by electronic excitation and ionisation in high velocity collisions*. Thesis, Université Pierre et Marie Curie - Paris VI.

- Moretto-Capelle, P., Bordenave-Montesquieu, D., and Bordenave-Montesquieu, A. (2000). Fragmentation of CO_2 into $\text{C}^+ + \text{O}^+ + \text{O}$, in collisions with protons. *Journal of Physics B: Atomic, Molecular and Optical Physics*, 33(15):L539, doi:10.1088/0953-4075/33/15/105.
- Murakami, M., Kirchner, T., Horbatsch, M., and Lüdde, H. J. (2012a). Quantum-mechanical calculation of multiple electron removal and fragmentation cross sections in $\text{He}^+ - \text{H}_2\text{O}$ collisions. *Phys. Rev. A*, 86:022719, doi:10.1103/PhysRevA.86.022719.
- Murakami, M., Kirchner, T., Horbatsch, M., and Lüdde, H. J. (2012b). Single and multiple electron removal processes in proton–water-molecule collisions. *Phys. Rev. A*, 85:052704, doi:10.1103/PhysRevA.85.052704.
- Nakai, Y. and Sataka, M. (1991). Electron capture and loss cross sections in collisions of C atoms with He. *Journal of Physics B: Atomic, Molecular and Optical Physics*, 24(3):L89, doi:10.1088/0953-4075/24/3/009.
- Olson, R. E. and Salop, A. (1977). Charge-transfer and impact-ionization cross sections for fully and partially stripped positive ions colliding with atomic hydrogen. *Phys. Rev. A*, 16:531–541, doi:10.1103/PhysRevA.16.531.
- Pascoli, G. and Lavendy, H. (1999). Are C_nN^- clusters really bent? *Chemical Physics Letters*, 312(2):333 – 340, doi:10.1016/S0009-2614(99)00963-X.
- Peterson, K. A. (1995). Accurate multireference configuration interaction calculations on the lowest $^1\Sigma^+$ and $^3\Pi$ electronic states of C_2 , CN^+ , BN , and BO^+ . *The Journal of Chemical Physics*, 102(1):262–277, doi:10.1063/1.469399.
- Pons, B. (2000a). Ability of monocentric close-coupling expansions to describe ionization in atomic collisions. *Phys. Rev. A*, 63:012704, doi:10.1103/PhysRevA.63.012704.
- Pons, B. (2000b). Monocentric close-coupling expansion to provide ejected electron distributions for ionization in atomic collisions. *Phys. Rev. Lett.*, 84:4569–4572, doi:10.1103/PhysRevLett.84.4569.
- Rakovic, M. J., Schultz, D. R., Stancil, P. C., and Janev, R. K. (2001). On quantum-classical correspondence in classical studies of atomic processes. *Journal of Physics A: Mathematical and General*, 34(22):4753, doi:10.1088/0305-4470/34/22/314.
- Reinhold, C. O. and Falcón, C. A. (1986). Classical ionization and charge-transfer cross sections for $\text{H}^+ + \text{He}$ and $\text{H}^+ + \text{Li}^+$ collisions with consideration of model interactions. *Phys. Rev. A*, 33:3859–3866, doi:10.1103/PhysRevA.33.3859.
- Reinköster, A., Werner, U., Kabachnik, N. M., and Lutz, H. O. (2001). Experimental and theoretical study of ionization and fragmentation of C_{60} by fast-proton impact. *Phys. Rev. A*, 64:023201, doi:10.1103/PhysRevA.64.023201.

- Rienstra-Kiracofe, J. C., Tschumper, G. S., Schaefer, H. F., Nandi, S., and El-lison, G. B. (2002). Atomic and molecular electron affinities: Photoelectron experiments and theoretical computations. *Chemical Reviews*, 102(1):231–282, doi:10.1021/cr990044u. PMID: 11782134.
- Sampoll, G., Heber, O., Maurer, R., Scott, P., and Watson, R. (1989). Two-fragment coincidence studies of molecular coulomb explosions induced by heavy ion impact. *Nuclear Instruments and Methods in Physics Research Section B: Beam Interactions with Materials and Atoms*, 40-41:308 – 312, doi:https://doi.org/10.1016/0168-583X(89)90986-5.
- Sampoll, G., Watson, R. L., Heber, O., Horvat, V., Wohrer, K., and Chabot, M. (1992). Dissociation of multicharged CO molecular ions produced in collisions with 97-MeV Ar¹⁴⁺: Total-kinetic-energy distributions. *Phys. Rev. A*, 45:2903–2914, doi:10.1103/PhysRevA.45.2903.
- Sánchez, J. P., Aguirre, N. F., Diaz-Tendero, S., Martin, F., and Alcamí, M. (2016). Structure, ionization, and fragmentation of neutral and positively charged hydrogenated carbon clusters: C_nH_m^{q+} (n=1-5, m=1-4, q=0-3). *The Journal of Physical Chemistry A*, 120(4):588–605, doi:10.1021/acs.jpca.5b10143. PMID: 26683517.
- Toburen, L. H., DuBois, R. D., Reinhold, C. O., Schultz, D. R., and Olson, R. E. (1990). Experimental and theoretical study of the electron spectra in 66.7–350-keV/u C⁺+He collisions. *Phys. Rev. A*, 42:5338–5347, doi:10.1103/PhysRevA.42.5338.
- Tsuchida, H., Itoh, A., Nakai, Y., Miyabe, K., and Imanishi, N. (1998). Cross sections for ionization C₆₀ and fragmentation of by fast H⁺ impact. *Journal of Physics B: Atomic, Molecular and Optical Physics*, 31(24):5383, doi:doi.org/10.1088/0953-4075/31/24/019.
- Valiron, P., Gayet, R., McCarroll, R., Masnou-Seeuws, F., and Philippe, M. (1979). Model-potential methods for the calculation of atom-rare-gas interaction: application to the h-he system. *Journal of Physics B: Atomic and Molecular Physics*, 12(1):53, doi:10.1088/0022-3700/12/1/014.
- Vergnes, M. (1977). Tandem physics in orsay. *Nuclear Instruments and Methods*, 146(1):81 – 88, doi:10.1016/0029-554X(77)90501-8.
- Vernhet, D., Rozet, J., Wohrer, K., Adoui, L., Stéphan, C., Cassimi, A., and Ramillon, J. (1996). Excitation in swift heavy ion-atom collisions. *Nuclear Instruments and Methods in Physics Research Section B: Beam Interactions with Materials and Atoms*, 107(1):71 – 78, doi:10.1016/0168-583X(95)00807-1.
- Wakelam, V., Herbst, E., Loison, J.-C., Smith, I. W. M., Chandrasekaran, V., Pavone, B., Adams, N. G., Bacchus-Montabonel, M.-C., Bergeat, A., Béroff, K., Bierbaum, V. M., Chabot, M., Dalgarno, A., van Dishoeck, E. F., Faure, A., Geppert, W. D., Gerlich, D., Galli, D., Hébrard, E., Hersant, F., Hickson, K. M., Honvault, P.,

- Klippenstein, S. J., Picard, S. L., Nyman, G., Pernot, P., Schlemmer, S., Selsis, F., Sims, I. R., Talbi, D., Tennyson, J., Troe, J., Wester, R., and Wiesenfeld, L. (2012). A kinetic database for astrochemistry (kida). *The Astrophysical Journal Supplement Series*, 199(1):21, doi:10.1088/0067-0049/199/1/21.
- Watson, R. and Maurer, R. (1987). Time-of-flight analysis of dissociation products from collisions of 40 MeV Ar¹³⁺ with molecular oxygen. *Nuclear Instruments and Methods in Physics Research Section A: Accelerators, Spectrometers, Detectors and Associated Equipment*, 262(1):99 – 105, doi:https://doi.org/10.1016/0168-9002(87)90196-3.
- Werner, U., Kabachnik, N. M., Kondratyev, V. N., and Lutz, H. O. (1997). Orientation effects in multiple ionization of molecules by fast ions. *Phys. Rev. Lett.*, 79:1662–1665, doi:10.1103/PhysRevLett.79.1662.
- Wiberg, K. B. and Rablen, P. R. (1993). Comparison of atomic charges derived via different procedures. *J. Comput. Chem*, pages 1504–1518, doi:10.1002/jcc.540141213.
- Wohrer, K., Chabot, M., Fossé, R., and Gardès, D. (2000). A method for “on-line” determination of beam-jet overlaps; application to cluster fragmentation studies. *Review of Scientific Instruments*, 71(5):2025–2032, doi:10.1063/1.1150572.
- Wohrer, K., Chabot, M., Rozet, J. P., Gardès, D., Vernhet, D., Jacquet, D., Negra, S. D., Brunelle, A., Nectoux, M., Pautrat, M., Beyec, Y. L., Attal, P., and Maynard, G. (1996). Swift cluster-atom collisions: experiment and model calculations. *Journal of Physics B: Atomic, Molecular and Optical Physics*, 29(20):L755, doi:10.1088/0953-4075/29/20/006.
- Wohrer, K., Chabot, M., Touati, A., and Watson, R. (1994). Model calculations of multi-ionization cross sections in high velocity ion-cluster collisions. *Nuclear Instruments and Methods in Physics Research Section B: Beam Interactions with Materials and Atoms*, 88(1):174 – 179, doi:https://doi.org/10.1016/0168-583X(94)96100-X.
- Wohrer, K. and Watson, R. L. (1993). Model calculations of multielectron ionization of O₂ molecules by fast-heavy-ion impact. *Phys. Rev. A*, 48:4784–4786, doi:10.1103/PhysRevA.48.4784.

List of Figures

1-1	Schematic diagram of the AGAT setup	11
1-2	A general view of the experimental set-up	13
1-3	View of the HICONEX 384 ion source	14
1-4	Picture of the wheel cones of the source HICONEX 384	14
1-5	Relation between mass and magnetic field	16
1-6	A picture of the Tandem accelerator	18
1-7	Outside view of AGAT set-up	21
1-8	Interior of the collision chamber	22
1-9	Gas injection system	23
1-10	Jet profile	24
1-11	Electrostatic deflector plates	25
1-12	Deflector plates under operation	26
1-13	Schematic view of the interior of the detection chamber	29
1-14	Enlargement of the depletion zone	31
1-15	Calibration of “ C^{+++} ” detector with the tri-alpha source.	32
1-16	Sketch of a cross section of the CCD sensor.	33
1-17	View of the detectors in runs of March 2015	35
1-18	View of the detectors in runs of February 2016.	36
1-19	Electronics schematic diagram	37
1-20	Principle of the acquisition	39
1-21	A live CVISU during the run	40
2-1	Current signal output before treatment; on x-axis, 0.5 ns per canal.	44

2-2	Amplitude fragmentation resolution of C_2 vs $2C$ as a function of the filtering points number of current signal.	45
2-3	Energy response of " C^+ " detector at the impact of one or several C^+ , N^+ and CN^{++} fragments ($C_3N^+ - He$ collision)	46
2-4	Mass calibration of " C^+ " detector in runs of February 2016 and October 2016.	47
2-5	DP2 window showing a coincidence between two detectors, neutral and " C^+ "	49
2-6	Loss rate calculation vs coulomb explosion energy E_c for C^+ and N^+ fragments.	51
2-7	Simulating the C^+ and N^+ hits for a well centered 14 mm \times 14 mm detector and for $E_c = 18$ eV	51
2-8	Comparison between raw (broken line and open symbols), corrected (black line and full symbols) final C_2N^{Q+} probabilities (normalized to $Q = 0$) recorded in March 2015 and results of the October 2016 run (red line and red symbols); collision $C_2N^+ - He$	52
2-9	Energy spectrum of " CN^- " detector without time selection	53
2-10	Same spectrum of Figure 2-9 with timing selection of t_{CN^-}	54
2-11	2D coincidence between " C^+ " and " CN^- " detectors without time selection t_{CN^-}	55
2-12	Same 2D spectrum as in Figure 2-11 with time selection	56
2-13	Correlation between the shape of the current signal and the fragmentation state of the projectile	57
2-14	2D (Energy \times amplitude) spectrum of $\{C_2\}$ (a) and projections (b) and (c).	58
2-15	Comparison between current signals from CN (red curve) and C_2 (black curve). Top: raw results; down: normalized signals.	59
2-16	Comparison between current signals from C (red curve) and N (black curve); top: raw results; down: normalized signals.	60
2-17	Mass resolution of the CCD camera	61

2-18	Distribution of distances between two impacts measured in the collision $C_2N^+ - He$	62
2-19	Schematic illustration of beam and jet relative positions.	65
2-20	An example of beam-jet profile fitted to a Gaussian function.	66
2-21	Dependence of $C^-/C/N/C^+$ probability with B_{jet}	68
2-22	Probabilities as a function of B_{jet}	70
3-1	Schematic view of the molecule-atom collision	72
3-2	Cross section calculation, for a given process, in ion-atom (a), ion-linear molecule (b) and general ‘3D molecule-atom’ (c) configurations.	76
3-3	A schematic diagram showing a 3 body collision	80
3-4	Comparison of the quantum and microcanonical distributions of $H(1s)$ in the coordinate and momentum spaces.	82
3-5	Comparison of radial densities in N and N^+ with V_{mod} (solid line) or with Hartree-Fock (broken line) potential.	86
3-6	$2e^-$ exclusive probabilities as a function of the impact parameter b in $C^+ - He$, $v=2.25$ au with 100×100 , 500×500 , 1000×1000 and 1500×1500 trajectories.	87
3-7	Target ionization in $C(2p)-He$ collision. $1e^-$ calculations.	89
3-8	Target ionization and target electron loss in $C^+(2p)-He$ collision. $1e^-$ and $2e^-$ calculations.	90
3-9	Model potentials and its derivatives for $He-e^-$ system	91
3-10	Projectile ionization in $N-He$ system. Comparison between $1e^-$ calcu- lation using $V1(\alpha \neq 0)$ and $2e^-$ calculations.	92
3-11	Projectile excitation in $N-He$ system. Comparison between $1e^-$ calcu- lation using $V1(\alpha \neq 0)$ and $2e^-$ calculations.	92
3-12	Classical domains for classical n_c values of C electronic spectrum for different values of the classical kinetic momentum L	94

3-13	$2s$ - $2p$ excitation probability $P(b)$ as a function of b in H^+ - $N(2s)$ collision ($v = 2.25au$). Comparison between quantum calculations and classical calculations with different bin ranges	95
4-1	General view of the geometries of the first isomers of C_nN^+ ($n=1-3$).	106
4-2	Geometry of the lowest energy isomer of CN^+ molecule.	107
4-3	Geometry of the lowest energy isomer of C_2N^+ molecule.	107
4-4	Geometry of the lowest energy isomer of C_2N^+ molecule in cyclic configuration.	107
4-5	Geometry of the lowest energy isomer of C_3N^+ molecule	108
4-6	Geometry of the lowest energy isomer of C_3N^+ molecule in cyclic configuration.	108
4-7	Measured Carbon K shell ionization cross sections in $C^+ - He$ collisions as a function of the projectile energy $E(\text{MeV/u})$	113
4-8	Measured projectile ionization cross sections in $C_3H^+ - He$ collisions at $v=4.5$ au. Solid line: IAE including inner shell ionization; dashed line: IAE without inner shell ionization.	113
4-9	Comparison between experimental cross sections and IAE/CTMC predictions for projectile ionization (CTMC $2e^-$ calculation).	114
4-10	Comparison between experimental cross sections and IAE/CTMC predictions for projectile ionization (CTMC $1e^-$ calculation).	115
4-11	Comparison between measured dissociative excitation cross sections and projectile excitation cross sections predicted by the IAE/CTMC model.	116
4-12	Comparison between experiment and IAE/CTMC model for projectile neutralization cross sections.	117
4-13	Comparison between experiment and IAE/CTMC model for anionic production cross sections.	118
5-1	Internal energy distribution of C_2N (solid line) and C_3N (dashed line) extracted from measured $BR(N_f)$	123

5-2	Internal energy distribution of C_2N^+ (solid line) and C_3N^+ (dashed line) extracted from measured $BR(N_f)$	125
5-3	Calculated $K_d/(K_d + K_e)$ ratios as a function of C_n^- internal energy where K_d and K_e are calculated rates for dissociation and electron emission respectively.	132
5-4	Energy deposit in C_2N^+ by single electron excitation calculated by IAE/CTMC	138
5-5	Energy deposit in C_2N^+ by single and multiple electron excitation calculated by IAE/CTMC	139
5-6	Energy deposit in C_2N^+ by single and multiple electron excitation and including excitation to autoionizing states calculated by IAE/CTMC	139
5-7	Calculated energy deposit in CN^+ without (solid line) and with (broken line) inclusion of the autoionizing states following single and multiple excitation in CN^+ -He collisions.	140
5-8	Calculated energy deposit in C_2N^+ without (solid line) and with (broken line) inclusion of the autoionizing states following single and multiple excitation in C_2N^+ -He collisions.	141
5-9	Calculated energy deposit in C_3N^+ without (solid line) and with (broken line) inclusion of the autoionizing states following single and multiple excitation in C_3N^+ -He collisions.	141
5-10	Comparison between calculated and semiempirical internal energy deposits due to single and multiple excitation of C_2N^+ in C_2N^+ -He collisions.	142
5-11	Comparison between calculated and semiempirical internal energy deposits due to single and multiple excitation of C_3N^+ in C_3N^+ -He collisions.	143
5-12	Measured BR for IPD dissociation of C_nN^{Q+} species as a function of Q for different species: CN^{Q+} (circles), C_2N^{Q+} (squares) and C_3N^{Q+} (triangles).	144

5-13 Measured BR for IPD dissociation of C_n^{q+} species as a function of q
and n. From Launoy et al. (2017) 145

List of Tables

1.1	Beam intensities obtained with a cone made of 50 % of TiN and 50 % of graphite	15
1.2	Species most probable internal energy.	17
1.3	Voltages at the terminal for the production of iso-velocity C_nN^+ species.	19
1.4	Deviations of the fragments at the detector positions during the run of March 2015; $\Delta V = 26kV$	27
1.5	Deviations of the fragments at the detector positions during the run of February and October 2016; $\Delta V = 42kV$	28
1.6	Detector configuration of March 2015 ($\Delta V = 26kV$).	34
1.7	Detector configuration of February 2015 ($\Delta V = 42kV$).	36
2.1	Mass calibration of " C^+ " detector.	48
2.2	Comparison between simulated and measured loss rates of C^+ in C^+/N^{q+} fragmentation channels	50
2.3	Comparison between dissociation BR measured with the CCD camera and with the shape analysis method ($C_2N^+ - He$) collision.	63
2.4	Measured B_{jet} in the experiments	67
3.1	Energy levels of V_{mod} compared to NIST values for N atom.	86
3.2	Energy levels of V_{mod} compared to NIST values for N^+ atom.	86
3.3	The optimised A, B, C parameters for the projectile-electron model potential.	86

3.4	Percentage (%) of projectile excitation into final n levels in $N(2s, 2p)$ - He collision (2.25 au); $1e^-$ calculation ($V1, \alpha \neq 0$)	96
3.5	Comparison between measured and calculated cross sections with $2e^-$ calculation for projectile ionization.	97
3.6	Comparison between measured and calculated cross sections with $1e^-$ calculation for projectile ionization.	98
4.1	Measured cross sections for various electronic processes in the CN^+ - He ($v= 2.2$ au) collision.	102
4.2	Measured cross sections for various electronic processes in the C_2N^+ - He ($v= 2.2$ au) collision.	103
4.3	Measured cross sections for various electronic processes in the C_3N^+ - He ($v= 2.2$ au) collision.	103
4.4	Measured cross sections for various electronic processes in the $C^+ - He$ and $N^+ - He$ collision ($v=2.2$ au).	104
4.5	Position of the atoms in the barycentre of the molecules and Mulliken charges.	105
4.6	Total energies of atomic and molecular systems of interest here. Cal- culations by N. Aguirre and S. Diaz-Tendero.	109
4.7	Role of the charge position on predicted cross sections.	110
4.8	Role of the molecular shape on predicted cross sections.	112
5.1	Measured dissociation BR of excited CN species produced by electron capture in CN^+ -He collisions.	122
5.2	Measured dissociation BR of excited C_2N species produced by electron capture in C_2N^+ -He collisions.	122
5.3	Measured dissociation BR of excited C_3N species produced by electron capture in C_3N^+ -He collisions.	122
5.4	Measured dissociation BR of excited CN^+ species produced by projec- tile electronic excitation in CN^+ -He collisions	124

5.5	Measured dissociation BR of excited C_2N^+ species produced by projectile electronic excitation in C_2N^+ -He collisions	124
5.6	Measured dissociation BR of excited C_3N^+ species produced by projectile electronic excitation in C_3N^+ -He collisions	124
5.7	Measured dissociation BR of excited CN^{++} species produced by projectile single ionisation in CN^+ -He collisions.	126
5.8	Measured dissociation BR of excited C_2N^{++} species produced by projectile single ionisation in C_2N^+ -He collisions.	126
5.9	Measured dissociation BR of excited C_3N^{++} species produced by projectile single ionisation in C_3N^+ -He collisions.	127
5.10	Measured dissociation BR of excited CN^{+++} species produced by projectile double ionisation in CN^+ -He collisions.	128
5.11	Measured dissociation BR of excited C_2N^{+++} species produced by projectile double ionisation in C_2N^+ -He collisions.	128
5.12	Measured dissociation BR of excited C_3N^{+++} species produced by projectile double ionisation in C_3N^+ -He collisions.	129
5.13	Measured dissociation BR of excited CN^{++++} species produced by projectile triple ionisation in CN^+ -He collisions.	129
5.14	Measured dissociation BR of excited C_2N^{++++} species produced by projectile triple ionisation in C_2N^+ -He collisions.	129
5.15	Measured dissociation BR of excited C_3N^{++++} species produced by projectile triple ionisation in C_3N^+ -He collisions.	130
5.16	Measured dissociation BR of excited CN^- species produced by double electron capture in CN^+ -He collisions.	131
5.17	Measured dissociation BR of excited C_2N^- species produced by double electron capture in C_2N^+ -He collisions.	131
5.18	Measured dissociation BR of excited C_3N^- species produced by double electron capture in C_3N^+ -He collisions.	131
5.19	Experimental electron affinities used in the calculation of channel dissociation energies of C_nN^- anionic species.	132

5.20	Energies of reachable states in carbon atom starting from the ground state $2s^2 2p^2 \ ^3P_0$	135
5.21	Energies of reachable states in the C^+ ion starting from the ground state $2s^2 2p \ ^2P_{1/2}$	136
5.22	Energies of reachable states in Nitrogen atom starting from the ground state $2s^2 2p^3 \ ^4S_{3/2}$	137
B.1	Measured branching ratios within ion pair dissociation of C_2N excited species.	174
B.2	Measured branching ratios within ion pair dissociation of C_2N^+ excited species.	174
B.3	Measured branching ratios within ion pair dissociation of C_2N^{++} excited species.	174
B.4	Measured branching ratios within ion pair dissociation of C_2N^{+++} excited species.	175
B.5	Measured branching ratios within ion pair dissociation of C_3N excited species.	175
B.6	Measured branching ratios within ion pair dissociation of C_3N^+ excited species.	176
B.7	Measured branching ratios within ion pair dissociation of C_3N^{++} excited species.	176
B.8	Measured branching ratios within ion pair dissociation of C_3N^{+++} excited species.	176

Titre: Excitation et fragmentation des molécules C_nN^+ ($n = 1-3$) en collision avec des atomes de He à vitesse intermédiaire; aspects fondamentaux et application à l'astrochimie.

Mots clés: Molécules, Collisions, Rapports de branchement de fragmentation, Astrochimie, Sections efficaces, La méthode Monte Carlo de trajectoires classiques (CTMC).

Résumé: Dans cette thèse nous avons étudié des collisions entre des projectiles C_nN^+ ($n=0,1,2,3$) et des atomes d'Hélium à vitesse intermédiaire (2.25 u.a). A cette vitesse, proche de la vitesse des électrons sur les couches de valence externe des atomes et molécules, de nombreux processus électroniques prennent place avec une forte probabilité: ionisation (simple et multiple), excitation électronique, capture d'électron (simple et double). Nous avons mesuré les sections efficaces absolues de tous ces processus. Un autre aspect intéressant de la collision concerne la fragmentation des molécules excitées, que nous avons également mesurée précisément grâce à un dispositif dédié.

Les expériences ont été effectuées auprès de l'accélérateur Tandem d'Orsay avec des faisceaux de quelques MeV d'énergie cinétique. Le dispositif AGAT a permis de réaliser les collisions (en condition de collision unique) et de mesurer tout à la fois les sections efficaces des processus et la fragmentation associée.

Parallèlement nous avons simulé ces collisions d'un point de vue théorique en utilisant le modèle à Atomes et Electrons Indépendants (IAE) couplé à des calculs CTMC (Classical trajectory

Monte Carlo). Sur cette base, nous avons prédit les sections efficaces qui se sont trouvées être en bon accord avec les mesures, à l'exception de la double capture d'électrons. Par ailleurs les rapports de branchement de dissociation des C_nN^+ après excitation électronique sont bien reproduits en utilisant la distribution d'énergie interne des espèces calculées avec le même modèle IAE/CTMC.

Ces expériences nous ont permis de construire des « Breakdown Curves » (BDC), véritables cartes d'identité des molécules qui permettent de prévoir, dans le cadre d'une fragmentation statistique comment va fragmenter un système dont on connaît l'énergie interne. Avec ces BDC nous avons pu prédire et recommander des rapports de branchement pour des voies de sortie de processus physiques et chimiques d'intérêt astrochimique. Ces données seront insérées dans la base internationale d'astrochimie the Kinetic Data Base for Astrochemistry KIDA.

Cette thèse a été réalisée dans le cadre de l'École Doctorale Ondes et Matière (EDOM) à l'Institut des Sciences Moléculaires d'Orsay (ISMO), à l'Université Paris-Sud (Université Paris Saclay).

Title: Excitation and fragmentation of C_nN^+ ($n=1-3$) molecules in collisions with He atoms at intermediate velocity; fundamental aspects and application to astrochemistry.

Keywords: Molecules, Collisions, Fragmentation branching ratios, Astrochemistry, Cross sections, Classical Trajectory Monte Carlo.

Abstract: This thesis studies the aftermath of collision between singly positively charged Nitrogenated carbon species C_nN^+ ($n=0,1,2,3$) and neutral Helium atom at a velocity of 2.25 au. At this velocity, close to the velocity of outer electrons in atoms and molecules, several electronic processes take place and are near their maximum of probability such as ionisation (single, double, triple...), electronic excitation and electron capture (single and double). We looked at their cross sections and how their evolution with the molecule size. Following the collision the molecule can fragment, which leads to another interesting aspect, the fragmentation branching ratios.

Collision experiments were done using a Tandem accelerator at Orsay that produced the C_nN^+ projectiles and a dedicated set-up, AGAT, to capture the flying fragments/intact molecule after collision according to their charge to mass ratio. Knowing the number of particles that are shot and the fact that our set-up allows no loss of fragments/intact molecule, we could get the probabilities of various fragments formed. Using these probabilities and a knowledge of the Helium jet profile used, we could measure their cross sections. The probabilities alone are sufficient to obtain the fragmentation branching ra-

tios.

The next step was to use a theoretical model to simulate the collision. We used Independent Atom and Electron (IAE) model coupled with Classical Trajectory Monte Carlo (CTMC) method to calculate the desired cross sections. A general good agreement was obtained, with the exception of double electron capture. The model could also predict, through the calculation of the species internal energy, the fragmentation branching ratios of cations C_nN^+ after electronic excitation. Also, the branching ratios were used to construct semi-empirical Breakdown Curves (BDCs), which are internal energy dependent dissociation branching ratios specific to each molecule, type, size and charge. With those, we could recommend products branching ratios to be used for various processes of astrochemical interest. The products branching ratios will be made available for a wider network of researchers under the international Kinetic Database for Astrochemistry (KIDA).

This thesis was realized under the doctoral programme of École Doctorale Ondes et Matière (EDOM) with Institut des Sciences Moléculaires d'Orsay (ISMO) where the author was given an office and Université Paris-Sud (Université Paris-Saclay) where the author is formally enrolled.

